Technische Universität München

TUM School of Natural Sciences

TUM

Synthesis and Evaluation of Performance Enhanced Re(I)/Ru(II)-based Catalysts for the Photocatalytic Reduction of CO$_2$

Christopher Thomas

Vollständiger Abdruck der von der TUM School of Natural Sciences der Technischen Universität München zur Erlangung eines

Doktors der Naturwissenschaften (Dr. rer. nat.)

genehmigten Dissertation.

Vorsitz: Prof. Dr. Martin Stutzmann

Prüfer*innen der Dissertation:

1. Prof. Dr. Dr. h.c. Bernhard Rieger
2. Prof. Dr. Tom Nilges

Die Dissertation wurde am 24.04.2023 bei der Technischen Universität München eingereicht und durch die TUM School of Natural Sciences am 23.06.2023 angenommen.

I

"*walk the footsteps of a stranger,*

you'll learn things you never knew

you never knew"

Pocahontas

Die vorliegende Arbeit wurde in der Zeit von Januar 2019 bis Juli 2022 am WACKER-Lehrstuhl für Makromolekulare Chemie, Technische Universität München, unter Betreuung von Herrn Prof. Dr. Dr. h.c. Bernhard Rieger angefertigt.

Acknowledgements

Ein besonderer Dank gilt allen voran meinem Doktorvater Professor Rieger, für die Möglichkeit an Ihrem Lehrstuhl meine Promotion durchzuführen. Sie haben mir Ihr Vertrauen geschenkt und mich während dieser Zeit mit viel Input unterstützt. Ich habe die Freiheiten, eigene Ideen zu verfolgen, sehr genossen und konnte mich dadurch fachlich und persönlich optimal entfalten.

Als nächstes möchte ich mich bei Carsten bedanken, der für die Organisation am Lehrstuhl unersetzlich ist und bei technischen Problemen an Geräten immer eine helfende Hand hat. Zusätzlich hat dein Talent am Grill uns den ein oder anderen erinnerungswürdigen Sommerabend beschert. Sergei, bei dir möchte ich mich für die ausgiebige Hilfe bei den zahlreichen fachlichen Fragen bedanken. Du hattest immer ein offenes Ohr und bist dadurch Ideengeber von so einigen erfolgreichen Projekten. Vielen Dank Frau Bauer für die Hilfe bei den ganzen organisatorischen Fragen, da haben Sie mir bei den ganzen Anträgen, Formularen und Terminen viel Arbeit abgenommen.

Ganz besonders möchte ich mich bei meinen Lehrstuhlkollegen für das großartige Arbeitsklima bedanken, weshalb ich jeden Tag gerne ins Labor gekommen bin. Insbesondere möchte ich die Nordseite hervorheben und mich nochmal bei den Alumnis wie Basti und Andi und den jüngeren Kollegen Alina, Kerstin, Lena, Moritz, Simon, Lucas, Jonas, Philipp und Lukas bedanken.

Ein riesiges Dankeschön gilt meinen Kooperationspartnern Johannes, Philip und Moritz, die mit einer Hingabe und einem Eifer an den Projekten gearbeitet haben, welche nicht selbstverständlich sind. Danke, dass wir die Themen gemeinsam so erfolgreich gestalten konnten.

Einen weiteren Dank möchte ich noch all meinen Studenten und insbesondere meinen Masteranden Marina und Toni aussprechen. Ihr habt großartige Arbeit geleistet und es war mir eine Freude mit euch gemeinsam zu forschen.

Natürlich gilt ein großer Dank meinen Wapplerinnen und Wapplern aus der Heimat. Bei euch konnte immer gut abschalten und meine Akkus durch gemeinsame Aktivitäten aufladen.

Mein ganz besonderer Dank gilt meiner Familie. Danke Mama und Papa für die Unterstützung während der langen Studien- und Promotionszeit. Raphi, du hast mir bei schwierigen Entscheidungen geholfen und stehst immer hinter mir; Dankeschön!

Und zu guter Letzt und am allerwichtigsten, möchte ich mich bei meiner besseren Hälfte bedanken. Danke Michi, dass du immer ein offenes Ohr für meine Probleme hast, auch wenn diese mit Orbitalen zu tun haben. Du bist der wichtigste Mensch in meinem Leben.

List of Abbreviations

AFM	atomic force microscopy
ALD	atomic layer deposition
Al(i-Bu)$_3$	triisobutylaluminum
ATR FTIR	attenuated total reflection *Fourier*-transform-infrared-spectrometry
BIH	1,3-dimethyl-2-phenyl-2,3-dihydro-1H-benzo[d]imidazole
BNAH	1-benzyl-1,4-dihydronicotinamide
BNA$_2$	1-benzyl-1,4-dihydronicotinamide dimer
bpy	2,2′-bipyridine
cat	catalyst
CO	carbon monoxide
CO$_2$	carbon dioxide
D	donor
dcbpy	dicarboxy-2,2′-bipyridine
DFT	density-functional theory
DMA	N,N-dimethylacetamide
DMAP	N,N-dimethylpyridin-4-amine
dmb	4,4'-dimethyl-2,2'-bipyridine
dmb-dmb	1,2-bis[4-(4'-methyl-2,2'-bipyridyl)]ethane
EDC	3-(((ethylimino)methylidene)amino)-N,N-dimethylpropan-1-amine
EDTA	ethylenediaminetetraacetic acid
eV	electronvolt
FLP-GTP	group transfer polymerisation with frustrated *Lewis*-pairs
FRET	*Förster* resonance energy transfer
Gt	gigatonne
HOMO	highest occupied molecular orbital
ICP-MS	inductively coupled plasma mass spectrometry
IC	internal conversion
IL/CT	intraligand-charge-transfer
IR	infrared
ISC	intersystem crossing
LED	light-emitting diode
LUMO	lowest unoccupied molecular orbital
^{1}MLCT	singlet metal-to-ligand-charge-transfer

^{3}MLCT	triplet metal-to-ligand-charge-transfer
NEXAFS	near edge X-ray absorption fine structure
nm	nanometer
OEOS	one-electron-oxidised-species
OERS	one-electron-reduced-species
PÐI	polydispersity index
PL	photoluminescence
PMe$_3$	trimethylphosphine
POM	polyoxometalate
ppm	parts per million
ppy	*fac*-tris(2-phenylpyridine)
PVBpy	poly-4-vinyl-4′-methyl-2,2′-bipyridine
PS	photosensitiser
Re	Re(4,4'-dimethyl-2,2'-bipyridine)(CO)$_3$Cl
Ru	[Ru(4,4'-dimethyl-2,2'-bipyridine)$_3$](PF$_6$)$_2$
RuRe	[Re(CO)$_3$Cl(dmb-dmb)Ru(dmb)$_2$](PF$_6$)$_2$
RuRe2	[Re(CO)$_3$Cl(dmb-dmb)Ru(dmb)(dmb-dmb)Re(CO)$_3$Cl](PF$_6$)$_2$
RuRe3	[Ru(Re(CO)$_3$Cl(dmb-dmb))$_3$](PF$_6$)$_2$
qpy	qpy = 2,2′:6′,2″:6″,2‴-quaterpyridine
SCE	saturated calomel electrode
SPEM	scanning photoelectron microscopy
SHE	standard hydrogen electrode
TaON	tantalum(V) oxynitride
TEA	triethylamine
TEOA	triethanolamine
TOF	turnover frequency
TON	turnover number
UiO	Universitet i Oslo
V	volts
vbpy	4-vinyl-4′-methyl-2,2′-bipyridine
XPS	X-ray photoelectron spectroscopy
XRR	X-ray reflectometry

Publications List

- Johannes D. Bartl,[‡*] <u>Christopher Thomas</u>,[‡*] Alex Henning, Martina F. Ober, Gökcen Savasci, Bahar Yazdanshenas, Peter S. Deimel, Elena Magnano, Federica Bondino, Patrick Zeller, Gregoratti, Matteo Amati, Claudia Paulus, Francesco Allegretti, Anna Cattani-Scholz, Johannes V. Barth, Christian Ochsenfeld, Bert Nickel, Ian D. Sharp, Martin Stutzmann, and Bernhard Rieger, *J. Am. Chem. Soc.* **2021**, *143*, 19505-19516, "Modular Assembly of Vibrationally and Electronically Coupled Rhenium Bipyridine Carbonyl Complexes on Silicon."

- Anton S. Maier,[‡] <u>Christopher Thomas</u>,[‡] Moritz Kränzlein,[‡] Thomas M. Pehl, and Bernhard Rieger,* *Macromolecules* **2022**, *55*, 7039-7048, "Macromolecular Rhenium–Ruthenium Complexes for Photocatalytic CO_2 Conversion: From Catalytic Lewis Pair Polymerization to Well-Defined Poly(Vinyl Bipyridine)–Metal Complexes. "

- <u>Christopher Thomas</u>,[‡] Marina Wittig,[‡] and Bernhard Rieger,* *ChemCatChem* **2022**, *14*, e202200841, "The Puzzling Question about the Origin of the Second Electron in the Molecular Photocatalytic Reduction of CO_2."

Publications beyond the Scope of this Thesis

- Philip M. Stanley, <u>Christopher Thomas</u>, Erling Thyrhaug, Alexander Urstoeger, Michael Schuster, Jürgen Hauer, Bernhard Rieger, Julien Warnan,* Roland A. Fischer,* *ACS Catal.* **2021**, 11, 871-882, "Entrapped Molecular Photocatalyst and Photosensitiser in Metal−Organic Framework Nanoreactors for Enhanced Solar CO_2 Reduction."

- Philip M. Stanley, Johanna Haimerl, <u>Christopher Thomas</u>, Alexander Urstoeger, Michael Schuster, Natalia B. Shustova, Angela Casini, Bernhard Rieger, Julien Warnan, Roland A. Fischer,* *Angew. Chem.* **2021**, *60*, 17854-17860, "Host-Guest Interactions in Metal-Organic Framework Isoreticular Series for Molecular Photocatalytic CO_2 Reduction."

Conference Contribution

- <u>Christopher Thomas</u>, Markus Pschenitza, Simon Meister, Bernhard Rieger, e-conversion **2019**, Venice, poster presentation, "Suppression of Deactivation Processes in the Photocatalytic Reduction of CO_2."

- <u>Christopher Thomas</u>, Bernhard Rieger, Pacifichem **2021**, virtual talk, "The supportive role of the third Re-unit in the photocatalytic CO_2-reduction of supramolecular complexes."

- <u>Christopher Thomas</u>, Marina Wittig, Bernhard Rieger, ACS Spring conference **2022**, San Diego, poster presentation, "Photocatalytic Reduction of CO_2 to CO using Dendrimeric Ru(II)/Re(I)-catalysts."

Table of Contents

1.   Introduction

The growing world population in combination with the technological progress leads to an increased demand for resources and energy.[1] A large part of the rising energy request is covered by limited fuels such as coal, natural gas, and oil.[2] By converting these fossil fuels carbon dioxide (CO_2) is emitted and added to the carbon cycle. This anthropogenic production cannot be fully absorbed by natural carbon sinks, such as terrestrial ecosystems and oceans, resulting in an accumulation in the atmosphere. Before humanity started commercially burning fossil fuels, the concentration of CO_2 in the atmosphere was 280 ppm.[3] Starting with the industrial revolution, CO_2 concentration increased steadily to more than 410 ppm today.[3] Next to water vapor, chlorofluorocarbons, nitrous oxide, and methane, CO_2 is one of the main greenhouse gases contributing to global climate change, as these molecules can absorb the infrared radiation emitted by the surface of the earth and reemit these electromagnetic waves back.[4] Global warming leads to an increased probability for extreme weather phenomena like heat waves, droughts, and storms. Furthermore, coastal cities are facing an enormous challenge with rising sea levels, due to melting ice caps. Hence, a paradigm change is critical to control emissions and therefore fight man-made global change, a paradigm change is critical. To provide a secure and CO_2-neutral energy supply, a switch to non-fossil energy sources such as wind, solar, nuclear, and geothermal energy, and the development of methods for transforming this energy into forms that can be stored, transported, and used upon demand is required. In the medium term and for processes in which CO_2 emissions are unavoidable, an important approach is to consider CO_2 as a cheap and abundant resource rather than a pollutant. In this context, CO_2 can be used as a new feedstock for fuels, basic chemicals, or plastics, which are currently produced mainly from limited fossil resources.[5]

A potential method for a climate-friendly production of higher-energy materials is the photocatalytic conversion of CO_2. One of the most common products of this light-initiated reaction is carbon monoxide. This reduction of CO_2 to CO can be followed by the *Fischer-Tropsch* synthesis to yield high-value hydrocarbons as solar fuels.[6] This approach not only tackles the shortage of fossil resources but also establishes an alternative carbon source without adding carbon to the atmosphere.[7] To ensure an environmentally friendly and sustainable CO_2 conversion, sunlight should provide the energy required for this process. Additionally, the resulting solar fuels represent an attractive opportunity for storage with a high-density solar energy using a climate-friendly and abundant resource.[8] Special CO_2 reducing photocatalysts have been developed to use light as an energy source. Rhenium-based photocatalysts, which enable a selective reduction of CO_2 to CO, have been described 40 years ago.[9] However, these metal complexes are not yet usefully employed on an industrial scale, as they show weaknesses in productivity and stability.[8, 10] For these reasons, further

Introduction

research is required in order to develop more stable, efficient, and powerful systems, that can contribute to a climate-neutral fuel production using CO_2 as substrate.

2.   Theoretical Background

2.1   Greenhouse Gas CO_2

Carbon dioxide along with other infrared active gases such as water vapor, nitrous oxide, or methane are known for their contribution to greenhouse effect. These molecules partially absorb the infrared rays emitted by the earth, preventing some of this energy from escaping into the extraterrestrial. Without this energy absorption by the greenhouse gases, the average temperature on the earth's surface would be -18 °C.[11] Due to human activity, atmospheric concentrations of several greenhouse gases have increased since the industrial era.[12] CO_2 is one of the most prominent examples, having been released in the largest quantity over the last 200 years due to the depletion of fossil resources (Figure 1).
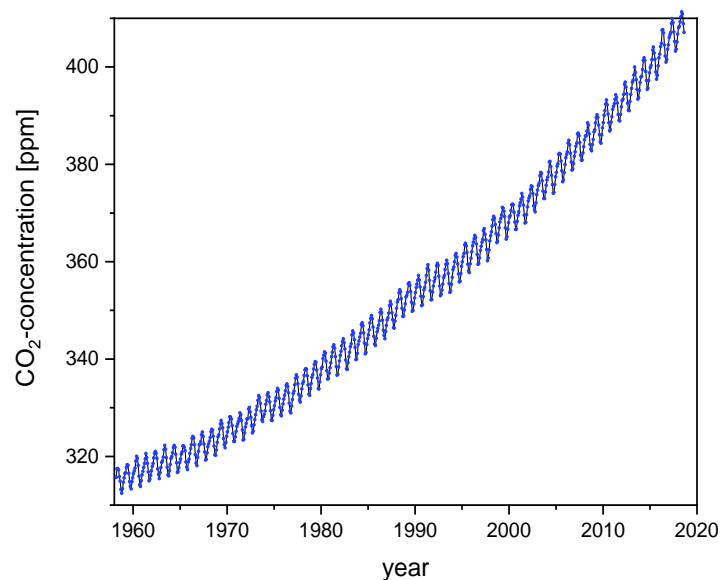

Figure 1: Monthly measurements of atmospheric carbon dioxide concentration beginning in 1958 (location: Mauna Loa Observatory).[13]

These additional greenhouse gases in the atmosphere increase the amount of absorbed infrared radiation, temporarily causing the earth to absorb more energy via the sun's radiation than is released to the universe. As a result, the earth's surface and air temperature increases, which we observe as the human-induced global warming.[14] Even if humanity manages to limit this global warming to 2 °C, as stated in the 2015 Paris Agreement, the impacts include melting glaciers, ocean level rise, more frequent extreme weather and bigger land areas to be uninhabitable.[15] To minimise these negative impacts and meet the 2 °C target, countermeasures such as saving or reusing climate-active gases are part of a global effort.

2.2 CO_2 Emissions Savings

Only about half of the annual anthropogenic CO_2 emissions of about 35 Gt are absorbed by forests, peatlands, and aquatic systems in the natural carbon cycle.[16] The second half contributes to the additional carbon dioxide accumulation in the atmosphere with the consequences on the climate as described in chapter 2.1. Reducing CO_2 emissions is so far the most important and viable option to limit the growing CO_2 concentration in the atmosphere. As versatile as the ways for CO_2 emission are also the possibilities to save them. In the short term, a fuel shift from coal to gas can decrease CO_2 emissions per kWh by almost 50%.[16b] More climate-friendly and unavoidable in the medium term, however, are the extensive conversion of electricity production from fossil resources to renewable energy sources and the general improvement of efficiency in energy utilisation. Low CO_2 emitting energy sources include wind, solar, biomass, hydropower, or geothermal energy.[17] It must be mentioned here that although these provide a stable base load in electricity in some cases, they cannot respond to peaks in demand from the electricity consumer.[18] Therefore, a successful conversion to renewable energies is linked to the possibility of storing high amounts of electricity and releasing them when required.[19] This could be accomplished with an international electricity grid and electricity-powered vehicles connected to it. The latter could not only serve as storage, but electrify the area of mobility, increasing the efficiency of energy resources.[20] Furthermore, the insulation of buildings coupled with the general more conscious personal attitude towards energy use are important points to reduce CO_2 emissions.[16b]

Despite all the potential, it will be difficult to avoid all man-made CO_2 emissions. Many industry and construction-related processes produce CO_2 as a byproduct that cannot be replaced or reduced as things stand today.[21] For this reason, there are also approaches to deal with unavoidable CO_2 emissions.

2.3 CO_2 in the Case of Unavoidable Emissions

Even, if the generation of CO_2 cannot be pushed below the level that the natural carbon cycle can absorb, the accumulation of climate-active gas in the atmosphere can be avoided. The so-called carbon capture and storage (CCS) principle describes the collection, purification, and storage of produced CO_2 to limit the emission into the environment.[16b, 22] However, the separation of CO_2 from exhaust gas is currently still an energy-intensive process and reduces the efficiency of power plants using this technology.[22] In addition, the CCS technology is to be viewed critically due to the uncertainty about the long-term stability of underground storage sites regarding the possibility of leakage.

A more reasonable approach is the carbon capture and utilisation (CCU) approach. In this context, CO_2 is used as a feedstock for the chemical industry and is thus transformed into a resource. This technology would reduce both the need for extraction of fossil carbon and the emission of CO_2 due to recycling the carbon.[16b] However, only a small amount of CO_2-emission is suitable for this conversion method and thus the current climate crisis cannot be solved with this approach alone. Rather, it represents one solution among many for unavoidable CO_2 emissions. The CCU concept offers a new, accessible, and inexpensive feedstock as an alternative to fossil carbon sources, which is of great economic interest.[23] In order to activate the thermodynamically stable CO_2, making the molecule accessible for a wide variety of chemical reactions, it must first be reduced by electron input.[23a, 23c] In addition to the electrons needed, a high energy barrier must be passed for this conversion.[24] A particularly sustainable approach is to obtain the energy needed for conversion from solar radiation. For this nature mimicking process catalysts are required that absorb light and use this energy for the specific conversion of CO_2.

2.4 Basics of Photochemistry

The most important direct energy source, the sun, can be harvested efficiently via photochemical reactions. One of the central processes is the photosynthesis, which was crucial for the development of life, is vital for plant growth, and determines the atmospheric composition.[25] The absorbed sunlight provides the activation energy for the chemical reactions by stimulating a molecule into an excited state. In general, photochemical reactions by definition do not occur exclusively in the electronic ground state of the involved molecules.[26] Due to this excited state, photochemistry offers a wide range of applications from the [2+2]-cycloaddition to photoisomerisation to the conversion of CO_2, which are not as accessible under the absence of irradiation sources.[27] To understand the light-matter-interaction, quantum mechanics describes the molecules in their respective states by the corresponding wave functions.[26]

Molecules in the excited state differ significantly from their ground state analogue. Energy absorption results in a redistribution of electron density, as there is a depopulation of the electronic ground state and a simultaneous population of an electronically excited state. As a result, physical properties such as molecular geometry and bond distances are affected and the redox potentials of the molecule change due to the energetically high lying electrons.[26, 28] The electronic transitions can be described by means of the *Franck-Condon* principle.[29] The principle is based on the *Born-Oppenheimer* approximation, which states that electron motion can be considered decoupled from the associated atomic nuclear motion.[28] This can be assumed as the electrons (10^{-15} s) of a system move three orders of magnitude faster than the

inert atomic nuclei (10^{-12} s) due to their much smaller masses. Due to this discrepancy in particle inertia, the excitation of molecules by photons can be described as vertical absorption, in which the nuclear coordinates remain fixed according to the *Franck-Condon* principle. Here, the transition probability is the highest when the vibrational wave function of the excited electronic state has the largest possible overlap with that of the electronic ground state.[30] Figure 2 shows the vertical absorption by excitation from the singlet ground state S_0 into the first electronically excited singlet state S_1 (Figure 2, orange).
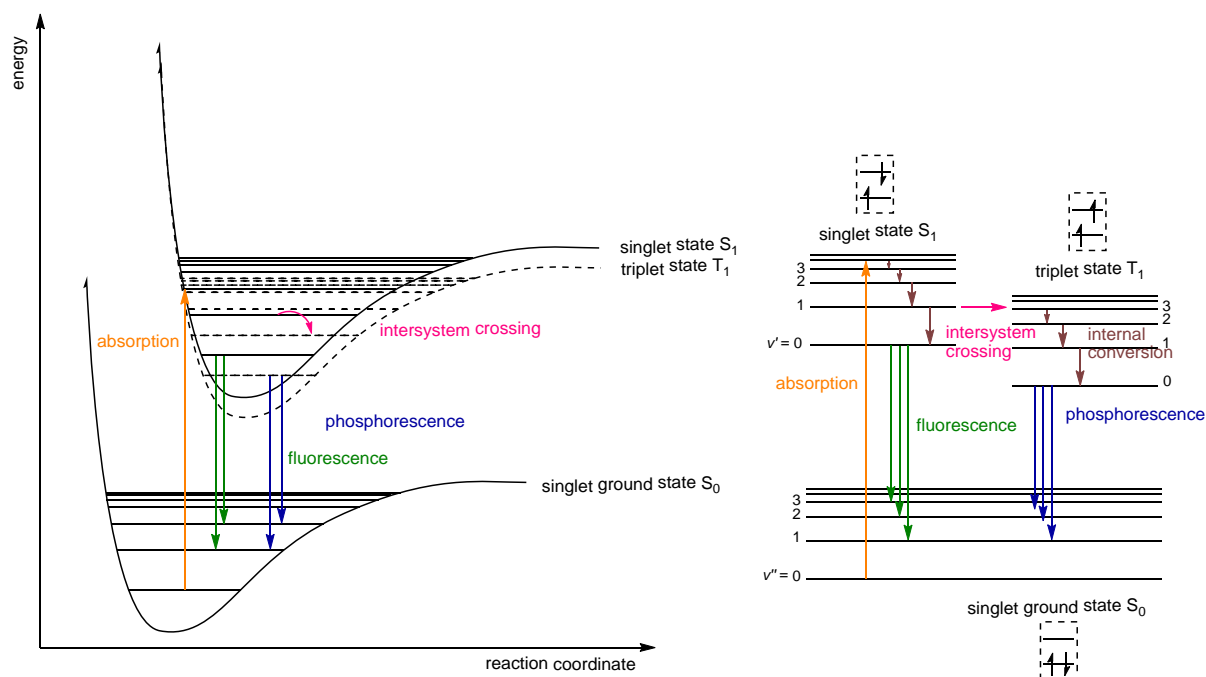

Figure 2: Left: Representation of the *Morse* potential with the different vibrational levels of the electronic ground state S_0, the excited singlet S_1 and the excited triplet T_1. Right: Simplified *Jabłoński*-diagram showing absorption (orange), internal conversion (dark red), intersystem crossings (magenta), fluorescence (green) and phosphorescence (blue) as transitions.[30] The energy levels of the electronic ground state S_0, the lowest excited singlet state S_1, and the lowest excited triplet state T_1 are subdivided into several vibrational states (v'', v').[31] Redesigned with permission from Ref. [31]. Copyright 2001 John Wiley and Sons.

After the molecule is excited to S_1, it undergoes rapid vibrational relaxation by internal conversion to the vibrational ground state of this level (v' = 0) according to *Kasha*'s rule.[32] The deactivation of this excited state can take place non-radiative via energy release to translational, rotational, or vibrational degrees of freedom, by photochemical processes or occur via luminescence.[28] The radiative de-excitation by emitting a photon can proceed as fluorescence or phosphorescence. Fluorescence describes the transition from the vibrational ground state (v' = 0) of S_1 to the singlet ground state S_0 by emission of electromagnetic waves (Figure 2, green).[33] Since the two energy levels involved are singlet states, both of which have a total spin quantum number of S = 0, this transition is quantum mechanically allowed and thus occurs rapidly.[34]

Theoretical Background

A non-radiative transition from one excited state to another excited state with a different spin multiplicity is called intersystem crossing (ISC) (Figure 2, magenta).[34] The required spin flip of an unpaired electron is coupled with a change in angular momentum to follow the *El-Sayed* rules.[35] The vibrational ground state (v' = 0) of the triplet state (T_1) reached via internal conversion (Figure 2, dark red) exhibits a longer lifetime than the corresponding S_1 level. The excited triplet state with the lowest energy is lower than the corresponding singlet state according to *Hund*'s rule.[28] To leave the excited T_1 state, the molecule has only the radiation-coupled relaxation to S_0, which is called phosphorescence. In contrast to fluorescence, however, this transition is associated with a new spin flip and is thus quantum mechanically forbidden by the spin selection rule. Due to spin-orbit coupling, the molecules can nevertheless be slowly de-excited with the result that T_1 is a long-lived excited state and phosphorescence can be observed over a longer period of time (Figure 2, blue).[26, 28, 36] All described transitions are shown in a simplified *Jabłoński*-diagram in Figure 2.

The ratio of photons emitted after excitation and photons originally absorbed for excitation can be expressed by the quantum yield (Φ). For photochemical reactions, the quantum yield is an important value that can describe the efficiency of the system (Equation (1)).[37]

$$\Phi\ (\lambda) = \frac{number\ of\ events}{number\ of\ photons\ absorbed} \tag{1}$$

In this work, both ruthenium(II)- and rhenium(I)-catalysts are stimulated into an excited state applying suitable wavelengths, which enables them to subsequently initiate the reduction of CO_2. Here, both classes of compounds can undergo ISC after excitation, which extends the lifetime of the excited state.[38] Long excited state lifetimes are desired because photochemical reactions originate from the excited states S_1 or T_1 of the respective molecules.[28]

Ru(II)-complexes with the structure $[Ru(L)_3]^{2+}$ (L = bipyridine and analogues ligands) show strong absorption bands in the visible region, due to the spin allowed ^{1}MLCT (metal-to-ligand-charge-transfer) transition from d-orbital of the Ru(II)-centre to the π^*-orbital of the ligand.[39] The subsequent ISC to the ^{3}MLCT excited state takes place rapidly and efficiently.[38c] The resulting ^{3}MLCT state has the long emission lifetime of several hundred nanoseconds, which is desired for these kinds of catalytic reactions.[10a]

Similar electronic transitions can be detected for the Re(I)-complexes.[40] For photocatalysts of the type $[Re(CO)_3(N,N)L]^n$ (with N,N = 2,2'-bipyridine or phenanthroline; L = Cl; n = charge) two additional excited triplet states at equilibrium were observed (Figure 3).[41] Both can be accessed via intersystem crossing, one being the triplet intraligand charge-transfer (^{3}IL/CT) state, which occurs after a π to π^*-transition within the ligand. Reaching the ^{3}MLCT state also occurs via ISC or within a few picoseconds via the ^{3}IL/CT, which are situated in equilibrium.[41]

Theoretical Background

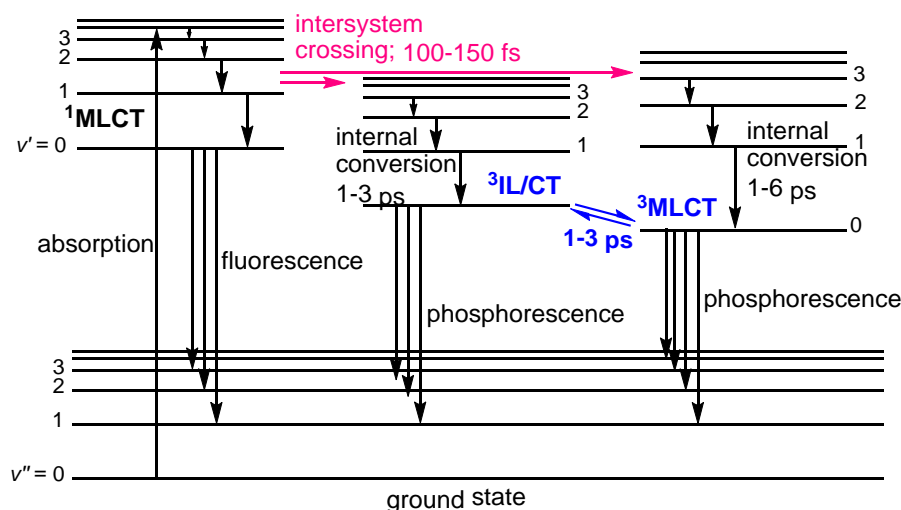**Figure 3:** Electronic transitions between the ground state, ^{1}MLCT, ^{3}IL/CT, and ^{3}MLCT including the transition times during the light-induced excitation of rhenium(I)-based photocatalysts.[41] Redesigned with permission from Ref. [41]. Copyright 2011 American Chemical Society.

2.5   Photosensitisation in Photochemical Reactions

A photosensitiser can be used to achieve efficient and targeted excitation of chemical compounds that do not interact at all or interact only weakly with light under given conditions. The substrate can therefore be photochemically or photophysically be altered as a result of initial absorption of radiation by another molecule called the photosensitiser (PS).[37] For the energy transfer between molecules, two different types have been identified. These are the *Förster* resonance energy transfer (FRET) and the *Dexter* mechanism.[37, 42] The FRET is characterised through an energy transfer facilitated by dipole-dipole coupling that depends mainly on the spectral overlap between emission of the sensitiser and absorption of the substrate, as well as on the intermolecular distance.[43] The distance-dependent law expressing the rate of resonance energy transfer is R^{-6}, where R describes the distance between PS and substrate.[44] The short-range FRET mechanism starts with the photosensitiser absorbing a photon, followed by internal conversion or intersystem crossing, to reach the vibrational ground state of S_1 or T_1.[45] Originating from these levels, relaxation into a vibrationally state of S_0 takes place either by the emission of a photon or by non-radiative processes. The energy released in this process can then excite the substrate in spatial proximity in turn.[45] Since often no fluorescence occurs during this step from the PS, it is referred to as a "*virtual*" photon.[44] This photon is redshifted compared to the photon originally absorbed by the PS, due to internal conversion decreasing the energy gap to the ground state. This also explains why the excitation can only occur in this direction from PS to the substrate. In summary, in the FRET mechanism, excitation is passed through electromagnetic waves from the PS to the substrate.

8

Theoretical Background

The electrons, on the other hand, change excitation states but do not migrate between the molecules during this transfer process.[44] The mentioned energetic processes of PS and substrate in the FRET are shown in Scheme 1.[46]
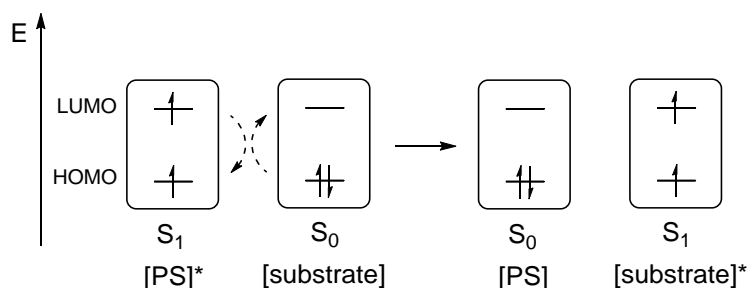
Scheme 1: Schematic representation of *Förster* resonance energy transfer (FRET) between photosensitiser (PS) and the substrate. After the initial excitation of the PS, the energy transfer excites the substrate while the PS relaxes back to the ground state. The excited substrate can then enter photochemical reactions. Redesigned with permission from Ref. [46]. Copyright RSC Publishing.

In the second mechanism, the *Dexter* energy-transfer, electrons do migrate between the involved molecules, resulting in an ultra-short-range process (Scheme 2).[42, 46] For this mechanism, an overlap of the wavefunctions of the energy donor (PS) and the energy acceptor (substrate) is required.[47] Since this mechanism predominantly starts from the triplet state of the PS, a high rate of ISC is desirable to achieve a sufficient population of the T_1 state.[37, 48] The efficiency of the ISC depends on the *El-Sayed* rules and on the energy difference between S_1 and T_1.[35a, 49] Furthermore, the prohibition of the spin transition can be weakened by the heavy atom effect, which facilitates the ISC.[28, 36, 48, 50] For this reason, transition metal complexes such as Ru(bpy)$_3$X$_2$ (bpy = bipyridine) or Ir(ppy)$_3$ (ppy = *fac*-tris(2-phenylpyridine) are popular PS in photochemistry.[48]
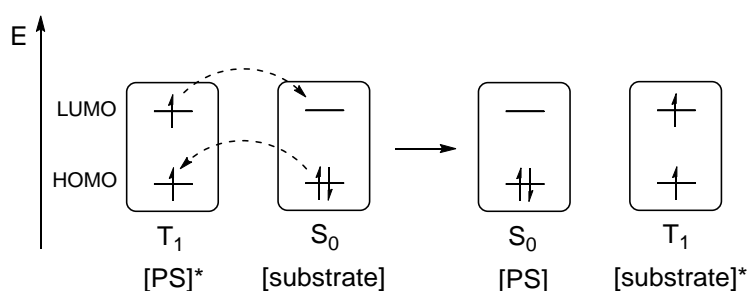

Scheme 2: Schematic diagram of the *Dexter* mechanism of the triplet-triplet energy transfer. After excitation of the PS and the ISC to the long-lived triplet state, the excited electron is transferred to the substrate while simultaneously an electron from the ground state is passed back to the PS. The substrate is then in the excited triplet state and can undergo photochemical reactions. Redesigned with permission from Ref. [46]. Copyright RSC Publishing.

Within the electron transfer from PS to catalyst, a fundamental distinction can be made between two different types of initiation reactions.[51] The oxidative quenching describes the process, where the excited photosensitiser (PS*) is oxidatively quenched by the acceptor (e.g.

catalyst) (Scheme 3). Therefore, the one-electron-oxidised-species (OEOS) of the PS is formed before the subsequent electron transfer from the donor (D) takes the PS back to the initial state.
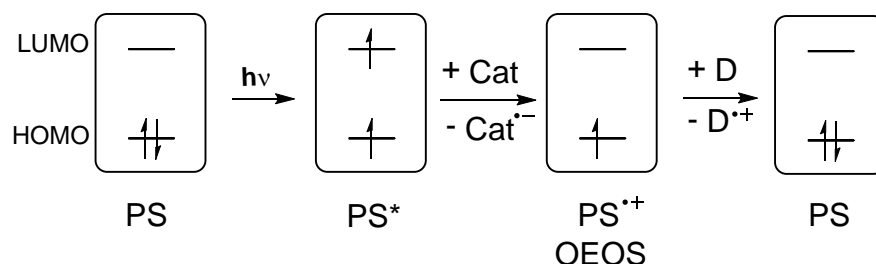
Scheme 3: Excitation of the photosensitiser (PS) followed by an oxidative quenching process by the catalyst (Cat) and the electron transfer from the donor (D) to return to the initial state.[52]

In the reductive quenching process, the excitation first creates an electron hole in the highest occupied molecular orbital (HOMO) of the PS, which is occupied by an electron transferred from a donor (D). The resulting one-electron-reduced-species (OERS) can relax to the initial state by donating the electron to the catalyst (Scheme 4).[53]
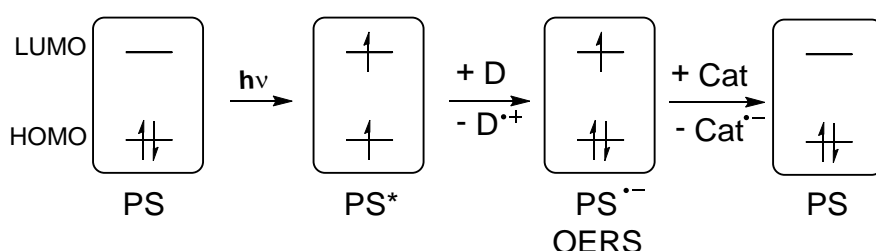
Scheme 4: Excitation of the photosensitiser (PS) followed by reductive electron transfer from the donor (D) and the subsequent electron transfer to the catalyst (Cat) to return to the initial state.[52]

The photocatalytic reduction of CO_2 is mostly taking advantage of the reductive quenching as the reduction potentials of the catalysts are too negative for the PS^* to efficiently inject an electron. The OERS of the PS, on the other hand, has strong enough reduction power to transfer an electron to the catalyst. Furthermore, the reduction of CO_2 requires a "reductive" environment, where OEOS of the PS is unfavourable.[10a]

In general, the properties of the PS in the photocatalytic reduction of CO_2 are demanding. In order to find or produce a suitable PS, the desired properties must be defined. Firstly, a strong absorption in the visible range of the light spectra for an efficient utilisation of the solar light is desirable. Furthermore, this photophysical property should preferrable be combined with long emission lifetimes. In addition, the excited state should possess strong oxidation power to

accept an electron from the donor efficiently. However, the OERS formed has to be highly stable to avoid side reactions and rapid deactivation.[10a]

2.6 Homogenous Photocatalytic Reduction of CO_2

Carbon dioxide represents the ultimate source of fossil fuels for our energy supply.[54] The conversion of CO_2 to the gases, liquids, and solids, which we use as energy resources, was carried out by the carbon fixation process of plants called photosynthesis. This conversion of water and carbon dioxide into reduced organic materials with the energy input of sunlight is estimated to cover $385 * 10^9$ tons of carbon fixation annually.[54] The counteracting CO_2 emission exceeds this value, resulting in increasing CO_2 concentration in the atmosphere.[55] While it is well-known for the combustion of fossil fuels to release CO_2, industrial process such as concrete production can be accounted for major CO_2 emissions as well..[21] In order to utilise this cheap and well available substrate selectively for synthetic fuels, photocatalytic reactions may be employed. Nonetheless, regarding the production of synthetic fuels, the 2008 Bell/DOE report stated: "The major obstacle preventing efficient conversion of carbon dioxide into energy-bearing products is the lack of catalysts...".[54, 56]

For this reason, research has been conducted in recent decades into various ways of using CO_2. The aim is to convert CO_2 into higher energy molecules such as CO, CH_2O, CH_3OH, HCOOH, or CH_4.[57] In addition, CO_2 is being investigated for the synthesis of organic compounds, such as in carboxylation, amidation, or hydrogenation reactions, and as a building block in polymers.[58] Unfortunately, establishing an industrial process using carbon dioxide as the starting molecule is challenging due to its high stability owing its low energy level.[23a, 54, 59] The carbon in this symmetrically linear molecule is present in its highest oxidation state of +IV. In order to make CO_2 accessible for the above mentioned diverse chemical conversion, this molecule must be activated by reduction, i.e. the addition of electrons.[57g] The reduction of CO_2 directly on metal surfaces requires exceedingly high overpotentials and the catalyst shows fast deactivation by the reduction products.[60] Molecular catalysts can reduce the required overpotential for CO_2 reduction by stabilising the generated intermediates and providing multiple electrons.[57g] The energy for this process can be introduced by an applied voltage (electrocatalysis), by light and current (photoelectrocatalysis), or by light only (photocatalysis).[61] The catalysts that provide this energy source to the carbon dioxide molecule can be divided into heterogeneous and homogeneous catalysts. The heterogeneous catalysts consist mostly of semiconductor materials, which in some instances have been additionally optimised with molecular catalysts on the surface to form hybrid systems (chapter 2.9).[62] Homogeneous catalysts are mostly based on transition metal complexes such as rhenium, ruthenium, or iridium, or on more abundant metals such as manganese, iron, cobalt,

nickel, or copper.[9, 63] These catalysts have multiple tasks to complete the reduction of CO_2. They need to have the ability to accept electrons from a donor or photosensitiser, accumulate multiple electrons, and activate CO_2 by forming one or several temporary bonds. In addition, hydrogen evolution should be avoided by catalysts as this process competes with the formation of CO.[10a]

The first studies on the photocatalytic reduction of CO_2 were conducted by *Lehn et al.* in the early 1980s and are based on earlier work by *Gafney* and *Adamson*.[64] Here, the PS $[Ru(bpy)_3]^{2+}$, which is still in use today, was applied in combination with the catalyst $CoCl_2$. Other research approaches used Ni(II)-cyclam complexes as catalysts instead of cobalt compounds.[65] To increase the selectivity for the generation of CO, the rhenium-based catalyst $[Re(bpy)(CO)_3X]$ (X = Cl, Br), which acts as both a photosensitiser and the reduction centre, was first described by *Lehn et al.* in 1983 (Figure 4).[9] Since then, numerous publications have investigated this highly selective photocatalyst and various derivatives even more intensively, which is why it is still considered a model system to this day.[8, 10b, 38a, 38b, 66]
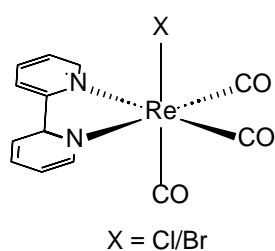

Figure 4: Illustration of the Re(I)-model catalyst $[Re(bpy)(CO)_3X]$ for the photocatalytic reduction of CO_2 with visible light.[9]

Among the studied variations of the catalyst are replacement of the halogen ligand by other (pseudo)halides (cyanide, thiocyanate)[66a, 66c, 67] and uncharged ligands such as pyridines,[68] phosphines[66c, 69], or NHC ligands.[70] In addition, modifications of the bipyridine ligand-like substitutions at the 4- and 4'-positions, use of bipyrimidyl, phenanthroline, and similar ligands have also been published.[38a, 66c, 67, 71] As part of these publications, the catalytic cycle of the Re-based photocatalysts was also investigated in more detail.[10b, 66d, 72] A simplified catalysis cycle is shown in Scheme 5 using $[Re(bpy)(CO)_3X]$ as an example catalyst.

The reduction process is initiated by the excitation of the Re(I)-system to the ^{1}MLCT through suitable wavelengths. The subsequent ^{3}MLCT-state is reached via ISC and is characterised by an increased reduction potential ($E_{red}^* = 1.15$ V vs SHE) compared to the electronic ground state ($E_{red}^0 = -1.35$ V vs SHE).[73] Therefore, the excited state can accept an electron from an electron donor by reductive quenching, resulting in a 19-valence-electrons complex.[61a] This OERS could be identified by both time-resolved absorption spectroscopy and steady-state irradiation.[10a] The energetically unfavourable complex splits off the halide or solvent molecule, forming the 17-electron species $[Re^0(bpy)(CO)_3]$.[66c, 72b] Via a slow proceeding nucleophilic

attack, the electrophilic carbon of the CO_2 molecule binds to the free coordination site of the Re-complex.[61a, 74] The second electron required for CO_2 reduction is provided by a further single-electron transfer to the complex. The source of this second electron is an ongoing discussion in the literature and is one main focuses of this work.[8, 61a, 66a, 66c, 66d, 72a, 74a, 75]

While *Lehn et al.* postulated that the second electron originates from the sacrificial electron donor,[61a] *Ishitani et al.* and *Rieger et al.* suggest that another long-lived OERS in proximity represent the source of the second electron.[8, 66a, 66c, 75a, 75b] In the subsequent step, a hydroxide ion and a CO molecule are released from the complex. The regeneration of the catalyst takes place via the coordination of a solvent molecule (or a halide) to the vacant coordination site.[52]
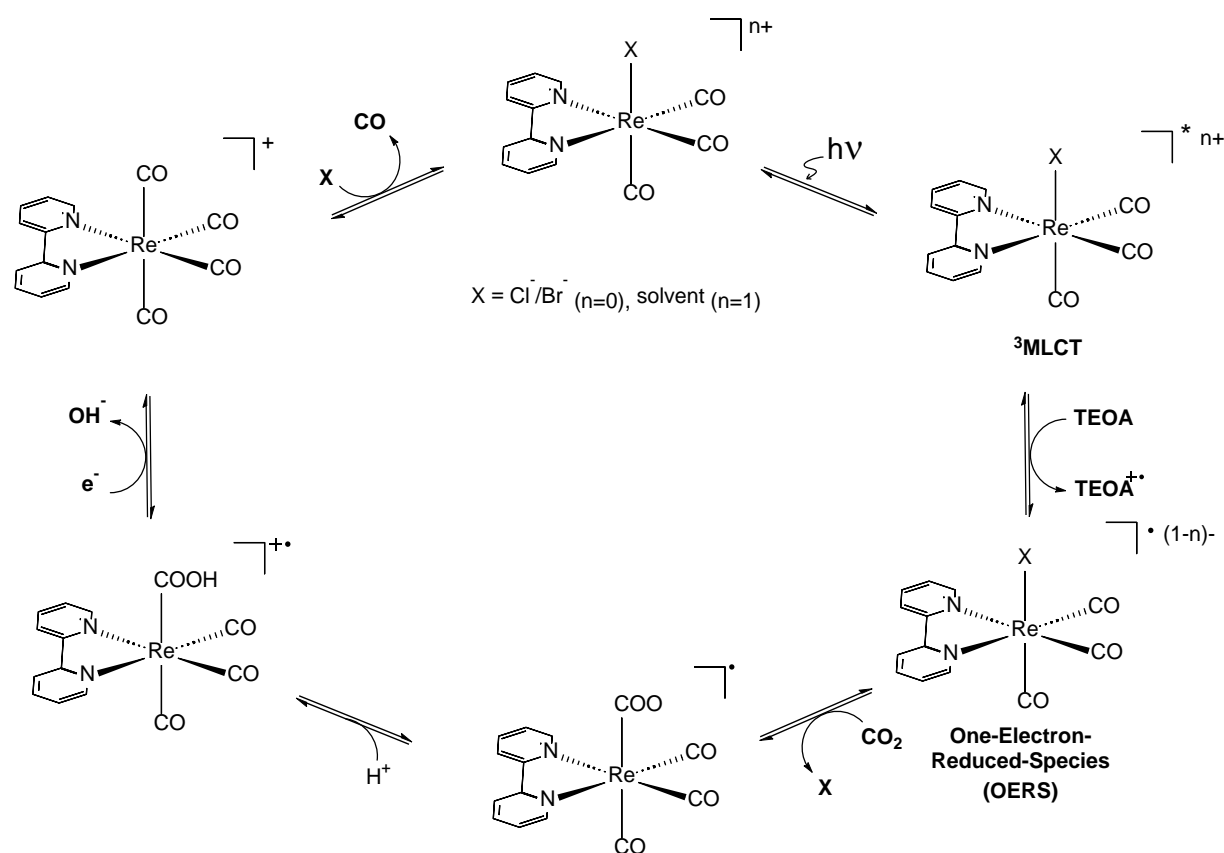
Scheme 5: Simplified catalytic cycle of the photocatalytic reduction of CO_2 to CO with $Re(bpy)(CO)_3X$ ($X = Cl^-/Br^-$) as model catalyst. Triethanolamine (TEOA) as sacrificial electron donor initiates the one electron transfer.[52]

Schwalbe et al. proposed a more complex catalytic cycle in which several different cycles run simultaneously.[66d] It depends on conditions such as catalyst concentration, proton availability, electron donor, or excitation wavelength,[9, 66d, 74b, 76] whether the process suggested by *Kou et al.* proceeds.[72a] In this case, a Re-Re-bonding occurs before the dimer is able to carry out the two-electron-reduction of CO_2, which mechanism was first assumed by *Kubiak* and *Fujita*.[66d, 77] Under modified experimental conditions, another dimer is suggested via a $[CO_2^{2-}]$-bridged Re-Re-intermediate initially followed by a Re-Re-dimer with a CO_2-CO_2-bridge, when no proton source was present[66d, 73a, 77b, 77c]

Despite all the improvement efforts since the discovery of the photocatalytic properties of Re(I)-complexes and the intermediates in catalysis studied in detail, the Re-based molecules still suffer from major weaknesses.[10b] Even though the catalysts show satisfying activity and high selectivity, deactivation occurs fast, leading to low turnover numbers. Furthermore, Re(I)-based systems have only weak absorption of the visible part of the light spectrum, which limits their application as photocatalysts with sunlight as energy source. A third major drawback are the electron donors, which can be used with this catalytic system to date. These often lack sufficient reducing power and therefore lead to an inefficient quenching process.[78] Improvements could be achieved by synthesising and applying so-called "supramolecular photocatalysts". [75b, 79] These multinuclear complexes consist of several units with different functions to reach a more efficient reduction process. Multinuclear molecules with a Ru(II)-photosensitiser unit and a Re(I)-catalyst are presented in the next chapter.

2.7 Multinuclear Supramolecules Consisting of Ru(II)/Re(I)-Complexes

Re(I)-based systems are among the best performing CO_2-photocatalysts with acceptable activity (turnover frequency; TOF), good efficiency (quantum yield), and high selectivity towards CO.[9, 61a, 67] Nevertheless, the stability (turnover number; TON) of the Re(I)-based complexes is insufficient, which can be explained by a rapid decomposition of the catalysts.[8, 10] The underlying deactivation processes were studied in detail by *Rieger et al.*[10b] Based on the OERS of the Re(I)-catalyst, two undesired side reactions were identified. One mechanism is the reaction of the OERS with TEOA radicals formed after the transfer of the first electron (Scheme 6, blue boxes).[80]
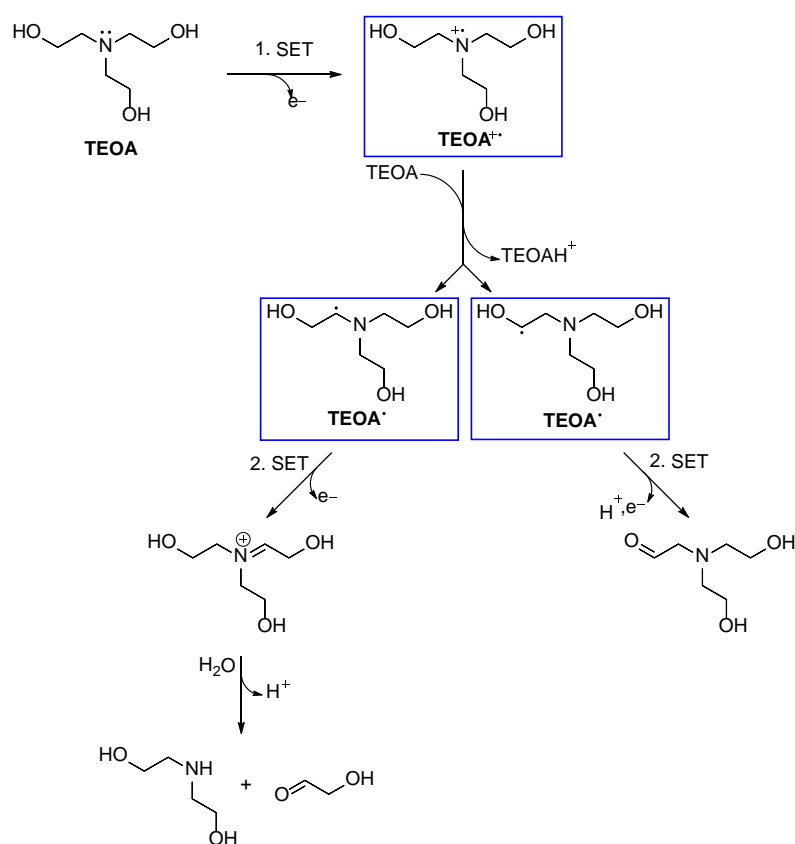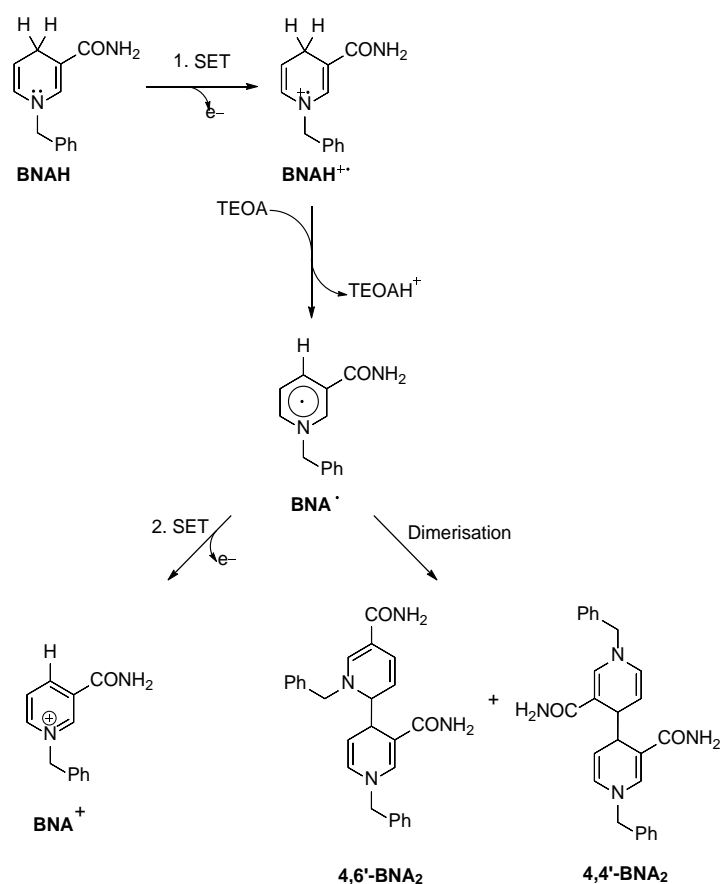

Scheme 6: Illustration of the oxidation mechanism of triethanolamine (TEOA) by two single-electron-transitions (SET). The radicals that are marked with blue boxes are present as intermediary products and facilitate undesirable side reactions.[81]

The second deactivation process is the overexcitation of the OERS through irradiation, which leads to the decomposition of the catalyst.[82] In addition to the instability, these photocatalysts are unsuitable as collectors of solar energy due to insufficient overlap of their absorption range (350-450 nm) with the emission spectrum of the sun.[52, 83] One way to tackle these drawbacks and achieve performance improvements is to separate the sensitisation process and the reduction event by combining multiple metallic centres.[84] The best-known multinuclear

homogeneous photocatalysts for CO_2 reduction consist of Re(I)- and Ru(II)-units.[75b, 85] Photosensitisers of the type Ru(II)-trisdiimine exhibit extended absorption into the visible region, allowing for excitation wavelengths above 500 nm.[10a, 52] With a lifetime of about 800 ns, the resulting ³MLCT is much more stable compared to rhenium(I) systems in this state (about 25 ns), which increases the probability of the subsequent reductive quenching by the electron donor.[38a, 39, 52, 86] This resulting OERS of the Ru(II)-complex is capable of reducing the rhenium catalyst in the subsequent step.[75b] By applying this mechanism with separated functionalities, the Re(I)-moiety does not require interaction with light, which prevents the deactivation process via overexcitation.[10b] In addition, radical deactivation can also be suppressed since more efficient electron donors can be used for the reductive quenching of Ru(II)-photosensitisers with 1-benzyl-1,4-dihydronicotinamide (BNAH) and 1,3-dimethyl-2-phenyl-2,3-dihydro-1H-benzo[d]imidazole (BIH).[78, 81b] Tertiary aliphatic amines such as triethylamine (TEA, E_{ox}^P = 1.2 V vs SHE)[10a, 87] or triethanolamine (TEOA, E_{ox}^P = 1.0 V vs SHE)[10a, 66c, 88] used for the reduction of Re(I)-complexes are not capable to efficiently quench the excited state of the Ru(II)-trisdiimine PS due to insufficient reducing power.[78] Although BNAH, with a lower oxidation potential (E^{ox} = 0.81 V vs SHE)[89], can donate an electron to the excited Ru-complex, it shows several disadvantages.[78, 90] The quenching efficiency of the excited state of the Ru(II)-photosensitiser unit with BNAH is relatively low (η_q = 60%).[78, 91] In addition, the donated electrons can be transferred back from the reduced PS to the oxidised form of BNAH, as BNAH˙+ is not acidic enough for a fast deprotonation process (Scheme 7).[91] Furthermore, 4,4'-BNA$_2$, resulting from the deprotonation of BNAH˙+ and the subsequent dimerisation, inhibit the photocatalytic reaction. This happens due to the strong electron donation potential (E^{ox} (4,4'-BNA$_2$) = 0.26 V)[92] in combination with the high likeliness of back electron transfer from the reduced PS to the BNA$_2$˙+ formed in the previous step.[78]

Theoretical Background

Scheme 7: Illustration of the oxidation mechanism of 1-benzyl-1,4-dihydronicotinamide (BNAH). After the first SET BNAH˙+ can undergo deprotonation followed by either a second SET to a stable BNA+ or a dimerisation to 4,6'-BNA2 (left) or 4,4-BNA2 (right). These dimers are strong electron donors, but the oxidised dimer species formed by the electron transfer acts as an electron acceptor, resulting in obstruction of the photocatalysis.[78, 81b]

Another widely applied two electron and one proton source is BIH.[93] In contrast to BNAH, BIH has a greater reducing ability (($E_{1/2}^{ox}$ (BIH/BIH˙+) = 0.57 V vs SHE)[94], which leads to quantitatively quenching of the excited state of Ru(II)-photosensitisers.[85b] The resulting OEOS BIH˙+ has a very acidic character and loses the proton 100 times faster than the OEOS of BNAH, which limits the undesired back electron transfer.[78] Furthermore, BIH acts reliably as two electron donor and, therefore, can provide both electrons for the reduction of CO_2 to CO.[81b] After the second electron donation the resulting BI+ does not interfere with the catalyst, leading to no diminishment of the photocatalytic ability.[78] The two SET and the respective intermediates are shown in Scheme 8.
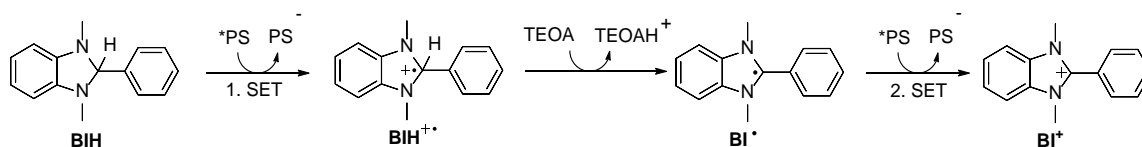
Scheme 8: Illustration of the two SETs of BIH onto the photosensitiser. After the first SET BIH+˙ is deprotonated by a base (TEOA) to the uncharged BI˙. This radical is capable of a second SET to the stable molecule BI+. With this three steps one BIH can create a OERS of two PS-molecules.[78]

17

An important factor for the efficiency of the photocatalytic process is the electron transfer between PS and reduction centre. This can take place via multiple mechanisms, as already discussed in chapter 2.5. All of the electrons transfer procedures take place via collision processes or over very close ranges and are therefore strongly dependent on the concentration of the individual components.[95] A method to force spatial proximity between the metal centres is by covalently linking them to each other.[75b, 85b, 96] Through such a connection of the individual units, an acceleration of the electron transfer between the components of the supramolecular photocatalyst is achieved.[85a] This improves the performance of the photocatalytic system and leads to higher durability of the PS unit because its unstable excited and reduced state can be processed more rapidly. Furthermore, the TOF of the conversion might be increased by faster and more efficient electron transfer between the PS and the catalyst-unit.[57i] Consequently, multinuclear catalysts are observed to be superior over a mixture of the corresponding model complexes in quantum yield, TON, and TOF.[57i, 85a]

The type and length of the bridging ligand has a non-negligible influence on the performance of the photocatalysis as many studies have investigated.[96c, 96d, 97] Research on binuclear Re(I)/Ru(II)-complexes with alkyl compounds of different lengths have shown that short linkers are best suited for the electron transfer.[96c] Conjugated spacers can deliver electrons to the reduction centre faster than their saturated counterparts. Unfortunately, these linkers also change the complex to a more positive reduction potential, making them less efficient in the photocatalytic conversion of CO_2.[97a] For this reason, short-chain saturated carbon chains are suitable for efficient electron transfer while maintaining the required redox properties of the catalyst. In most cases, an ethylene chain is used for this purpose.[57h, 85a, 96e, 97b]

2.8 Alternatives to Re/Ru-Based Systems

In addition to the presented photocatalysts with Re(I)- and Ru(II)-centres, research on nickel, manganese, iron, cobalt and copper catalysts has also increased in recent years.[57d, 57e, 98] Although noble metal complexes are well-studied systems for the photocatalytic reduction of CO_2, the starting materials are rare on earth, making them environmentally unfriendly to mine and expensive to purchase.[85b, 91, 99] In order to achieve the goal of a sustainable conversion of CO_2, it is therefore essential to find a favourable earth-abundant metal complex that can efficiently carry out this reduction process. The discovery of the photocatalytic activity of a nickel *N*-heterocyclic carbene-isoquinoline complex in 2013 led to excessive research in this field.[57e, 98a] In combination with an iridium PS and TEA as electron donor, the Ni-complex developed by *Chang et al.* achieves a TON of 98000 and a TOF of 3.9 s^{-1} in the conversion of CO_2 to CO. Unfortunately, due to the very low quantum yield of 0.01%, only small amounts of CO could be produced.[98a] Iron is one of the most common earth-abundant elements that

shows photocatalytic activity. In combination with a Cu-based PS, the Fe(II)-complex of *Ishitani et al.* is able to reach a TON of 273 for CO and a TON of 75 for H_2 production. BIH was used as electron donor in a CH_3CN-TEOA (5:1 v/v) solution.[98e] Similarly, using a copper-based PS and BIH as an electron donor, *Beller et al.* employed a catalyst with iron as the central atom.[98f] With this system, the group achieved a conversion of CO_2 to CO with a selectivity of 99% and a TON of 487. As third iron-based catalyst $[Fe(qpy)(OH_2)_2]^{2+}$ (qpy = 2,2':6',2":6",2'"-quaterpyridine) was reported in 2016 by *Lau et al.*, which produced TONs of over 3000 combined with a selectivity of 95%.[98g] On a cobalt-basis, *Lu et al.* were able to develop a photocatalyst, which in combination with a ruthenium-based PS and TEAO as electron donor, achieves the conversion of CO_2 to CO with a TON of 16896 at a selectivity of 98%.[98h] Manganese is considered a possible candidate for photocatalytic reduction as it is in the same group in the periodic table as rhenium and shares several properties. With a *fac*-Mn(bpy)(CO)$_3$Br-catalyst the group of *Ishitani* was able to convert CO_2 to HCOOH with a TON of 149 and a selectivity of 85%.[98i] *Robert et al.* developed the copper-based complex $[Cu(qpy)]^{2+}$, which reduces CO_2 with a Ru(II)-photosensitiser and BIH/TEOA as sacrificial reductant in acetonitrile. A turnover number of >12000 and a selectivity of 97% reported for this system.[98d]

2.9   Photocatalysis with Hybrids

In 1979, before the first homogeneous photocatalysts for CO_2 reduction had been developed, inorganic heterogenous catalysts had been tested for this conversion of CO_2.[100] Various photosensitive semiconductor powders such as TiO_2, ZnO, CdS, GaP, and SiC were evaluated in their ability to reduce CO_2.[100] Under irradiation, these semiconductors suffer from poor selectivity for the produced carbon species, like formic acid, formaldehyde, or methanol, and show preferential hydrogen evolution. [99d, 100-101] To circumvent these disadvantages and to control the photochemical and photophysical properties more precisely, so-called hybrids consisting of heterogeneous and homogeneous photocatalysts were developed.[57h, 102] These can enhance photochemical stability of the applied molecular catalysts,[57g, 103] increase activity and product selectivity,[102d, 104] and make the light harvesting easily adjustable.[104a, 104c, 105] Therefore, photocatalytically active transition metal complexes have been applied in combination with a broad range of solid materials, e.g., semiconductors, electrodes, photoelectrodes, mesoporous organosilicas (PMOs), and metal-organic frameworks (MOFs).[10a, 57f, 106]

One of the first hybrids combining photoactive semiconductors with metal complexes was reported by *Sato et al.* in 2010.[106b] Functionalisation of nitrogen-doped Ta_2O_5 particles with

ruthenium-based catalysts demonstrated the conversion of CO_2 to HCOOH with a selectivity of 75% and a TON of 89 (Figure 5). In this mode of operation, the semiconductor is excited by visible light and receives an electron from the sacrificial electron donor TEOA. This is passed on to the ruthenium catalyst, which is responsible for the CO_2 conversion.[106b] For this system, similar to the multinuclear complexes, it was found that the linkage of the two components is essential to increase the reaction rate.[106b]
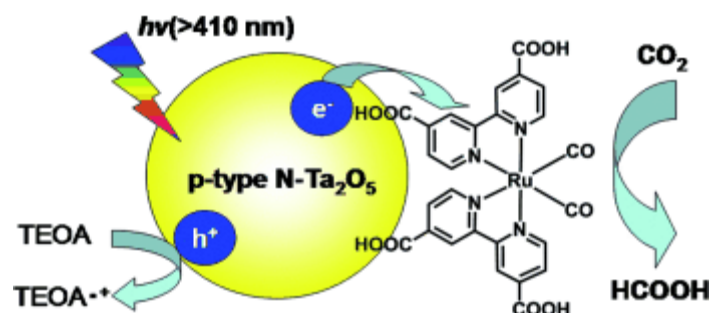

Figure 5: Schematic representation of the processes for the reduction of CO_2 to HCOOH by the hybrid illustrated. Initiated by the excitation of the semiconductor with visible light, *N*-Ta_2O_5 is reduced by the sacrificial donor TEOA. This electron can then be passed to the bound Ru-based photocatalysts. The reduced photocatalysts are capable of catalytically converting CO_2 into HCOOH in the final step of the process.[106b] Reprinted with permission from Ref. [106b]. Copyright 2010 John Wiley and Sons.

An example for a hybrid containing rhenium(I)-catalysts on an inorganic solid was published by *Poblet et al*. in 2016.[107] The abundant and inexpensive polyoxometalate (POM) serves as an electron reservoir and donor with the potential to replace sacrificial electron agents. By using density-functional theory (DFT) calculations, the mechanism of the CO_2 photoreduction to CO could be clarified for this hybrid. After the photoexcitation and the first electron transfer from POM to the Re-centre, the *N,N*-dimethylacetamide (DMA) solvent molecule disassociates, followed by the attachment of a CO_2 molecule and a proton. POM donates a second electron to complete the prior reduction, through a subsequent protonation water and the product CO is released. To close the catalytic cycle DMA can coordinate again to the free coordination site of the Re-complex.[107] In summary this reduction process is very similar to the mechanism of homogeneous photocatalysis of Re(I)-photocatalysts, with the difference that no external electron donor has to be used and thereby the source of the second electron could be identified for this case. Based on these results, some approaches developed the hybrids even further, linking multinuclear catalysts to solid surfaces.[57f, 104b, 105d, 106d, 108] The idea behind this research is the model of photosynthesis proceeding according to a "Z-scheme".[109] Step by step, the reduction potential of the resulting electrons, and the oxidation potential of the associated electron holes can thereby be increased. In nature, the plant is able to use visible light to bind CO_2 and oxidise water through this two-step process. Applying this method, *Ishitani et al*. were able to create a hybrid system of a binuclear Ru(II)-complex linked to a

surface of tantalum(V) oxynitride (TaON), which was modified with silver particles (Figure 6). This hybrid achieved a TON of 750 from CO_2 to CO with the electron source ethylenediaminetetraacetic acid (EDTA).[108a]
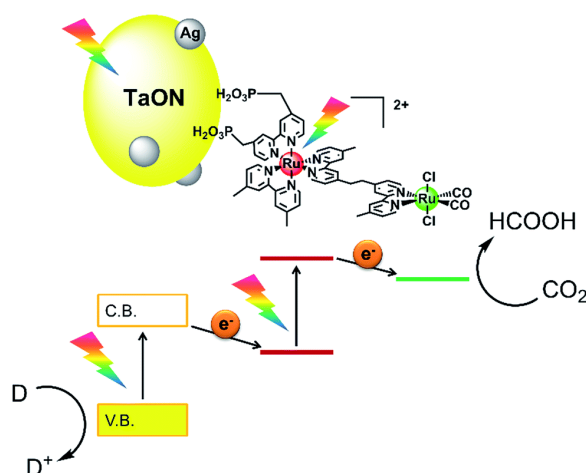

Figure 6: Illustration of the hybrid consisting of a binuclear ruthenium-catalyst linked to Ag-modified TaON. The step-by-step photoexcitation of the TaON and the Ru(II)-photosensitiser proceeds via a "Z-scheme" to transfer the electron to the Ru(II)-catalyst.[108a] Reprinted with permission from Ref. [108a]. Copyright Royal Society of Chemistry.

Another inorganic material that was investigated for CO_2 reduction is NiO as metal oxide electrode. For this purpose the highly active photocatalysts containing Ru(II)-photosensitisers and Re(I)-catalysts were connected to the electrode through phosphonic acid groups. This hybrid photocathode reached TONs of 32 and a faradaic efficiency of 62% by an irradiation of $\lambda > 460$ nm.[57f] A more recent work connected the multinuclear RuRe-complex to Al_2O_3 particles. In this system, the Al_2O_3 functions as a solid surface, but it was possible to conclude that the reduction of CO_2 towards CO can be adjusted by the adsorption density according to speed and durability (Figure 7).[105d]
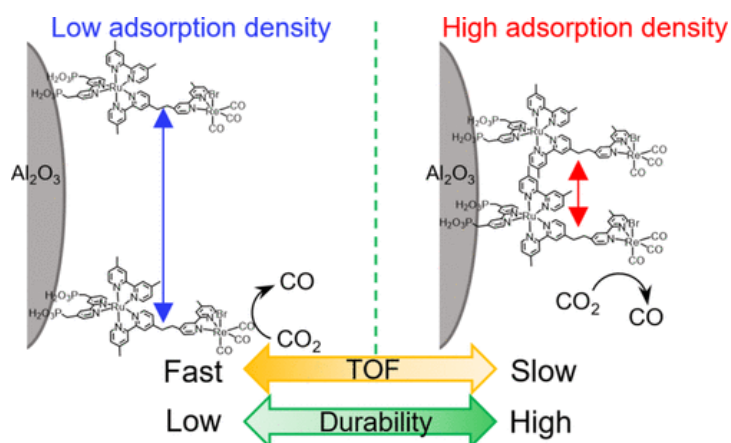
Theoretical Background

Figure 7: Illustation of the dinuclear ReRu-photocatalyst connected to the aluminium-oxide surface. Close spatial proximity between the molecules due to higher absoption density causes increased durability but slows down the reaction rate of the CO_2 to CO reduction.[105d] Reprinted with permission from Ref. [105d]. Copyright 2020 American Chemical Society.

In other artificial photosynthesis approaches, water could be applied as a reductant in photoelectrochemical experiments with CO, H_2, and O_2 as products. [108c] The synthesised Ru(II)/Re(I)-CuGaO$_2$ photocatalyst combined with a CoO$_x$/TaON photoanode could shift the onset potential for the CO_2 reduction to 0.5 V vs SCE, which is 0.4 V more positive with respect to the onset potential of the Ru(II)/Re(I)-NiO electrode mentioned earlier.[57f, 57h, 108c]

To achieve the goal of using water as an electron source, some work has focused on titanium dioxide (TiO_2) as a PS. This semiconductor is considered promising as its electronic band structure matches both the oxidation potential of water and the reduction potential of CO_2.[103e, 110] However, TiO_2 as a PS requires high-energy ultraviolet light for excitation and the conduction band is close to the thermodynamic potential for hydrogen production.[111] An alternative photoactive material is the most prominent semiconductor silicon, which was already applied as a solid surface for multiple catalytic reactions.[112] In the photocatalytic reduction of CO_2, this material represents a promising candidate as a carrier for the molecular catalysts due to its availability, price, and outstanding as well as adjustable electronic properties.

Another suitable alternative is the III-V semiconductor gallium nitride (GaN), which excels with mechanical and thermal stability and excellent electronic conductivity.[113] The large band gap of 3.4 eV at room temperature explains the use of GaN as a material in electronic and optoelectronic applications.[114] GaN light-emitting diodes are employed in the fields of solid-state lighting, backlight units, automobile lighting, and outdoor full colour display.[115] These not only have a longer lifetime and higher brightness than conventional incandescent light bulbs, but also require less energy to operate.[115] In addition, it is possible to vary the band gap via alloys, which extends the field of application of these chemically extremely stable compounds to bioelectronics as they match the typical HOMO-LUMO gaps match of organic molecules.[116]

Theoretical Background

The spectral range of indium gallium nitride-based LEDs covers from ultraviolet to green with high light emission efficiencies.[115] These properties enable the LEDs to be used for the targeted excitation of molecular catalysts in CO_2 reduction or water splitting.[117] In addition to continuous irradiation, these LEDs can also be used for pulsed mode, which suppresses light-induced deactivation of Re(I)-photocatalysts.[82, 115] The metal co-catalysts to be excited can be selectively attached to rod-like GaN nanowire structures and supplied with the necessary photons and electrons from the surface. Here, the semiconductor can introduce electrons by applying a current, and act as an efficient light-emitting diode (LED) to selectively excite these co-catalysts, which makes GaN a promising support material for the photocatalytic reduction of CO_2. A system in which photocatalysts on GaN nanowires successfully reduced CO_2 into CO and CH_4 was published by *Mi et al.* in 2015.[117b]

3.   Aim of this Thesis

Humanity faces three interrelated challenges with ever-increasing energy demand, the scarcity of fossil resources, and global warming.[7, 118] Reduction of CO_2 using homogeneous photocatalysts offers an approach for the first step of climate-friendly development of organic molecules with high energy densities such as liquid hydrocarbons and methanol. Converted by sunlight, these products are suitable for energy storage or transportation to less light-rich but energy-demanding regions. Furthermore, the reduction of CO_2 opens the possibility to establish an alternative carbon source to fossil resources and can therefore tackle carbon shortage, energy shortage, and global warming simultaneously. However, photocatalysts with the ability to reduce CO_2 to CO exhibit low activities (TOFs) and insufficient stabilities (TONs) to date.[8, 10] For this reason, the aim of this work is to develop and implement new concepts that increase the stability of these photocatalysts.

The first concept concerns the use of hybrids to combine the positive properties of semiconductor surfaces and molecular photocatalysts. First experiments of Re-catalysts on silicon nanoparticles showed that an increase of activity and stability can be achieved by a solid support. In combination with the possibility to dispense sacrificial donors by introducing the electrons via electrical voltage, an efficient, long-lived system could be developed by this approach. The ultimate goal is to introduce not only electrons but also photons precisely into the molecular catalyst through the semiconductor.[119] This is achievable through the highly ordered nanowires gallium nitride can grow, which can act as LEDs. Continuous irradiation as well as pulsed light can be passed over these structures, potentially increasing the lifetime of Re(I) complexes further.[82] In addition, nanowires with a maximum diameter of 100 nm exhibit a large surface-to-volume ratio, which makes them particularly promising for catalytic applications (Figure 8).[117a, 119b, 120]
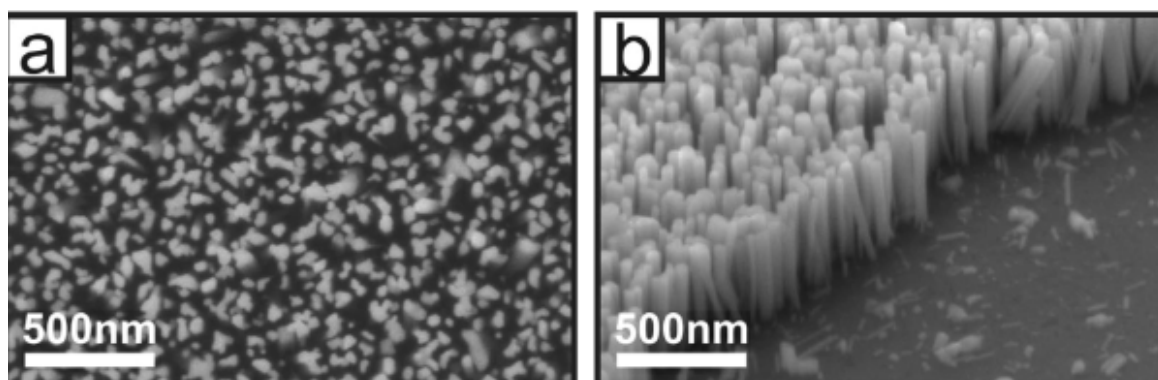

Figure 8: Top view (a) and tilted view (b) SEM image of self-assembled GaN Nanowires on silicon substrate.[119b] Reprinted with permission from Ref. [119b]. Copyright 2016 Elsevier.

Due to the nanowire structure of GaN, enhanced activity has already been observed in reactions such as photocatalytic water splitting.[120a, 120b] The molecular, Re(I)-based catalysts

are to be linked to the surface via phosphonic acid linkers. This chemical loading is a well-known way of functionalising GaN surfaces.[121] The linker should be connected to the bipyridine of the catalyst, since variations at this site are well studied and rarely disturb the catalytic properties.[38a, 66c, 67, 71] A mild, simple and very broadly applicable method is the *Steglich*-esterification.[122] For this, the linker needs to own a hydroxy-group and the bipyridine must be derivatised as carboxylic acid at the positions 4 and 4'. The target hybrid is shown in Figure 9 and is to be approached via a number of simplification steps.
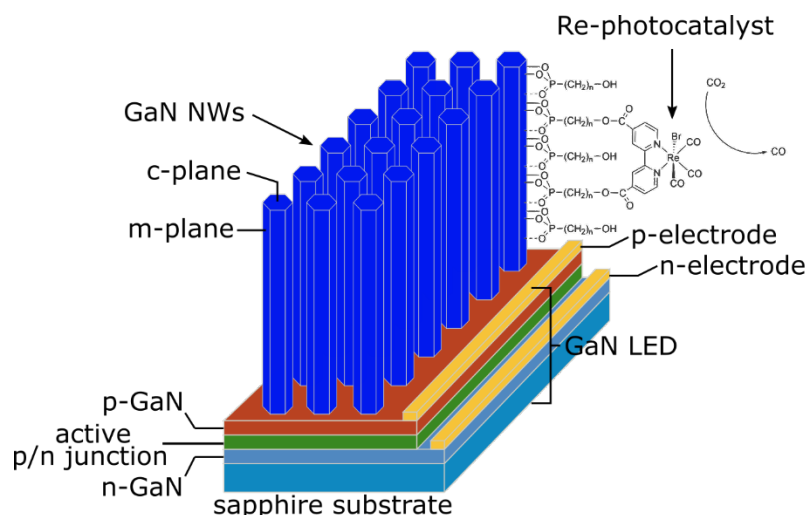
Figure 9: Schematic illustration of an integrated hybrid device for the selective photocatalytic reduction of CO_2 to CO. Light of suitable wavelengths, emitted by a highly efficient LED, is coupled into a gallium nitride nanowire array, which initiates CO_2 conversion by the organophosphonate-anchored rhenium(I) bipyridine photocatalyst.[123] Reprinted with permission from Johannes D. Bartl.

First, two-dimensional, flat wafers are to be functionalised with the linkers to simplify the complexity. Therefore, the nanowires, which are costly and time consuming to manufacture, are only implemented after a detailed loading plan has been worked out and successfully tested (Figure 10). Furthermore, Si wafers are to be used in addition to GaN wafers, as they are cheaper, more readily available and easy to cut into shape. Since phosphonic acid chemistry does not work on silicon wafers, these are to be coated with a thin AlO_x layer in an initial step. Atomic layer deposition will be used for this. The linkers will be synthesised at different lengths to evaluate the influence of electronic interactions on the semiconductor surface. These will then be immobilised via an immersion process as phosphonic acids bind strongly to AlO_x surfaces.[124] The linkage to the Re(I)-catalyst will be achieved via a carbon ester unit, which will be formed by *Steglich*-esterification.
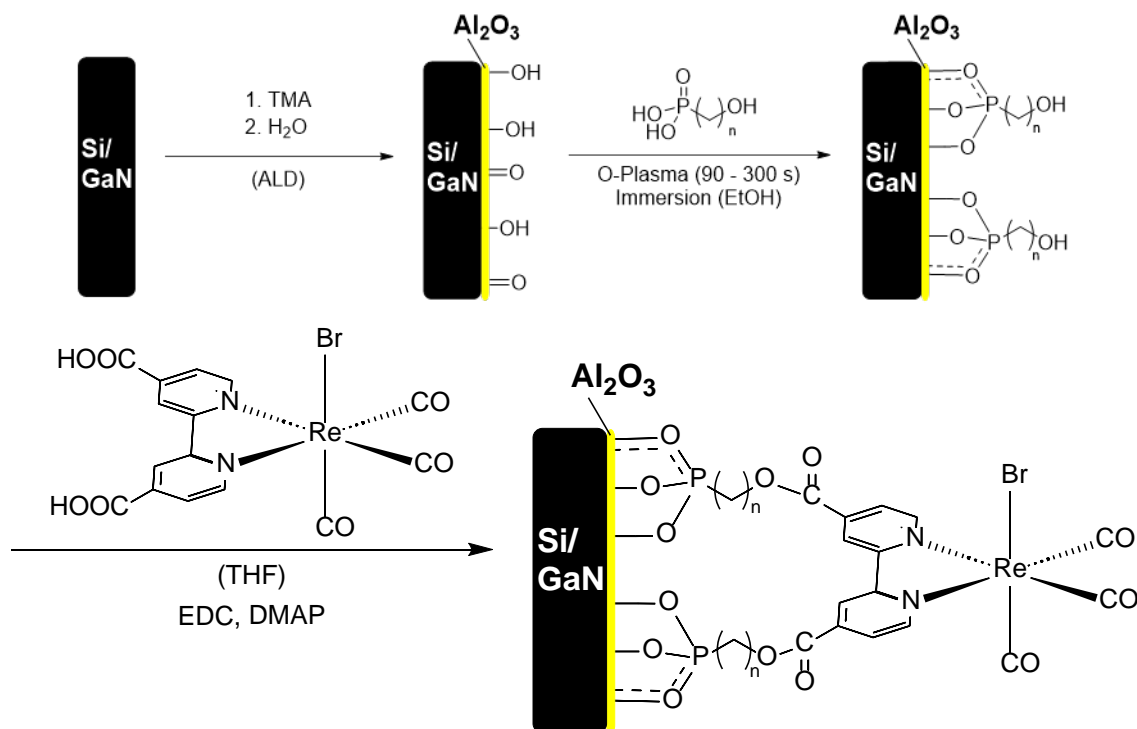
Figure 10: Modular assembly approach starting with atomic layer deposition (ALD) on the semiconductor surface of silicon (Si) or gallium nitride (GaN). The phosphonic acid linkers are loaded via immersion followed by the Steglich-esterification with 3-(((ethylimino)methylidene)amino)-*N,N*-dimethylpropan-1-amine (EDC) and *N,N*-dimethylpyridin-4-amine (DMAP) to connect the carboxylic acid modified Re(I)-photocatalysts. This method enables a controlled surface coupling of various photocatalytic active molecular species on different nanostructured semiconducting devices.

In addition, catalysts with alkyl residues of different lengths at position 4 and 4' of the bipyridine are to be prepared, at the end of which a phosphonic acid group is located (Figure 11). This will allow the described stepwise approach to be compared with direct immobilisation of the entire organic complex for order and packing density.
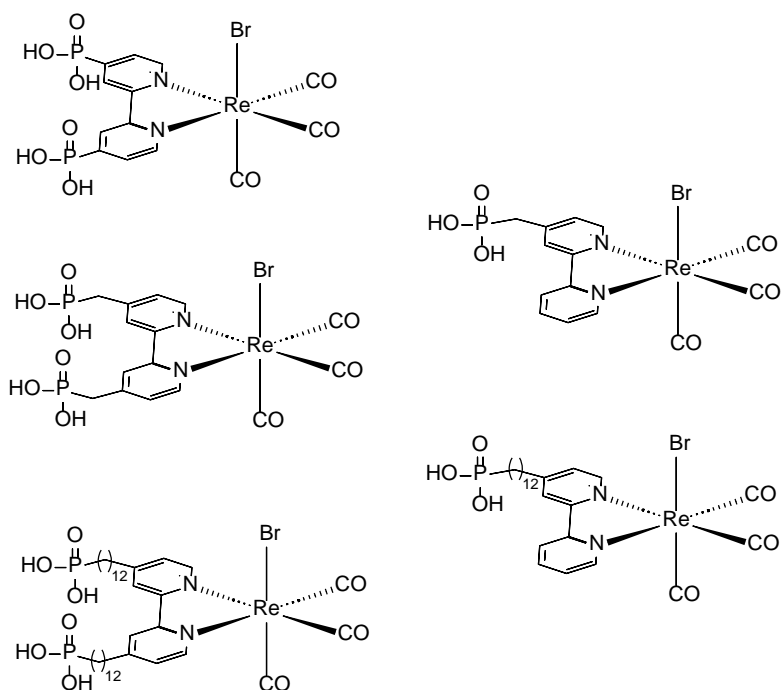
Figure 11: Illustration of the five different Re(I)-complexes that were synthesised to attach directly to the semiconductor surface without the need of linkers. The molecules differ in the length of the alkyl chains between bipyridine and phosphonic acid groups and in the number of possible binding sites for the surface.

A second approach to increase the stability of Re(I)-catalysts is by ensuring spatial proximity to electron-donating PS and other reduction catalysts. The underlying reason for the distance-dependent stability is that the catalytic cycle can run most efficiently if all components are available when required. If there is a delay in the catalytic process, the molecules will remain unnecessarily long in a reactive state and are more likely to undergo undesirable side reactions (chapter 2.7).[10b] One of the states, from which several side reactions can start, is the OERS of Re(I)-catalysts. Several studies have already shown that over-excitation or increased radical concentration lead to a deterioration of the conversion numbers due to decomposition of the catalyst.[10b, 80, 82] *Rieger et al.* proved that the stability of photocatalysts can be increased by covalently linking two Re(I)-centres.[66a] Another significant improvement can be reached by splitting the single tasks among the different metal centres.[75b] In this case, the Re(I)-complex no longer acts as a PS and catalyst all in one, but is only responsible for the reduction step, while a Ru(II)-PS is specialised in light absorption. Here, the absorption properties of Ru(II)-complexes allow the use of longer wavelength light and electron donors with stronger reduction power can be used.[78, 125] In order to guarantee spatial proximity, these molecules should be covalently linked, which ensures intramolecular electron transfer and positively affects the reaction rate and stability of the complexes.[85c, 126] Several publications have further shown that systems consisting of more than two metal centres achieve even better TONs.[57i, 75b, 85a, 85b, 96e] These multinuclear frameworks increase the possible pathways for intramolecular electron transfer between Ru(II)- and Re(I)-complexes and create spatial proximity between

multiple Re(I)-centres to also ensure Re(I)-Re(I)-interaction.[66a] The main advantage of these covalent bonds is the reduced concentration dependence compared to mononuclear Re(I) and Ru(II), as the process relies less on collision probability.[75b] Furthermore, increases in the size of the catalyst system yielded higher stabilities.[75b, 85a, 85b] Thus, systems with three connected catalytic units achieve higher TONs than RuRe2 molecules, which in turn are more stable than RuRe complexes. To extend this concept even further, the aim of this approach is to combine as many photocatalytically active metal centres as possible in one molecule. For this purpose, a macromolecular ligand is to be produced from a large number of covalently linked bipyridine units and then loaded with the metal precursors. The loading of polymer structures with metal centres is well-known and the spatial proximity that this combination creates could facilitate the formation of stable photocatalysts.[127] The first step is to design the monomer in such a way that the chelating bipyridine units in the corresponding polymer have the shortest possible non-conjugated linkage. In several publications, this type of covalent linkage has been proven as the most efficient.[84-85, 96c, 96d, 97a] The subsequent polymerisation of the bipyridines should proceed catalytically in order to produce a well-defined, long-chained backbone with low PÐI. For this purpose, group transfer polymerisation with frustrated *Lewis*-pairs (FLP GTP) will be employed, as the polymerisation of various *Michael* monomers, and the extended *Michael* system 4-VP has already been extensively studied by *Rieger et al.*[128] The monomer must be particularly pure for this type of polymerisation, which is to be achieved by sublimation of the crude monomer. The polymers shall then be loaded with Re(I)- and Ru(II)-centres in different ratios. The loading shall be characterised with suitable elemental analyses and investigated for photophysical differences. In irradiation experiments, these new polymer-based photocatalysts will be evaluated for their stability and activity in the CO_2-to-CO reduction and the results interpreted with respect to the loading ratios and the catalyst structure. Using this method, the influence of the covalent linkage of the metal centres can be assessed and an optimal Re(I)/Ru(II) ratio can be found. The methodology shown in Scheme 9 would be a straightforward and fast way to bring varying ratios of photosensitiser and catalyst into spatial proximity and to evaluate them. This approach does not require complex synthesis for every individual ratio to be tested as it is the case for dendrimeric structures such as RuRe3.
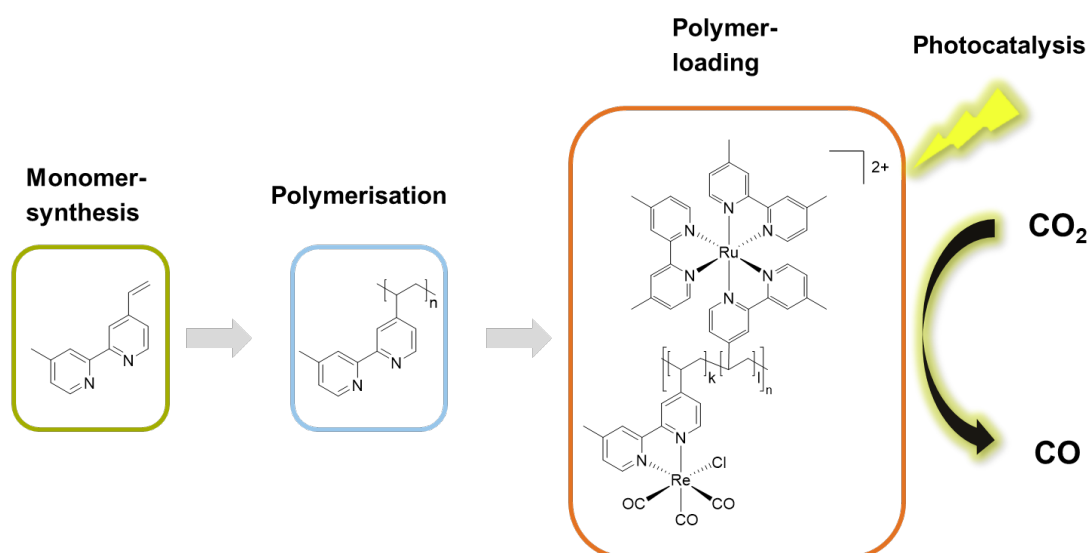
Scheme 9: Schematic illustration of the synthetic approach for the preparation of multinuclear, polymer-based Re(I)/Ru(II) photocatalysts. Starting with the monomer synthesis followed by the catalytic polymerisation and the subsequent loading of the backbone with metal centres. The ultimate goal is to test different photocatalytically active polymers in the reduction of CO_2.

The third concept for improving the performance of Re(I)-based photocatalysts is essentially analogous to the polymeric approach. In this method, Ru(II)-photosensiser units will be applied to perform the absorption of the light, again. Here, these units also have the task of increasing the stability of the system by using less energy-rich light (520 nm) and more efficient electron donors such as BIH. In this case, Ru(II) is to be attached to the catalytically active Re(I)-centres via a non-conjugated ethyl bridge. These covalent bonds ensure efficient electron transfer between the metal centres without disturbing the excitation in the first step by electronic interactions in the ground state.[85a, 97a, 129] Photocatalysts that exploit these advantages have already been published with the multinuclear photocatalysts RuRe and RuRe2 and studied in detail by our group (Figure 12).[85a, 96c, 130]
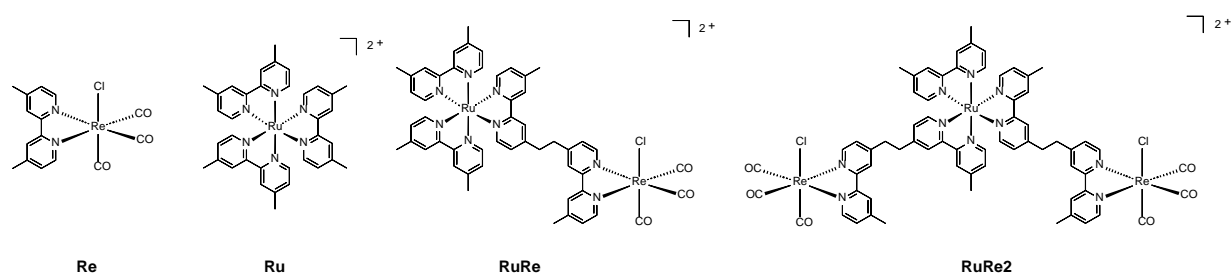

Figure 12: Illustration of photocatalyst $Re(dmb)(CO)_3Cl$ (Re), the photosensiser $[Ru(dmb)_3]^{2+}$ (Ru), and the multinuclear photocatalysts $[Re(CO)_3Cl(dmb-dmb)Ru(dmb)_2]^{2+}$ (RuRe) and $[Re(CO)_3Cl(dmb-dmb)Ru(dmb)(dmb-dmb)Re(CO)_3Cl]^{2+}$ (RuRe2). All charged complexes are present in the salt form with $[PF_6]^-$ as the counterion.

In comparison with the non-linked reference system, namely a mixture of $[Ru(dmb)_3]^{2+}$ (dmb = 4,4'-dimethyl-2,2'-bipyridine) (Ru) and $[Re(dmb)(CO)_3Cl]$ (Re), these supramolecules

showed improved catalytic activity and durability.[9, 66a, 75b, 78] RuRe achieves TONs of 180 with the electron donor BNAH (1-benzyl-1,4-dihydronicotinamide), while RuRe2 even shows TONs of 315.[85a, 96c] The more efficient catalytic properties of RuRe2 compared to RuRe are attributed to the close proximity of the active metal centres. A binuclear mechanism of two Re(I)-centres for the two-electron reduction of CO_2 has already been proposed.[66a, 84, 96b] In addition, the availability of two catalysis centres could reduce the lifetime of both the excited state and the OERS of the Ru(II)-photosensitiser, therefore increasing the stability of the system.[96e] In both cases, the spatial proximity of multiple Re(I)-centres to each other and to a Ru(II)-photosensitiser is beneficial. For this reason, a new tetramolecular, dendrimeric photocatalyst will be synthesised in this work, which consists of a Ru(II)-unit and three surrounding, fixed Re(I)-catalysts. This arrangement should ensure that the OERS of Ru(II)-centre has several paths to donate the electron (Figure 13). In addition, an effort is made to avoid steric hindrance by placing the reduction catalysts on the exterior in order to ensure good access to the CO_2 dissolved in the solvent. Using the comparative systems RuRe, RuRe2 and the respective mononuclear components, the mechanism of second electron donation in the case of RuRe3 shall also be investigated. This late step in the catalysis cycle is still part of a debate that has not been fully clarified.[8, 61a, 66a, 66c, 66d, 72a, 75b, 75c] The specific synthesis of these supramolecular compounds with well-defined dendrimeric structures will allow a more detailed understanding of the effects of inter- and intramolecular interactions on the catalytic reduction of CO_2.
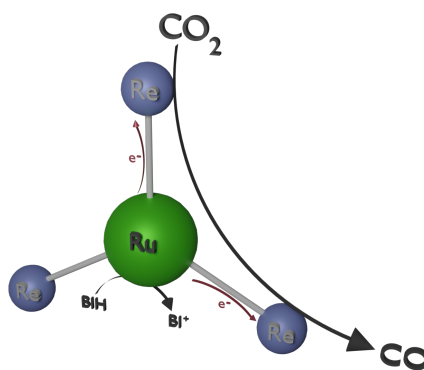

Figure 13: Schematic representation of the process of photocatalytic reduction of CO_2 by RuRe3. After the excitation of the Ru(II)-centre (green) and the subsequent reduction process by BIH, the intramolecular interaction of two Re(I)-centres (blue) is beneficial to carry out the two-electron reduction to CO.

4. Modular Assembly of Vibrationally and Electronically Coupled Rhenium Bipyridine Carbonyl Complexes on Silicon

4.1 Bibliographic Data
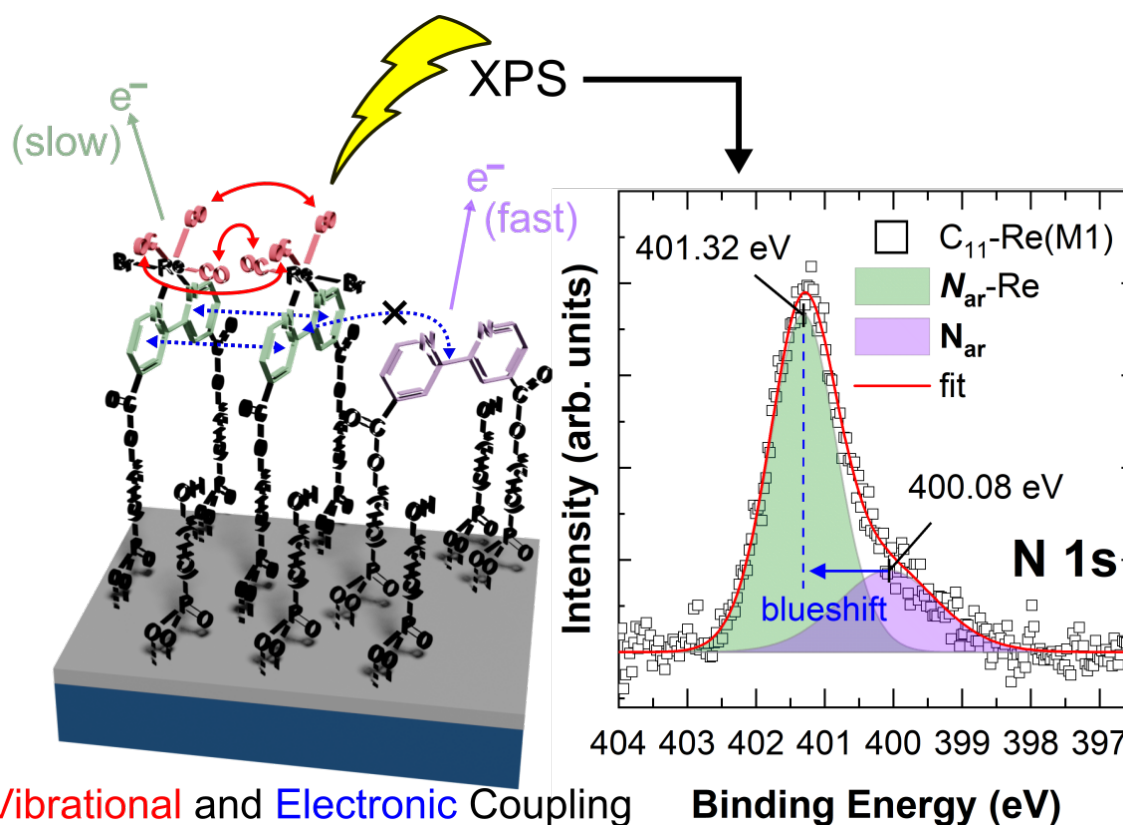
Title: "Modular Assembly of Vibrationally and Electronically Coupled Rhenium Bipyridine Carbonyl Complexes on Silicon"

Status: Full Paper, published online 12th November 2021

Journal: J. Am. Chem. Soc. 2021, 143, 46, 19505–19516

Publisher: American Chemical Society

Link/DOI: https://doi.org/10.1021/jacs.1c09061

Authors: Johannes D. Bartl,[‡*] Christopher Thomas,[‡*] Alex Henning, Martina F. Ober, Gökcen Savasci, Bahar Yazdanshenas, Peter S. Deimel, Elena Magnano, Federica Bondino, Patrick Zeller, Luca Gregoratti, Matteo Amati, Claudia Paulus, Francesco Allegretti, Anna Cattani-Scholz, Johannes V. Barth, Christian Ochsenfeld, Bert Nickel, Ian D. Sharp, Martin Stutzmann, and Bernhard Rieger

Modular Assembly of Vibrationally and Electronically Coupled Rhenium Bipyridine Carbonyl Complexes on Silicon

[‡]These authors contributed equally. Johannes D. Bartl conceptualised the experimental studies and carried out the experiments regarding the surface. Christopher Thomas carried out the experiments regarding the synthesis and the functionalisation. All the authors supported the work by valuable discussions and experiments. Johannes D. Bartl and Christopher Thomas wrote the manuscript. All work was carried out under supervision of Martin Stutzmann and Bernhard Rieger.

4.2   Summary

Hybrids of molecular complexes combined with a semiconducting surface can unite the strengths of both individual components. Thus, stable, efficient, and controllable systems can be generated that are promising for use in photocatalysis, photovoltaic, or chemical sensing. In this work a new surface functionalisation is presented, which allows to deposit organic molecules on semiconductors with high selectivity. In particular, this is demonstrated by covalently attaching molecular Re(I)-photocatalysts to silicon supports via phosphonic ester bonds using modular surface assembly. This approach can be extended to other surface materials by first growing a chemically independent aluminium oxide cover on the semiconductor by atomic layer deposition. The new surface is not only stable and passivated, it also enables well-defined area-selective functionality with high surface coverage. In this work different linkers were anchored site-specifically on the substrate or aluminium oxide, which can then be loaded via straight-forward chemical methods such as *Steglich*-esterification. Due to the spatial arrangement, the applied photocatalysts exhibit strong intermolecular vibrational and electronic coupling, as demonstrated by infrared spectroscopy, photoluminescence, and X-ray photoelectron spectroscopy analysis. The developed step-by-step loading approach is characterised by its precision and flexibility. It is possible to select any substrate on which aluminium oxide coverage can be applied via atomic layer deposition. In addition to the variety of surface materials, a wide range of linkers, varying in length and functional groups can be attached. This flexibility also allows a wide variety of active complexes to be mounted on the specially adapted functionalities. The described approach can be realised for a variety of applications involving the introduction of electrons via semiconductors or requiring a region of selective functionality.

Article

Modular Assembly of Vibrationally and Electronically Coupled Rhenium Bipyridine Carbonyl Complexes on Silicon

Johannes D. Bartl,[*,&] Christopher Thomas,[*,&] Alex Henning, Martina F. Ober, Gökcen Savasci, Bahar Yazdanshenas, Peter S. Deimel, Elena Magnano, Federica Bondino, Patrick Zeller, Luca Gregoratti, Matteo Amati, Claudia Paulus, Francesco Allegretti, Anna Cattani-Scholz, Johannes V. Barth, Christian Ochsenfeld, Bert Nickel, Ian D. Sharp, Martin Stutzmann, and Bernhard Rieger

Cite This: *J. Am. Chem. Soc.* 2021, 143, 19505−19516

Read Online

ACCESS | Metrics & More | Article Recommendations | Supporting Information

ABSTRACT: Hybrid inorganic/organic heterointerfaces are promising systems for next-generation photocatalytic, photovoltaic, and chemical-sensing applications. Their performance relies strongly on the development of robust and reliable surface passivation and functionalization protocols with (sub)molecular control. The structure, stability, and chemistry of the semiconductor surface determine the functionality of the hybrid assembly. Generally, these modification schemes have to be laboriously developed to satisfy the specific chemical demands of the semiconductor surface. The implementation of a chemically independent, yet highly selective, standardized surface functionalization scheme, compatible with nanoelectronic device fabrication, is of utmost technological relevance. Here, we introduce a modular surface assembly (MSA) approach that allows the covalent anchoring of molecular transition-metal complexes with sub-nanometer precision on any solid material by combining atomic layer deposition (ALD) and selectively self-assembled monolayers of phosphonic acids. ALD, as an essential tool in semiconductor device fabrication, is used to grow conformal aluminum oxide activation coatings, down to sub-nanometer thicknesses, on silicon surfaces to enable a selective step-by-step layer assembly of rhenium(I) bipyridine tricarbonyl molecular complexes. The modular surface assembly of molecular complexes generates precisely structured spatial ensembles with strong intermolecular vibrational and electronic coupling, as demonstrated by infrared spectroscopy, photoluminescence, and X-ray photoelectron spectroscopy analysis. The structure of the MSA can be chosen to avoid electronic interactions with the semiconductor substrate to exclusively investigate the electronic interactions between the surface-immobilized molecular complexes.
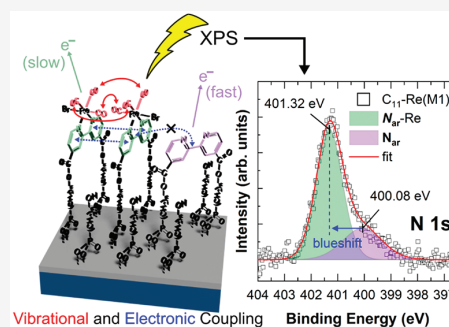
■ INTRODUCTION

Advances in high-performance semiconductor electronic devices depend strongly on the development of robust and reliable surface passivation and functionalization schemes.[1] This is especially evident for next-generation photocatalytic and photovoltaic devices,[1] where inorganic semiconductor interfaces functionalized with small organic molecules are promising hybrid systems.[2−5] The surface structure, stability, and chemistry of the semiconductor generally determine the functionality of the hybrid device and its relevance for specific applications.[1,6] The ability to tailor the chemical and electronic properties of semiconductors via the surface chemistry with molecular control has, thus, become a driving force behind the development of state-of-the-art semiconductor technology. Although a plethora of different surface modification and functionalization schemes are available, they are specific to the unique surface properties of the individual materials.[6−9] This specificity limits the application range of established surface functionalization approaches, including cycloaddition and dissociation chemistry, carbonization, oxidation, and hydrolytic

condensation reactions, as well as hydrosilylation and various other wet chemical approaches.[6,9−11] A standardized surface functionalization approach, which circumvents the limitations of material-specific functionalization routes, is of utmost technological relevance in order to streamline the fabrication and development of hybrid inorganic/organic heterointerfaces. Different from a static bottom-up functionalization, which adapts to the surface chemistry of the semiconductor,[6,12] a dynamic approach relies on the modification of the semiconductor to adopt a specific surface chemistry.[1,6,12]

In this work, we introduce a modular surface assembly (MSA) approach to covalently anchor molecular complexes

Modular Assembly of Vibrationally and Electronically Coupled Rhenium Bipyridine Carbonyl Complexes on Silicon

with sub-nanometer precision on solid substrates (Scheme 1) by tailoring the surface chemistry of silicon (Si), which remains

Scheme 1. Modular Surface Assembly (MSA) Approach[a]
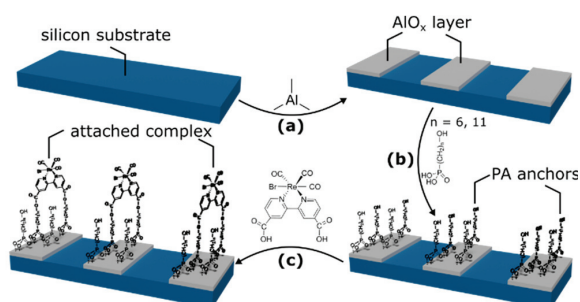
[a]The Si substrate is covered by a micropatterned aluminum oxide (AlO$_x$) activation layer of variable thickness (3 to ~0.3 nm) (a), followed by area-selective surface grafting of a functional phosphonic acid (PA) anchor layer with a variable backbone (b). Finally, molecular transition-metal complexes ([here, rhenium(I) bipyridine tricarbonyl moieties] are attached to the underlying PA anchor layer via a Steglich esterification reaction (c), finalizing the fabrication of the modular surface assembly (MSA).

the most relevant technological semiconductor.[13] To this end, we employ atomic layer deposition (ALD) to grow ultrathin and conformal aluminum oxide (AlO$_x$) coatings (ranging from 3 to ~0.3 nm) on Si substrates (a), effectively altering its surface chemistry to enable phosphonic acid (PA) grafting via simple immersion (b). Ultrathin AlO$_x$ films have been applied in the photovoltaics industry, *e.g.*, for the field-effect passivation of contacts in Si solar cells,[14,15] but also to improve stability and interfacial charge transport in devices based on emerging materials such as planar perovskites and two-dimensional materials.[16] However, these coatings have not yet been applied as universal activation layers for functional hybrid inorganic/organic heterointerfaces on a large scale. The PA grafting introduces a stable hydroxyl functionality (OH reactive sites) to the terminal surface, which is subsequently used to covalently attach molecular transition-metal complexes [here, rhenium(I) bipyridine tricarbonyl moieties] to the functionalized Si surface via a mild Steglich esterification reaction (c).

Such a step-by-step layer assembly circumvents unwanted steric and electrostatic effects induced by the molecular complexes during direct surface functionalization, which is a common strategy for the fabrication of dye-sensitized solar cells,[17−20] and generates a highly ordered hybrid functional interface. Due to the modular character of this approach, individual components of the hybrid interface such as the semiconductor substrate, PA anchor, auxiliary coupling agents, and molecular complex can be flexibly modified and tuned to the requirements of the device.

We utilize highly p-doped Si (>1.2 × 10^{19} cm^{-3}; degenerate doping) to minimize electronic effects between the substrate and the molecular complexes to freely investigate intercomplex interactions. Furthermore, we focus on self-assembled monolayers (SAMPs) of phosphonic acids (SAMPs) as organic functional anchors due to their high thermal and hydrolytic stability compared to other self-assembled monolayers (SAMs), such as silanes.[21] In addition, we exploit the poor reactivity of Si with PAs to achieve a spatially selective functionalization. PA

surface chemistry with native silicon oxide (SiO$_x$) is only accessible via specific reverse Langmuir−Blodget techniques, *i.e.*, tethering by aggregation and growth (T-BAG),[22] which is specifically designed for SAMPs deposition on technologically relevant metal oxides, such as ITO,[23] TiO$_2$,[24] and ZnO.[25] However, these techniques suffer from elaborate and time-consuming experimental requirements. By contrast, PAs strongly bind to AlO$_x$ surfaces.[26,27] The concept of target-site selectivity was initially introduced by Laibinis et al.[28] by defining the term "orthogonal" SAMs, which sparked the development of a plethora of orthogonal chemical transformations, comprehensively discussed in ref 29. Rhenium(I) bipyridine tricarbonyl complexes and their derivates have been utilized for photo- and electrocatalysis,[30−32] dye-sensitized solar cells,[33,34] sensing,[35] and as model systems for elucidating charge injection into semiconducting materials.[36−38]

We couple these molecular complexes onto PA-functionalized surfaces to investigate intercomplex interactions. Through the MSA approach, localized ensembles with strong intermolecular vibrational and electronic coupling are generated and placed at a controlled distance to the substrate surface with sub-nanometer precision. Furthermore, precise lateral structuring of the molecular complexes is demonstrated on lithographically patterned Si with sub-nanometer thin AlO$_x$. The influence of the backbone spacer length on the apparent substrate/complex distance, the degree of molecular order, and the strength of vibrational and electronic coupling between the molecular complexes is investigated by comparing PAs of two different alkyl chain lengths (C$_{11}$ and C$_6$). The chemical structure and nomenclature of these materials are presented in section S0 of the Supporting Information (SI).

RESULTS AND DISCUSSION

As a starting point to elucidate the MSA approach, we assessed the structure and configuration of the different functional coatings. Figure 1 shows tapping-mode atomic force microscopy (AFM) micrographs from a series of Si substrates at each stage of the MSA approach (see Scheme 1). Conformal coatings are formed for all MSA stages without indication of (pin)holes to within the resolution of the AFM (tip radius of ~8 nm). The surface roughness does not increase during the combined AlO$_x$ growth and oxygen plasma surface activation step, which is important since the surface roughness is a key parameter, determining the interface quality of integrated systems and heterostructures.[39] However, the surface roughness of the PA−C$_6$ (306 ± 20 pm) is significantly higher than that of the PA−C$_{11}$ anchors (186 ± 7 pm), which is attributed to a higher degree of disorder in the PA−C$_6$ layer. For SAMs consisting of saturated aliphatic alkyl backbones, the degree of order scales with the length of the alkyl chain, which has been attributed to the larger strength of intermolecular interactions.[40,41] Surprisingly, the surface roughness decreases upon complex [Re(M1)] attachment to the PA−C$_6$ anchor by 98 ± 22 pm. The effect is less pronounced for the PA−C$_{11}$ layer but still discernible, since the root mean square (RMS) roughness decreases to the initial values found on the bare Si substrate. Contrary to expectation, disorder in the PA anchor layer is only partially translated to the subsequently attached Re(M1) layer. The Re complexes possess bipyridine ligands with an extended π-system (SI Scheme 1), which can form strong π−π stacking interactions if a favorable surface orientation is adopted.[42] Our results indicate that the surface morphology of the Re(M1) terminal layer is predominantly defined by such
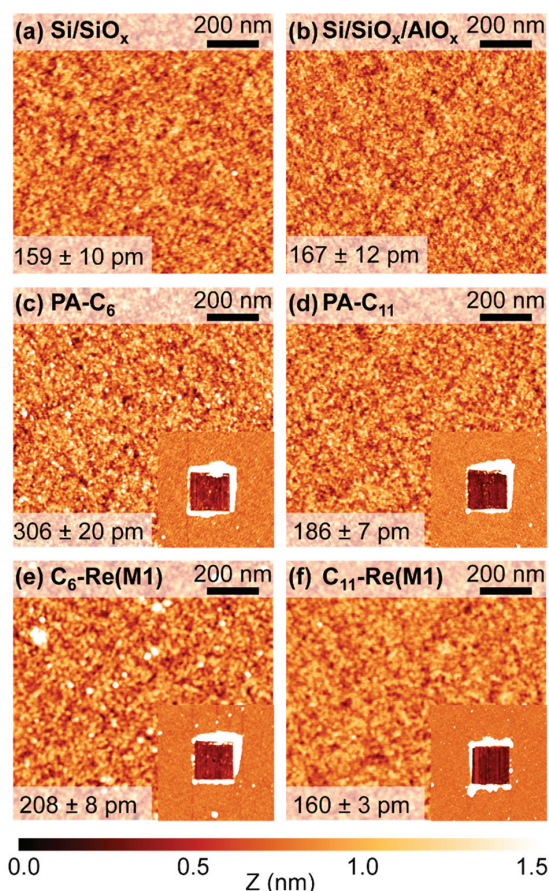
Modular Assembly of Vibrationally and Electronically Coupled Rhenium Bipyridine Carbonyl Complexes on Silicon

Figure 1. Tapping-mode AFM micrographs ($1 \times 1\ \mu m^2$) from a series of Si substrates after solvent cleaning and before ALD growth (a), after deposition of 3 nm AlO$_x$ and *in situ* oxygen plasma activation (b), after surface functionalization with PA−C$_6$ (c) and PA−C$_{11}$ (d), and after Re(M1) attachment to form C$_6$−Re(M1) (e) and C$_{11}$−Re(M1) (f). RMS roughness values (bottom of each panel) were averaged over at least three regions distributed over the same sample. The insets show the removal of ∼$1 \times 1\ \mu m^2$ of the organic overlayer in contact AFM mode.

interactions, which is further elucidated by X-ray reflectivity (XRR) and near edge X-ray absorption fine structure (NEXAFS) analysis (*vide infra*). The thickness (d_{OL}) and the molecular tilt angle (θ) of the organic constituents were determined from the measured step height after removal of the organic layer using contact mode AFM, as shown by the insets in Figure 1 and explained in detail in section S3 (SI). The thickness of the Re(M1) terminal layer, determined by subtracting the PA layer thickness from the total thickness of

the assembly, appears to be primarily independent of the anchor layer thickness (Table 1), further indicating that its structural properties are governed by intermolecular interactions within the metal complex layer.

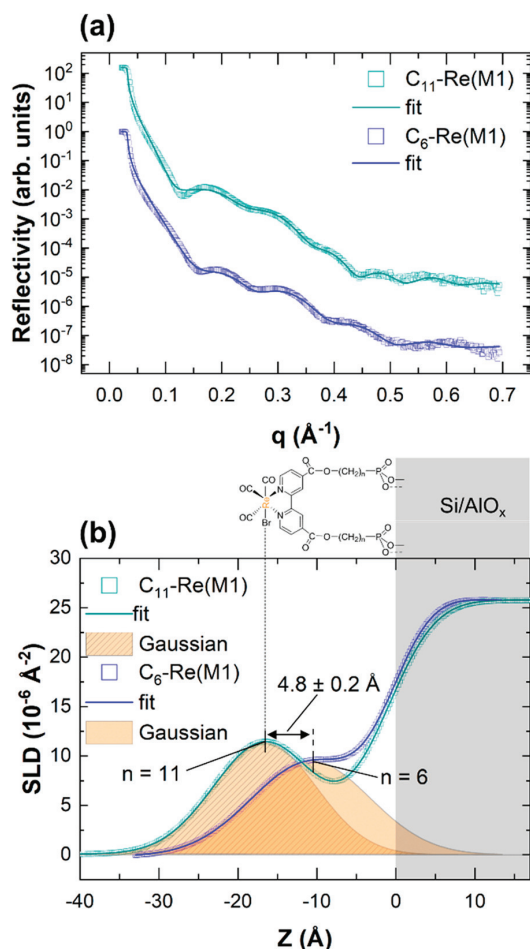Complementary XRR measurements were performed to verify the AFM-derived thickness at the macro scale and to probe the internal structure of the MSA layers. Figure 2a shows normalized XRR curves as a function of the momentum transfer (q) from C$_6$−Re(M1) (blue) and C$_{11}$−Re(M1) (cyan) on 3 nm AlO$_x$-coated Si substrates. The measured reflectivity is presented together with simulated intensities based on a four-layer slab model on top of the Si substrate (solid lines), which is described in detail in section S5 (SI). The relatively large scattering cross section of the Re metal centers gives rise to a pronounced Gaussian-shaped scattering length density (SLD) profile (orange, Figure 2b), indicative of a highly ordered surface layer for both PA anchors. We note that the fwhm difference between the SLD Gaussian profiles falls within the inner layer resolution of ∼4 Å and does not allow a quantitative estimate of the relative degree of order. Conversely, the distance between the Re centers and the substrate surface can be determined with high precision, as reflected by the small corresponding errors. This distance was calculated by the spacing between the Gaussian peak center and the inflection point of an error function, representing the Si/AlO$_x$ substrate (combined fit shown as solid lines in Figure 2b), which results in 1.03 ± 0.01 and 1.51 ± 0.01 nm for C$_6$−Re(M1) and C$_{11}$−Re(M1), respectively, consistent with AFM results (Table 1). Thus, the reflectivity data suggest that the different organic layers are, indeed, homogeneously distributed over the whole sample surface. It is also confirmed that the PA layers do not only act as simple anchors but also as efficient barrier and spacer layers, effectively localizing the molecular complexes at a well-defined distance from the substrate surface, which increases by 0.10 ± 0.02 nm per CH$_2$ group present in the PA alkyl backbone.

To investigate the long-range order of the molecular complexes and determine their surface orientation, we performed NEXAFS measurements. The strong and relatively sharp 1π* resonance, found at ∼399.3 eV attributed to a N 1s → π* transition of the aromatic nitrogen in the bipyridyl moiety, was used to evaluate the surface orientation of the molecular complexes (SI Figure 6). Both modular assembled and a directly attached Re complex [C$_1$−Re(M0); SI Scheme 1] exhibit a small, but measurable, dichroism, indicating a preferential ordering in the complex layers, on average. Since C$_1$−Re(M0) exhibits a comparable dichroism to C$_6$−Re(M1) and C$_{11}$−Re(M1), the apparent ordering in the Re layers is attributed to π−π stacking between individual bipyridyl moieties,[42] which implies the structural feasibility of an electronic interaction between individual molecular complexes over the bipyridine ligands. Following the method described in section S6 (SI), the NEXAFS-derived molecular tilt angle with

Table 1. Overview of the Organic Layer Thickness Determined by AFM and XRR, along with the Molecular Tilt Angles Obtained by AFM and NEXAFS Measurements

| Si/AlO$_x$ (3 nm) | d_{OL} (nm) | | $d_{Re(M1)}$ (nm) (AFM) | θ^a (deg) (AFM) | $\alpha_N{}^a$ (deg) (NEXAFS) |
	AFM	XRR			
C$_6$−Re(M1)	1.11 ± 0.15	1.03 ± 0.01	0.53 ± 0.17	54.9 ± 0.2	34 ± 7
C$_{11}$−Re(M1)	1.56 ± 0.13	1.51 ± 0.01	0.59 ± 0.16	50.2 ± 0.2	38 ± 7

^{a}All tilt angles are given with respect to the surface normal.

Modular Assembly of Vibrationally and Electronically Coupled Rhenium Bipyridine Carbonyl Complexes on Silicon

Figure 2. Normalized XRR curves as a function of the momentum transfer (q) of C_6–Re(M1) (blue) and C_{11}–Re(M1) (cyan) on 3 nm AlO$_x$-coated Si substrates (a). For clarity, the curves are shifted vertically along the intensity axis. The measured reflectivity is presented together with simulated intensities based on a four-layer slab model on top of the Si substrate (solid lines), which is described in detail in section S5 (SI). All model-related parameters are summarized in SI Table 3. SLD profiles are well-described by a Gaussian peak fitting solution (orange) (b). The contribution of the Si/AlO$_x$ substrate to the SLD profile is highlighted in gray.

respect to the surface normal (α_N) of 34°, 38°, and 32° is obtained with an empirically estimated accuracy of ±7° for C_6–Re(M1), C_{11}–Re(M1), and C_1–Re(M0), respectively. These values differ from AFM-derived molecular tilt angles (θ) (Table 1), suggesting that the attachment of the Re(M1) layer introduces a structural rearrangement to the underlying PA anchors. This difference is higher for C_6–Re(M1), which is in qualitative agreement with the observed surface roughness decrease, as measured by AFM (Figure 1).

To deepen our analysis of the electronic properties of the MSA layers and determine their elemental composition, coverage, and structural integrity, we conducted X-ray photoelectron spectroscopy (XPS) measurements. In Figure 3 high-resolution XPS spectra of the P 2p region are presented for the two PA anchors on 3 nm AlO$_x$-covered Si substrates. The PA coverages were calculated using the method suggested
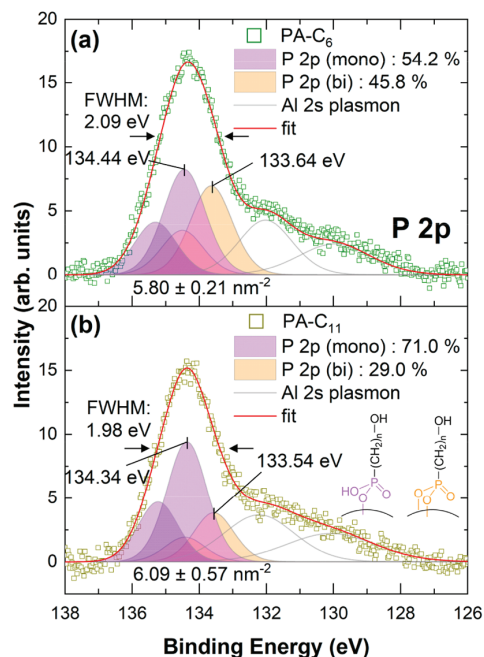
Figure 3. High-resolution XPS spectra of the P 2p region for PA–C_6 (a) and PA–C_{11} (b) on 3 nm AlO$_x$-covered Si substrates. Components colored in light purple and light orange refer to a monodentate and bidentate binding motif, respectively (inset in part b). Components colored in gray refer to Al 2s plasmon loss features.

by Kim et al. (section S7, SI) and are listed in Table 2. The coverage of the two PA types is comparable and, therefore,

Table 2. Overview of the PA and Molecular Complex Surface Coverage Obtained from XPS Measurements for Different Stages of the MSA Approach on 3 nm AlO$_x$-Coated Si Substrates[a]

Si/AlO$_x$ (3 nm)	PA coverage (nm^{-2})	Re(M1) coverage (nm^{-2})	PA/Re(M1) ratio
C_6–Re(M1)	5.80 ± 0.21	0.58 ± 0.04	10.00 ± 0.78
C_{11}–Re(M1)	6.09 ± 0.57	1.08 ± 0.06	5.64 ± 0.61

[a]Errors correspond to the standard deviation considering three different samples for each type.

independent of the PA backbone chain length. Apparently, disorder in the SAMPs layer, as indicated by AFM characterization for PA–C_6 (Figure 1), has no significant impact on the attainable surface coverage. The determined PA coverages are higher compared to experimental estimates obtained from the molar volume of phosphorus acid (4.25 nm^{-2})[43] and to the previously predicted theoretical limit of 4.3–4.7 nm^{-2} for crystalline aluminum oxide surfaces by density functional theory (DFT).[44] However, by considering the structural dimensions of the PAs used, possible surface loadings between 1.67 and 11.24 nm^{-2} for PA–C_{11} (section S4, SI) are theoretically obtainable, which depend on the molecular tilt with respect to the surface normal and are limited by the size of the phosphorus headgroup (SI Table 2). This implies that the maximum achievable PA surface coverage has a stronger dependence on the amount of accessible surface binding sites than previously assumed.[43,44] Therefore, the density, morphol-
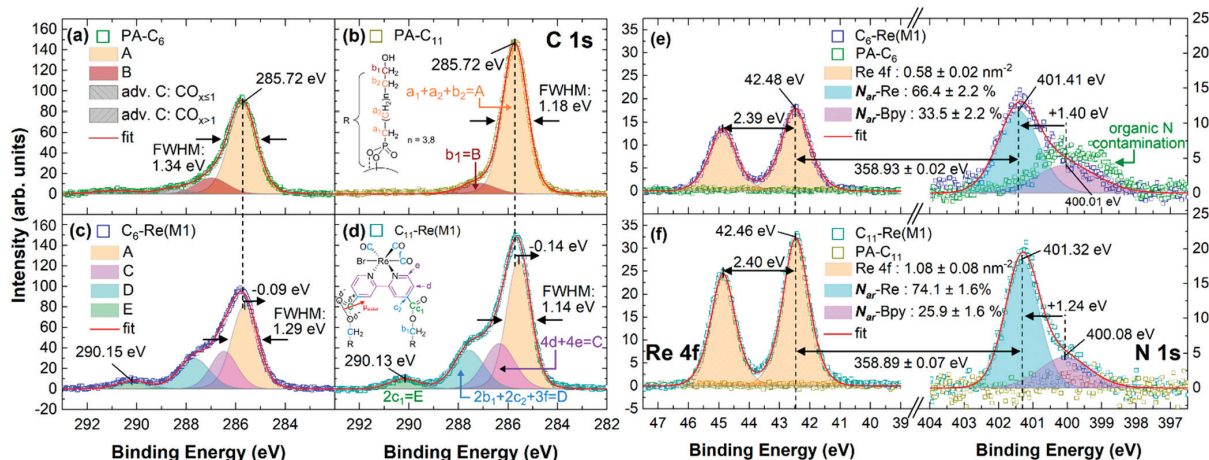
Modular Assembly of Vibrationally and Electronically Coupled Rhenium Bipyridine Carbonyl Complexes on Silicon

Figure 4. High-resolution XPS spectra of the C 1s region, together with the best fit for PA−C_6 (a), PA−C_{11} (b), C_6−Re(M1) (c), and C_{11}−Re(M1) (d) on 3 nm AlO_x-coated Si substrates. The chemical structure of the PA anchors and molecular complexes are shown as insets in parts b and d, respectively. The orientation of the ester group's dipole moment (μ_{ester}) is marked in red. Chemical functionalities with relative binding energy (BE) shifts of ≤0.3 eV (instrumental resolution) are grouped into single components (A−E). The theoretically and experimentally determined carbon ratios are summarized in SI Table 5. Corresponding high-resolution XPS spectra of the Re 4f and N 1s region, together with the best fit solution for PA−C_6 and C_6−Re(M1) (e), as well as for PA−C_{11} and C_{11}−Re(M1) (f). High-resolution XPS spectra of the Br 3d region are presented in SI Figure 9.

ogy, and surface termination of the AlO_x activation layer are likely defining factors.

To elaborate on this hypothesis, we compared the coverage of PA−C_{11} anchors on Si substrates covered by thinner AlO_x coatings (SI Table 4), the thicknesses of which were estimated by spectroscopic ellipsometry (SE) to be 1 nm, ∼0.45 nm (20 ALD cycles), and ∼0.25 nm (3 ALD cycles; submonolayer), respectively (section S1, SI). AlO_x layers below 1 nm thickness were grown by plasma-enhanced atomic layer deposition (PE-ALD)[45] (section S1, SI). The PA loading on 1 nm AlO_x (5.86 nm^{-2}) is comparable to a 3 nm AlO_x layer. However, the coverage is lower on a continuous 0.45 nm AlO_x (4.22 nm^{-2}) coating and, as expected, noticeably reduced on a 0.25 nm AlO_x coating (2.28 nm^{-2}). With the exception of inert metals and low-energy van der Waals surfaces, thermally grown AlO_x layers are known to be continuous on hydroxylated surfaces for a layer thickness ≥1 nm,[46] which is supported by the comparable PA coverage for 1 and 3 nm AlO_x. Due to the steric hindrance of trimethylaluminum (TMA),[46] the formation of a closed AlO_x surface layer is not possible for a three-cycle growth, which is reflected by the significantly lower PA coverage on a 0.25 nm AlO_x coating. Recently,[47] we demonstrated PA−C_{11} surface functionalization of a continuous ∼0.3 nm thick monolayer AlO_x grown on gallium nitride with a PA coverage of 4.5 ± 0.3 nm^{-2}, suggesting that the 0.45 nm AlO_x on Si is, indeed, continuous and that the PA coverage depends on the availability of AlO_x surface binding sites until a coverage of ∼6.09 ± 0.57 nm^{-2} is reached. We note that the underlying silicon substrate is entirely inaccessible by phosphonate chemistry under the applied reaction conditions (SI Figure 13a).

Despite a theoretical spin−orbit splitting of 0.86 ± 0.05 eV,[48,49] the P 2p peaks are broad (fwhm: ∼2.09 and 1.98 eV for PA−C_6 and PA−C_{11}) and nearly symmetric [for PA−C_6 slightly asymmetrical to lower binding energy (BE)], which is indicative of a mixed binding motif (inset in Figure 3b).[50,47] Interestingly, the best P 2p fit of PA−C_6 (Figure 3a) suggests a

mixed binding configuration, of which the monodentate mode is slightly dominant (54.2%), whereas for the PA−C_{11} (Figure 3b), a predominantly monodentate (71.0%) binding motif can be observed. We note that this distribution of binding modes was found on all measured samples (three in total for each PA type used). Previous results on atomically well-defined oxide surfaces attributed the evolution from higher to lower denticities to an increasing SAMPs surface coverage.[50,51] Since both PA coverages are similar, we conclude that the PA backbone structure influences the binding mode, even though the structural difference consists of only five methylene moieties. We speculate that the attainable degree of order during SAMPs formation is a decisive factor.

After attachment of the molecular complexes, three additional components can be identified in the C 1s spectrum (Figure 4a−d). Components C (purple), D (blue), and E (green) are attributed to bipyridine moieties, neighbors of the ester group, and carbonyl ligands as well as the ester group, respectively. The experimentally determined carbon ratios are in good agreement with the chemical structure of the PA anchors and are slightly overestimated for the molecular complexes (SI Table 5), which we explain by the presence of demetallized pyridine (*vide infra*). Noteworthy, the BE of carbon moieties localized in the Re(M1) layer is collectively blue-shifted, independent of the PA anchor type, by ∼1 eV compared to literature values,[52−54] which is clearly visible for the carbon moieties of the ester groups [∼290.15 and 290.13 eV for C_6−Re(M1) and C_{11}−Re(M1) vs 288.8−289.3 eV[52]]. In contrast, the BE of carbon moieties attributed to the PAs, *i.e.*, below the ester group (Figure 4b,d) is unaffected by this blue-shift. A similar effect was observed for midchain ester-functionalized SAMs on Au{111}, for which the photoelectron kinetic energies were consistently shifted by 0.85 ± 0.03 eV between the top and bottom methylene alkyl segments independent of the relative chain lengths.[55] The effect was attributed to a strong electric dipole layer formed in the SAM. Considering the orientation of the dipole moment of the ester

38

group (inset in Figure 4d) and the corresponding molecular tilt angles ($57.4° \pm 0.1°$ and $56.4° \pm 0.1°$ vs $31° \pm 4°$[55]), a correlated shift of 1.00 ± 0.01 and 1.00 ± 0.04 eV for C_6–Re(M1) and C_{11}–Re(M1), respectively, cannot be comprehensively explained. Notably and contrary to the results in ref 55, the BE of the ester group carbon moiety is also blue-shifted by ~1 eV, suggesting that the effect is at least partly related to electron delocalization over the Re(M1) moiety. The presence of Re in a single chemical environment and nitrogen in two different environments is observed (Figure 4e,f). The coverage of the molecular complexes (section S7, SI) is roughly 2 times lower for C_6–Re(M1) (0.58 ± 0.02 nm^{-2}) compared to C_{11}–Re(M1) (1.08 ± 0.08 nm^{-2}) and, in both cases, lower than the highest possible coverage of 1.43 ± 0.01 nm^{-2} estimated from QCC calculations (section S4, SI). The lower coverage on C_6–Re(M1) is attributed to a lower density of reactive hydroxyl terminal groups for PA–C_6, supported by a ~10° higher water static contact angle compared to a PA–C_{11}-coated surface (SI Table 1). Similar to carbon, the BE of Re $4f_{7/2}$ [42.46 and 42.48 eV for both C_6–Re(M1) and C_{11}–Re(M1)] is found to be ~1 eV higher than the expected literature value for a +1 oxidation state[53,54]. A similar BE shift was reported for structured rhenium bipyridine tricarbonyl dyes, modified by flexible or aromatic bridges and assembled on SiO$_2$ and TiO$_2$ by Langmuir–Blodgett techniques,[56] but the origin of the shift was not explained. In addition, the BE difference between the lower BE (purple) and higher BE (cyan) N 1s component is ~1 eV (Figure 4e,f), which is consistent with the observed C 1s and Re 4f BE shift. A BE of ~400 eV is typical for pyridinic nitrogen,[57] i.e., the aromatic nitrogen of the bipyridine moiety, which we verified by XPS measurement taken from a thin layer of PA–modified bipyridine ligands (SI Scheme 1), deposited on an Au surface via drop-casting (SI Table 6). The amount of pyridinic nitrogen found on C_{11}–Re(M1) ($25.9 \pm 1.6\%$) coincides well with the amount needed to achieve full surface coverage ($24.5 \pm 6.3\%$) estimated from quantum-chemical calculations (QCC) (S4). Therefore, we suggest that the pyridinic nitrogen component is related to a demetallized complex, i.e., a molecular complex, from which the metal center is removed. The amount of pyridinic nitrogen on C_6–Re(M1) is slightly higher ($33.5 \pm 2.2\%$), which is, however, related to a minor contamination present already in the PA–C_6 anchor (Figure 4e).

To elucidate the origin of the correlated BE shift (Figure 4), a molecular complex was directly attached to a 3 nm AlO$_x$-coated surface [C_1–Re(M0); SI Scheme 1], i.e., without the presence of an ester group as a coupling agent. In addition, a Ti/Pt (15/150 nm) layer was grown on top of a Si substrate by electron beam evaporation and a thin layer of uncoupled molecular complexes [Re(M1) (free); SI Scheme 1] was deposited on the Pt-covered surface via drop-casting (physisorption). SI Table 6 shows the results of the XPS characterization. The Re $4f_{7/2}$ BE of the uncoupled complex, physisorbed on the Pt-covered substrate, is 41.45 ± 0.14 eV, which is in good agreement with a +1 oxidation state[53,54] and translates to a red-shift of 1.12 ± 0.01 and 1.14 ± 0.05 eV compared to the BEs of C_6–Re(M1) and C_{11}–Re(M1), respectively. Furthermore, the corresponding N 1s BE is 400.24 ± 0.03 eV and, thus, comparable to that of the nitrogen of the demetallized bipyridine moiety. Surprisingly, the observed Re $4f_{7/2}$ BE shift for C_1–Re(M0) is 0.87 eV and, thus, slightly lower than that of MSA layers but still significantly higher than that of an uncoupled complex. The

correlated BE shifts for the MSA layers on thinner AlO$_x$ coatings are comparable to the 3 nm benchmark (SI Table 6). Therefore, we conclude that while the collective BE shifts observed by XPS measurement are partly generated by the embedded dipole moment of the ester groups, they are primarily induced by electronic interactions between individual molecular complexes. In our understanding, the electron density of the Re metal centers, mainly provided by d-orbital contributions from the Re(CO)$_3$Br moieties, is delocalized between two or more complexes, which is mediated by the bipyridine ligands via mixed electronic orbitals (π–π stacking), already partly suggested by NEXAFS measurements (SI Figure 6). This would also explain the BE difference between the metallized and demetallized pyridinic nitrogen of ~1 eV (Figure 4), as the primary source of electron density is lost upon decomposition of the complex, also suggesting that the demetallized bipyridine ligand does not participate in the electron density distribution process. Due to the size of the Re metal center ($Z = 75$), a surface-immobilized, demetallized bipyridine is likely to adopt a different surface orientation compared to the metallized complexes, which is consistent with the small dichroism determined by NEXAFS measurements (SI Figure 6).

We further investigated the intercomplex interactions via changes of the vibrational modes of bound and unbound molecular complexes by attenuated total reflectance Fourier-transform infrared (ATR-FTIR) spectroscopy (Figure 5). A sketch of the three characteristic Re–carbonyl (CO) vibrational stretching modes,[30] i.e., the in-phase symmetric a′(1), antisymmetric a″, and out-of-phase symmetric a′(2) stretch are presented at the top of Figure 5. The maxima and relative intensities of the Re–CO vibrational modes of C_6–Re(M1) and C_{11}–Re(M1) are comparable and, therefore, independent of the chain length of the PA anchor, suggesting no vibrational interactions with the underlying substrate, as previously observed on TiO$_2$ surfaces.[37] However, the vibrational spectra are appreciably different from those of the unbound molecular complex [C_{11}–Re(M1) (free)] (Figure 5a). Two Gaussian components (orange)[58] were used to fit the a′(1) vibrational mode of the surface-bound complex to account for the doublet structure observed for C_{11}–Re(M1) (free). Compared to the unbound complex, the a′(1) doublet feature is slightly broadened and the doublet intensity ratio is inverted. However, the vibrational energies are nearly identical. Conversely, the signal intensity of the a′(1) relative to a″ and a′(2) of the surface-bound complex is significantly increased compared to that of the unbound complex, indicating that an in-phase symmetric stretch is strongly favored over an antisymmetric or out-of-phase symmetric stretch. The a″ and, in particular, the a′(2) stretching modes are blue-shifted, which we attribute to vibrational coupling between individual complexes as a consequence of spatial confinement upon attachment to the surface-bound PA anchors. Similar vibrational coupling was reported, e.g., for ReCl(CO)$_3$(bypy)CO$_2$H clusters directly deposited on TiO$_2$ nanoparticles[38] and ReCl(CO)$_3$(bypy)CO$_2$H/ReCl-(CO)$_3$(bypy) (CO$_2$H)$_2$ films on nanocrystalline TiO$_2$.[59] Generally, the coupling between metal carbonyl groups is large enough to excitonically delocalize the vibrations across multiple carbonyl groups on neighboring molecules.[59] In addition, reports[38,59] suggest a blue-shift for coupled vibrational modes around 10–15 cm^{-1} per Re "dimer" aggregate, i.e., vibrational coupling between two surface-bound com-
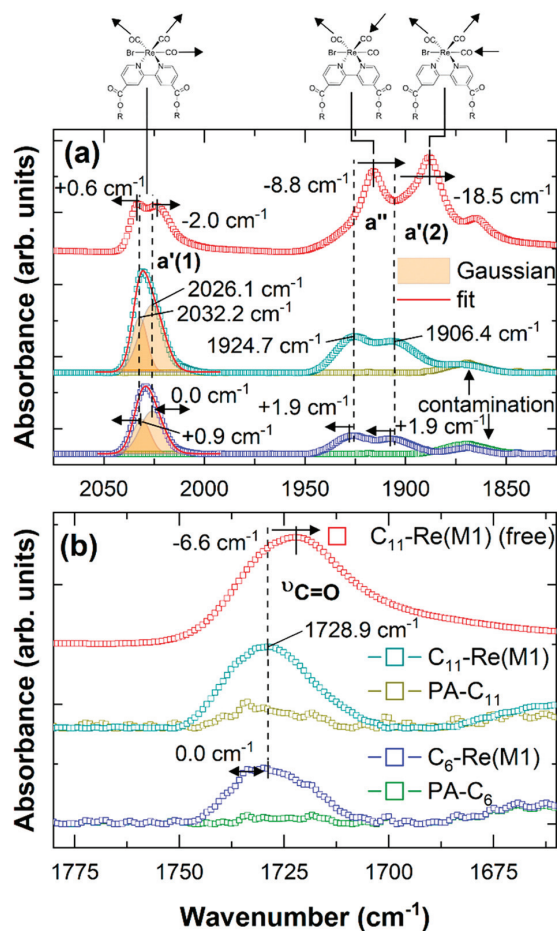
Modular Assembly of Vibrationally and Electronically Coupled Rhenium Bipyridine Carbonyl Complexes on Silicon

Figure 5. ATR-FTIR spectra of the three Re−carbonyl (C≡O) stretching modes (a), as well as the C=O stretching mode from the ester moiety (b), presented for an unbound molecular complex coupled to PA−C_{11} anchor molecules [C_{11}−Re(M1) (free); red], as well as for PA−C_{11} (dark yellow) and C_{11}−Re(M1) (cyan) and for PA−C_6 (green) and C_6−Re(M1) (blue) on 3 nm AlO_x-covered Si substrates. For clarity, the IR spectra are shifted vertically along the intensity axis. A sketch of the three Re−CO vibrational stretching modes, *i.e.*, the in-phase symmetric a′(1), antisymmetric a″, and out-of-phase symmetric a′(2) stretch, are shown at the top of part a. The spectrum of C_{11}−Re(M1) (free) was taken from a powder. A corresponding comparison between an uncoupled and a coupled molecular complex can be found in SI Figure 10.

plexes. For a trimer, the vibrational energies would increase further by ∼10 cm^{-1}. Judging from the observed blue-shift for both MSA layers (∼9−18 cm^{-1}), the vibrational coupling is most likely limited to only two adjacent Re complexes. We note that the vibrational energies and relative intensities of the Re−CO vibrational modes are stable up to ∼58 d, *i.e.*, on a month scale (SI Figure 10d), indicating the stability of the vibrational coupling and, thus, of the Re terminal layers. We further note that the position of the C=O stretching mode relative to that of the ester group of C_{11}−Re(M1) (free), identical for the surface-bound molecular complexes (1728.9 cm^{-1}) (Figure 5b), confirms that both carboxylic acid modifications of Re(M1) are involved in the covalent attachment of the molecular complexes.

To substantiate our analysis of the intercomplex interactions, we performed photoluminescence (PL) measurements on C_{11}−Re(M1) (free) dissolved in DMF and C_{11}−Re(M1) assembled on a 3 nm AlO_x-covered Si substrate (SI Figure 11). Modular assembly of the Re(M1) promotes a blue-shift of the PL emission of ∼30 nm. Recently, blue-shifted emissions arising from π−π stacking interactions between two nitrogen-donor ligands were reported for luminescent rhenium tricarbonyl complexes,[60] suggesting that charge transfer, mediated by π−π stacking between individual bipyridine ligands, is feasible. We conclude that the collective BE blue-shift measured by the XPS measurements (Figure 4 and SI Table 6) is, indeed, related to charge transfer between individual Re metal centers. To our knowledge, this is the first time that XPS has been used to establish a quantitative connection between vibrational and electronic coupling of surface-assembled rhenium(I) bipyridine tricarbonyl molecular complexes. Since no dependence of the PA or AlO_x layer thickness could be observed either by XPS or ATR-FTIR measurements, the observed phenomena are purely related to intercomplex interactions. Furthermore, the strength of the intermolecular coupling (either vibrational or electronic) appears to be independent of the molecular complex surface coverage, suggesting that a lower threshold aggregation density, for which such interactions are diminished or even suppressed is not reached for coverages of ≥0.58 ± 0.04 nm^{-2}.

To evaluate the selectivity of the MSA approach, we applied a low-temperature PE-ALD process compatible with photo-lithography (section S1, SI) to create an AlO_x micropattern on a Si substrate. The surface topography of the AlO_x-patterned substrate, evaluated by AFM, is presented in SI Figure 12. As a proof of concept, we opted to use PA−C_{11} anchors due to the higher order in the SAMPs and the higher surface coverage of the molecular complexes. Scanning photoelectron microscopy (SPEM) measurements were performed to elementally map the micropatterned and functionalized substrates. The spatial resolution (∼150 nm) is notably higher than for laboratory-based XPS setups, which allowed the characterization of core level emission from individual stripes (∼4 μm in width) of the AlO_x-patterned surface. Figure 6 shows Al 2p (a) and Re 4f (b) SPEM maps of C_{11}−Re(M1) on an AlO_x-patterned n-type Si substrate. The characteristic Re 4f signal of the molecular complex (bottom part of Figure 6c) is exclusively found on the AlO_x, which uniformly follows the pattern of the activation layer, demonstrating that the MSA was formed selectively on the AlO_x micropattern. We note that the SPEM-derived Re 4f spectrum shows a tail to higher BE, which can be fitted by a second Re species with a significantly higher oxidation state. We attribute the origin of this second species to the highly focused X-ray beam, which likely led to partial decomposition of the organic constituents of the MSA layer. For comparison, a laboratory XPS Re 4f spectrum of the same sample prior to SPEM characterization is shown in the top part of Figure 6c, indicating the presence of Re in only one distinct chemical environment.

■ CONCLUSION AND OUTLOOK

With the modular surface assembly (MSA) approach investigated in this work, a stable and area-selective functionality can be introduced to any solid substrate independent of the specific chemical affinity of the surface. As a proof of concept, MSA layers based on rhenium(I) bipyridine tricarbonyl moieties are placed with sub-nanometer
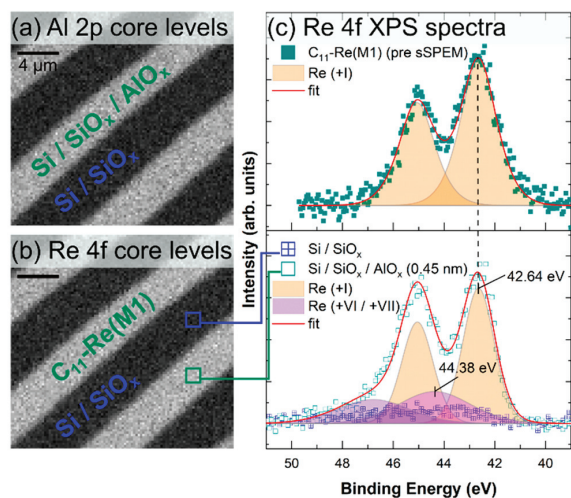
Modular Assembly of Vibrationally and Electronically Coupled Rhenium Bipyridine Carbonyl Complexes on Silicon

Figure 6. SPEM Al 2p (a) and Re 4f (b) maps of C_{11}−Re(M1) on an AlO$_x$-patterned, n-type Si substrate and the corresponding Re 4f spectra (bottom graph in part c) obtained from the areas indicated in part b. For comparison, a Re 4f spectrum of the same sample prior to SPEM characterization obtained by conventional XPS is shown in the top part of panel c. The characteristic Re 4f signal of the molecular complex is exclusively found on the AlO$_x$-covered parts, uniformly following the pattern of the activation layer (bottom graph of part c).

precision on aluminum oxide (AlO$_x$)-covered silicon substrates to generate precisely structured spatial ensembles with strong intermolecular vibrational and electronic coupling. We demonstrate that both the vibrational and electronic couplings are related, and that the electronic coupling can be monitored by X-ray photoelectron spectroscopy via a correlated shift to higher electron binding energies of the functional groups located in the molecular complexes. By carefully selecting the structure of the MSA, electronic interactions with the semiconductor substrate can be disentangled to exclusively investigate the interactions between the surface-immobilized molecular complexes. The MSA approach can be transferred to any substrate on which a conformal aluminum oxide growth via atomic layer deposition is feasible. The approach combines surface passivation and surface functionalization in one step to create well-defined and scalable hybrid functional interfaces, which opens a new avenue in semiconductor device fabrication. As an example, we have recently shown that PA−C$_{11}$ anchors can be grafted onto a monolayer AlO$_x$ surface layer grown on gallium nitride (GaN) by PE-ALD with a high surface coverage, creating a well-defined semiconductor/dielectric/PA anchor hybrid interface,[47] which motivates additional studies. Due to its high flexibility, the approach can be further expanded, e.g., by inclusion of metal−polypyridyl coordination chemistry,[61,62] to bridge the gap toward multiple metal−organic layers, which are highly relevant for device applications.[31,63] Furthermore, additional functionalities can be introduced on uncovered Si surface areas, e.g., via silane chemistry[64,65] or, more specifically, via aryldiazonium cation reduction[66] to create a network of area-selective functionalities for applications in electronic devices, biosensors, and photovoltaic or photoelectrochemical cells. Furthermore, the conformal nature of the ALD growth and the experimentally simple chemistry of the MSA approach compels

the focus on delicate, high aspect ratio, nanostructured semiconductors, e.g., for sensing applications.[67,68]

■ EXPERIMENTAL SECTION

General. Unless stated otherwise, all chemicals were purchased from Sigma-Aldrich, ABCR, or TCI Europe and used without further purification. All reactions with air- and moisture-sensitive substances were carried out under an argon (Ar) 5.0 (99.9990%, Westfalen AG) atmosphere using standard Schlenk techniques. Prior to use, all glassware was heat-dried under a vacuum. Toluene, tetrahydrofuran, and dichloromethane were dried using an MBraun SPS-800 solvent purification system and stored over 3 Å molecular sieves. Liquid chromatography−mass spectrometry (LC−MS)-grade acetonitrile and methanol were purchased from VWR. Single side polished, 381 ± 25 μm nominally thick, highly p-doped [B-doped, <0.005 Ω·cm (>1.2 × 10^{19} cm$^{−3}$); degenerate doping] Si(100) wafers grown by the Czochralski (CZ) method were ordered from Si-Mat (Kaufering, Germany) and diced into 1 × 1 cm^2 pieces. In addition, single side polished, 525 ± 20 μm nominally thick, n-doped (As-doped, <0.005 Ω·cm) Si(100) wafers grown by the Czochralski (CZ) method were obtained from SIEGERT WAFER (Aachen, Germany) and diced into 1 × 1 cm^2 pieces. Prior to any surface treatment, the diced wafer pieces were subsequently cleaned in an ultrasonic bath (37 kHz, 120 W) with acetone (Merck, VLSI Selectipur, >99.9%), 2-propanol (BASF, VLSI Selectipur, >99.9%), and deionized water (DI H$_2$O; 18.2 MΩ·cm at 25 °C, Merck Millipore) for 10 min, respectively, and dried under a stream of nitrogen (N$_2$).

Preparation of Self-assembled Monolayers of Phosphonic Acids (SAMPs). SAMPs of 6-hydroxyhexylphosphonic acid (≥98% (GC); referred to as PA−C$_6$) and 11-hydroxyundecylphosphonic acid (≥99% (GC); referred to as PA−C$_{11}$) (SiKÉMIA, Montpellier, France) were prepared via an immersion technique recently reported in detail for monolayer AlO$_x$ grown on c-plane, Ga-polar GaN substrates.[47]

Attachment of Re(2,2′-bipyridine-4,4′-dicarboxylic Acid)-(CO)$_3$Br [Re(M1) (free)]. Re(M1) (free) was synthesized following a procedure reported in ref 69. A detailed description of the synthetic route and characterization of all metal complexes are presented in section S12 (SI). Both carbon acid modifications of Re(M1) were coupled to the OH end groups of the respective PA anchor layers via a mild Steglich esterification reaction,[70] which we adopted and optimized accounting for the constraints of a surface reaction. The PA-functionalized wafer pieces (mounted on a Teflon sample holder) were immersed vertically in a 30 mL tetrahydrofuran (THF; anhydrous, HPLC-grade, ≥99.9%,) solution of Re(M1) (free) (3 mg, 5.05 μmol, 1 equiv), N-(3-(dimethylamino)propyl)-N′-ethyl-carbodiimide hydrochloride (EDCl; 29 mg, 0.15 mmol, 30 equiv), and 4-(dimethylamino)pyridine (DMAP; 3 mg, 25 μmol, 5 equiv). The reaction was stirred under light exclusion and an Ar atmosphere at 50 °C for 12 h. After the esterification reaction, the pieces were cleaned subsequently with N,N-dimethylformamide (DMF; Sigma-Aldrich, 99.8%), THF (Sigma-Aldrich, anhydrous, inhibitor-free, ≥99.9%), DMF, methanol (MeOH; Sigma-Aldrich, 99.8%), and DI H$_2$O in an ultrasonic bath (37 kHz, 60 W) for 5 min, respectively, to remove excess reactants and byproducts, dried under N$_2$, and stored in a desiccator (~10$^{−2}$ mbar).

Attachment of Re(([2,2′-bipyridin]-4-ylmethyl)phosphonic Acid)(CO)$_3$Br [C$_1$−Re(M0) (free)]. C$_1$−Re(M0) (free) was synthesized following procedures presented in detail in section S12 (SI). C$_1$−Re(M0) was directly attached to the in situ oxygen-plasma-activated AlO$_x$-coated substrate by vertical immersion of the wafer pieces (mounted on a Teflon sample holder) in a 40 mL ethanol (EtOH; VWR, ethanol absolute ≥99.8%, AnalaR NORMAPUR, ACS, Reag. Ph. Eur.) solution containing 5 × 10$^{−4}$ mol·L$^{−1}$ of PA−C$_1$−ReBpy (free) and stored for 24 h vibration-free in the dark under an N$_2$ atmosphere at room temperature.

Atomic Force Microscopy (AFM). Surface topography and roughness were investigated by AFM on a commercial setup (MultiMode 8, Bruker, Billerica, MA) in amplitude-modulated (AM) tapping-mode (TM) under ambient conditions. In addition,

the organic layer thickness was probed by AFM operated in contact mode (CM) and AM-TM. AFM "scratching" experiments were performed on a commercial setup (Nanoscope V Controller, Dimension V Controller, Bruker Nano GmbH, Berlin, Germany) operated under ambient conditions. A detailed description of AFM setups and experimental procedures is given in section S3 (SI).

X-ray Reflectivity (XRR). XRR measurements were performed on an in-house built X-ray reflectometer equipped with an Mo source (Mo $K\alpha$ = 17.45 keV) under ambient conditions. A detailed description of the setup can be found elsewhere.[71] The reflected intensity was measured by ($\theta-2\theta$) scans of sample and detector angle and corrected by subtraction of background scans with an offset angle $\Delta\theta$ of 0.1°. A beam footprint correction was performed to account for the effective beam height at low angles.[72] A detailed description of the data processing and fitting can be found in section S5 (SI). Mean values and standard deviations are obtained by comparing two samples of two different batches.

X-ray Photoelectron Spectroscopy (XPS). XPS measurements were performed on a Kratos Axis Supra XPS setup (Kratos Analytical Ltd., Manchester, UK; base pressure ≤8 × 10⁻⁹ mbar) equipped with a monochromatic Al X-ray source (Al $K\alpha$ = 1486.7 eV) operated with an emission current of 15 mA. XPS spectra were acquired in the hybrid lens mode at a pass energy (PE) of 10 eV and a takeoff angle of 0°. The beam area was set to ~2 × 1 mm² using the slot collimation mode. The binding energy of the hemispherical analyzer was calibrated with *in situ* sputter-cleaned silver (Ag 3d, 1118.51 eV), gold (Au 4f, 1402.73 eV), and copper (Cu 2p, 554.07 eV) standards (given in kinetic energy) with an accuracy of 0.025 eV. An instrumental broadening of 0.30 eV was determined by fitting the measured Ag 3d core level spectrum of an Ag calibration sample with a Voigt function.[47] No charge neutralization was performed, as no measurable binding energy shifts were observed for nonfunctionalized substrates). All recorded spectra were processed with CasaXPS (Casa Software Ltd., ver. 2.3.19). A detailed description of the data processing, fitting procedure, and methodology can be found in section S7 (SI).

Attenuated Total Reflectance Fourier-Transform Infrared Spectroscopy (ATR-FTIR). ATR-FTIR measurements were performed on a VERTEX 70v vacuum FTIR spectrometer (Bruker, Billerica, MA) equipped with a liquid nitrogen cooled MCT detector, using a grazing angle ATR accessory (VariGAT, Harrick Scientific Products, New York, NY) with a single reflection Germanium ATR crystal (Pike Technologies, Fitchburg, WI), significantly larger than the dimensions of the sample. An incidence angle of 65° was applied. Prior to measurements, samples were stored in the pumped measurement chamber overnight immediately after cleaning. All surface IR spectra were averaged over 2000 scans with a resolution of 2 cm⁻¹ and background-referenced to the clean ATR crystal measured against vacuum. Data acquisition and processing were performed with the software OPUS (ver. 8.129, Bruker, Billerica, MA). For surface IR spectra a rubberband baseline correction was applied, and IR bands were fitted by Gaussian components to a linear background.[58]

Near-Edge X-ray Absorption Fine Structure (NEXAFS). NEXAFS measurements were performed at the BACH beamline at the Elettra synchrotron (Trieste, Italy) in Auger electron yield (AEY) mode using a SCIENTA R3000 hemispherical electron energy analyzer (base pressure ≤2 × 10⁻¹⁰ mbar). Technical details of the BACH end station can be found in ref 73. All measurements were performed at low temperature (130−160 K) to minimize X-ray-induced damage to the organic layers. A detailed description of the data processing and methodology can be found in section S6 (SI).

Scanning Photoelectron Microscopy (SPEM). SPEM measurements were performed at the ESCA Microscopy beamline at the Elettra synchrotron (Trieste, Italy). Technical details of the SPEM setup can be found in ref 74. The X-ray photon energy was set to 638.00 eV with a (Gaussian) X-ray focal diameter of ~150 nm. Elemental maps and spatially resolved spectra were taken by fixing the PE of the electron analyzer to 40 and 20 eV, respectively. Local XPS spectra were acquired by illuminating the point of interest with the submicron X-ray probe. The beamline settings resulted in an overall instrumental broadening of 0.35 eV, as determined by the Au 4f from an internal gold standard.

Quantum-Chemical Calculations (QCC). Investigated model compounds were optimized at the PBE0-D3/def2-TZVP[75−78] level of theory using the TURBOMOLE[79,80] program package ver. V7.3.

ASSOCIATED CONTENT

Supporting Information

The Supporting Information is available free of charge at https://pubs.acs.org/doi/10.1021/jacs.1c09061.

Introduced nomenclature (section S0); detailed descriptions of experimental procedures and supplementary figures and tables [ALD growth and *in situ* SE (section S1), water SCA measurements (section S2), AFM (sections S3 and S10), QCC (section S4), XRR (section S5), NEXAFS (section S6), XPS (section S7), ATR-FTIR (section S8), PL (section S9), achromatic XPS (section S11)]; and molecular synthesis (section S12) with detailed descriptions of experimental procedures and supplementary figures and tables [FTIR, EA, ESI-MS, NMR (¹H, ¹³C, and ³¹P), UV/vis] (PDF)

AUTHOR INFORMATION

Corresponding Authors

Johannes D. Bartl − *Walter Schottky Institute and Physics Department, Technische Universität München, 85748 Garching bei München, Germany; Department of Chemistry, WACKER-Chair for Macromolecular Chemistry, Technische Universität München, 85747 Garching bei München, Germany;* orcid.org/0000-0003-3767-8782; Email: johannes.bartl@tum.de

Christopher Thomas − *Department of Chemistry, WACKER-Chair for Macromolecular Chemistry, Technische Universität München, 85747 Garching bei München, Germany;* Email: christopher.thomas@tum.de

Authors

Alex Henning − *Walter Schottky Institute and Physics Department, Technische Universität München, 85748 Garching bei München, Germany;* orcid.org/0000-0003-0419-4992

Martina F. Ober − *Faculty of Physics and Center for Nanoscience (CeNS), Ludwig-Maximilians-Universität München, 80539 München, Germany*

Gökcen Savasci − *Max Planck Institute for Solid State Research, 70569 Stuttgart, Germany; Department of Chemistry, University of Munich, LMU, 81377 Munich, Germany; Cluster of Excellence E-conversion, 85748 Garching, Germany;* orcid.org/0000-0002-6183-7715

Bahar Yazdanshenas − *Walter Schottky Institute and Physics Department, Technische Universität München, 85748 Garching bei München, Germany;* Present Address: Physics Department E59, Technische Universität München, James-Franck-Straße 1, 85748 Garching bei München, Germany; orcid.org/0000-0001-9882-4443

Peter S. Deimel − *Physics Department E20, Technische Universität München, 85748 Garching bei München, Germany*

Elena Magnano − *IOM CNR, Laboratorio TASC, 34149 Trieste, Italy; Department of Physics, University of Johannesburg, Auckland Park 2006, South Africa;* orcid.org/0000-0001-6465-807X

42

Modular Assembly of Vibrationally and Electronically Coupled Rhenium Bipyridine Carbonyl Complexes on Silicon

Federica Bondino − *IOM CNR, Laboratorio TASC, 34149 Trieste, Italy;* orcid.org/0000-0001-6505-9319

Patrick Zeller − *Elettra-Sincrotrone Trieste SCpA, 34149 Trieste, Italy;* Present Address: Helmholtz-Zentrum Berlin für Materialien and Energie GmbH, BESSY II, Albert-Einstein-Straße 15, 12489 Berlin, Germany; Present Address: Fritz-Haber-Institute der Max-Planck-Gesellschaft, Department of Inorganic Chemistry, Faradayweg 4-6, 14195 Berlin, Germany

Luca Gregoratti − *Elettra-Sincrotrone Trieste SCpA, 34149 Trieste, Italy*

Matteo Amati − *Elettra-Sincrotrone Trieste SCpA, 34149 Trieste, Italy*

Claudia Paulus − *Walter Schottky Institute and Physics Department, Technische Universität München, 85748 Garching bei München, Germany*

Francesco Allegretti − *Physics Department E20, Technische Universität München, 85748 Garching bei München, Germany*

Anna Cattani-Scholz − *Walter Schottky Institute and Physics Department, Technische Universität München, 85748 Garching bei München, Germany; Center for Nanoscience (CeNS), Ludwig-Maximilians-Universität München, 80539 München, Germany;* orcid.org/0000-0003-4974-8629

Johannes V. Barth − *Physics Department E20, Technische Universität München, 85748 Garching bei München, Germany*

Christian Ochsenfeld − *Max Planck Institute for Solid State Research, 70569 Stuttgart, Germany; Department of Chemistry, University of Munich, LMU, 81377 Munich, Germany; Cluster of Excellence E-conversion, 85748 Garching, Germany*

Bert Nickel − *Faculty of Physics and Center for Nanoscience (CeNS), Ludwig-Maximilians-Universität München, 80539 München, Germany*

Ian D. Sharp − *Walter Schottky Institute and Physics Department, Technische Universität München, 85748 Garching bei München, Germany;* orcid.org/0000-0001-5238-7487

Martin Stutzmann − *Walter Schottky Institute and Physics Department, Technische Universität München, 85748 Garching bei München, Germany*

Bernhard Rieger − *Department of Chemistry, WACKER-Chair for Macromolecular Chemistry, Technische Universität München, 85747 Garching bei München, Germany;* orcid.org/0000-0002-0023-884X

Complete contact information is available at:
https://pubs.acs.org/10.1021/jacs.1c09061

Author Contributions

&J.D.B. and C.T. contributed equally to this work. All authors have given approval to the final version of the manuscript.

■ **ACKNOWLEDGMENTS**

■ **REFERENCES**

(1) Jiang, Y.; Tian, B. Inorganic semiconductor biointerfaces. *Nat. Rev. Mater.* **2018**, *3*, 473−490.

(2) Diercks, C. S.; Liu, Y.; Cordova, K. E.; Yaghi, O. M. The role of reticular chemistry in the design of CO_2 reduction catalysts. *Nat. Mater.* **2018**, *17*, 301−307.

(3) O'Regan, B.; Grätzel, M. A Low-Cost, High-Efficiency Solar Cell Based on Dye-Sensitized Colloidal TiO_2 Films. *Nature* **1991**, *353*, 737−740.

(4) Xu, C.; Yang, W.; Ren, Z.; Dai, D.; Guo, Q.; Minton, T. K.; Yang, X. Strong Photon Energy Dependence of the Photocatalytic Dissociation Rate of Methanol on $TiO_2(110)$. *J. Am. Chem. Soc.* **2013**, *135*, 19039−19045.

(5) Jeong, K. S.; Pensack, R. D.; Asbury, J. B. Vibrational Spectroscopy of Electronic Processes in Emerging Photovoltaic Materials. *Acc. Chem. Res.* **2013**, *46*, 1538−1547.

(6) Teplyakov, A. V.; Bent, S. F. Semiconductor surface functionalization for advances in electronics, energy conversion, and dynamic systems. *J. Vac. Sci. Technol., A* **2013**, *31*, 050810.

(7) Bent, S. F.; Kachian, J. S.; Rodríguez-Reyes, J. C. F.; Teplyakov, A. V. Tuning the reactivity of semiconductor surfaces by functionalization with amines of different basicity. *Proc. Natl. Acad. Sci. U. S. A.* **2011**, *108*, 956−960.

(8) Vilan, A.; Cahen, D. Chemical Modification of Semiconductor Surfaces for Molecular Electronics. *Chem. Rev.* **2017**, *117*, 4624−4666.

(9) Wieszczycka, K.; Staszak, K.; Woźniak-Budych, M. J.; Litowczenko, J.; Maciejewska, B. M.; Jurga, S. Surface functionalization—The way for advanced applications of smart materials. *Coord. Chem. Rev.* **2021**, *436*, 213846.

(10) Peczonczyk, S. L.; Mukherjee, J.; Carim, A. I.; Maldonado, S. Wet Chemical Functionalization of III−V Semiconductor Surfaces: Alkylation of Gallium Arsenide and Gallium Nitride by a Grignard Reaction Sequence. *Langmuir* **2012**, *28*, 4672−4682.

(11) Lee, S. H.; Kang, J. S.; Kim, D. A Mini Review: Recent Advances in Surface Modification of Porous Silicon. *Materials* **2018**, *11* (12), 2557.

(12) Meng, X. An overview of molecular layer deposition for organic and organic−inorganic hybrid materials: mechanisms, growth

characteristics, and promising applications. *J. Mater. Chem. A* **2017**, *5*, 18326−18378.

(13) Garrido-Diez, D.; Baraia, I. Review of wide bandgap materials and their impact in new power devices. *ECMSM* **2017**, 1−6.

(14) Deckers, J.; Cornagliotti, E.; Debucquoy, M.; Gordon, I.; Mertens, R.; Poortmans, J. Aluminum Oxide-aluminum Stacks for Contact Passivation in Silicon Solar Cells. *Energy Procedia* **2014**, *55*, 656−664.

(15) Schmidt, J.; Veith, B.; Werner, F.; Zielke, D.; Brendel, R. Silicon surface passivation by ultrathin Al_2O_3 films and Al_2O_3/SiN_x stacks. *2010 35th IEEE Photovoltaic Specialists Conference*; IEEE, 2010; pp 000885−000890.

(16) Brinkmann, K. O.; Gahlmann, T.; Riedl, T. Atomic Layer Deposition of Functional Layers in Planar Perovskite Solar Cells. *Solar RRL* **2020**, *4*, 1900332.

(17) Martinson, A. B. F.; Elam, J. W.; Hupp, J. T.; Pellin, M. J. ZnO Nanotube Based Dye-Sensitized Solar Cells. *Nano Lett.* **2007**, *7*, 2183−2187.

(18) Hoffeditz, W. L.; Son, H.-J.; Pellin, M. J.; Farha, O. K.; Hupp, J. T. Engendering Long-Term Air and Light Stability of a TiO_2-Supported Porphyrinic Dye via Atomic Layer Deposition. *ACS Appl. Mater. Interfaces* **2016**, *8*, 34863−34869.

(19) Veronese, L.; Procopio, E. Q.; De Rossi, F.; Brown, T. M.; Mercandelli, P.; Mussini, P.; D'Alfonso, G.; Panigati, M. New dinuclear hydrido-carbonyl rhenium complexes designed as photosensitizers in dye-sensitized solar cells. *New J. Chem.* **2016**, *40*, 2910−2919.

(20) Sharma, K.; Sharma, V.; Sharma, S. S. Dye-Sensitized Solar Cells: Fundamentals and Current Status. *Nanoscale Res. Lett.* **2018**, *13*, 381.

(21) Cattani-Scholz, A. Functional Organophosphonate Interfaces for Nanotechnology: A Review. *ACS Appl. Mater. Interfaces* **2017**, *9*, 25643−25655.

(22) Hanson, E. L.; Schwartz, J.; Nickel, B.; Koch, N.; Danisman, M. F. Bonding Self-Assembled, Compact Organophosphonate Monolayers to the Native Oxide Surface of Silicon. *J. Am. Chem. Soc.* **2003**, *125*, 16074−16080.

(23) Hanson, E. L.; Guo, J.; Koch, N.; Schwartz, J.; Bernasek, S. L. Advanced Surface Modification of Indium Tin Oxide for Improved Charge Injection in Organic Devices. *J. Am. Chem. Soc.* **2005**, *127*, 10058−10062.

(24) Adden, N.; Gamble, L. J.; Castner, D. G.; Hoffmann, A.; Gross, G.; Menzel, H. Phosphonic Acid Monolayers for Binding of Bioactive Molecules to Titanium Surfaces. *Langmuir* **2006**, *22*, 8197−8204.

(25) Hotchkiss, P. J.; Malicki, M.; Giordano, A. J.; Armstrong, N. R.; Marder, S. R. Characterization of phosphonic acid binding to zinc oxide. *J. Mater. Chem.* **2011**, *21*, 3107−3112.

(26) Zhao, R.; Rupper, P.; Gaan, S. Recent Development in Phosphonic Acid-Based Organic Coatings on Aluminum. *Coatings* **2017**, *7*, 133.

(27) Ringk, A.; Li, X.; Gholamrezaie, F.; Smits, E. C. P.; Neuhold, A.; Moser, A.; Van der Marel, C.; Gelinck, G. H.; Resel, R.; de Leeuw, D. M.; Strohriegl, P. N-Type Self-Assembled Monolayer Field-Effect Transistors and Complementary Inverters. *Adv. Funct. Mater.* **2013**, *23*, 2016−2023.

(28) Laibinis, P. E.; Hickman, J. J.; Wrighton, M. S.; Whitesides, G. M. Orthogonal self-assembled monolayers: alkanethiols on gold and alkane carboxylic acids on alumina. *Science* **1989**, *245* (4920), 845−847.

(29) Nebhani, L.; Barner-Kowollik, C. Orthogonal Transformations on Solid Substrates: Efficient Avenues to Surface Modification. *Adv. Mater.* **2009**, *21*, 3442−3468.

(30) Hawecker, J.; Lehn, J.-M.; Ziessel, R. Photochemical and Electrochemical Reduction of Carbon Dioxide to Carbon Monoxide Mediated by (2,2′-Bipyridine)tricarbonylchlororhenium(I) and Related Complexes as Homogeneous Catalysts. *Helv. Chim. Acta* **1986**, *69*, 1990−2012.

(31) Stanley, P. M.; Thomas, C.; Thyrhaug, E.; Urstoeger, A.; Schuster, M.; Hauer, J.; Rieger, B.; Warnan, J.; Fischer, R. A. Entrapped Molecular Photocatalyst and Photosensitizer in Metal−Organic Framework Nanoreactors for Enhanced Solar CO_2 Reduction. *ACS Catal.* **2021**, *11*, 871−882.

(32) Clark, M. L.; Ge, A.; Videla, P. E.; Rudshteyn, B.; Miller, C. J.; Song, J.; Batista, V. S.; Lian, T.; Kubiak, C. P. CO_2 Reduction Catalysts on Gold Electrode Surfaces Influenced by Large Electric Fields. *J. Am. Chem. Soc.* **2018**, *140*, 17643−17655.

(33) Veronese, L.; Procopio, E. Q.; De Rossi, F.; Brown, T. M.; Mercandelli, P.; Mussini, P.; D'Alfonso, G.; Panigati, M. New dinuclear hydrido-carbonyl rhenium complexes designed as photosensitizers in dye-sensitized solar cells. *New J. Chem.* **2016**, *40*, 2910−2919.

(34) Veronese, L.; Quartapelle Procopio, E.; Moehl, T.; Panigati, M.; Nonomura, K.; Hagfeldt, A. Triarylamine-based hydrido-carboxylate rhenium(i) complexes as photosensitizers for dye-sensitized solar cells. *Phys. Chem. Chem. Phys.* **2019**, *21*, 7534−7543.

(35) Carreño, A.; Solís-Céspedes, E.; Zúñiga, C.; Nevermann, J.; Rivera-Zaldívar, M. M.; Gacitúa, M.; Ramírez-Osorio, A.; Páez-Hernández, D.; Arratia-Pérez, R.; Fuentes, J. A. Cyclic voltammetry, relativistic DFT calculations and biological test of cytotoxicity in walled-cell models of two classical rhenium (I) tricarbonyl complexes with 5-amine-1,10-phenanthroline. *Chem. Phys. Lett.* **2019**, *715*, 231−238.

(36) Coleman, A.; Brennan, C.; Vos, J. G.; Pryce, M. T. Photophysical properties and applications of Re(I) and Re(I)−Ru(II) carbonyl polypyridyl complexes. *Coord. Chem. Rev.* **2008**, *252*, 2585−2595.

(37) Paoprasert, P.; Laaser, J. E.; Xiong, W.; Franking, R. A.; Hamers, R. J.; Zanni, M. T.; Schmidt, J. R.; Gopalan, P. Bridge-Dependent Interfacial Electron Transfer from Rhenium−Bipyridine Complexes to TiO_2 Nanocrystalline Thin Films. *J. Phys. Chem. C* **2010**, *114*, 9898−9907.

(38) Oudenhoven, T. A.; Joo, Y.; Laaser, J. E.; Gopalan, P.; Zanni, M. T. Dye aggregation identified by vibrational coupling using 2D IR spectroscopy. *J. Chem. Phys.* **2015**, *142*, 212449.

(39) Alam, A. U.; Howlader, M. M. R.; Deen, M. J. The effects of oxygen plasma and humidity on surface roughness, water contact angle and hardness of silicon, silicon dioxide and glass. *J. Micromech. Microeng.* **2014**, *24*, 035010.

(40) Tao, Y. T. Structural comparison of self-assembled monolayers of n-alkanoic acids on the surfaces of silver, copper, and aluminum. *J. Am. Chem. Soc.* **1993**, *115*, 4350−4358.

(41) Fukuda, K.; Hamamoto, T.; Yokota, T.; Sekitani, T.; Zschieschang, U.; Klauk, H.; Someya, T. Effects of the alkyl chain length in phosphonic acid self-assembled monolayer gate dielectrics on the performance and stability of low-voltage organic thin-film transistors. *Appl. Phys. Lett.* **2009**, *95*, 203301.

(42) Benson, E. E.; Kubiak, C. P. Structural investigations into the deactivation pathway of the CO_2 reduction electrocatalyst Re(bpy)-$(CO)_3$Cl. *Chem. Commun.* **2012**, *48*, 7374−7376.

(43) D'Andre, S. C.; Fadeev, A. Y. Covalent Surface Modification of Calcium Hydroxyapatite Using n-Alkyl- and n-Fluoroalkylphosphonic Acids. *Langmuir* **2003**, *19*, 7904−7910.

(44) Luschtinetz, R.; Oliveira, A.; Duarte, H.; Seifert, G. Self-assembled Monolayers of Alkylphosphonic Acids on Aluminum Oxide Surfaces − A Theoretical Study. *Z. Anorg. Allg. Chem.* **2010**, *636*, 1506−1512.

(45) Henning, A.; Bartl, J. D.; Wolz, L.; Christis, M.; Zeidler, A.; Bissolo, M.; Grünleitner, T.; Eichhorn, J.; Zeller, P.; Amati, M.; Gregoratti, L.; Finley, J. J.; Rieger, B.; Stutzmann, M.; Sharp, I. D. Sub-nanometer thin Conformal Aluminum Oxide Coating Created by Interconversion of SiO_2 via Hydrogen Plasma-Assisted Atomic Layer Deposition. 2021, arXiv:2111.00054 [cond-mat.mtrl-sci]. arXiv.org e-Print archive. https://arxiv.org/abs/2111.00054 (accessed 2021-11-02).

(46) Puurunen, R. L. Surface chemistry of atomic layer deposition: A case study for the trimethylaluminum/water process. *J. Appl. Phys.* **2005**, *97*, 121301.

44

Modular Assembly of Vibrationally and Electronically Coupled Rhenium Bipyridine Carbonyl Complexes on Silicon

(47) Henning, A.; Bartl, J. D.; Zeidler, A.; Qian, S.; Bienek, O.; Jiang, C.-M.; Paulus, C.; Rieger, B.; Stutzmann, M.; Sharp, I. D. Aluminum Oxide at the Monolayer Limit via Oxidant-Free Plasma-Assisted Atomic Layer Deposition on GaN. *Adv. Funct. Mater.* **2021**, *31*, 2101441.

(48) Wagner, C. D.; Naumkin, A. V.; Kraut-Vass, A.; Allison, J. W.; Powell, C. J.; Rumble, J. R., Jr. *NIST Standard Reference Database 20, ver. 3.4 (web version)*, 2003; https://srdata.nist.gov/xps/Default.aspx (accessed 2021-06-16).

(49) Barrie, A.; Drummond, I.; Herd, Q. Correlation of calculated and measured 2p spin-orbit splitting by electron spectroscopy using monochromatic x-radiation. *J. Electron Spectrosc. Relat. Phenom.* **1974**, *5*, 217−225.

(50) Wagstaffe, M.; Thomas, A. G.; Jackman, M. J.; Torres-Molina, M.; Syres, K. L.; Handrup, K. An Experimental Investigation of the Adsorption of a Phosphonic Acid on the Anatase TiO2(101) Surface. *J. Phys. Chem. C* **2016**, *120*, 1693−1700.

(51) Schuschke, C.; Schwarz, M.; Hohner, C.; Silva, T. N.; Fromm, L.; Döpper, T.; Görling, A.; Libuda, J. Phosphonic Acids on an Atomically Defined Oxide Surface: The Binding Motif Changes with Surface Coverage. *J. Phys. Chem. Lett.* **2018**, *9*, 1937−1943.

(52) Gengenbach, T. R.; Major, G. H.; Linford, M. R.; Easton, C. D. Practical guides for x-ray photoelectron spectroscopy (XPS): Interpreting the carbon 1s spectrum. *J. Vac. Sci. Technol., A* **2021**, *39*, 013204.

(53) Greiner, M.; Rocha, T.; Johnson, B.; Klyushin, A.; Knop-Gericke, A.; Schlögl, R. The Oxidation of Rhenium and Identification of Rhenium Oxides During Catalytic Partial Oxidation of Ethylene: An In-Situ XPS Study. *Z. Phys. Chem.* **2014**, *228*, 521−541.

(54) Popov, D. A.; Luna, J. M.; Orchanian, N. M.; Haiges, R.; Downes, C. A.; Marinescu, S. C. A 2,2′-bipyridine-containing covalent organic framework bearing rhenium(i) tricarbonyl moieties for CO2 reduction. *Dalton Trans.* **2018**, *47*, 17450−17460.

(55) Cabarcos, O. M.; Shaporenko, A.; Weidner, T.; Uppili, S.; Dake, L. S.; Zharnikov, M.; Allara, D. L. Physical and Electronic Structure Effects of Embedded Dipoles in Self-Assembled Monolayers: Characterization of Mid-Chain Ester Functionalized Alkanethiols on Au111. *J. Phys. Chem. C* **2008**, *112*, 10842−10854.

(56) Joo, Y.; Spalenka, J. W.; McElhinny, K. M.; Schmitt, S. K.; Evans, P. G.; Gopalan, P. Structured Layer of Rhenium Dye on SiO2 and TiO2 Surfaces by Langmuir−Blodgett Technique. *Langmuir* **2014**, *30*, 6104−6113.

(57) Beamson, G.; Briggs, D. *High Resolution XPS of Organic Polymers, the Scienta ESCA300 Database*; Wiley: Chichester, UK, 1992; p 295.

(58) Chadefaux, C.; Le Hô, A.-S.; Bellot-Gurlet, L.; Reiche, I. Curve-fitting micro-ATR-FTIR studies of the amide I and II bands of type I collagen in archaeological bone materials. *e-Preserv. Sci.* **2009**, *6*, 129−137.

(59) Laaser, J. E.; Christianson, J. R.; Oudenhoven, T. A.; Joo, Y.; Gopalan, P.; Schmidt, J. R.; Zanni, M. T. Dye Self-Association Identified by Intermolecular Couplings between Vibrational Modes As Revealed by Infrared Spectroscopy, and Implications for Electron Injection. *J. Phys. Chem. C* **2014**, *118*, 5854−5861.

(60) Cantero-López, P.; Hidalgo-Rosa, Y.; Sandoval-Olivares, Z.; Santoyo-Flores, J.; Mella, P.; Arrué, L.; Zúñiga, C.; Arratia-Pérez, R.; Páez-Hernández, D. The role of zero-field splitting and π-stacking interaction of different nitrogen-donor ligands on the optical properties of luminescent rhenium tricarbonyl complexes. *New J. Chem.* **2021**, *45*, 11192−11201.

(61) Sakamoto, R.; Katagiri, S.; Maeda, H.; Nishimori, Y.; Miyashita, S.; Nishihara, H. Electron Transport Dynamics in Redox-Molecule-Terminated Branched Oligomer Wires on Au(111). *J. Am. Chem. Soc.* **2015**, *137*, 734−741.

(62) Singh, A. P.; Samuel, P. P.; Roesky, H. W.; Schwarzer, M. C.; Frenking, G.; Sidhu, N. S.; Dittrich, B. A Singlet Biradicaloid Zinc Compound and Its Nonradical Counterpart. *J. Am. Chem. Soc.* **2013**, *135*, 7324−7329.

(63) Cancelliere, A. M.; Puntoriero, F.; Serroni, S.; Campagna, S.; Tamaki, Y.; Saito, D.; Ishitani, O. Efficient trinuclear Ru(ii)−Re(i) supramolecular photocatalysts for CO2 reduction based on a new tris-chelating bridging ligand built around a central aromatic ring. *Chem. Sci.* **2020**, *11*, 1556−1563.

(64) Wang, L.; Schubert, U. S.; Hoeppener, S. Surface chemical reactions on self-assembled silane based monolayers. *Chem. Soc. Rev.* **2021**, *50*, 6507−6540.

(65) Herzer, N.; Hoeppener, S.; Schubert, U. S. Fabrication of patterned silane based self-assembled monolayers by photolithography and surface reactions on silicon-oxide substrates. *Chem. Commun.* **2010**, *46*, 5634−5652.

(66) Cottineau, T.; Morin, M.; Bélanger, D. Surface band structure of aryl-diazonium modified p-Si electrodes determined by X-ray photoelectron spectroscopy and electrochemical measurements. *RSC Adv.* **2013**, *3*, 23649−23657.

(67) Ahoulou, S.; Perret, E.; Nedelec, J.-M. Functionalization and Characterization of Silicon Nanowires for Sensing Applications: A Review. *Nanomaterials* **2021**, *11*, 999.

(68) Khan, M.; Rao, M. V. Gallium Nitride (GaN) Nanostructures and Their Gas Sensing Properties: A Review. *Sensors* **2020**, *20* (14), 3889.

(69) Pfennig, B. W.; Chen, P.; Meyer, T. J. Photophysics and Photochemistry of Chromophore−Quencher Assemblies on Glass and Powdered Silica. *Inorg. Chem.* **1996**, *35*, 2898−2901.

(70) Neises, B.; Steglich, W. Simple Method for the Esterification of Carboxylic Acids. *Angew. Chem., Int. Ed. Engl.* **1978**, *17*, 522−524.

(71) Blaschke, B. M.; Böhm, P.; Drieschner, S.; Nickel, B.; Garrido, J. A. Lipid Monolayer Formation and Lipid Exchange Monitored by a Graphene Field-Effect Transistor. *Langmuir* **2018**, *34*, 4224−4233.

(72) Nelson, A. R. J.; Prescott, S. W. refnx: neutron and X-ray reflectometry analysis in Python. *J. Appl. Crystallogr.* **2019**, *52*, 193−200.

(73) Zangrando, M.; Finazzi, M.; Paolucci, G.; Comelli, G.; Diviacco, B.; Walker, R. P.; Cocco, D.; Parmigiani, F. BACH, the beamline for advanced dichroic and scattering experiments at ELETTRA. *Rev. Sci. Instrum.* **2001**, *72*, 1313−1319.

(74) Zeller, P.; Amati, M.; Sezen, H.; Scardamaglia, M.; Struzzi, C.; Bittencourt, C.; Lantz, G.; Hajlaoui, M.; Papalazarou, E.; Marino, M.; Fanetti, M.; Ambrosini, S.; Rubini, S.; Gregoratti, L. Scanning Photoelectron Spectro-Microscopy: A Modern Tool for the Study of Materials at the Nanoscale. *Phys. Status Solidi A* **2018**, *215*, 1800308.

(75) Ernzerhof, M.; Scuseria, G. E. Assessment of the Perdew-Burke-Ernzerhof exchange-correlation functional. *J. Chem. Phys.* **1999**, *110*, 5029−5036.

(76) Adamo, C.; Barone, V. Toward reliable density functional methods without adjustable parameters: The PBE0 model. *J. Chem. Phys.* **1999**, *110*, 6158−6170.

(77) Grimme, S.; Antony, J.; Ehrlich, S.; Krieg, H. A consistent and accurate ab initio parametrization of density functional dispersion correction (DFT-D) for the 94 elements H-Pu. *J. Chem. Phys.* **2010**, *132*, 154104.

(78) Schäfer, A.; Huber, C.; Ahlrichs, R. Fully optimized contracted Gaussian basis sets of triple zeta valence quality for atoms Li to Kr. *J. Chem. Phys.* **1994**, *100*, 5829−5835.

(79) *TURBOMOLE* V7.3 2018; TURBOMOLE GmbH, 2007; http://www.turbomole.com (accessed 2021-08-26).

(80) Ahlrichs, R.; Bär, M.; Häser, M.; Horn, H.; Kölmel, C. Electronic structure calculations on workstation computers: The program system turbomole. *Chem. Phys. Lett.* **1989**, *162*, 165−169.

45

4.4   Reprint Permission Copyrighted Content

CCC | RightsLink

Home　Help ∨　Email Support　Sign in　Create Account

ACS Publications
Most Trusted. Most Cited. Most Read.

Modular Assembly of Vibrationally and Electronically Coupled Rhenium Bipyridine Carbonyl Complexes on Silicon

Author: Johannes D. Bartl, Christopher Thomas, Alex Henning, et al
Publication: Journal of the American Chemical Society
Publisher: American Chemical Society
Date: Nov 1, 2021

Copyright © 2021, American Chemical Society

PERMISSION/LICENSE IS GRANTED FOR YOUR ORDER AT NO CHARGE

This type of permission/license, instead of the standard Terms and Conditions, is sent to you because no fee is being charged for your order. Please note the following:

- Permission is granted for your request in both print and electronic formats, and translations.
- If figures and/or tables were requested, they may be adapted or used in part.
- Please print this page for your records and send a copy of it to your publisher/graduate school.
- Appropriate credit for the requested material should be given as follows: "Reprinted (adapted) with permission from {COMPLETE REFERENCE CITATION}. Copyright {YEAR} American Chemical Society." Insert appropriate information in place of the capitalized words.
- One-time permission is granted only for the use specified in your RightsLink request. No additional uses are granted (such as derivative works or other editions). For any uses, please submit a new request.

If credit is given to another source for the material you requested from RightsLink, permission must be obtained from that source.

BACK　　CLOSE WINDOW

5. Macromolecular Rhenium–Ruthenium Complexes for Photocatalytic CO_2 Conversion: From Catalytic Lewis Pair Polymerization to Well-Defined Poly(vinyl bipyridine)-Metal Complexes

5.1 Bibliographic Data
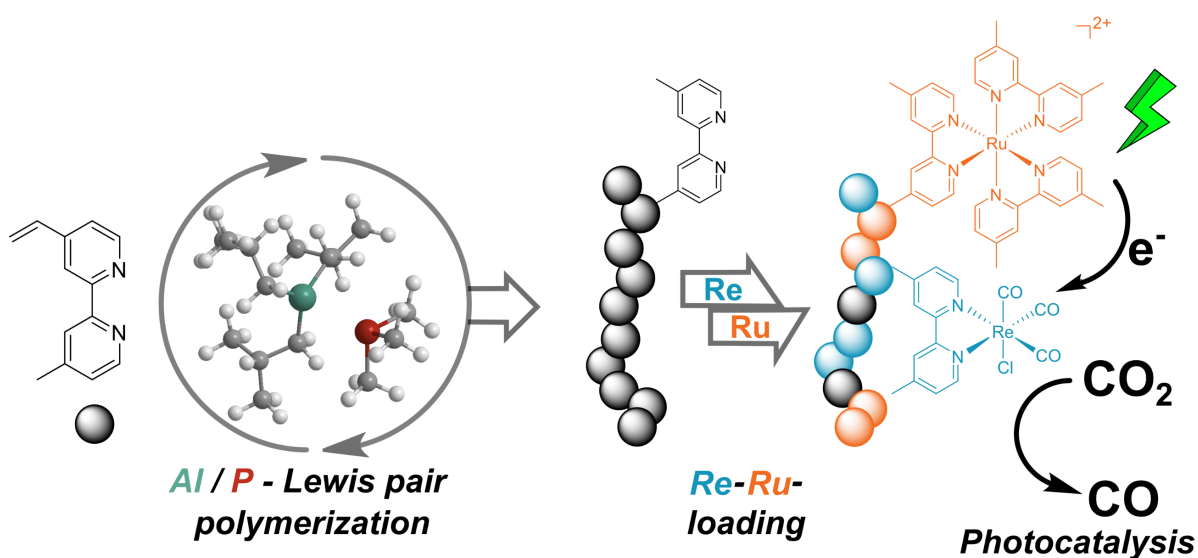
AI / P - Lewis pair polymerization

Re-Ru-loading

Photocatalysis

Authors: Anton S. Maier,[‡] Christopher Thomas,[‡] Moritz Kränzlein,[‡] Thomas M. Pehl, and Bernhard Rieger*

[‡]These authors contributed equally. Christopher Thomas and Moritz Kränzlein conceptualized the experimental studies and carried out part of the experiments. Anton S. Maier carried out most of the experiments. Anton S. Maier, Christopher Thomas, and Moritz Kränzlein wrote the manuscript. Thomas M. Pehl contributed with valuable ideas and discussions. All work was carried out under supervision of Bernhard Rieger.

Macromolecular Rhenium–Ruthenium Complexes for Photocatalytic CO2 Conversion: From Catalytic Lewis Pair Polymerization to Well-Defined Poly(vinyl bipyridine)-Metal Complexes
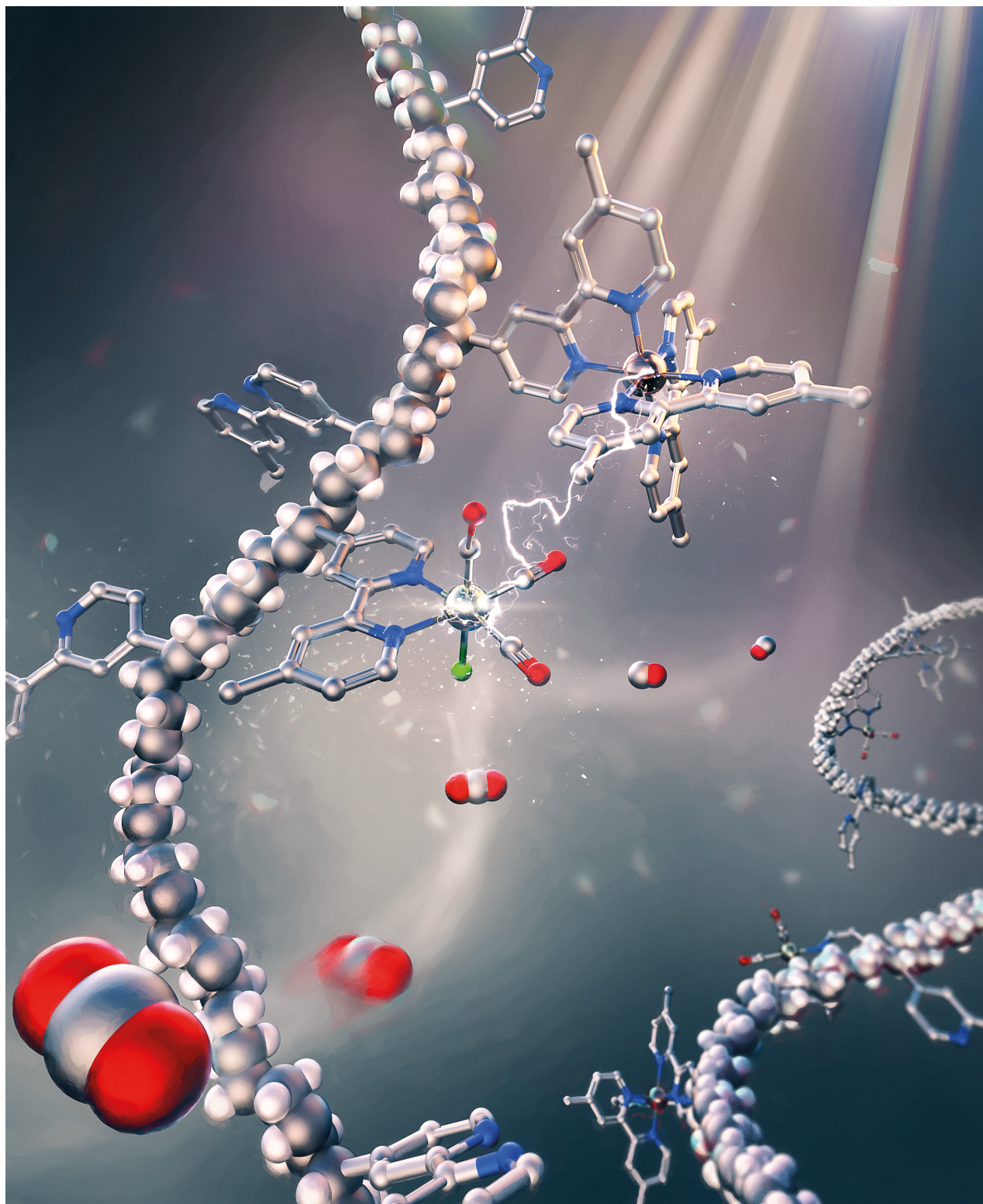
Cover art designed and created by Dr. Johannes Richers. Reprinted with permission of Dr. Johannes Richers.

5.2   Summary

The spatial proximity of metal-centres increases the efficiency of the photocatalytic conversion of CO_2 by molecular catalysts. Therefore, in this work, a system was prepared in which the catalyst Re(dmb)(CO)$_3$Cl (dmb = 4,4'-dimethyl-2,2'-bipyridine) and the PS [Ru(dmb)$_3$]$^{2+}$ were covalently bound to each other. With this approach, it is not only possible to easily adjust the ratios of the metal centres, but also to apply them in very large numbers. Accordingly, 4-vinyl-4'-methyl-2,2'-bipyridine (VBpy) was catalytically polymerized for the first time and yielded the underlying framework for the photocatalytically active polymer. The linkage of this extended Michael-type monomer was achieved via aluminium-phosphorus *Lewis* pair-mediated group-transfer polymerisation. With conversions up to 80%, high initiator efficiencies of 45%-51%, and narrow polydispersities below 1.36, a combination of *Lewis* acidic tri-iso-butyl aluminum and *Lewis* basic trimethyl phosphine was identified as a suitable catalyst system. The well-defined polymers were utilised as macroligands and loaded in two consecutive steps with different ratios of the precursors Re(CO)$_5$Cl and Ru(dmb)$_2$Cl$_2$. The resulting photocatalytically active rhenium(I)−ruthenium(II) polymer complex are characterised with ultraviolet−visible (UV/Vis), photoluminescence (PL), and IR spectroscopy to qualitatively evaluate the metal loading. Furthermore, inductively coupled plasma mass spectrometry ICP-MS determined the quantitative number of metals attached to the polymer. The nonquantitative loading of the metal centres can be explained by steric hinderance and the secondary structural motifs of the polymers. For the irradiation experiments, four polymers with different rhenium to ruthenium loadings were tested regarding their activity and stability. In the photocatalytic reduction of CO_2 to CO, the polymer with the lowest Re/Ru ratio reaches particularly high photostabilities and activities (TON = 5650, TOF = 66 h^{-1}). This was attributed to the spatial proximity of a photocatalytically active rhenium moiety and ruthenium PS, enabling a fast and efficient electron transfer and therefore decreasing the extent of side reactions. By varying the concentration of the loaded polymers in the irradiation experiments, the study demonstrated that higher concentrations resulted in increased photostability. This could be explained by the higher number of absorbing Ru(II)-centres, protecting the Re-catalysts from overexcitation and degradation. Throughout all applied concentrations, the tested polymers reached similar initial TOFs, indicating that the main path of electron transfer proceeds intramolecularly along the polymer chain.

5.3   Manuscript

Macromolecules

Article

Macromolecular Rhenium−Ruthenium Complexes for Photocatalytic CO_2 Conversion: From Catalytic Lewis Pair Polymerization to Well-Defined Poly(vinyl bipyridine)−Metal Complexes

Anton S. Maier,[†] Christopher Thomas,[†] Moritz Kränzlein,[†] Thomas M. Pehl, and Bernhard Rieger*

Cite This: *Macromolecules* 2022, 55, 7039–7048

Read Online

ACCESS | Metrics & More | Article Recommendations | Supporting Information

ABSTRACT: Herein, the first catalytical polymerization of 4-vinyl-4′-methyl-2,2′-bipyridine (VBpy) via Lewis pair-mediated group-transfer polymerization using different combinations of Lewis acidic trialkyl aluminum compounds and Lewis basic phosphines is reported. In this context, a broad screening of different Lewis pairs is conducted, demonstrating the necessity of an adjustment of the steric and electronic properties of the Lewis pair to the demands of the monomer. Further, end-group analysis of short-chain oligomers via electrospray ionization mass spectrometry (ESI-MS) for the experimentally determined optimum combination Al(*i*-Bu)$_3$/PMe$_3$ (Đ = 1.31–1.36, I.E. = 45–51%) reveals the presence of two initiation pathways via conjugate addition and deprotonation. The well-defined polymers are subsequently loaded in a two-step synthesis protocol with different ratios of Re(CO)$_5$Cl and Ru(dmb)$_2$Cl$_2$, forming a photocatalytically active rhenium−ruthenium polymer complex with poly(vinyl bipyridine) as the macroligand. Catalyst loadings are characterized thoroughly by means of Ultraviolet−visible (UV−vis), photoluminescence (PL), and IR spectroscopy as well as inductively coupled plasma (ICP)-MS. Finally, a comparison of the photocatalytic CO$_2$ reduction performance of the polymeric catalysts in irradiation experiments is presented, revealing particularly high photostabilities and activities for **PVBpy**$^{5/95}$ (TON = 5650, TOF = 66 h^{-1}). This is due to an efficient electron transfer of the Ru(II)-one-electron-reduced species (OERS) to the rhenium centers facilitated by the spatial proximity of both metals attached to the macromolecular ligand PVBpy.
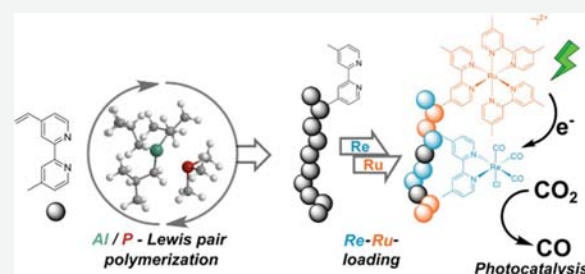
INTRODUCTION

Mononuclear rhenium complexes of the type [Re(dmb)-(CO)$_3$X] (X = Cl$^-$, Br$^-$) with 4,4′-dimethyl-2,2′-bipyridine (dmb) ligands were established as catalysts for the photocatalytic reduction of CO$_2$ to CO due to their high activity and excellent product selectivity, favoring the formation of CO over other reduction products. In this context, the Re(I) centers were shown to act as photosensitizers, as well as the photocatalytic units, in the CO$_2$ conversion.[1,2] However, those photocatalysts suffer from premature catalyst deactivation due to the insufficient photostability of the Re(I)-OERS.[3] An increase in the photostability of Re(I)-based catalyst systems was achieved upon covalent linkage of rhenium centers, resulting in a binuclear mechanism that combines an effective two-electron transfer caused by the spatial proximity of the metal centers with the smooth generation of a free coordination site.[4] Further enhancement of the photocatalytic performance of multinuclear rhenium complexes is possible upon integration of ruthenium moieties as photosensitizing units for light capture.[5,6] The incorporation of Ru(II) into the rhenium-based photocatalytic systems allows for the utilization of lower energy light and thus helps suppress light-induced deactivation reactions.[7] Among those multinuclear systems for

photocatalytic CO$_2$ reduction, particularly catalysts with [Ru(dmb)$_3$]$^{2+}$ moieties as photosensitizers covalently linked to [Re(dmb)(CO)$_3$Cl] derivatives, as the catalytic centers are very well studied.[8–10] Upon light absorption, the exclusive population of the ^{3}MLCT (metal-to-ligand charge-transfer) state of the ruthenium complexes was observed, which was transformed into the Ru(II)-OERS by reductive quenching with a suitable electron donor. Subsequent intramolecular electron transfer to the covalently bound Re(I) unit leads to the generation of the Re(I)-OERS capable of entering the catalytic cycle for the reduction of CO$_2$. In this context, the rate of the intramolecular electron transfer is of secondary importance, as the reduction of CO$_2$ at the Re(I) center was identified as the rate-limiting step of the overall process.[7] Nevertheless, studies revealed that supramolecular rhenium−ruthenium complexes with short, saturated linkers between the
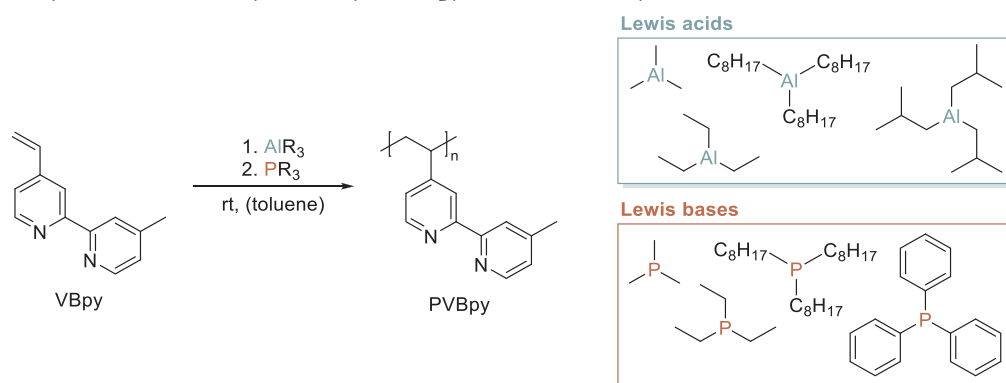
7039

Macromolecular Rhenium–Ruthenium Complexes for Photocatalytic CO2 Conversion: From Catalytic Lewis Pair Polymerization to Well-Defined Poly(vinyl bipyridine)-Metal Complexes

Scheme 1. Polymerization of 4-Vinyl-4′-methyl-2,2′-bipyridine Mediated by Different Lewis Pairs

metal centers exhibited the highest photocatalytic activities and stabilities.[11,12] This was attributed to π-conjugation significantly lowering the reduction potential of the Re(I)-OERS, therefore worsening the photocatalytic abilities of complexes with conjugated bridging ligands.[13] A concept for a trinuclear photocatalyst bearing two rhenium and one ruthenium moiety was introduced by Ishitani et al., revealing high photostability and high catalytic activities due to an efficient intramolecular electron transfer.[14] This fast and quantitative electron transfer is the main reason for a substantial stability increase, as light-induced deactivation reactions of the Ru(II)-OERS are generally considered the main route for catalyst degradation.[3,15] One main advantage regarding the photocatalytic performance of multinuclear rhenium–ruthenium complexes is their lower concentration dependency compared to a combination of mononuclear systems of Ru(II) and Re(I).[7] This is again due to the efficient electron transfer from photosensitizer to catalyst unit because of the covalent linkage of both key components of the photocatalytic system, enabling the electron and energy transfer also at very low concentrations.[7,16] To facilitate more spatial proximity for the photocatalytically active units, covalent linkages of multiple bipyridine units to a macromolecular ligand might be beneficial for the catalysts' stability.[17] Such polymers acting as macroligands for metal complexes have been long-known, and application of this principle to the photocatalytic reduction of CO_2 can eventually facilitate the formation of highly stable photocatalysts combining photocatalysis with properties inherent to polymers.[17–19] Usually, vinyl bipyridines can be applied in this context, being polymerized using free-radical polymerization,[20,21] atom-transfer radical polymerization (ATRP),[22] or electropolymerization,[17,23,24] yet accessing well-defined, controllable polymers with narrow dispersities remains a major challenge. One approach might comprise Lewis pair-mediated polymerization as a facile tool toward defined poly(vinyl bipyridines) as metal complex anchoring sites. In contrast to classical Lewis acid–base adducts,[25] Stephan et al. introduced the notion of frustrated Lewis pairs (FLPs) as a new concept for the description of combinations of sterically hindered Lewis acids and equally hindered Lewis bases.[26] Due to the steric repulsion of Lewis acid and base, the formation of a Lewis pair based upon donor–acceptor interactions is suppressed, resulting in an unusual and synthetically appealing reactivity of those frustrated Lewis pairs.[26] The first application of FLPs in polymerization catalysis allowed for the polymerization of methyl methacrylate

(MMA) and two methylene butyrolactones utilizing highly Lewis acidic $Al(C_6F_5)_3$ in combination with appropriate phosphines and N-heterocyclic carbenes as Lewis bases.[27] In analogy to the rare-earth metal-mediated group-transfer polymerization, monomers for Lewis pair-mediated polymerizations comprise α,β-unsaturated molecules (1,4-Michael acceptors) with a double bond conjugated to a heteroatom moiety allowing coordination to a catalytically active center. Besides MMA and a series of lactones, also polymers from the polar vinyl monomers 2-isoprenyl-2-oxazoline (iPOx) and 2-vinylpyridine (2VP), bearing a C=C–C=N functionality, were accessible applying a combination of $Al(C_6F_5)_3$ and N-heterocyclic carbenes as polymerization catalysts.[28] In 2016, the scope of available monomers was broadened by Rieger et al., reporting the controlled polymerizations of diethyl vinylphosphonate (DEVP), dimethyl acrylamide (DMAA), as well as the extended 1,6-Michael system 4-vinylpyridine (4VP) with several combinations of highly interacting Lewis pairs (HIPs) compromising organoaluminum compounds with less steric demand and small phosphines.[29] For these experiments, an adjustment of the steric and electronic parameters of the Lewis pairs to the steric and electronic properties of the respective monomers was necessary to achieve living type polymerizations while maintaining narrow polydispersities. In addition to that, the initiation mechanism of the polymerization was investigated by means of electrospray ionization mass spectrometry (ESI-MS) analyses of short-chain oligomers, revealing a terminal phosphine group and hence, strongly suggesting a conjugate addition pathway.[29] These examples demonstrate the broad applicability of Lewis pair catalysis for the polymerization of polar monomers that might not be accessible by other polymerization types. Transferring this concept to new monomers, the first catalytic polymerization of 4-vinyl-4′-methyl-2,2′-bipyridine using different Lewis pairs is reported. Using these well-defined polymers, rhenium–ruthenium-loaded polymeric metal complexes are prepared using a two-step synthesis protocol, and their photocatalytic activity in CO_2 reduction is investigated.

■ LEWIS PAIR POLYMERIZATION SCREENING

While polymeric forms of 4-vinyl-4′-methyl-2,2′-bipyridine are well known as macroligands for photocatalytically active complexes, no catalytically controlled polymerization procedure for this monomer is known so far, as most examples involve less defined electropolymerization or radical mechanisms.[17,18,20–24] In 2016, Rieger et al. published the first

Macromolecular Rhenium–Ruthenium Complexes for Photocatalytic CO2 Conversion: From Catalytic Lewis Pair Polymerization to Well-Defined Poly(vinyl bipyridine)-Metal Complexes

Table 1. Polymerization of 4-Vinyl-4′-methyl-2,2′-bipyridine Using Different Lewis Pairs; LA = Lewis Acid, LB = Lewis Base

entry	Lewis acid	Lewis base	$[VBpy]/[LA]/[LB]^a$ [equiv.]/[equiv.]/[equiv.]	$t_R{}^b$ [h]	$X_{VBpy}{}^c$ [%]	$M_{n,theo}{}^d$ [kg/mol]	$M_{n,abs}{}^e$ [kg/mol]	$Đ^e$ [-]	I.E.^{f} [%]
1	AlMe$_3$	PMe$_3$	200/2/1	15	38	14.9	209	2.34	7.1
2	AlEt$_3$	PMe$_3$	100/2/1	7	87	17.4	151	2.08	12
3	AlEt$_3$	PMe$_3$	200/2/1	23	94	36.9	173	1.34	21
4	AlEt$_3$	PMe$_3$	400/2/1	68	35	27.5	90.8	1.41	30
5	AlEt$_3$	PEt$_3$	200/2/1	21	80	31.3	89.7	1.74	35
6	AlOct$_3$	PMe$_3$	200/2/1	43	59	23.1	91.0	1.66	25
7	AlOct$_3$	PEt$_3$	200/2/1	21	39	15.4	52.4	1.35	29
8	Al(i-Bu)$_3$	PMe$_3$	200/2/1	41	38	15.0	29.6	1.36	51
9	Al(i-Bu)$_3$	PMe$_3$	100/2/1	24	79	15.6	35.0	1.31	45
10	Al(i-Bu)$_3$	POct$_3$	100/2/1	65	89	17.6	36.9	1.35	48
11	Al(i-Bu)$_3$	PPh$_3$	100/2/1	9	61	12.0	40.8	1.35	29

^{a}Desired reactant ratio. ^{b}1.02 mmol VBpy in 2 mL of toluene, room temperature, Lewis acid and monomer were premixed, and the polymerization was started by addition of Lewis base. ^{c}Determination of conversion via aliquot-^{1}H NMR; for a detailed calculation, see the Supporting information, Figure S2. ^{d}Theoretical molecular weight determined via $M_{n,theo} = X_{VBpy} \times M_{VBpy} \times [VBpy]/[LB]$, assuming full initiator efficiency. ^{e}Absolute molecular weight and polydispersity determined using SEC with triple detection in DMF with added LiBr (25 mmol/L) at 30 °C using the experimentally determined dn/dc = 0.190 mL g^{-1} (Supporting information, Figure S5). ^{f}Initiator efficiency I.E. = $M_{n,theo}/M_{n,abs} \times 100\%$.

Scheme 2. Initiation Pathways of Lewis Pair-Mediated Polymerization of VBpy with the Lewis Pair Al(I-Bu)$_3$/PMe$_3$ via Conjugate Addition (Upper Pathway, Red) or Deprotonation (Lower Pathway, Green) Either Leading to Phosphine or Olefin-Terminated Polymer Chains[29]
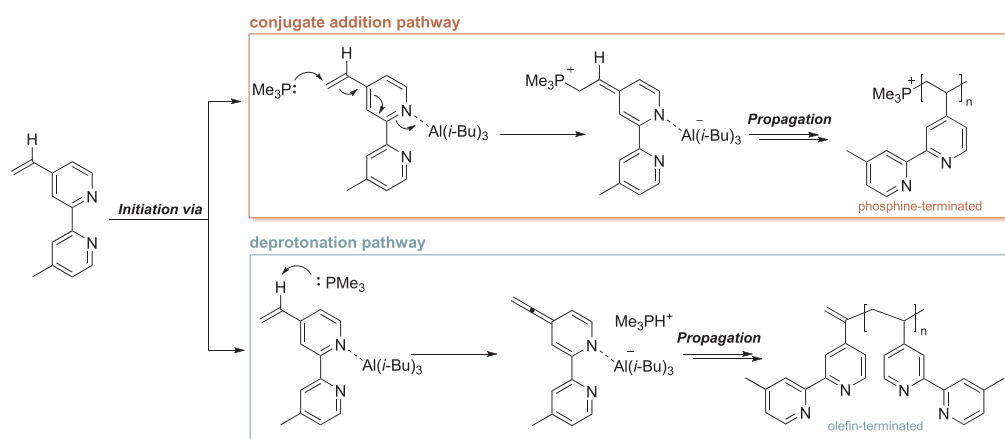
controlled polymerization of the extended Michael-type system 4-vinylpyridine, which is related to VBpy.[29] This concept is transferred onto the polymerization of VBpy for the synthesis of defined macroligands, as shown in Scheme 1.

For the polymerization of VBpy, different Lewis pairs with varying steric demands and, thus, different interactions were tested; the results are shown in Table 1. All polymerizations were performed in toluene at room temperature, and the obtained polymers were characterized for their chemical structure using ^{1}H NMR and ^{13}C NMR. The absolute molecular weight distribution was determined via size-exclusion chromatography (SEC), and in terms of their thermal properties by differential scanning calorimetry (DSC) and thermogravimetric analysis (TGA).

Initial experiments with the two least sterically hindered acids and bases AlMe$_3$ and PMe$_3$ (Table 1, entry 1) yielded a conversion of 38% with a broad, bimodal dispersity ($Đ$ = 2.34) and low initiation efficiency (I.E. < 10%). For the combination AlEt$_3$/PMe$_3$ (Table 1, entries 2–4), high conversions (X > 85%) with low to moderate polydispersities ($Đ$ = 1.34–2.08) were obtained, only limited in conversion by higher monomer

loadings (Table 1, entry 4) while maintaining initiator efficiencies in the range of 12–30%. This limitation might be caused by monomer overload at the catalytic center or an overall increase of side reactions, or the reaction mixture's viscosity due to a higher monomer concentration. However, all combinations using small, sterically less demanding Lewis acids produced polymers with more or less pronounced bimodal character, as observed in the corresponding SEC traces (see the Supporting information, Figures S6–S10). This bimodality is most likely attributed to the presence of two initiation pathways, namely, conjugate addition of the phosphine and a deprotonation route, which differ in their reaction rates.[29] Switching to the sterically highly demanding AlOct$_3$ with small Lewis bases PMe$_3$ (Table 1, entry 6) and PEt$_3$ (Table 1, entry 7), VBpy conversion decreases with increasing steric demand of the Lewis base (59% for PMe$_3$ vs 39% for PEt$_3$). However, the polydispersity decreased from 1.66 to 1.35, while initiation efficiencies between 25 and 29% were observed for both systems. To facilitate higher conversion, the sterically less demanding Lewis acid Al(i-Bu)$_3$ is selected in combination with PMe$_3$ (Table 1, entries 8–9). Despite showing a severe

Macromolecular Rhenium–Ruthenium Complexes for Photocatalytic CO2 Conversion: From Catalytic Lewis Pair Polymerization to Well-Defined Poly(vinyl bipyridine)-Metal Complexes

Scheme 3. Synthesis of Macromolecular Photocatalysts in a Two-Step Synthesis by Subsequent Loading of PVBpy1−3 with Re(CO)$_5$Cl and Ru(dmb)$_2$Cl$_2$
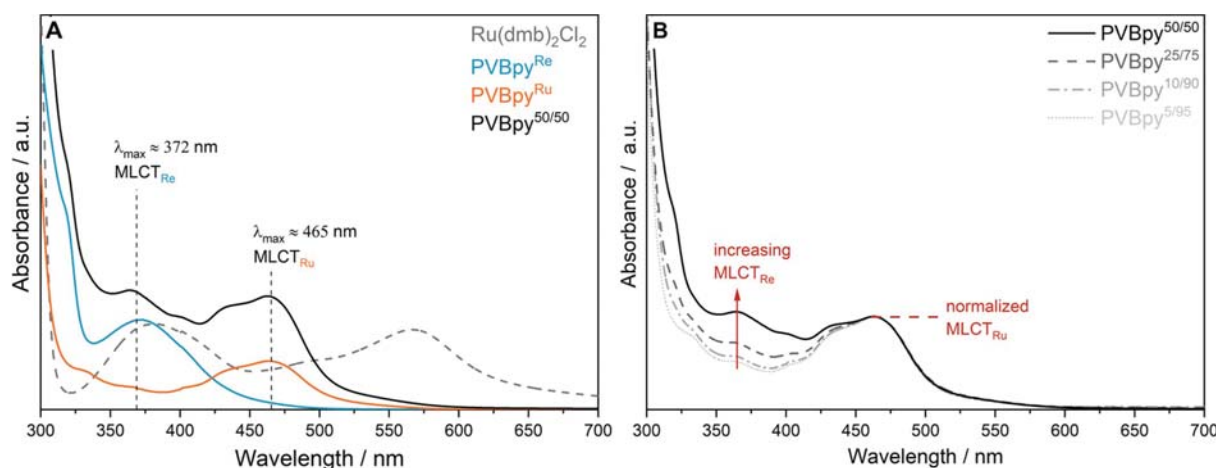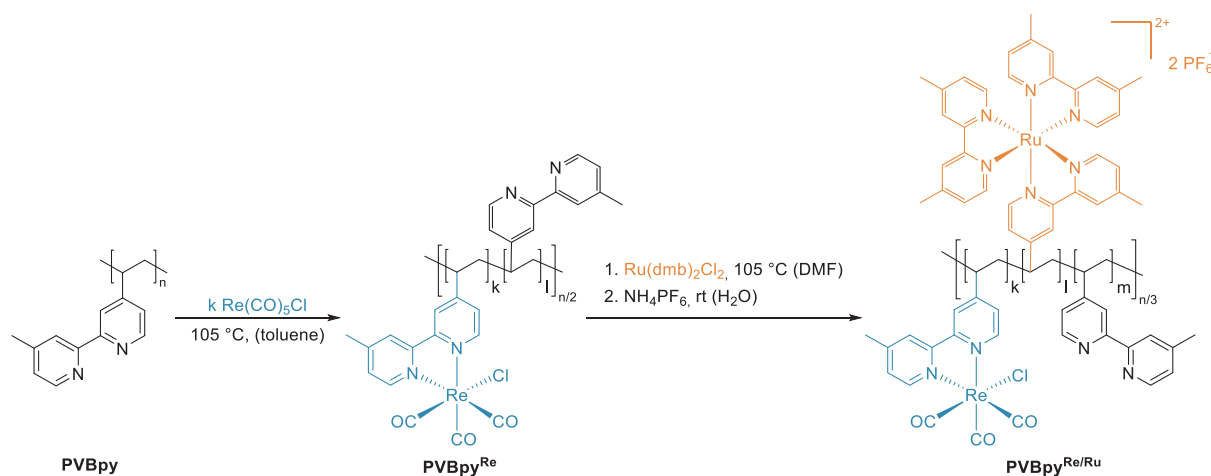
Figure 1. UV−vis spectroscopy for (A) photophysical investigation of the electronic ground state of different metal-loaded PVBpy samples with characteristic absorption maxima of Ru(dmb)$_2$Cl$_2$ (gray, dashed), Re-loaded PVBpy^{Re} (blue), Ru-loaded PVBpy^{Ru} (orange), and photocatalyst **PVBpy$^{50/50}$** (black) and (B) qualitative comparison of rhenium loading in different polymer samples via normalization of the respective MLCT$_{Ru}$.

decrease of the conversion with increasing monomer-to-Lewis pair ratio (100/2/1 with X = 79% vs 200/2/1 with X = 38%), this combination shows narrow dispersities ($Đ \leq 1.36$) as well as the highest initiator efficiencies (I.E. = 45−51%) among all tested Lewis pairs. Increasing the steric demand of the Lewis base using P(n-Oct)$_3$ (Table 1, entry 10) or PPh$_3$ (Table 1, entry 11) improved the overall conversion (89 and 61%) while maintaining narrow polydispersities ($Đ \leq 1.35$) and high initiation efficiencies (I.E. = 48 and 29%). Comparing the sterically more demanding Lewis pairs to the small Lewis pairs in terms of polymer dispersity, monomodal polymers were obtained, surpassing the limitation of less demanding Lewis pairs suffering from a less controlled initiation (Supporting information, Figures S11−S16). ESI-MS end-group analysis of PVBpy oligomers prepared with the Lewis pair Al(i-Bu)$_3$/PMe$_3$ (Supporting information, Figure S20), however, revealed the presence of species terminated by a phosphine or an olefin (Scheme 2). This indicates the presence of both initiation pathways, conjugate addition and deprotonation, in systems

with sterically more demanding Lewis acids as well. These results are in accordance with previous observations reported by Rieger et. al.[29] Nevertheless, monomodal polymers with narrow polydispersities were obtained, most likely due to conjugate addition and deprotonation, exhibiting similar reaction rates during initiation. Therefore, the Lewis pair Al(i-Bu)$_3$/PMe$_3$ emerged as the most appropriate combination among the investigated systems for the polymerization of VBpy as an extended Michael-type monomer.

Overall, tuning of the Lewis pair interaction allowed the first catalytically controlled polymerization of VBpy, giving access to defined and thoroughly characterized polymers as macro-ligands for metal complex loading. As a model system for further experiments, the combination Al(i-Bu)$_3$/PMe$_3$ with a ratio of 100/2/1 (Table 1, entry 9) was chosen, as it exhibited the smallest dispersity and yielded only monomodal polymers while maintaining high initiation efficiencies and reaching a conversion of 79% within the tested reaction times. Different polymers PVBpy1−3 for metal loading experiments were

53

Table 2. Catalyst Compositions of PVBpy$^{5/95}$, PVBp$^{10/90}$, PVBpy$^{25/75}$, and PVBpy$^{50/50}$ and Photocatalyst-to-Photosensitizer Ratio R$_{Re/Ru}$

sample	theoretical loading Re/Ru [%/%]	theoretical Re/Ru ratio R$_{Re/Ru,theo}$ [-]	calculated Re/Ru ratio R$_{Re/Ru,calc}$^{a} [-]	Re-loaded VBpy-units^b [%]	Ru-loaded VBpy-units^b [%]	unoccupied VBpy-units^b [%]	total metal loading of PVBpy [%]
PVBpy$^{5/95}$	5/95	0.05	0.25	2.70	11.1	86.2	13.8
PVBpy$^{10/90}$	10/90	0.11	0.80	6.60	8.20	85.2	14.8
PVBpy$^{25/75}$	25/75	0.33	1.70	19.9	11.6	68.5	31.5
PVBpy$^{50/50}$	50/50	1.00	4.70	34.1	7.30	58.6	41.4

^{a}Calculated from the rhenium and ruthenium loadings [μmol/mg$_{polymer}$] determined via ICP-MS (see the Supporting information, Table S2 and eqs 1–3). ^{b}Calculated from the rhenium and ruthenium masses found via ICP-MS of the microwave-digested samples (see the Supporting information, Table S2 and eqs 4–11).

prepared using the same procedure; the results can be found in the Supporting information, Table S1, and Figures S17−S19. The obtained polymers are amorphous powders with a glass-transition temperature of 142 °C and a thermal decomposition onset temperature of 368 °C (for DSC and TGA, see the Supporting information, Figures S21 and S22).

SYNTHESIS OF MACROMOLECULAR METAL COMPLEXES

Metal loading onto the polymers was done in a two-step synthesis (Scheme 3). As the initial step, polymers 1−3 were reacted with Re(CO)$_5$Cl, followed by subsequent complexation with an excess of the ruthenium precursor complex Ru(dmb)$_2$Cl$_2$. The introduction of Re units into the polymers was accomplished by dissolution of the polymers in toluene and reaction with Re(CO)$_5$Cl at elevated temperatures. As the polymers exhibited a high solubility in methanol after loading with the ruthenium precursor, removal of Ru(dmb)$_2$Cl by washing with MeOH was not possible. However, the macromolecular rhenium−ruthenium complexes were successfully isolated by salt metathesis upon dissolution in methanol, followed by precipitation in an aqueous NH$_4$PF$_6$ solution. Subsequently, the Ru(dmb)$_2$Cl$_2$ precursor could be removed by washing with methanol, whereas the loaded polymers with the PF$_6^-$ counterions remained insoluble.

This approach enabled the synthesis of various macromolecular photocatalysts with different amounts of Re and Ru units. Successful incorporation of the metal centers was confirmed via Ultraviolet−visible (UV−vis) spectroscopy for all macromolecular complexes (Figure 1A). Moreover, the characteristic absorption maxima of Re and Ru, respectively, allowed for a qualitative determination of the Re(I)/Ru(II) ratio (Figure 1B). Spectroscopic investigation of the Ru precursor complex Ru(dmb)$_2$Cl$_2$ in N,N-dimethylformamide showed absorption maxima at 568 and 382 nm, which are in good agreement with the literature.[16] Compared to that, a polymer exclusively loaded with Ru centers exhibited a significant blue shift of the absorption maximum to lower wavelengths. This hypsochromic shift results from the substitution of the electron-withdrawing chloride ligands at the ruthenium center by the bipyridine ligands of the polymer chain. As a result of that, the stabilization of the π* orbitals of the bipyridine ligands at the ruthenium is lost. Therefore, the formerly red-shifted, characteristic MLCT transition (dπ → π*) occurs at a lower wavelength of 465 nm.[7] As opposed to that, a Re-loaded polymer shows the characteristic MLCT transition of bipyridine-substituted Re(I) complexes at a wavelength of 372 nm.[16] The appearance of both mentioned transitions in the UV−vis spectrum of **PVBpy$^{50/50}$** therefore

demonstrates the successful incorporation of Re and Ru centers into the PVBpy polymer, and the missing band at 568 nm confirms the complete removal of Ru(dmb)$_2$Cl$_2$ (Figure 1A).

UV−vis measurements were further employed for the qualitative comparison of the Re(I)/Ru(II) ratios of the photocatalysts (Figure 1B). Normalization of the UV−vis spectra to the MLCT transition of the Ru moieties allows the evaluation of the respective Re loading in each sample. Figure 1B clearly demonstrates a correlation of the intensity of the MLCT (Re) transition (λ_{max} = 372 nm) with the rhenium amount incorporated into the respective PVBpy sample, validating the synthetic approach toward different Re(I)/Ru(II) ratios. Besides UV−vis spectroscopy, also photoluminescence as well as IR spectra further confirmed the successful incorporation of Re and Ru centers into the polymers (for photoluminescence (PL) and IR spectra, see the Supporting information, Figures S23 and S24). IR spectra of the polymeric metal complexes after loading with Re-(CO)$_5$Cl revealed the characteristic Re-CO signals (in phase a′(1) (ν = 2015 cm^{-1}), antisymmetric a″ (ν = 1908 cm^{-1}), and out-of-phase symmetric a″(2) (ν = 1873 cm^{-1})). Further, attachment of ruthenium units was confirmed via IR spectroscopy by the relative decrease of the carbonyl stretches compared to the stretching of the bipyridine ligands observable at ν = 1616 cm^{-1} (I_{CO}/I_{Bpy} (PVBpy^{Re}) = 3.4 vs I_{CO}/I_{Bpy} (PVBpy$^{Re/Ru}$) = 3.0) (Figure S23).[30,31] Photoluminescence spectra of the macromolecular metal complexes upon irradiation at 365 nm are dominated by a strong emission at a wavelength of 639 nm caused by the ruthenium centers (Figure S24).[30] Emission of the Re units at 614 nm is negligibly small due to a low quantum yield of rhenium bipyridine complexes.[16] Additionally, the emission of the rhenium center is further reduced by the intramolecular energy transfer of the Re(I) centers to the Ru(II) centers. Excitation of the samples at 365 nm leads to an excited state of the Re complexes, which is energetically higher than the ^{3}MLCT (Ru) state, therefore enabling an energy transfer from Re to Ru, effectively decreasing the rhenium-centered emission and increasing the emission of the ruthenium moieties.[14] Overall, the results of the photoluminescence measurements demonstrate that the lowest energy level which is responsible for the observed luminescence is located at the ruthenium moieties of the polymers.

Quantification of the metal loadings of the polymers via ICP-MS analysis revealed a nonquantitative attachment of the Re and Ru centers in the desired ratios (Table 2; for calculations, see the Supporting information, eqs 1−11).

As indicated by the ICP-MS results presented in Table 2, total loadings of PVBpy between 13.8 and 41.4% were
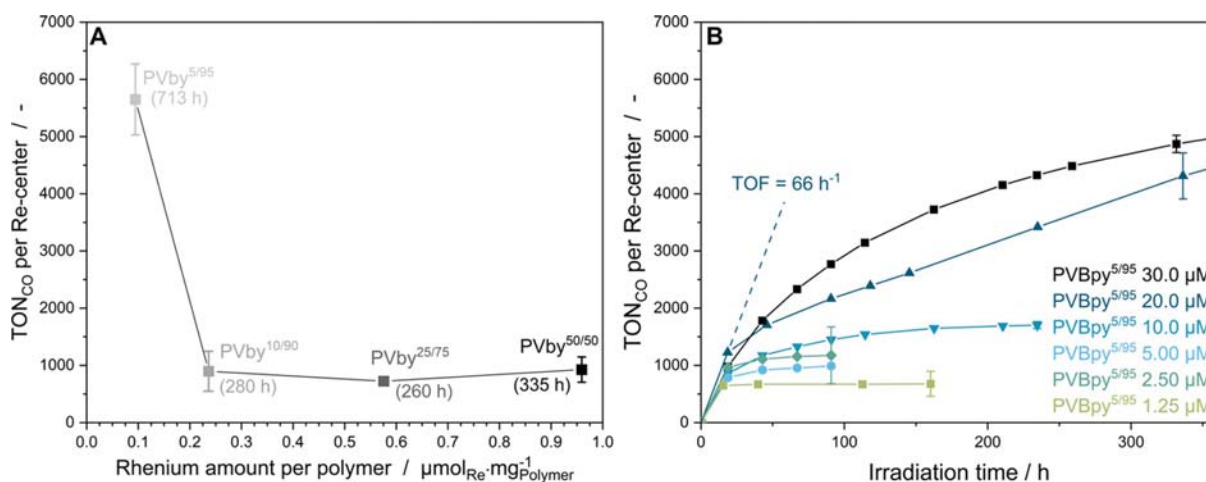
Figure 2. Photocatalytic experiments for (A) different macromolecular photocatalysts with varying rhenium loadings at a rhenium concentration of 20 μM (irradiation times corresponding to the reported TONs are denoted in brackets) and (B) **PVBpy**$^{5/95}$ with different catalyst concentrations. The catalyst-containing, CO_2-saturated (15 min) DMF solution with BIH ([BIH]/[Re] = 10 000) and TEOA (1.72 M) was irradiated at λ = 520 nm.

generated applying the two-step approach introduced in this work. Samples with lower theoretical rhenium loadings (**PVBpy**$^{5/95}$ and **PVBpy**$^{10/90}$) exhibit an overall metal content below 15% referred to the number of VBpy repetition units available for metal complexation. However, increasing the amount of $Re(CO)_5Cl$ applied in the first step of the synthesis resulted in an increase of the total metal loading after the subsequent ruthenium loading with the respective calculated amounts of $Ru(dmb)_2Cl_2$. In this context, photocatalyst **PVBpy**$^{50/50}$ revealed a total metal loading of 41%, significantly exceeding the metal contents of **PVBpy**$^{5/95}$ and **PVBpy**$^{10/90}$. Whereas complexation of the Re-precursor $Re(CO)_5Cl$ occurs to a large extent considering the targeted values, the values for ruthenium fall below the expected loading. This can be attributed to the steric demand of $Ru(dmb)_2Cl_2$ leading to a high steric crowding on the polymer chains on the one hand, and in case of highly rhenium-loaded polymers, a repulsion from polymer-bound Re units on the other hand. Additionally, electrostatic repulsion due to the cationic charges of the $[Ru(dmb)_3]^{2+}$ moieties could hinder the complexation of further ruthenium centers. Besides the mentioned metal–metal interactions, also the polymer secondary structure, i.e., coiling of the polymer chains, could interfere with the loading process of the polymers. Despite the application of a slight excess of the ruthenium precursor complex $Ru(dmb)_2Cl_2$, similar ruthenium loadings (7−12%) were found for all photocatalysts, hence suggesting that the ruthenium complexation step is limiting regarding the overall metal loading of PVBpy. Generally, however, the ICP-MS results demonstrate a slightly higher total ruthenium loading in polymers with low rhenium loadings, which represents the expected trend as more empty coordination sites are available for Ru complexation in polymers with low initial Re loading. The similar amounts of ruthenium centers despite varying rhenium loadings are reflected in the different Re(I)/Ru(II) ratios significantly increasing from **PVBpy**$^{5/95}$ to **PVBpy**$^{50/50}$. These ratios become particularly important in photocatalytic experiments as the Re(I)/Ru(II) ratio displays the ratio of the photocatalyst to the photosensitizer, which are the two main components affecting the photostability and efficiency of the catalytic

system. In summary, all macromolecular photocatalysts are considered to be statistical copolymers composed of empty bipyridine units, Re moieties, and Ru sites. As opposed to conventional, rather tedious electropolymerization,[32,33] the presented polymerization procedure with subsequent two-step metal loading toward multinuclear metal complexes combines the simple synthesis of the catalysts with the facile adjustment of the Re(I)/Ru(II) ratio.

■ PHOTOCATALYTIC CO$_2$-CONVERSION

First, the rhenium−ruthenium-loaded polymers **PVBpy**$^{5/95}$, **PVBpy**$^{10/90}$, **PVBpy**$^{25/75}$, and **PVBpy**$^{50/50}$ were tested for the reduction of CO_2 in photocatalytic experiments upon irradiation at 520 nm to evaluate the effect of different catalyst loadings. The irradiation setup consisted of eight green light-emitting diodes (LEDs) of the type LXZ1-PM01 from *Lumileds*, supplied by roughly 23 V and 60 mA with a radiometric power of 100 mW per LED. The reaction flasks containing pressurized, CO_2-saturated solutions of the photo-catalytically active substances in *N,N*-dimethylformamide were placed at a distance of 10 cm to the light source. Triethanolamine (TEOA) was added as a base and 1,3-dimethyl-2-phenyl-2,3-dihydro-1*H*-benzo[*d*]imidazole (BIH) ([BIH]/[Re] = 10 000) was applied as sacrificial electron donor due to its strong reduction potential and the inertness of the formed oxidation products.[34,35] In the irradiation experiments, all photocatalysts showed catalytic activity toward the conversion of CO_2 to CO (Figure 2A). Control experiments confirmed that CO evolution originates from the reported reaction cycle for photocatalytic reduction of CO_2 (Supporting information, Figure S26 and Table S4).[8] Gas chromatographic measurements during irradiation of the polymeric photo-catalysts using a thermal conductivity detector revealed the exclusive formation of CO without the detection of side products. Furthermore, NMR spectroscopic investigations of the reaction mixture did not indicate the formation of soluble side products during CO_2 reduction. A more detailed analysis of the gas-phase composition during the initial period of irradiation using a gas chromatograph equipped with a

reduction gas detector revealed the formation of traces of hydrogen. However, this detection technique could not be applied during routine gas chromatographic measurements due to the risk of destruction of the detector by the high amounts of CO formed. Compared to the supramolecular photocatalysts with a fixed stoichiometry defined by their molecular structure introduced by Rieger et al.[16] and Ishitani et al.,[7,36] the loaded polymers contain a much higher number of metal centers per molecule. Besides that, the herein established approach allows for a facile modification of the Re(I)/Ru(II) ratio upon catalyst synthesis. The rhenium catalyst concentration was adjusted to 20.0 μM based on the ICP-MS results shown in the Supporting information, Table S2, to facilitate a comparison of the effects of inter- and intramolecular Re(I)–Re(I) interactions, as those are known to be beneficial for the photocatalytic performance.[4]

The results presented in Figure 2A reveal increased photostabilities at low rhenium loadings with the turnover number of **PVBpy$^{5/95}$** (TON = 5650) competing with the TON per rhenium center values of literature-known benchmark catalysts (TON = 6038).[36] In this context, common turnover numbers for the photocatalytic reduction of CO_2 with supramolecular rhenium–ruthenium catalysts and BIH as the sacrificial electron donor range from values between 100 and the mid-1000s.[9,37] Despite the apparent contradiction to the previously stated beneficial effect of Re(I)–Re(I) interactions,[4] the trend of **PVBpy$^{5/95}$** exhibiting the highest turnover numbers can be most likely attributed to the stabilizing effect of Ru(II) photosensitizing units in the catalyst system.[38] In this respect, high concentrations of ruthenium moieties in photocatalytic systems protect the catalytic sites as well as other Ru(II) centers from deactivation of the OERS by overexcitation, as will be discussed in more detail later.[3,38,39] Additionally, **PVBPy$^{5/95}$** exhibits the highest Ru(II)/Re(I) ratio (see Table 2), which increases the probability of a close proximity between a catalytic reduction site and photosensitizers. All catalysts have long lifetimes of over seven days, and in the case of **PVBpy$^{5/95}$**, the catalyst showed activity even after 30 days of irradiation (see the Supporting information, Figure S25). This catalyst lifetime is most likely due to the high amount of ruthenium photosensitizer in this macromolecular complex. In this context, losses of the photosensitizer due to light-induced deactivation reactions of the Ru(II)-OERS, which are generally considered the main route for catalyst degradation, are compensated by the high number of ruthenium centers in such systems.[3,15] Another contribution to the increased photostability of polymers with a high Ru(II)/Re(I) ratio, such as **PVBpy$^{5/95}$**, is the aforementioned elevated probability of spatial proximity between a photocatalytically active rhenium center and photosensitizing ruthenium units. This potential neighborhood enables an efficient electron transfer from the Ru(II)-OERS to the Re(I)-complexes, which is reflected in the high photostability (TON = 5650) and the long lifetime (30 days) of the catalyst. In photocatalysts with high Ru(II)/Re(I) ratios, excitation and reductive quenching by the electron donor accompanied by the formation of the Ru(II)-OERS occurs in large quantities. As a result of the subsequent electron transfer, also the Re(I)-OERS capable of entering the catalytic cycle of CO_2 reduction is formed in high amounts. As this becomes the main route of the overall process, the occurrence of side reactions, such as radical deactivation and overexcitation of the Re(I)-OERS, is significantly reduced.[3] In general, a good correlation between

the photostability, expressed as the turnover number, and the catalytic activity, expressed as the initial turnover frequency, was received (see the Supporting information, Table S3). Fast initial CO_2 conversion was observed in systems with high Ru(II)/Re(I) ratios, such as **PVBpy$^{5/95}$** ($R_{Ru(II)/Re(I)}$ = 4.07, TOF = 66 h^{-1}), as excitation of the ruthenium photosensitizers occurs to a large extent and thus, the formed Ru(II)-OERS are able to provide the rhenium centers with electrons in high quantities. In comparison, **PVBPy$^{50/50}$**, exhibiting a significantly lower Ru(II)/Re(I) ratio ($R_{Ru(II)/Re(I)}$ = 0.21), showed a decreased turnover frequency of 4.2 h^{-1}. Besides intramolecular interactions of the ruthenium and rhenium units due to covalent linkage, also an intermolecular contribution of the electron transfer from Ru(II)-OERS to rhenium centers is expectable. To elucidate the role of intermolecular interactions, the best performing system **PVBpy$^{5/95}$** was tested for the photocatalytic reduction of CO_2 in different concentrations (Figure 2B). In this context, catalyst solutions with concentrations ranging from 30.0 μM to 1.25 μM (see the Supporting information, Table S3 for concentrations) were irradiated, and the calculated turnover numbers were plotted against the reaction time (Figure 2B). Good photostabilities were obtained at high concentrations of the macromolecular complex (c_{Re} = 20.0 μM and c_{Re} = 30.0 μM). However, no significant increase of the turnover number upon further increase of the catalyst concentration was observable. On the one hand, this could be explained by the CO_2 reduction as the rate-limiting step of the overall process.[40] On the other hand, this well-known phenomenon can be assigned to the primary inner filter effect. In highly concentrated solutions and at low irradiation intensity, incident light is absorbed to a large extent by the part of the sample facing the light source.[41] In the context of photocatalysis, this inner filter effect leads to consistent photocatalytic results without further improvement above a certain catalyst concentration,[4] as only a partial excitation of all metal centers in the solution takes place.[42] In other words, this causes a limitation of the number of excited Ru(II) centers regardless of their overall concentration, and as a consequence of the electron transfer from Ru(II)-OERS to the rhenium catalyst units, a threshold of the CO_2 reduction is reached. In the low-concentration regime (c_{Re} <20.0 μM), the TONs significantly dropped to values below 1000. First, this can be attributed to a more pronounced degradation of the catalytic sites as well as the photosensitizers, which both are present in lower amounts due to overexcitation and other side reactions by excess irradiation.[3,15] Second, this could be a hint toward a decreasing contribution of intermolecular interactions involved in the two-electron reduction upon dilution. Despite the high amount of potential interaction partners of the metal centers along the polymer chain, intermolecular electron transfer between the polymer chains could likely assume a role for the photocatalytic reduction. To evaluate the impact of intermolecular interactions, initial turnover frequencies for all investigated catalyst concentrations of **PVBPy$^{5/95}$** are considered, as catalyst decomposition should be less pronounced within the first hours of irradiation. All five concentrations of **PVBPy$^{5/95}$** (c_{Re} = 30.0−1.25 μM) exhibit similar initial turnover frequencies (Figure 2B). This might be attributed to a comparably efficient, intramolecular electron transfer between the covalently linked ruthenium and rhenium centers because of the fixed catalyst composition, as the comparison of the various tested catalysts (Figure 2A) indicated a strong correlation between the Ru(II)/Re(I) ratio and the TOF. The

Macromolecular Rhenium–Ruthenium Complexes for Photocatalytic CO2 Conversion: From Catalytic Lewis Pair Polymerization to Well-Defined Poly(vinyl bipyridine)-Metal Complexes

comparable initial TOFs among the investigated concentrations indicate a secondary role of the intermolecular interactions regardless of the applied catalyst amount. At elevated reaction times, a decrease of the turnover frequency was observed for all concentrations; however, this trend is more pronounced for the low polymer concentrations. In these cases, the total ruthenium content in solution is smaller, leading to lower total absorption, a weaker inner filter effect, and, therefore, exposing the ruthenium units to more light.[4] As a consequence, the ruthenium moieties are more prone to side reactions, such as overexcitation,[3] effectively decreasing their amount, which cannot be compensated as well in dilute systems due to the low initial ruthenium concentration.

CONCLUSIONS

Herein, the first catalytic polymerization of the extended Michael-type monomer 4′-vinyl-4-methyl-2,2′-bipyridine facilitated by different aluminum–phosphorus Lewis pairs is presented. A broad screening of the Lewis acids and bases used for the polymerization regarding achievable conversion, polydispersity, and initiator efficiency was performed, revealing the combination of tri-*iso*-butyl aluminum and trimethyl phosphine to show the best results with conversions of up to 80% while exhibiting high initiator efficiencies of 45–51% and maintaining narrow polydispersities below 1.36. End-group analysis revealed the presence of two initiation pathways, conjugate addition and deprotonation, yet precise control of the initiation rates gave access to polymers with monomodal, narrow weight distributions. These well-defined poly(vinyl bipyridine) polymers are amorphous with a thermal decomposition onset of 368 °C and a glass transition at 142 °C. Overall, this catalytic approach toward defined polymers allows the synthesis of tailor-made poly(vinyl bipyridines). This features advantages such as adjustable properties or block copolymerization with other Michael-type monomers like dialkyl vinyl phosphonates. The prepared poly(vinyl bipyridines), acting as macroligands due to the incorporated bipyridine motif, were subsequently loaded with rhenium and ruthenium centers. In this context, the facile two-step synthesis protocol using the precursor complexes $Re(CO)_5Cl$ and $Ru(dmb)_2Cl_2$ allows for an effortless variation of the $Re(I)/Ru(II)$ ratio. UV–vis-, photoluminescence-, and IR spectroscopy were applied to qualitatively evaluate the metal loading on the polymer ligand, whereas quantification of the metal loading via ICP-MS revealed nonquantitative attachment to the metal centers, most likely due to steric reasons and the secondary structural motifs of the polymers. However, the expected trends in metal loading experiments were observable, and higher total polymer loadings upon optimization of the synthetic approach is a topic of current research. By means of the presented experimental procedure, a statistical copolymer composed of empty bipyridine side groups, rhenium, and ruthenium-loaded sites with a well-characterized $Re(I)/Ru(II)$ ratio was accessible, exhibiting a highly defined structure in terms of polymer chain length and polydispersity. Four different polymeric complexes (**PVBpy$^{5/95}$**, **PVBpy$^{10/90}$**, **PVBpy$^{25/75}$**, and **PVBpy$^{50/50}$**) with varying rhenium to ruthenium loading were prepared, thoroughly characterized, and investigated regarding their activity and stability in the photocatalytic reduction of CO_2 to CO. In this context, **PVBpy$^{5/95}$** revealed particularly high photostabilities and activities (TON = 5650, TOF = 66 h^{-1}), competing with the respective values of literature-known benchmark catalysts.

This was attributed to the high probability of a spatial proximity between a photocatalytically active rhenium center and ruthenium photosensitizers, enabling an efficient electron transfer and decreasing the extent of side reactions. Among the tested catalysts, a correlation of the TON and the TOF according to the $Ru(II)/Re(I)$ ratio of the respective catalyst was observed. Similar initial turnover frequencies of **PVBpy$^{5/95}$** in a concentration study were assigned to the fixed catalyst composition; comparison with the TOFs found for the other catalysts, however, indicated a secondary role of intermolecular contributions to the electron transfer from ruthenium to rhenium. Whereas the positive effect on the photostability at higher concentrations was assigned to the protection of $Re(I)$ centers due to an attenuation of the excitation beam by the increased number of photosensitizing $Ru(II)$ units, the accelerated catalyst decomposition in the low-concentration regime was attributed to the absence of this effect.

In conclusion, aluminum–phosphorus Lewis pair-mediated polymerization has clearly proved to be a promising tool for the synthesis of well-defined poly(vinyl bipyridines). The polymers were successfully used as macromolecular ligands for the synthesis of multinuclear rhenium–ruthenium complexes, yielding well-characterized, polymeric photocatalysts. These catalysts revealed high activities and stabilities in the photocatalytic reduction of CO_2 to CO.

ASSOCIATED CONTENT

Ⓢ Supporting Information

The Supporting Information is available free of charge at https://pubs.acs.org/doi/10.1021/acs.macromol.2c00440.

> General experimental and synthesis/polymerization details, dn/dc-determination, SEC-data, thermal polymer characterization and end-group analysis, photocatalyst synthesis and characterization, as well as photocatalysis and control experiment results (PDF)

AUTHOR INFORMATION

Corresponding Author

Bernhard Rieger − *WACKER-Chair of Macromolecular Chemistry, Department of Chemistry, Technical University of Munich, 85748 Garching, Germany;* ⓞ orcid.org/0000-0002-0023-884X; Email: rieger@tum.de

Authors

Anton S. Maier − *WACKER-Chair of Macromolecular Chemistry, Department of Chemistry, Technical University of Munich, 85748 Garching, Germany*

Christopher Thomas − *WACKER-Chair of Macromolecular Chemistry, Department of Chemistry, Technical University of Munich, 85748 Garching, Germany*

Moritz Kränzlein − *WACKER-Chair of Macromolecular Chemistry, Department of Chemistry, Technical University of Munich, 85748 Garching, Germany;* ⓞ orcid.org/0000-0001-9851-0735

Thomas M. Pehl − *WACKER-Chair of Macromolecular Chemistry, Department of Chemistry, Technical University of Munich, 85748 Garching, Germany*

Complete contact information is available at:
https://pubs.acs.org/10.1021/acs.macromol.2c00440

Macromolecular Rhenium–Ruthenium Complexes for Photocatalytic CO2 Conversion: From Catalytic Lewis Pair Polymerization to Well-Defined Poly(vinyl bipyridine)-Metal Complexes

Author Contributions

[†]A.S.M., C.T., and M.K. contributed equally. The manuscript was written through contributions of all authors. All authors have given approval to the final version of the manuscript.

■ ABBREVIATIONS

VBpy, 4-vinyl-4′-methyl-2,2′-bipyridine; PVBpy, poly(4-vinyl-4′-methyl-2,2′-bipyridine); FLP, frustrated Lewis pair; LA, Lewis acid; LB, Lewis base; $AlOct_3$, tri-*n*-octylaluminum; $POct_3$, tri-*n*-octylphosphine; SEC, size-exclusion chromatography; DSC, differential scanning calorimetry; TGA, thermogravimetric analysis; BIH, 1,3-dimethyl-2-phenyl-2,3-dihydro-1*H*-benzo[*d*]imidazole; TEOA, triethanolamine; OERS, one-electron-reduced species; MLCT, metal-to-ligand charge-transfer; TON, turnover number; TOF, turnover frequency; I.E., initiator efficiency; ESI-MS, electrospray ionization mass spectrometry; ICP-MS, inductively coupled plasma mass spectrometry; dmb, 4,4′-dimethyl-2,2′-bipyridine; LED, light-emitting diode

■ REFERENCES

(1) Hawecker, J.; Lehn, J.-M.; Ziessel, R. Efficient photochemical reduction of CO_2 to CO by visible light irradiation of systems containing $Re(bipy)(CO)_3X$ or $Ru(bipy)_3^{2+}$ $-Co^{2+}$ combinations as homogeneous catalysts. *J. Chem. Soc., Chem. Commun.* **1983**, 536–538.

(2) Lehn, J. M.; Ziessel, R. Photochemical generation of carbon monoxide and hydrogen by reduction of carbon dioxide and water under visible light irradiation. *Proc. Natl. Acad. Sci. U.S.A.* **1982**, *79*, 701–704.

(3) Meister, S.; Reithmeier, R. O.; Tschurl, M.; Heiz, U.; Rieger, B. Unraveling Side Reactions in the Photocatalytic Reduction of CO_2: Evidence for Light-Induced Deactivation Processes in Homogeneous Photocatalysis. *ChemCatChem* **2015**, *7*, 690–697.

(4) Bruckmeier, C.; Lehenmeier, M. W.; Reithmeier, R.; Rieger, B.; Herranz, J.; Kavakli, C. Binuclear rhenium(I) complexes for the photocatalytic reduction of CO2. *Dalton Trans.* **2012**, *41*, 5026–5037.

(5) Balzani, V.; Bergamini, G.; Marchioni, F.; Ceroni, P. Ru(II)-bipyridine complexes in supramolecular systems, devices and machines. *Coord. Chem. Rev.* **2006**, *250*, 1254–1266.

(6) Juris, A.; Balzani, V.; Barigelletti, F.; Campagna, S.; Belser, P.; Zelewsky, A. von. Ru(II) polypyridine complexes: photophysics, photochemistry, eletrochemistry, and chemiluminescence. *Coord. Chem. Rev.* **1988**, *84*, 85–277.

(7) Gholamkhass, B.; Mametsuka, H.; Koike, K.; Tanabe, T.; Furue, M.; Ishitani, O. Architecture of supramolecular metal complexes for photocatalytic CO_2 reduction: ruthenium-rhenium bi- and tetranuclear complexes. *Inorg. Chem.* **2005**, *44*, 2326–2336.

(8) Kamogawa, K.; Shimoda, Y.; Miyata, K.; Onda, K.; Yamazaki, Y.; Tamaki, Y.; Ishitani, O. Mechanistic study of photocatalytic CO_2 reduction using a Ru(ii)-Re(i) supramolecular photocatalyst. *Chem. Sci.* **2021**, *12*, 9682–9693.

(9) Tamaki, Y.; Ishitani, O. Supramolecular Photocatalysts for the Reduction of CO_2. *ACS Catal.* **2017**, *7*, 3394–3409.

(10) Furue, M.; Naiki, M.; Kanematsu, Y.; Kushida, T.; Kamachi, M. Intramolecular energy transfer in covalently linked polypyridine rhenium(I)/ruthenium(II) complexes. *Coord. Chem. Rev.* **1991**, *111*, 221–226.

(11) Bian, Z.-Y.; Chi, S.-M.; Li, L.; Fu, W. Conjugation effect of the bridging ligand on the CO_2 reduction properties in difunctional photocatalysts. *Dalton Trans.* **2010**, *39*, 7884–7887.

(12) Koike, K.; Naito, S.; Sato, S.; Tamaki, Y.; Ishitani, O. Architecture of supramolecular metal complexes for photocatalytic CO_2 reduction. *J. Photochem. and Photobiol.* **2009**, *207*, 109–114.

(13) Takeda, H.; Ishitani, O. Development of efficient photocatalytic systems for CO_2 reduction using mononuclear and multinuclear metal complexes based on mechanistic studies. *Coord. Chem. Rev.* **2010**, *254*, 346–354.

(14) Bian, Z.-Y.; Sumi, K.; Furue, M.; Sato, S.; Koike, K.; Ishitani, O. Synthesis and properties of a novel tripodal bipyridyl ligand tb-carbinol and its Ru(II)-Re(I) trimetallic complexes: investigation of multimetallic artificial systems for photocatalytic CO_2 reduction. *Dalton Trans.* **2009**, 983–993.

(15) Umemoto, A.; Yamazaki, Y.; Saito, D.; Tamaki, Y.; Ishitani, O. Synthesis of a Novel Re(I)-Ru(II)-Re(I) Trinuclear Complex as an Effective Photocatalyst for CO_2 Reduction. *BCSJ* **2020**, *93*, 127–137.

(16) Meister, S.; Reithmeier, R. O.; Ogrodnik, A.; Rieger, B. Bridging Efficiency within Multinuclear Homogeneous Catalysts in the Photocatalytic Reduction of Carbon Dioxide. *ChemCatChem* **2015**, *7*, 3562–3569.

(17) Kamata, R.; Kumagai, H.; Yamazaki, Y.; Sahara, G.; Ishitani, O. Photoelectrochemical CO2 Reduction Using a Ru(II)-Re(I) Supramolecular Photocatalyst Connected to a Vinyl Polymer on a NiO Electrode. *ACS Appl. Mater. Interfaces* **2019**, *11*, 5632–5641.

(18) Schubert, U. S.; Eschbaumer, C. Macromolecules Containing Bipyridine and Terpyridine Metal Complexes: Towards Metallosupramolecular Polymers. *Angew. Chem., Int. Ed.* **2002**, *41*, 2892–2926.

(19) Adams, F.; Pschenitza, M.; Rieger, B. Yttrium-Catalyzed Synthesis of Bipyridine-Functionalized AB-Block Copolymers: Micellar Support for Photocatalytic Active Rhenium-Complexes. *ChemCatChem* **2018**, *10*, 4309–4316.

(20) Pitt, C. G.; Bao, Y.; Seltzman, H. H. The synthesis of polymers containing the 2,2′-bipyridine ligand. *J. Polym. Sci., Part C: Polym. Lett.* **1986**, *24*, 13–16.

(21) Sumi, K.; Furue, M.; Nozakura, S.-I. Preparation and luminescence properties of tris(bipyridine) ruthenium(II)-containing vinyl polymers: $Ru(bpy)_2$ (poly-6-vinyl-2,2′-bipyridine)Cl_2 and Ru-$(bpy)_2$(poly-4-methyl-4′-vinyl-,2,2′-bipyridine)Cl_2. *J. Polym. Sci. Polym. Chem. Ed.* **1984**, *22*, 3779–3788.

(22) Pefkianakis, E. K.; Tzanetos, N. P.; Kallitsis, J. K. Synthesis and Characterization of a Novel Vinyl-2,2′-bipyridine Monomer and Its Homopolymeric/Copolymeric Metal Complexes. *Chem. Mater.* **2008**, *20*, 6254–6262.

(23) Gould, S.; Strouse, G. F.; Meyer, T. J.; Sullivan, B. P. Formation of thin polymeric films by electropolymerization. Reduction of metal complexes containing bromomethyl-substituted derivatives of 2,2′-bipyridine. *Inorg. Chem.* **1991**, *30*, 2942–2949.

(24) Elliott, C. M.; Baldy, C. J.; Nuwaysir, L. M.; Wilkins, C. L. Electrochemical polymerization of 4-methyl-4′-vinyl-2,2′-bipyridine-containing metal complexes: polymer structure and mechanism of formation. *Inorg. Chem.* **1990**, *29*, 389–392.

(25) Lowry, T. M. Valence and the structure of atoms and molecules. By Prof. G. N. Lewis. Pp. 172. American Chemical Monograph Series. New York: The Chemical Catalog Co., Inc., 1923. Price $3. *J. Chem. Technol. Biotechnol.* **1924**, *43*, 17.

(26) McCahill, J. S. J.; Welch, G. C.; Stephan, D. W. Reactivity of "Frustrated Lewis Pairs": Three-Component Reactions of Phosphines, a Borane, and Olefins. *Angew. Chem.* **2007**, *119*, 5056−5059.

(27) Zhang, Y.; Miyake, G. M.; Chen, E. Y.-X. Alane-Based Classical and Frustrated Lewis Pairs in Polymer Synthesis: Rapid Polymerization of MMA and Naturally Renewable Methylene Butyrolactones into High-Molecular-Weight Polymers. *Angew. Chem.* **2010**, *122*, 10356−10360.

(28) He, J.; Zhang, Y.; Chen, E. Synthesis of Pyridine- and 2-Oxazoline-Functionalized Vinyl Polymers by Alane-Based Frustrated Lewis Pairs. *Synlett* **2014**, *25*, 1534−1538.

(29) Knaus, M. G. M.; Giuman, M. M.; Pöthig, A.; Rieger, B. End of Frustration: Catalytic Precision Polymerization with Highly Interacting Lewis Pairs. *J. Am. Chem. Soc.* **2016**, *138*, 7776−7781.

(30) Bian, Z.-Y.; Wang, H.; Fu, W.-F.; Li, L.; Ding, A.-Z. Two bifunctional RuII/ReI photocatalysts for CO_2 reduction: A spectroscopic, photocatalytic, and computational study. *Polyhedron* **2012**, *32*, 78−85.

(31) Castellucci, E.; Angeloni, L.; Neto, N.; Sbrana, G. IR and Raman spectra of A 2,2′-bipyridine single crystal: internal modes. *Chem. Phys.* **1979**, *43*, 365−373.

(32) Portenkirchner, E.; Gasiorowski, J.; Oppelt, K.; Schlager, S.; Schwarzinger, C.; Neugebauer, H.; Knör, G.; Sariciftci, N. S. Electrocatalytic Reduction of Carbon Dioxide to Carbon Monoxide by a Polymerized Film of an Alkynyl-Substituted Rhenium(I) Complex. *ChemCatChem* **2013**, *5*, 1790−1796.

(33) Orchanian, N. M.; Hong, L. E.; Skrainka, J. A.; Esterhuizen, J. A.; Popov, D. A.; Marinescu, S. C. Surface-Immobilized Conjugated Polymers Incorporating Rhenium Bipyridine Motifs for Electrocatalytic and Photocatalytic CO_2 Reduction. *ACS Appl. Energy Mater.* **2019**, *2*, 110−123.

(34) Tamaki, Y.; Koike, K.; Ishitani, O. Highly efficient, selective, and durable photocatalytic system for CO_2 reduction to formic acid. *Chem. Sci.* **2015**, *6*, 7213−7221. Published Online: Sep. 29, 2015.

(35) Tamaki, Y.; Koike, K.; Morimoto, T.; Ishitani, O. Substantial improvement in the efficiency and durability of a photocatalyst for carbon dioxide reduction using a benzoimidazole derivative as an electron donor. *J. Catal.* **2013**, *304*, 22−28.

(36) Cancelliere, A. M.; Puntoriero, F.; Serroni, S.; Campagna, S.; Tamaki, Y.; Saito, D.; Ishitani, O. Efficient trinuclear Ru(ii)-Re(i) supramolecular photocatalysts for CO_2 reduction based on a new tris-chelating bridging ligand built around a central aromatic ring. *Chem. Sci.* **2020**, *11*, 1556−1563.

(37) Kuramochi, Y.; Ishitani, O.; Ishida, H. Reaction mechanisms of catalytic photochemical CO2 reduction using Re(I) and Ru(II) complexes. *Coord. Chem. Rev.* **2018**, *373*, 333−356.

(38) Stanley, P. M.; Thomas, C.; Thyrhaug, E.; Urstoeger, A.; Schuster, M.; Hauer, J.; Rieger, B.; Warnan, J.; Fischer, R. A. Entrapped Molecular Photocatalyst and Photosensitizer in Metal−Organic Framework Nanoreactors for Enhanced Solar CO_2 Reduction. *ACS Catal.* **2021**, *11*, 871−882.

(39) Ghosh, A. C.; Legrand, A.; Rajapaksha, R.; Craig, G. A.; Sassoye, C.; Balázs, G.; Farrusseng, D.; Furukawa, S.; Canivet, J.; Wisser, F. M. Rhodium-Based Metal-Organic Polyhedra Assemblies for Selective CO2 Photoreduction. *J. Am. Chem. Soc.* **2022**, *144*, 3626−3636.

(40) Yamazaki, Y.; Ohkubo, K.; Saito, D.; Yatsu, T.; Tamaki, Y.; Tanaka, S.'I.; Koike, K.; Onda, K.; Ishitani, O. Kinetics and Mechanism of Intramolecular Electron Transfer in Ru(II)-Re(I) Supramolecular CO2-Reduction Photocatalysts: Effects of Bridging Ligands. *Inorg. Chem.* **2019**, *58*, 11480−11492.

(41) Kubista, M.; Sjöback, R.; Eriksson, S.; Albinsson, B. Experimental correction for the inner-filter effect in fluorescence spectra. *Analyst* **1994**, *119*, 417−419.

(42) Kumar Panigrahi, S.; Kumar Mishra, A. Inner filter effect in fluorescence spectroscopy: As a problem and as a solution. *J. Photochem. Photobiol., C* **2019**, *41*, No. 100318.

5.4   Reprint Permission Copyrighted Content

6. The Puzzling Question about the Origin of the Second Electron in the Molecular Photocatalytic Reduction of CO_2

6.1 Bibliographic Data
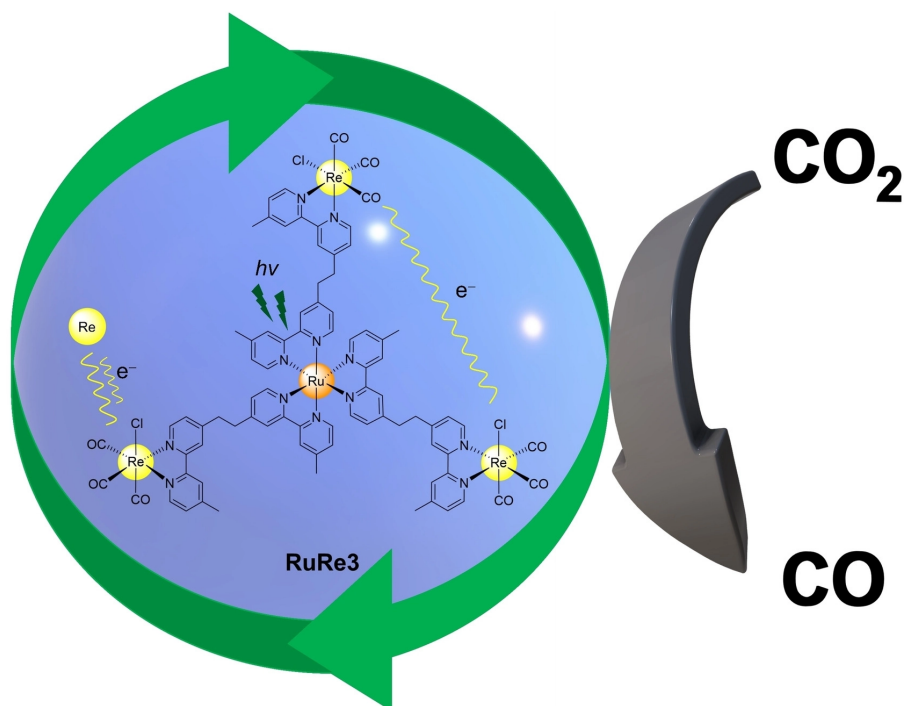
Title: "The Puzzling Question about the Origin of the Second Electron in the Molecular Photocatalytic Reduction of CO_2"

Status: Full Paper, published online 4th September 2022

Journal: ChemCatChem 2022, 14, e202200841

Publisher: Wiley-VCH

Link/DOI: https://doi.org/10.1002/cctc.202200841

Authors: Christopher Thomas,[‡] Marina Wittig,[‡] and Bernhard Rieger*

[‡]These authors contributed equally. Christopher Thomas conceptualised the experimental studies and carried out experiments. Marina Wittig carried out experiments. Christopher Thomas and Marina Wittig wrote the manuscript. All work was carried out under supervision of Bernhard Rieger.

6.2   Summary

The photocatalytic reduction of CO_2 to CO by Re(I)-based complexes suffers from low stability and excitation by high energy light. Multinuclear catalysts combining Re(I)-catalysts with Ru(II)-photosensitisers tackle these drawbacks by being excitable at higher wavelengths of the visible spectrum. In addition, these supramolecular systems demonstrate increased stability during irradiation due to the distribution of the individual steps on the different metal centres. As the better performance is correlated with the Re-Re-interaction, in particular, the electron transfer, a new photocatalyst containing three Re(dmb)(CO)$_3$Cl (dmb = 4,4'-dimethyl-2,2'-bipyridine) (Re) building blocks, which are connected through an ethylene bridge to one [Ru(dmb)$_3$]$^{2+}$-unit (Ru) was synthesised in this work. We compared the photophysical characteristics of this new tetranuclear RuRe3 with the literature-known complexes RuRe and RuRe2 and concluded that in the ground state the properties are very similar. Under irradiation, the three photocatalysts RuRe, RuRe2, and RuRe3 exhibit high activity and photostability for the reduction of CO_2 to CO, with RuRe3 achieving the highest TON (11800) reported to date for a Re(I)/Ru(II)-containing homogeneous catalyst. RuRe3 performs especially superior in the small catalyst concentration regime, which was attributed to an efficient second electron transfer via an intramolecular mechanism. This process was enhanced by the spatial proximity of three Re-centres. Regarding the conversion per Re-centre, RuRe (TON$_{Re}$ = 7582) outperforms all comparable systems to our best knowledge, which was associated with the high concentration of photosensitiser. Intermolecular transfer from small and mobile Re to RuRe motifs were found to also increase the catalytic performance of the system RuRe + 2 Re to a similar level (TON = 12100) of RuRe3. These synergistic effects were assigned to an efficient second electron provision, the mechanism of which has not been finally clarified for molecular systems to date. Our photocatalytic studies prove that the besides BIH, BIH-intermediates, and Ru-OERS as electron donors, the Re-Re interactions play a key role in the reduction of CO_2. Further, we could show that the ratio Re/Ru of 3 constitutes an optimum, which should be considered for future designs of efficient supramolecular CO_2-reducing photocatalysts.

Check for updates

Chemistry
Europe

European Chemical
Societies Publishing

The Puzzling Question about the Origin of the Second Electron in the Molecular Photocatalytic Reduction of CO_2

Christopher Thomas+,[a] Marina Wittig+,[a] and Bernhard Rieger*[a]

Herein, a new supramolecular photocatalyst **RuRe3** containing three Re(dmb)CO₃Cl (dmb = 4,4'-dimethyl-2,2'-bipyridine) (**Re**) building blocks connected through an ethylene bridge to one [Ru(dmb)₃]²⁺-unit (**Ru**) is presented. We investigated the photophysical properties of this novel tetranuclear complex and compared these to compounds with one (**RuRe**) and two (**RuRe2**) catalytic units. Under irradiation, all three photocatalysts exhibit high activity and photostability for the reduction of CO_2 to CO, with **RuRe3** achieving the highest turnover number (11800) reported to date for a Re(I)/Ru(II)-containing homogeneous catalyst. This tetranuclear complex is especially superior at small catalyst concentrations, which is attributed to an efficient second electron transfer via an intramolecular mechanism. Intermolecular electron transfer from small and mobile **Re** to **RuRe** motifs are found to also increase the catalytic performance of the system to a similar level (turnover number = 12100). These synergistic effects are attributed to an improved catalytic cycle, stabilizing the bi- and tetrametallic complexes by providing the electrons quickly and effectively. Since the second electron provision is not finally clarified for molecular systems until today, our photocatalytic studies present important insights into this crucial step. Further, these investigations should be considered for the design and synthesis of new and efficient supramolecular CO_2-reducing photocatalysts.

Introduction

The ever-increasing energy consumption and the associated carbon demand will aggravate in the years to come.[1] As fossil resources are limited and the products can act as greenhouse gases, an efficient way to convert CO_2 as an abundant carbon source into energy rich compounds is desirable. An environmentally benign procedure that utilizes renewable resources to provide the required energy for these reactions is represented in the photocatalytic reduction of CO_2 to CO. This two-electron reduction process can be performed by rhenium(I) catalysts ([Re(L)(CO)₃X] (L = α,α'-dipyridyl or phenanthroline; X = Cl⁻ or Br⁻) in the presence of a sacrificial electron donor like triethylamine or triethanolamine.[2] Nonetheless, we were previously able to show that these complexes suffer from low irradiation stability due to overexcitation and the side reactions with quencher radicals.[3] The most successful way to improve the turnover number (TON) of the rhenium catalysts in homogeneous solution is the outsourcing of the photosensitization to ruthenium-centered ([Ru(dmb)₃]²⁺ (dmb = 4,4'-dimethyl-2,2'-bipyridine)) complexes.[4] These covalently connected multinuclear catalysts exhibit superior CO_2 reduction ability due to the spatial separation of sensitization and reduction site.[5] The Ru-centered photosensitizer (PS) shifts the absorption maxima to higher wavelengths allowing excitation of the system with lower energy visible light and an increased absorption range. Furthermore, the subsequent reductive quenching of the excited ruthenium species by more efficient sacrificial electron donors like 1-benzyl-1,4-dihydronicotinamide (BNAH) or 1,3-dimethyl-2-phenyl-2,3-dihydro-1**H**-benzo[d]imidazole (BIH) is possible. BIH is especially suitable for the two-electron reduction of CO_2 in homogeneous solution as one molecule can donate both electrons. In addition, the resulting BI⁺ does not further interfere with the photocatalysis of Ru/Re-systems and suppresses the back electron transfer.[6] The covalent tethering of Ru(II) and Re(I) centers ensures an efficient photoinduced electron transfer starting from the one-electron-reduced Ru-PS to the rhenium catalysts without strong electronic interactions in the ground state of the molecule.[4a,7] Covalent linkage between these metal centers via saturated ethylene-bridges displays weak electronic interactions without enlarging the π-system accompanied by the efficiency optimization of the intramolecular electron transfer.[8] Therefore, these supramolecules exhibit improved catalytic activity and durability compared to the unconnected reference system, namely a mixture of [Ru(dmb)₃]²⁺ (**Ru**) and [Re(dmb)(CO)₃Cl] (**Re**).[9] In summary, these points are assumed to be the main reason for the increased TON by about two orders of magnitude in the CO_2 reduction of multinuclear Ru/Re-complexes compared to mono- or binuclear rhenium(I) catalysts.[2,6a,10] The positive effects of setting up a supramolecular catalyst with close proximity of the active metal centers can be seen in the performance of the **RuRe2** catalyst (TON = 199) synthesized by our group.[4a] These results are attributed to a binuclear reduction mechanism for the two-electron transfer to CO_2. As **RuRe2** contains two catalytically active sites this is possible intramolecularly, there-

[a] C. Thomas,+ M. Wittig,+ Prof. Dr. B. Rieger
Catalysis Research Center
Technische Universität München
WACKER-Chair of Macromolecular Chemistry
Ernst-Otto-Fischer Strasse 1
85748 Garching (Germany)
E-mail: rieger@tum.de
Homepage: https://www.ch.nat.tum.de/en/makro/home/
[+] These authors contributed equally to this work.

Supporting information for this article is available on the WWW under https://doi.org/10.1002/cctc.202200841

The Puzzling Question about the Origin of the Second Electron in the Molecular Photocatalytic Reduction of CO2

fore, the diffusion-controlled collision between two catalyst molecules is not required.[10–11] The increased probability of the electron transfer from the Ru based one-electron-reduced-species (OERS) to the Re(I)-moieties is a second rational explanation. Upon addition of more Re-units in proximity to the PS, the lifetime of the instable OERS of the Ru-units decreases.[12]

This study particularly targets the interplay between one PS and multiple covalently linked Re-catalysts and the resulting photocatalytic stability and activity. To incorporate the advantages of the above-mentioned short linkage between two metal centers, this study focusses on the synthesis of a new ethylene-bridged tetranuclear catalyst (**RuRe3**) and the comparison of spectroscopic and photocatalytic properties with the corresponding dinuclear (**RuRe**) and trinuclear (**RuRe2**) supramolecules (Figure 1). In this context, the mechanism of the second electron donation is examined by irradiating these molecules or their corresponding single component building blocks at different catalyst concentrations. The results are interpreted with respect to intra- and intermolecular interactions, which play a key role in the two-electron reduction of CO_2.

Results and Discussion

For the synthesis of **RuRe3** one equivalent of $[Ru(cod)Cl_2]_n$ (cod = 1,5-cyclooctadiene) and 3.5 equivalents of **Re**(dmb-dmb) (dmb-dmb = 1,2-bis[4-(4′-methyl-2,2′-bipyridyl)]ethane) were suspended in methanol and degassed. After two hours in a microwave reactor at 125 °C and 50 W in dynamic mode the solution was filtered and washed to yield the product as a red solid. The details of the synthesis are provided in the experimental section together with the synthesis of **RuRe** and **RuRe2**.

Photophysical properties

As well as **RuRe** and **RuRe2**, the new supramolecular photocatalysts **RuRe3** contains at least one *fac*-Re(dmb)(CO)$_3$Cl-moiety. These groups cause three characteristic Re-carbonyl vibrational stretching modes, *i.e.*, the in-phase symmetric a′(1), antisymmetric a″, and out of-phase symmetric a′(2), present in the FT-IR spectra (Figure S3) of all three molecules between 1730–2040 cm^{-1}.[11a,13] Two of these signals (a″, a′(2)) are not resolved well enough to appear separated. The IR bands at 1548 cm^{-1}, and 1616 cm^{-1} could be assigned to the stretching of the pyridine ligands.[14] As all spectra show the same peaks with comparable intensities and shifts of the Re-CO signals, a similar geometric and electronic environment for the Re-moieties in **RuRe**, **RuRe2**, and **RuRe3** can be assumed.[15]

All the complexes outlined in this work (**Re**, **Ru**, **RuRe**, **RuRe2**, **RuRe3**) were tested concerning the absorption in DMF at ambient conditions. The strong bands in the ultraviolet area (circa 300 nm) are assigned to intraligand-based $^1\pi$–π^* transitions (^{1}IL) of the bipyridyl-units of the complexes. The metal-to-ligand charge-transfer (^{1}MLCT) (dπ–π^*) transition of the rhenium(I)- and ruthenium(II)-moieties cause the signals at $\lambda =$ 365 and 460 nm, respectively.[14a] These bands appear also in the UV/Vis spectra of the supramolecular complexes **RuReX** (X = 1–3), which are shown in Figure 2 together with model complexes **Re** and **Ru** for comparison.

By superimposing the corresponding building blocks (x***Re** + **Ru**) of the multinuclear catalysts, the spectra can be almost identically replicated (Figure S8). Regarding the summation spectra, these similarities indicate the absence of strong electronic interaction through the ethylene linkers between metallic moieties of the supramolecules in the ground state.[16]

The emission spectra of the supramolecular complexes at room temperature were recorded after excitation at 365 nm and 460 nm. The shapes of the emission spectra of **RuReX** (X = 1–3) do not change significantly when irradiated with these two wavelengths despite 365 and 460 nm being mainly absorbed by the Re- and Ru-units, respectively (Figure S6 and Figure S7).[4c] At 365 nm irradiation, the normalized emission
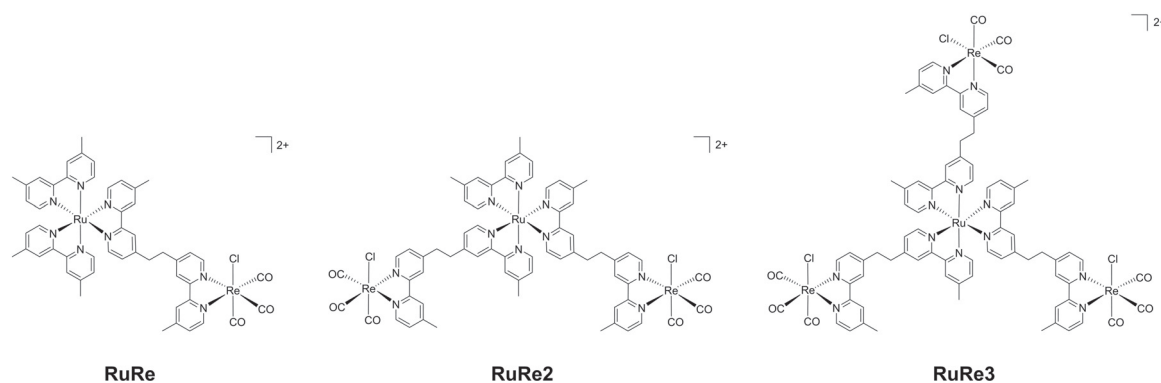
Figure 1. Structures and abbreviations of the synthesized complexes **RuRe**, **RuRe2**, and **RuRe3**. The counter anions are two Cl-ions$^-$ for all three multinuclear catalysts.

The Puzzling Question about the Origin of the Second Electron in the Molecular Photocatalytic Reduction of CO2
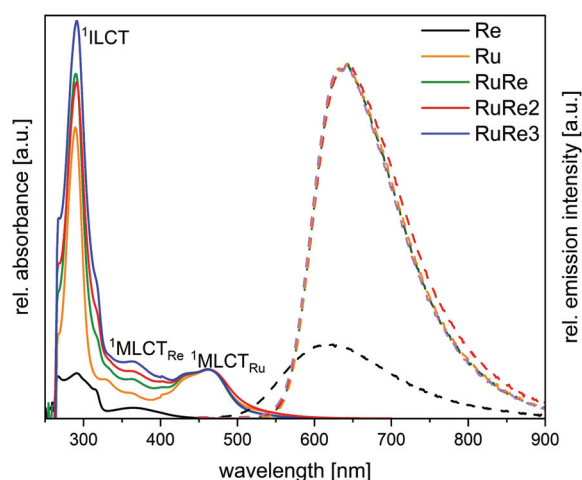
Figure 2. Absorbance (solid lines) and emission spectra (dotted lines) of **Re** (black), **Ru** (orange), **RuRe** (green), **RuRe2** (red), and **RuRe3** (blue) in DMF ($\lambda_{ex} = 365$ nm, 16.0 μM, 25 °C). The absorbance spectra of **Ru** and the multinuclear complexes are normalized to the ^{1}MLCT of ruthenium.
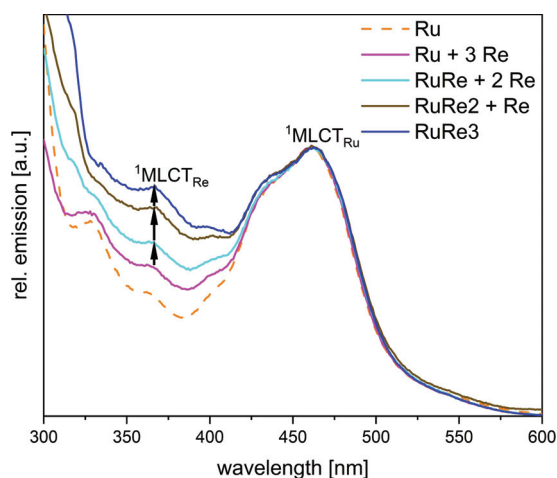
Figure 3. Normalized excitation spectra of **Ru** (orange, dashed line), **Ru + 3 Re** (magenta, solid line), **RuRe + 2 Re** (cyan, solid line), **RuRe2 + Re** (brown, solid line), **RuRe3** (blue, solid line) in DMF ($\lambda_{em} = 645$ nm, 20.0×10 μM, 25 °C).

spectra of all multinuclear complexes match the emittance of the mononuclear Ru-component. This indicates efficient quenching of the emission from the rhenium(I)-bipyridyl-unit, which is expected at 618 nm (Figure 2, Table S2). Energy transfer from the energetical higher lying ^{3}MLCT of Re(I)-bipyridyl-unit to the Ru(II)-complex through the bridging linker is a feasible downhill process, which has already been described previously.[5,7,9,11a,17] The excitation energy is then released by the strong fluorescent Ru(dmb)$_3$$^{2+}$ via light emission in the following step. Nonetheless, intermolecular energy transfer through the secondary inner filter effect also generates these redshifted spectra. The secondary inner filter effect describes the process of reabsorption of already emitted light of Re(I)-moieties and the subsequent second emission of higher wavelengths by the Ru(II)-units.

To evaluate the influence of electronic interaction between multiple molecules, excitation spectra of **RuRe3** and the corresponding single component building blocks in the same composition have been recorded (Figure 3). The spectra were recorded at an emission of 645 nm and for comparison, the emission of the Ru-unit at 462 nm was normalized. As already mentioned, the Ru-center is the main source of emission. Therefore, an increase in emission after the absorption at 365 nm indicates an energy transfer from the Re-metal towards the Ru-center. To see the excitation spectra without the Re(I) to Ru(II) energy transfer, the Ru(dmb)$_3$$^{2+}$ molecule was added as a reference. The **Ru + 3 Re** experiment containing one Ru(dmb)$_3$$^{2+}$ and three Re(dmb)(CO)$_3$Cl-units displays an increased emission as the Re-catalysts also show a low amount of emission itself and intermolecular energy transfer to Ru(II) takes place. Every connection of a Re-unit to the Ru-emitter amplifies the subsequent fluorescence and therefore the signal at 365 nm. This supports the claim for an improved energy transfer through the covalent ethylene chain towards the Ru-unit. The

most efficient system for electronic interaction is created by connecting all three Re-centers to the Ru-unit. This mechanism of intramolecular energy transfer from the Re-moieties to the Ru-unit is supported by the relatively high quantum yield of **RuRe3** (12.2%) compared to **RuRe2** (7.5%) and **RuRe** (8.3%) (Table S2). Therefore, the deactivation processes (internal conversion, vibrational relaxation, and intersystem crossing with subsequent non-radiative deactivation) of the excited Re-unit can be suppressed by the linkage to Ru(II)-units, and the short alkyl chains ensure efficient intramolecular energy transfer (IEnT) as previously reported.[18] These results indicate electronic properties that are desired in the photocatalysis, because an efficient energy transfer takes place to all of the three connected reduction centers in **RuRe3**.

Catalytic performance

The following photocatalytic investigations should deepen the understanding regarding the electron transfer of the above-mentioned Ru/Re catalysts. The multinuclear catalysts and their respective single components were dissolved in DMF followed by the addition of triethanolamine (TEOA). To support the function of TEOA as base and to ensure comparability, all the irradiation experiments were performed at a TEOA concentration of 1.72 M. Further BIH was added, as the sacrificial two electron donor for the reductive quenching of the excited ruthenium-centers. BIH was chosen due to its strong electron donating ability and its oxidized products being inert regarding the photocatalytic reaction.[6a,b] The solution was saturated with CO_2 and irradiated with a green LED light source ($\lambda = 520$ nm) to selectively excite the Ru-centers. In addition, initial experiments were performed with an irradiation wavelength of 450 nm and 360 nm. In both cases the Re-moieties as well as

The Puzzling Question about the Origin of the Second Electron in the Molecular Photocatalytic Reduction of CO2

the Ru-photosensitizer can be excited by the applied light. This results in high TOFs, but fast deactivation occurs, as the reaction mechanism can also proceed via the more unstable excited states of the Re-center. The light-initiated decomposition of the catalytic center leads to lower TONs for experiments with irradiation of 450 nm or 360 nm (Table S3). To manage repeatability in the photocatalytic experiments it was important to purify the BIH via recrystallization and ensure no air diffusing into the irradiated flasks.

The multinuclear catalysts **RuRe**, **RuRe2**, and **RuRe3** were tested in the photocatalytic CO_2 reduction to evaluate the impact of the amount of covalently linked rhenium-centers. During irradiation, all three catalysts show activity over long period of time in the production of CO, while possible side products like dihydrogen, formic acid or methane could not be detected via µGC- and ^{1}H-NMR-analysis. The catalyst solution was irradiated until the CO concentration in the gas phase of the reactor stayed constant. This value was used to calculate the TON, which is given either per system (multinuclear catalyst molecules or the systems **Ru + 3 Re**, **RuRe + 2 Re**, or **RuRe2 + Re**, respectively) (TON) or per catalytic center (TON_{Re}) as described in the following.

Concentration dependency

The reduction of CO_2 to CO is a two-electron process, whereas the OERS of Re is capable of solely transferring one electron at a time.[19] The elucidation of the exact CO_2 reduction mechanism with all incorporated intermediates is still discussed. Nonetheless, the main part of the interplay between supramolecular catalyst, TEOA, and BIH could be clarified.[19–20] In a first step, TEOA and one CO_2 molecule forms a carbonate ester adduct at the Re-center, which can be monitored by the stretching bands of the CO ligands.[21] After the excitation of Ru-PS and its reduction by BIH, the electron is relocated from the Ru-OERS towards the Re-catalyst site by fast intramolecular electron transfer. TEOA deprotonates the produced $BIH^{•+}$ to the radical $BI^•$, which in turn provides sufficient power to reduce the ground state of the supramolecular catalyst.[22] The subsequent reaction of the Re-OERS releasing a CO-molecule proceeds with a first-order rate.[20] Although the exact structure of the second intermediate remains unknown, possible sources for the second electron transfer are other electron donor molecules, corresponding BIH-intermediates or Ru-OERS in close proximity.[9,19,23] Furthermore, Re-centers, which are located in spatial vicinity, are also candidates for the donation of the second electron.[10,24] The intermolecular Re to Re electron transfer can be enabled by collision processes, leading to a strong catalyst concentration dependence with respect to the performance.[11b] In general, diluted experiments lower the probability of this direct encounter. Therefore, the lifetime of the OERS of the catalyst is extended and the possibility of decomposition by undesired side reactions is increased.[3a] Multiple Re(I)-centers incorporated in molecules, such as tris[(4'-methyl-2,2'-bipyridin-4-yl)methyl]carbinol-RuRe2,[11a] Re-Ru-Re,[4a] bpy₃Ph-RuRe2,[4c] or Ru-[bpyC₃bpyRe(CO)₃Cl]₃,[9] (bpy = 2,2'-bipyridine) have already

been synthesized to force spatial proximity of these catalytically active moieties. However, these complexes have never been tested with respect to their CO_2-reduction performance at low catalyst concentrations. This would provide information about the role of intramolecular interactions compared to intermolecular interplay between multiple catalyst molecules for an efficient two-step reduction process. In this context, the three multinuclear photocatalysts **RuRe**, **RuRe2**, and **RuRe3** synthesized in this work differ only in the number of covalently linked Re(I)-units per molecule. The literature-known 1,2-bis[4-(4'-methyl-2,2'-bipyridyl)]ethane linker (dmb-dmb) was chosen to minimize energetic interaction between the metal centers in the ground state and to enable the electron transfer originating from the Ru-OERS, thereby, ensuring comparability between theses supramolecules.[4a,8,15,25] The novel tetranuclear catalyst **RuRe3** was examined in a broad range of concentrations and compared with the photocatalytic performance of **RuRe**, **RuRe2**, and its single components **Ru + 3 Re** (Figure 4).

The concentration is illustrated as the amount of Re-units per volume to ensure an equitable consideration of the Re–Re-interaction, which is a key parameter for the catalytic performance.[10,26] As a consequence, 3 and 1.5 times the quantity of PS is present in the experiments of **RuRe** and **RuRe2**, respectively. Although the degeneration of the PS has been associated with the deterioration of the catalytic activity over time,[6c,12] the overall TON per molecule correlates with the number of Re-units. This was expected as more catalytically active centers per molecule are present and capable to convert CO_2. Therefore, **RuRe3** consistently achieves the highest TONs among all tested concentrations and catalysts, surpassing the benchmark photocatalyst **Ru2Re** (TON = 6038) in the concentration regime per Re-center above 5 µM.[4c] Furthermore, with a TON of 7582 **RuRe** attains the highest reported conversion number per Re-center (Figure 4 and Figure S9). All the results
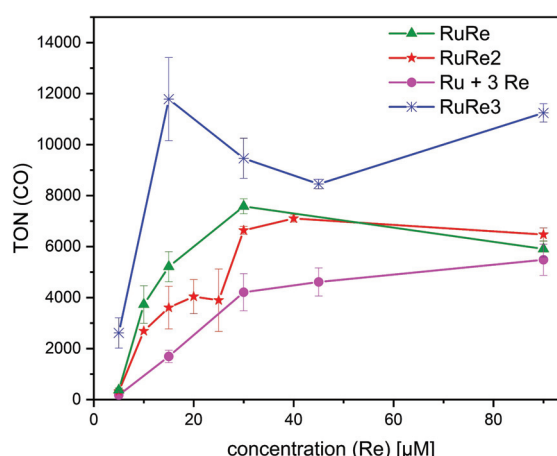
Figure 4. TON (CO) of the multinuclear catalysts **RuRe** (green), **RuRe2** (red), **RuRe3** (blue), and the model system **Ru + 3 Re** (magenta) at different concentrations of the Re-units. Turnovers were calculated based on the number of Ru-centers. BIH and catalyst containing CO_2-saturated DMF/TEOA (3.4/1) solutions were irradiated at 520 nm.

per Re-center are presented in Figure S9 as TON_{Re} function of the concentration (Re), whereby RuRe performs the best in higher concentrations. The maxima of the catalysts **RuRe** and **RuRe2** appear at similar Re-unit concentration regimes. This is attributed to the positive effect of intermolecular interactions between Re-centers.[10] The maximum conversion number of **RuRe3** is at slightly lower concentrations per Re-center of 15 μM, which is the first indication for superior intramolecular synergy.

In the case of **RuRe3**, **RuRe2**, and **RuRe** the assigned maxima correspond to a molecular concentration of 5 μM, 20 μM and 30 μM, respectively. As observed for all tested catalysts, a further increase of the molecular concentration does not result in higher TONs. On the one hand, this can be attributed to the CO_2 reduction step being rate-limiting for the catalytic cycle and no longer the second electron transfer.[22] The absence of a performance-improvement at increased concentrations could be explained by the inner filter effect, on the other hand.[10] At higher concentrations, the excitation can be the bottleneck of the overall process due to the attenuation of the light beam.[27] The consequent limitation of excited Ru(II)-centers causes a threshold of consecutive electron transfers to the Re(I)-catalysts and, as a result, also to the CO_2 molecules. These phenomena keep not only the turnover frequencies (TOFs) but also the TONs constant at a higher concentration, regardless of the assistive intermolecular communication.

In the diluted reactions, the conversion of all evaluated catalysts decreases, presumably because the probability of intermolecular interaction in this diffusion-controlled catalysis declines.[9–10] A second explanation is the minimized inner filter effect, whereby the Ru-PS are exposed to more irradiation at lower concentrations,[10] leading to an increased probability of side reactions, in particular the light-induced deactivation.[3a] Besides this Ru-Ru light protection, the shielding of Re-OERS

from overexcitation by the Ru-units weakens in diluted systems. These Re-OERS display absorption at 530 nm,[9] which is accessible by the applied light input, resulting in an undesired excitation of this reduced-species and the degradation of the catalytic unit.[3a] These aspects also occur in more concentrated solutions, but the deactivation processes are counteracted by the greater amount of metal centers.

One way to show the significance of the decreasing intermolecular interactions at lower concentrations is the comparison of the three catalysts RuRe, RuRe2, RuRe3, and the single components **Ru + 3 Re** at a Re-center concentration of 15 μM and 5 μM (Figure 5, **A**).

At the higher concentration level, all three catalysts are able to achieve large conversion numbers because an efficient intermolecular electron transfer is more to occur. As mentioned above, at a 5 μM Re-unit concentration the protecting inner filter effect and the collision frequency decreases. Therefore, the stability of the system and the probability of a second molecule as electron supplier declines.

For all three of the tested catalysts the lower concentration has a noteworthy negative effect on the performance, but while **RuRe**, **RuRe2**, and **Ru + 3 Re** drop 93%, 95%, and 89%, respectively, **RuRe3** decreases by 67%. For **Ru + 3 Re** and **RuRe** the results were expected since the second electron is unlikely to originate from the same molecule due to the single, solitary catalysis center. A second OER-species is assumed to be the electron source, which explains the diffusion limitation and the concentration dependency.[10,24a] Despite that an intramolecular mechanism would be conceivable for the **RuRe2** catalyst, the low performance indicates that intermolecular electron transfer is required for efficient CO_2 conversion. **RuRe3**, on the other hand, shows proportionally high TONs at an extremely low molecular concentration of 1.7 μM, which is attributed to an efficient intramolecular two-electron reduction process with
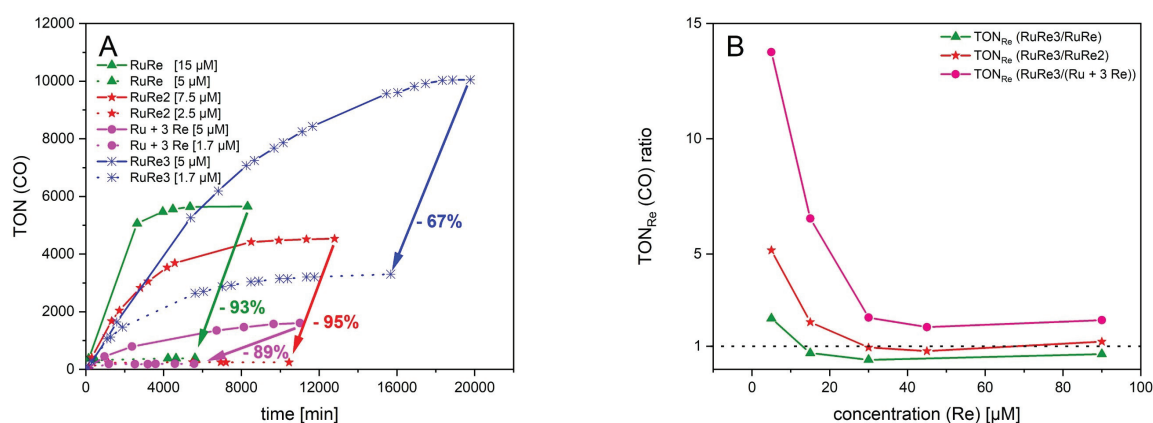
Figure 5. (**A**) Conversion (CO_2 to CO) vs time. plots of the three multinuclear catalysts **RuRe** (green), **RuRe2** (red), **RuRe3** (blue), and the building blocks **Ru + 3 Re** (magenta) at adjusted Re-center concentration and one third of this concentration, respectively. Turnover numbers were calculated based on the number of ruthenium metals. Irradiation was performed at 520 nm. (**B**) Concentration dependency of the relative TON_{Re} (per Re-center) of **RuRe3** with respect to the components **RuRe**, **RuRe2**, and **Ru + 3 Re**. The TON_{Re} ratio of the Re-centers in **RuRe3** to the Re-center of **RuRe** is depicted in green, the TON_{Re} ratio of the corresponding Re-centers of **RuRe3** and **RuRe2** is red, and the TON_{Re} ratio of the corresponding Re-centers of **RuRe3** and single components **Ru + 3 Re** is magenta. The concentration is interpreted as the amount of Re-centers and irradiation conditions were similar (DMF/TEOA 3.4/1, λ = 520 nm, BIH excess) for fair comparison.

three accessible catalytic units anchored. This result suggests a secondary role of the light-induced overexcitation to the intermolecular interaction, since otherwise the performance of **RuRe3** is expected to drop more than 90% at lower concentrations, too. Nonetheless, the 67% decrease from the 5 μM experiment indicates a significant requirement of an intermolecular interplay for a potent reduction mechanism of this tetranuclear molecule.

Regarding the TOF similar trends are observable, with strong negative effects on the diluted **Ru+3 Re**, **RuRe**, and **RuRe2** systems due to reduced intermolecular interactions (Table S3). On the other hand, **RuRe3** shows only small reductions of the TOF values at lower concentration of 1.7 μM, which is linked to an efficient catalytic process. Although the lifespan of the systems shortens at lower concentrations, which is explained by a decrease of the amount of the protective Ru-PS and therefore a diminishing inner filter effect, the diluted **RuRe3** system still exhibits conversion after 270 hours. It is assumed, that the efficient catalytic cycle of this tetranuclear molecule prevents side reactions, resulting in higher catalytic stability.

Furthermore, we compared **RuRe3** with **RuRe2**, **RuRe**, and **Ru+3 Re**, respectively, with regard to the number of Re-centers present (Figure 5, **B**) to evaluate the concentration-dependent effect on the performance of every single catalytic center (Re). The TON$_{Re}$ per every single Re(I) was calculated (SI Equation 7, Table S3) and put into relation with the other multinuclear catalysts.

As depicted, every Re-unit in **RuRe3** reaches higher conversion rates compared to the single components (**Ru+3 Re**) over all concentrations (Figure 5, **B**, magenta). Therefore, the tetranuclear catalyst shows not only enhanced catalytic performance per molecule, but also per Re-center. The catalytic units of the **RuRe2** and **RuRe** complexes exceed those of the **RuRe3** catalyst in concentration regime of 30 μM and above (Figure 5, **B**, red). It should be noted, that in this illustration the amount of Ru-PS in the **RuRe2** and **RuRe** setups is 1.5 and 3 times higher compared to the **RuRe3** experiments, respectively. As mentioned earlier, higher concentrations of photosensitizer are known to stabilize the photocatalytic system, which could explain the superiority of **RuRe** at increased concentrations.[6c,12,17]

At concentrations exceeding the 30 μM (Re-units) threshold all three curves depict a constant TON$_{Re}$ ratio of **RuRe3**/X, respectively. This result indicates similar concentration effects on Re-units independent of the structure and composition of the catalytic system in higher concentration ranges. We conclude, that above 30 μM the second electron supply via intermolecular electron transfer is not the rate-limiting step. Instead, upstream processes, i.e., the light absorption, the first electron transfer from the sacrificial electron donor or the coordination of CO$_2$ are assumed to primarily influence the catalytic cycle.[9–10,28] In contrast, a consistent trend in all ratios towards the superior **RuRe3** can be observed at lower concentration regimes. This further indicates that the structural features of **RuRe3** are especially advantageous in concentration ranges with a lower probability for intermolecular

interaction.[9,11b] As the overexcitation does not deteriorate one of these catalysts disproportionately, the superiority of **RuRe3** is ascribed to the forced proximity of three Re-units. This spatial vicinity ensures Re-Re communication and decreases the dependency on a second electron-donating molecule, leading to an efficient reduction mechanism.[9,26] Although **RuRe2** features two Re-centers in proximity, **RuRe3** offers the possibility for intermolecular synergy in three different Re–Re-combinations. Assuming that two Re-centers interact for the reduction process the third Re-moiety could remain in the ground state in **RuRe3**.

We hypothesize that this third Re-center could be capable of intercepting and absorbing additional and damaging excitation or electrons of the Ru-PS during the catalytic process. As consequence, the Ru-OERS is stabilized, leading to long-lived activity and high conversion numbers of the tetranuclear catalyst.

In summary, the experimental results of Figure 6 demonstrate, that forced spatial proximity of three reduction centers can stabilize the photocatalytically active molecule at low concentrations and minimize the relevance of intermolecular interactions for the two-electron reduction of CO$_2$.

To be able to compare the effect of the linkage and to ensure the same number of Re- and Ru-units, **RuRe3** at the concentration of 5 μM was recreated by its individual parts **Ru +3 Re**, **RuRe+2 Re** and **RuRe2+Re** (Figure 7). The concentration of 5 μM was chosen as **RuRe3** (depicted in blue) reaches a high TON (11800) while the reference molecule **RuRe** (depicted in green) deactivates after only 400 catalytic cycles. The individual moieties **Ru+3 Re** (depicted in magenta) achieve a TON$_{Re}$ of 655 per Re-center. The enhanced performance compared to the single molecule catalyst **RuRe** can, yet again, be explained by the higher concentration of Re-units and the resulting increased probability for intermolecular interaction.

When two Re-moieties are linked to **RuRe2** and one **Re** catalyst is added, this has a positive effect on the TON of the system, as it increases from 2693 (**RuRe2**) to 4014 (**RuRe2+Re**). Nonetheless, the TON$_{Re}$, calculated per Re-center, do not change by addition of the **Re** catalyst (Table S3). It is concluded that the electron transfer to the third mononuclear **Re** is inefficient due to the two Re-centers already linked directly to the Ru-PS.
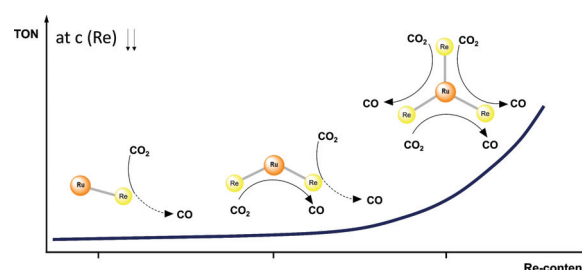
Figure 6. Schematic representation of TON vs. Re-content (dark blue line) at very low catalyst-unit (Re) concentrations of **RuRe**, **RuRe2**, or **RuRe3**. Illustration of the possible intramolecular Re-Re-interaction in the two-electron reduction process of CO$_2$ with solid and dotted lines.
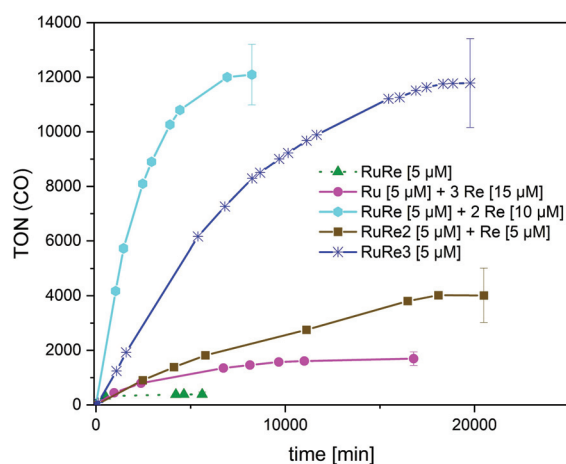
Figure 7. Conversion (CO_2 to CO) plots vs. time of **RuRe3** (blue) and the corresponding building blocks **Ru + 3 Re** (magenta), **RuRe + 2 Re** (cyan), **RuRe2 + Re** (brown) at a concentration of 5 μM in DMF. **RuRe** (green) at 5 μM was added as a model experiment for comparison. Turnovers were calculated based on the number of Ru-centers. Irradiation was performed at 520 nm.

Surprisingly, the system consisting of **RuRe + 2 Re** exceeds the TON_{Re} per Re of all identical comparison systems, including **RuRe3**. The two **Re** added to the main catalyst molecule **RuRe** cause a significant positive effect on the overall TON, beyond the expected influence due to increasing the number of catalytic centers. Synergistic cooperation between these molecules is assumed as mononuclear **Re** units are known for rapid deactivation with TONs below 100 in homogenous solution.[2,24a,29] In the **RuRe + 2 Re** composition each Re-center completes the catalytic cycle on average 4000 times, outperforming **RuRe** ($TON_{Re} = 386$) and **Ru + 3 Re** ($TON_{Re} = 564$) by far. This noteworthy improvement of the obtained conversions by the addition of **Re** units occurs primarily at the ratio of 1:2 (**RuRe/Re**).

Accordingly, testing a 1:1 and 1:3 ratio, the TON_{Re} obtained is 3214 and 1031, respectively. Even though more Re-centers increase spatial proximity further and therefore the probability of an efficient binuclear mechanism, there is an optimum concentration of **Re** for a synergistic effect between **RuRe** and **Re**. In diluted solutions with [**Re**] < 10 μM the quantity of small and mobile second-electron donors are too low, which results in an inefficient CO_2 reduction. On the contrary, higher concentrations ([**Re**] > 10 μM) might lead to an oversupply, which does not generate an improvement for the system and consequently decreases the considered TON_{Re}. This theory is supported by the fact that the addition of **Re** to **RuRe2** shows only a small positive effect on the conversion numbers. Accordingly, no photocatalytic enhancement is achieved by supporting **RuRe3** with **Re**. The Ru-center of these multinuclear catalysts is already surrounded by two (**RuRe2**) or three (**RuRe3**) electron-supplying Re-centers, respectively. The results indicate that both complexes already exhibit a sufficient number of

electron donors, which could explain the absence of a positive intermolecular cooperation by the addition of **Re**.

Concerning the high catalytic performance of **RuRe + 2 Re** in comparison to **RuRe**, **RuRe2**, and **RuRe3** molecules, it can be concluded, that the composition of Re/Ru-centers 3:1 represents an optimum, which shows the best performance per molecule or system at lower concentrations. The third Re-unit unbound or bound, thus produces synergistic effects beyond the expected proportional increase in TON.

Conclusion

In summary, we synthesized defined molecules with a catalyst-to-PS-unit ratio of one, two and three. The new catalyst **RuRe3** along with the literature known complexes **RuRe** and **RuRe2** were thoroughly investigated including their photophysical properties. As expected, the photophysical characteristics are predominantly similar with reference to the absorption and emission behavior, as well as the energy transfer in the ground and excited state. Further, we examined the photocatalytic CO_2 reduction performance of these three multinuclear complexes with regard to their concentration dependency. **RuRe3** attained the highest TON = 11800 reported for Ru(II)/Re(I)-supramolecules over a broad concentration range (5 μM ≤ c ≥ 50 μM). With respect to the conversion per Re-center, **RuRe** at 30 μM ($TON_{Re} = 7582$) outperformed all comparable systems to our best knowledge, which is associated with the high concentration of PS. At very low concentration ([Re] = 5 μM), the **RuRe3** molecule produces the highest conversion numbers, which is attributed to a fast intramolecular donation of the second electron. Moreover, the combination **RuRe + 2 Re** represents a very efficient system (TON = 12100) due to the addition of the mobile, mononuclear **Re** species acting as second electron supplier. Although BIH, BIH-intermediates and Ru-OERs were assumed to be vital part of the second electron provision, we were able to prove that Re-Re interactions play a key role for this still largely unexplored mechanism in molecular photocatalysis.[19] The second electron supply by either increasing the number of possible intramolecular pathways (**RuRe3**) or introducing small **Re** donors as delivery system strongly improves the efficiency of the reduction process, which leads to a more stable and powerful catalytic system. In this context, the ratio Re/Ru of 3 constitutes an optimum, which should be considered for future designs of supramolecules.

Experimental Section

Instrumentation and measurements

All air and moisture sensitive compounds were prepared using standard Schlenk techniques. Elemental analyses were performed on an Elementar Vario EL by the Laboratory for Microanalysis at the Institute of Inorganic Chemistry at the Technical University of Munich. ESI-MS spectra were recorded on a Varian ESI-MS 500 spectrometer in positive ionization mode (70 eV). The samples were dissolved in acetonitrile or methanol (LC-MS grade) and filtered

prior to the measurements. The recorded spectra were analyzed using the MS Data Review software. The gas phase composition in the reaction flask headspace during the photocatalytic reactions was analyzed with a Varian Micro 490-GC, equipped with a CO_x 1 m heated column at 80 °C column temperature, 200 kPa column pressure, auto detector sensitivity, 20 s sampling time and 300 s run time using helium (5.0) as a carrier gas. The parameters were chosen to ensure a complete and quantitative separation of potential hydrogen, nitrogen/air, CO, methane, and CO_2 in the sample. In addition to the micro-GC the gas phase composition of the reaction headspace was measured on a 8610C-GC from SRI Instruments Europe GmbH equipped with a methanizer, FID, RGD and a TCD detector, a MolSieve 13X and a silica gel column using helium (5.0) as carrier gas. The sample is injected onto the column at 50 °C and a temperature program is applied including 1.2 min temperature holding at 50 °C, heating to 100 °C with 10 °C min−1, temperature holding for 2.0 min, cooling to 50 °C with 50 °C min−1 and temperature holding for 5.0 min. The subsequent analysis over both columns and the chosen parameters provides complete and quantitative separation of potential hydrogen, nitrogen/air, CO, methane, and CO2 in the sample. The CO calibration proceeded via several reference ppm gases from Air Products GmbH for accurate quantification. FT-IR-spectra were recorded at room temperature on a Vertex-70 FT-IR spectrometer using a Platinum ATR from Bruker. The intensity of the signals is depicted as: light – l, medium – m and strong – s. Gas phase IR spectra were recorded with a ThermoScientific Nicolet 380-FT and the OMNIC™ Software. After 140 hours of irradiation under CO_2-pressure, 20 mL of the reaction gas phase were transferred to an evacuated gas IR cell (20 cm path length, KBr windows). Transmission spectra in the range of 4000-400 cm^{-1} were collected (64 scans, 0.241 cm^{-1} data spacing) for isotope labelling studies. ^{1}H-NMR spectra were recorded on a Bruker Ascend 400 MHz NMR-spectrometer at 400 MHz. All chemical shifts are given in parts per million (ppm) and referenced to the residual proton signal of the respective solvent. The NMR spectra were analyzed using the MestReNova software. Signal multiplicities are abbreviated as the following: s - singlet, m – multiplet. Microwave reactions were conducted in a reactor from CEM with a focused microwave beam. The syntheses were conducted at 50 W, a temperature of 125 °C and dynamic power supply. Emission spectra were recorded on an Edinburgh Instruments FS5 spectro-fluorometer with a 150 W CW ozone-free xenon arc lamp, Czerny-Turner design monochromators and a R928P photomultiplier emission detector. Excitation and emission spectra were recorded at room temperature in N,N-dimethylformamide in a QS 10x10 mm quartz cuvette from Hellma GmbH & Co. KG with 3 nm slit width, a dwell time of 0.2 s and a resolution of 1 nm. For time-resolved measurements a 373 nm laser diode with a bandwidth of approximately 5 nm and a pulse length of 65 ps was used. The total instrument response (i.e., maximum time-resolution) was approximately 70–80 ps. Each decay was measured over 5 μs. UV/Vis spectra were recorded on a PerkinElmer, Inc. Lambda 365 UV/Vis spectrophotometer. Spectra were measured from 250 nm to 950 nm with a spectral bandwidth of 1 nm and a scan rate of 300 nm min^{-1} at 25 °C. The samples were dissolved in N,N-dimethylformamide and analyzed in a QS 10×10 mm quartz glass cuvette from Hellma GmbH & Co. KG. A base line correction with the pure solvent was performed prior to sample measurements. Irradiation experiments were conducted in a darkened room and reaction flasks were protected from visible light irradiation by wrapping them in aluminum foil outside of the irradiation times to avoid light-induced deactivation processes. The amount of respective catalyst was weighed-in, dissolved in N,N-dimethylformamide (8.5 mL) and transferred to a Schlenk tube with known total volume and a constant volume of catalyst solution of 11 ml. After adding the electron donor 1,3-dimethyl-2-phenyl-2,3-dihydro-1H-

benzo[d]imidazole (BIH), as well as the base triethanolamine (TEOA) (2.5 mL), the reaction mixture was saturated with CO_2 (4.5) for 10 min by bubbling the gas into the stirred solution. The reaction flask was pressurized with CO_2 to receive an overpressure of 1.45 bar and sealed with a septum. For the photocatalytic experiments, the prepared samples are placed in front of eight green light-emitting diodes (λ = 520 ± 30 nm) of the type LXZ1-PM01 from Lumileds, supplied by roughly 23 V and 60 mA with a radiometric power of 100 mW per LED. The gas phase composition in the reaction flask headspace is analyzed via μ-GC or GC in regular time intervals. To validate the received turnover numbers (TONs) all experiments are repeated at least twice for each catalyst and are listed in Table S3.

Materials

Solvents were dried with the solvent purification system MB SPS-800 from MBraun or over activated alumina and stored over molecular sieve (3 or 4 Å). The gases argon (99.996 vol.–%), CO_2 (4.5), and He (5.0) were provided from Westfalen. Deuterated solvents were purchased from Sigma-Aldrich and dried over activated 3 Å molecular sieve. Unless otherwise stated, all chemicals were purchased from Sigma-Aldrich, ABCR GmbH or TCI Chemicals and used without further purification. The complex [Re-(dmb)(CO)$_3$Cl] (**Re**) was synthesized according to the published procedures from Rieger et al.,[4a] [Re(CO)$_3$Cl(dmb-dmb)] (**Re(dmb-dmb)**) was prepared as previously described by Guarr et al.[15]

Syntheses

1,2-bis[4-(4'-methyl-2,2'-bipyridyl)]ethane (dmb-dmb): The product was prepared by following a modified method from Blaney et al.[30] To a solution of diisopropylamine (3.06 mL, 21.7 mmol, 1.0 eq.) in THF (100 mL), n-butyllithium (2.5 M in hexanes, 8.7 mL, 21.7 mmol, 1.0 eq.) was added at −20 °C. After cooling to −78 °C, a solution of 4,4'-dimethyl-2,2'-bipyridine (dmb) (4.02 g, 21.7 mmol, 1.0 eq.) in THF (200 mL) was added over the course of 25 min. The solution was stirred for 1 h at −78 °C and for another 30 min at −10 °C. After cooling to −78 °C again, 1,2-dibromoethane (3.95 mL, 45.6 mmol, 2.1 eq.) was added and the solution was stirred for 5 min. The suspension was warmed to room temperature and stirred for 3 h at 25 °C. After the addition of deionized H_2O (100 ml) the solution was stirred overnight and extracted with diethylether (4×100 ml) and dichloromethane (3×100 ml). The organic phases were combined and the solvent was evaporated under reduced pressure to yield a white powder. Recrystallization from ethyl acetate afforded color-less crystals of dmb-dmb (2.85 g, 7.77 mmol, 74% yield). ^{1}H NMR (400 MHz, CDCl$_3$): δ = 8.56 (m, 4 H, Ar–H), 8.39-8.32 (s, 2 H, Ar–H), 8.26 (s, 2 H, Ar–H), 7.20–7.10 (m, 4 H, Ar–H), 3.11 (m, 4 H, CH$_2$), 2.45 ppm (s, 6 H, CH$_3$); IR (CO): $\tilde{v}$ = 2016 (m), 1882 (m), 1628 (m), 1592 (m) cm^{-1}; UV/Vis (DMF): λ_{max} = 290, 250, 232 nm; ESI-MS (CH$_3$CN): m/z (%) = 367.5 ([M+H]$^+$).

Ru(dmb)$_2$Cl$_2$ (**Cl$_2$Ru**): The product was synthesized according to a published procedure.[4a] Under an inert gas atmosphere, [Ru-(cod)Cl$_2$]$_n$ (76.1 mg, 27.2 μmol, 1.0 eq.), LiCl (98.9 mg, 2.33 mmol, 8.6 eq.) and dmb (100 mg, 54.3 μmol, 2.0 eq.) were suspended in dry N,N-dimethylformamide (20 ml), degassed, and heated in a closed vessel setup in a microwave reactor (125 °C, 50 W, dynamic mode, 2 h). After cooling to room temperature, the reaction mixture was filtered through a syringe filter and the solvent was removed under reduced pressure. The residue was suspended in water, filtered over a fine frit (Por. 4) and washed with a solution of water and acetonitrile (9/1, 100 ml). The crude product was eluted from the frit with chloroform and the solvent was removed under reduced pressure. Recrystallization of the crude product in

The Puzzling Question about the Origin of the Second Electron in the Molecular Photocatalytic Reduction of CO2

ChemCatChem

Research Article
doi.org/10.1002/cctc.202200841

Chemistry
Europe
European Chemical
Societies Publishing

acetonitrile (10 mL) yielded Ru(dmb)$_2$Cl$_2$ (60.5 mg, 11.2 μmol, 41%) as a purple to black powder. IR (CO): $\tilde{v}$ = 2918 (m), 2850 (l), 1616 (l), 1474 (m) cm^{-1}; UV/Vis (DMF): λ_{max} = 567, 384 nm; ESI-MS (CH$_3$CN): m/z (%) = 541.5 ([M + H]$^+$).

[Ru(dmb)$_3$](PF$_6$)$_2$ (**Ru**): The product was prepared according to a method from Blaney et al.[30] [Ru(cod)Cl$_2$]$_n$ (50.0 mg, 180 μmol, 1.0 eq.) was suspended in dry N,N-dimethylformamide (30 ml), dmb (100 mg, 540 μmol, 3.0 eq.) was added, degassed, and the suspension was heated in a closed vessel setup in a microwave reactor (125°C, 50 W, dynamic mode, 2 h). The reaction mixture was transferred to a flask, deionized H$_2$O (30 mL) was added, and the solution was stirred in an oil bath at 100°C for 6.5 h. After cooling to room temperature and passing the solution through a syringe filter, the solvent was evaporated under reduced pressure. The brown solid was dissolved in deionized H$_2$O (20 ml) and a solution of NH$_4$PF$_6$ (750 mg, 2.61 mmol, 25 eq.) in water (20 ml) was added. The precipitate was filtered over a fine frit (Por. 4) and washed with deionized H$_2$O (2 × 25 mL) and diethyl ether (3 × 25 mL). The solid was dried under vacuum to yield a red powder (161 mg, 171 mmol, 94% yield). ^{1}H NMR (400 MHz, CD$_3$CN) δ = (m, 6H, Ar–H), 7.51 (m, 6 H, Ar–H), 7.20 (m, 6 H, Ar–H), 2.51 ppm (s, 18 H CH$_3$); IR (CO): $\tilde{v}$ = 1617 (l), 1476 (l), 1424 (m) cm^{-1}; UV/Vis (DMF): λ_{max} = 290, 465 nm; PL (DMF): λ_{max} = 640 nm; ESI-MS (CH$_3$CN): m/z (%) = 327.3 [M-2 PF$_6$]$^{2+}$, 799 [M-PF$_6$]$^+$.

[Ru(dmb)$_2$(dmb-dmb)Re(CO)$_3$Cl]Cl$_2$ (**RuRe**): The product was prepared according to a modified method from Rieger et al.[4a] **Cl$_2$Ru** (56.4 mg, 104 μmol, 1.0 eq.) and **Re**(dmb-dmb) (70.0 mg, 104 μmol, 1.0 eq.) were dissolved in dry methanol (15 mL). The dark-violet solution was refluxed at 60°C for 70 h until a color change to a red solution was observed. The solution was allowed to cool to room temperature, and the solvent was removed under reduced pressure. The remaining red solid was washed with diethyl ether (3 × 30 mL) and acetone (3 × 30 mL) and finally dried to yield a rust-red solid (39.0 mg, 32.2 μmol, 31%). ^{1}H NMR (400 MHz, CD$_3$CN): δ = 8.82 (m,6 H, Ar–H), 8.40 (m, 4 H, Ar–H), 741 (m, 14 H, Ar–H), 3.29 (m, 4 H, CH$_2$), 2.49 ppm (m, 18 H, CH$_3$); IR (CO): $\tilde{v}$ = 2014 (m), 1904 (s), 1879 (s) cm^{-1}; UV/Vis (DMF): λ_{max} = 290, 365, 463 nm; PL (DMF): λ_{max} = 639 nm; ESI-MS (CH$_3$CN): m/z (%) = 570.6 [M-2 Cl]$^{2+}$.

[Re(CO)$_3$Cl(dmb-dmb)RuCl$_2$(dmb-dmb)Re(CO)$_3$Cl] (**Cl$_2$RuRe2**): The product was synthesized by following a modified method from Rieger et al.[4a] [Ru(cod)Cl$_2$]$_n$ (9.92 mg, 35.3 μmol, 1.0 eq.) and **Re**-(dmb-dmb) (35.6 mg, 53.0 mmol, 1.5 eq.) were suspended in dry DMF (10 mL), degassed, and heated in a closed vessel setup in a microwave reactor (125°C, 50 W, dynamic mode, 2 h). After cooling to room temperature, the solution was passed through a syringe filter and the solvent was removed under reduced pressure. The residue was washed with diethyl ether (3 × 30 mL) as well as acetone (2 × 20 ml) and dried under reduced pressure to yield a purple powder (30.1 mg, 19.8 μmol, 55%). IR (CO): $\tilde{v}$ = 2021 (s), 1886 (s) cm^{-1}; UV/Vis (DMF): λ_{max} = 569, 374, 290 nm; PL (DMF): λ_{max} = 673 nm; ESI-MS (CH$_3$CN): m/z (%) = 1481.2 [M−Cl]$^+$, 1517.8 [M + H]$^+$; elemental analysis calcd (%) for C$_{54}$H$_{44}$Cl$_4$N$_8$O$_6$Re$_2$Ru: C 42.78, H 2.93, N 7.39, found: C 42.44, H 3.70, N 7.39.

[Re(CO)$_3$Cl(dmb-dmb)(dmb)Ru(dmb-dmb)Re(CO)$_3$Cl] (**RuRe2**):The product was synthesized by following a modified method from Rieger et al.[4a] **Cl$_2$RuRe2** (32.4 mg, 21.3 μmol, 1.0 eq.) and dmb (7.91 mg, 43.0 μmol, 2.0 eq.) were dissolved in a mixture of MeOH/DMF (1/1, 20 mL) and heated to 65°C for 3 d under the exclusion of light. After cooling to room temperature, the solvent was removed under reduced pressure, and the resulting orange solid was dissolved in acetonitrile (9 mL). The solution was passed through a syringe filter and transferred into a flask containing toluene (200 mL). Cooling the solution to 0°C for 1 h afforded an orange precipitate, which was collected by filtration over a fine frit (Por. 4),

washed with toluene (3 × 5 mL), and eluted from the frit with acetonitrile. The addition of deionized H$_2$O (45 ml) caused slight precipitation of the complex, and subsequently acetonitrile was added until a clear orange solution remained. The solvent was evaporated under reduced pressure and the orange precipitate was collected by centrifugation and dissolved in acetonitrile. After evaporation of the solvent under reduced pressure and drying under vacuum an orange powder (14.1 mg, 8.65 μmol, 41%) is obtained. ^{1}H NMR (400 MHz, CD$_3$CN): δ = 8.85–8.67 (m, 4 H, Ar–H), 8.32–8.06 (m, 10 H, Ar–H), 7.22 (m, 16 H, Ar–H), 3.19 (m, 8 H, CH$_2$), 2.63–2.28 ppm (m, 18 H, CH$_3$); IR (CO): $\tilde{v}$ = 2019 (s), 1882 (s) cm^{-1}; UV/Vis (DMF): λ_{max} = 463, 363, 293 nm; PL (DMF): λ_{max} = 643 nm; ESI-MS (CH$_3$CN): m/z (%) = 815.7 ([M−2 Cl]$^{2+}$).

[Ru(Re(CO)$_3$Cl(dmb-dmb))$_3$]Cl$_2$ (**RuRe3**): [Ru(cod)Cl$_2$]$_n$ (14.6 mg, 52.1 μmol, 1.0 eq.) and **Re**(dmb-dmb) (123 mg, 183 μmol, 3.5 eq.) were suspended in anhydrous methanol (10 mL). The yellow suspension consisting of a dark-brown solid was degassed and heated in a microwave reactor (125°C, 50 W, dynamic mode, 2 h). The red-orange solution was allowed to cool to room temperature, passed through a syringe filter, and the solvent was removed under reduced pressure. The remaining solid was washed with diethyl ether (3 × 20 mL) and acetone (3 × 20 mL) and dried in vacuum to yield **RuRe3** as a red solid (85.1 mg, 38.6 μmol, 74%). ^{1}H NMR (400 MHz, DMF-d$_7$): δ = 9.03 (m, 18 H, Ar–H), 7.62 (m, 18 H, Ar–H), 3.42 (m, 12 H, CH$_2$), 2.59 ppm (m, 18 H, CH$_3$); IR (CO): $\tilde{v}$ = 2015 (s), 1904 (m), 1878 (s) cm^{-1}; UV/Vis (DMF): λ_{max} = 463, 364, 299 nm; PL (DMF): λ_{max} = 638 nm; ESI-MS (MeOH): m/z (%) = 1058.6 ([M−2Cl]$^{2+}$); elemental analysis calcd (%) for C$_{81}$H$_{66}$Cl$_3$N$_{12}$O$_9$Re$_3$RuCl$_2$: C 44.46, H 3.04, N 7.68, found: C 44.71, H 3.26, N 7.63.

Conflict of Interest

The authors declare no conflict of interest.
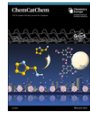
[1] U. Berardi, *Resour. Conserv. Recycl.* **2017**, *123*, 230–241.
[2] J. Hawecker, J.-M. Lehn, R. Ziessel, *J. Chem. Soc. Chem. Commun.* **1983**, 536–538.
[3] a) S. Meister, R. O. Reithmeier, M. Tschurl, U. Heiz, B. Rieger, *ChemCatChem* **2015**, *7*, 690–697; b) M. Pschenitza, S. Meister, A. von Weber, A. Kartouzian, U. Heiz, B. Rieger, *ChemCatChem* **2016**, *8*, 2688–2695.
[4] a) S. Meister, R. O. Reithmeier, A. Ogrodnik, B. Rieger, *ChemCatChem* **2015**, *7*, 3562–3569; b) Y. Tamaki, K. Watanabe, K. Koike, H. Inoue, T.

The Puzzling Question about the Origin of the Second Electron in the Molecular Photocatalytic Reduction of CO2

ChemCatChem | Research Article
doi.org/10.1002/cctc.202200841

Chemistry
Europe
European Chemical
Societies Publishing

Morimoto, O. Ishitani, *Faraday Discuss.* **2012**, *155*, 115–127; c) A. M. Cancelliere, F. Puntoriero, S. Serroni, S. Campagna, Y. Tamaki, D. Saito, O. Ishitani, *Chem. Sci.* **2020**, *11*, 1556–1563.

[5] Y. Tamaki, O. Ishitani, *ACS Catal.* **2017**, *7*, 3394–3409.

[6] a) Y. Tamaki, K. Koike, T. Morimoto, O. Ishitani, *J. Catal.* **2013**, *304*, 22–28; b) Y. Tamaki, K. Koike, O. Ishitani, *Chem. Sci.* **2015**, *6*, 7213–7221; c) P. M. Stanley, C. Thomas, E. Thyrhaug, A. Urstoeger, M. Schuster, J. Hauer, B. Rieger, J. Warnan, R. A. Fischer, *ACS Catal.* **2021**, *11*, 871–882.

[7] K. Ohkubo, Y. Yamazaki, T. Nakashima, Y. Tamaki, K. Koike, O. Ishitani, *J. Catal.* **2016**, *343*, 278–289.

[8] Z.-Y. Bian, S.-M. Chi, L. Li, W. Fu, *Dalton Trans.* **2010**, *39*, 7884–7887.

[9] B. Gholamkhass, H. Mametsuka, K. Koike, T. Tanabe, M. Furue, O. Ishitani, *Inorg. Chem.* **2005**, *44*, 2326–2336.

[10] C. Bruckmeier, M. W. Lehenmeier, R. Reithmeier, B. Rieger, J. Herranz, C. Kavakli, *Dalton Trans.* **2012**, *41*, 5026–5037.

[11] a) Z.-Y. Bian, K. Sumi, M. Furue, S. Sato, K. Koike, O. Ishitani, *Dalton Trans.* **2009**, 983–993; b) H. Takeda, O. Ishitani, *Coord. Chem. Rev.* **2010**, *254*, 346–354.

[12] A. Umemoto, Y. Yamazaki, D. Saito, Y. Tamaki, O. Ishitani, *Bull. Chem. Soc. Jpn.* **2020**, *93*, 127–137.

[13] J. D. Bartl, C. Thomas, A. Henning, M. F. Ober, G. Savasci, B. Yazdanshenas, P. S. Deimel, E. Magnano, F. Bondino, P. Zeller, L. Gregoratti, M. Amati, C. Paulus, F. Allegretti, A. Cattani-Scholz, J. V. Barth, C. Ochsenfeld, D. Nickel, I. D. Sharp, M. Stutzmann, B. Rieger, *J. Am. Chem. Soc.* **2021**, *143*, 19505–19516.

[14] a) Z.-Y. Bian, H. Wang, W.-F. Fu, L. Li, A.-Z. Ding, *Polyhedron* **2012**, *32*, 78–85; b) Y. Tamaki, T. Morimoto, K. Koike, O. Ishitani, *PNAS* **2012**, *109*, 15673–15678.

[15] S. Van Wallendael, R. J. Shaver, D. P. Rillema, B. J. Yoblinski, M. Stathis, T. F. Guarr, *Inorg. Chem.* **1990**, *29*, 1761–1767.

[16] a) Y. Yamazaki, J. Rohacova, K. Koike, O. Ishitani, *JACS Au* **2021**, *1*, 294–307; b) Y. Yamazaki, O. Ishitani, *Chem. Sci.* **2018**, *9*, 1031–1041.

[17] A. S. Maier, C. Thomas, M. Kränzlein, T. M. Pehl, B. Rieger, *Macromolecules* **2022**.

[18] M. Furue, M. Naiki, Y. Kanematsu, T. Kushida, M. Kamachi, *Coord. Chem. Rev.* **1991**, *111*, 221–226.

[19] Y. Kuramochi, O. Ishitani, H. Ishida, *Coord. Chem. Rev.* **2018**, *373*, 333–356.

[20] K. Kamogawa, Y. Shimoda, K. Miyata, K. Onda, Y. Yamazaki, Y. Tamaki, O. Ishitani, *Chem. Sci.* **2021**, *12*, 9682–9693.

[21] T. Morimoto, T. Nakajima, S. Sawa, R. Nakanishi, D. Imori, O. Ishitani, *J. Am. Chem. Soc.* **2013**, *135*, 16825–16828.

[22] Y. Yamazaki, K. Ohkubo, D. Saito, T. Yatsu, Y. Tamaki, S. I. Tanaka, K. Koike, K. Onda, O. Ishitani, *Inorg. Chem.* **2019**, *58*, 11480–11492.

[23] Y. Kou, Y. Nabetani, D. Masui, T. Shimada, S. Takagi, H. Tachibana, H. Inoue, *J. Am. Chem. Soc.* **2014**, *136*, 6021–6030.

[24] a) H. Takeda, K. Koike, H. Inoue, O. Ishitani, *J. Am. Chem. Soc.* **2008**, *130*, 2023–2031; b) P. Lang, R. Giereth, S. Tschierlei, M. Schwalbe, *Chem. Commun.* **2019**, *55*, 600–603.

[25] K. Koike, S. Naito, S. Sato, Y. Tamaki, O. Ishitani, *J. Photochem. Photobiol. A.* **2009**, *207*, 109–114.

[26] R. Giereth, P. Lang, E. McQueen, X. Meißner, B. Braun-Cula, C. Marchfelder, M. Obermeier, M. Schwalbe, S. Tschierlei, *ACS Catal.* **2021**, *11*, 390–403.

[27] S. Kumar Panigrahi, A. Kumar Mishra, *J. Photochem. Photobiol. C* **2019**, *41*, 100318.

[28] a) B. Kumar, M. Llorente, J. Froehlich, T. Dang, A. Sathrum, C. P. Kubiak, *Annu. Rev. Phys. Chem.* **2012**, *63*, 541–569; b) G. Sahara, O. Ishitani, *Inorg. Chem.* **2015**, *54*, 5096–5104.

[29] a) K.-H. Chen, N. Wang, Z.-W. Yang, S.-M. Xia, L.-N. He, *ChemSusChem* **2020**, *13*, 6284–6289; b) M. Pschenitza, S. Meister, B. Rieger, *Chem. Commun.* **2018**, *54*, 3323–3326.

[30] C. M. Elliott, R. A. Freitag, D. D. Blaney, *J. Am. Chem. Soc.* **1985**, *107*, 4647–4655.

6.4   Reprint Permission Copyrighted Content

Thank you for your order!

Dear Christopher Thomas,

Thank you for placing your order through Copyright Clearance Center's RightsLink® service.

Order Summary

Licensee: Technical University of Munich
Order Date: Oct 23, 2022
Order Number:5414700872922
Publication: ChemCatChem
Title: The Puzzling Question about the Origin of the Second Electron in the Molecular Photocatalytic Reduction of CO2
Type of Use: Dissertation/Thesis
Order Total: 0.00 USD

View or print complete details of your order and the publisher's terms and conditions.

Sincerely,

Copyright Clearance Center

Tel: +1-855-239-3415 / +1-978-646-2777
customercare@copyright.com
https://myaccount.copyright.com

CCC   RightsLink

7.   Summary and Outlook

Based on the work by *Gafney* and *Adamson*, *Lehn et al.* were able to construct a molecular photocatalytic system on a Re(I)-basis for the reduction of CO_2 in the early 1980's. [9, 64] Through continuous further development, especially by the group around *Osamu Ishitani*, the catalysts could be designed to be more stable, the electron donors became more specialised, and the reduction process improved in efficiency.[10a, 75b, 78, 84, 85b] In order to learn more about the mechanistic background, the electron transfer and the deactivation processes, *Rieger et al.* investigated the inter- and intramolecular interactions of the metal centres in this two-electron process.[66a] The insights gained into the binuclear mechanism enabled a multinuclear catalyst consisting of a Ru(II)-photosensitiser linked to two Re(I)-reduction sites, which achieved the highest turnover number to date.[85a] In addition, two undesired side reactions leading to decomposition of the active catalyst were identified.[10b] Both of these deactivation pathways start from the OERS after excitation and the first electron transfer to the Re(I)-catalyst. Further excitation of these radical species can lead to decomposition and deactivation of the catalyst. However, since all processes after the initial excitation can take place in the dark, these insights were used to increase the stability of the system with pulsed radiation, which excites the metal centre once at the beginning of the catalysis cycle.[82] As a second deactivation mechanism, side reactions with radical intermediates of the electron donors were found.[10b] For this reason, it is important to keep the concentration of these radicals low. This was realised by using an auxiliary base instead of the electron donor to adjust the pH-value.[80] With this transparent and weakly nucleophilic base, the concentration of the electron donor, which additionally acts as a base, can be significantly reduced. Both the turnover number and the activity were increased by this substitution.[80]

Despite all these improvements, Re(I)-catalysts still only achieve turnover numbers in the low double digits and require organic electron donors, which are consumed.[10a] In order to replace sacrificial donors and to obtain more stable Re(I)-catalysts, a new principle for the fixation of (metal)organic molecules on semiconductor surfaces was developed, implemented, and investigated in this work.[103c] The modular approach presented here has the advantage of being extremely flexible, which means that a wide variety of support materials can be linked to almost any catalyst. The surface of the materials is first coated with aluminium oxide via atomic layer deposition (ALD). In the subsequent step, organic linkers or directly the target molecules are linked to the AlO_x-layer via immersion. Any catalytically active molecule with a carboxylic acid unit can be attached to these anchors via simple organic synthesis. The individual steps mentioned above enable a universal applicability of this methodology, which can be transferred to all substrates on which aluminium oxide growth is possible. The thickness of the deposited film can be precisely controlled from 3 nm to about 0.3 nm, which opens the possibility to

control the electrical conductivity between semiconductor and catalyst. The AlO_x-layer not only changes the physical properties, but also serves as a passivation agent surface defects and creates a closed and stable coating. In addition, the chemical properties are changed, which enables simple phosphonic acid surface chemistry under standard conditions. Hence, all (metal)organic molecules or linkers can be selectively attached via the phosphonic acid groups onto the matrix. The resulting linkage between semiconductor and anchor molecules opens the possibility to covalently bind almost any molecule to the surface with sub-nanometer precision via their coupling functionalities. As a feasibility study, 1 cm × 1 cm two-dimensional silicon semiconductors were coated with an aluminium oxide layer in this work. Two saturated carbon chains of different lengths were then deposited with either C_6- or C_{11}-phosphonic acid linkers and the surface layer was examined for roughness using atomic force microscopy (AFM). The C_{11}-linkers achieve a more even structure because the longer carbon chains are positioned next to each other in a more sorted manner and less disorder is created. Re(I)-complexes can then be covalently bonded to the hydroxyl group at the head end via mild *Steglich*-esterification, which was detected via attenuated total reflection *Fourier*-transform-infrared-spectrometry (ATR-FTIR). This linkage of the hybrid to the metal complex further mitigates the roughness of the surface. This was attributed to the intermolecular π-π-interactions of the bipyridines of the Re(I)-complex by X-ray reflectometry (XRR) and near edge X-ray absorption fine structure (NEXAFS) (Figure 14). The deposited photocatalysts show strong intermolecular vibrational interaction and electronic coupling, as demonstrated by infrared (IR), photoluminescence (PL) and X-ray photoelectron spectroscopy (XPS). Large differences could be detected in the intermolecular interactions between free complexes and the complexes fixed on the surface. Bound to the semiconductor, there is even a charge transfer between the Re(I)-metal centres, which could be identified by XPS measurements and was confirmed by ATR-FTIR spectra. These correlations could not be influenced by changing the phosphonic acid linkers and the AlO_x-layer thickness, suggesting that this phenomenon only occurs through intermolecular interactions.
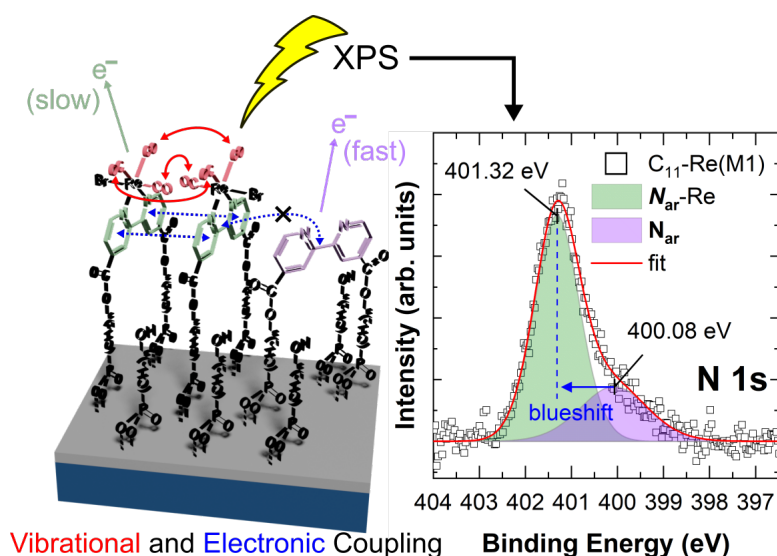
Figure 14: Graphical abstract of the publication entitled: "Modular Assembly of Vibrationally and Electronically Coupled Rhenium Bipyridine Carbonyl Complexes on Silicon". This is presented in chapter 4. The phosphonic acid linkers (black) are attached to the Si-semiconductor surface (blue), which is coated with AlO$_x$ (grey). Bipyridine ligands (purple) or Re(I)-metal complexes (black and red) are connected to linkers via a carboxylic acid ester bridge. In addition, the interactions between the bipyridines of the Re(I)-complexes are indicated, which were identified via XPS measurements.[103c] Reprinted with permission from Ref. [103c]. Copyright 2021 American Chemical Society.

The selectivity of the presented modular approach was demonstrated by an induced surface structure (Figure 15). The silicon semiconductor was coated with AlO$_x$ in stripes using a polymer mask and then loaded with linker and metal complex according to the scheme described above. Subsequently, scanning photoelectron microscopy (SPEM) was used to search the surface for the binding energy of Re 4f. Only at sites where AlO$_x$ was applied did the phosphonic acid anchors bind, which is why Re(I)-complexes were only found there. In the stripes where silicon was not coated, no spacer could bind due to the low reactivity of phosphonic acid groups towards silicon and thus no Re-catalyst could be applied. This can be used in future approaches to introduce other molecules with synergetic effects onto the unloaded silicon in a targeted, site-dependent manner. This is feasible, for example, via silane chemistry or aryldiazonium-cation reduction.[131]

Summary and Outlook
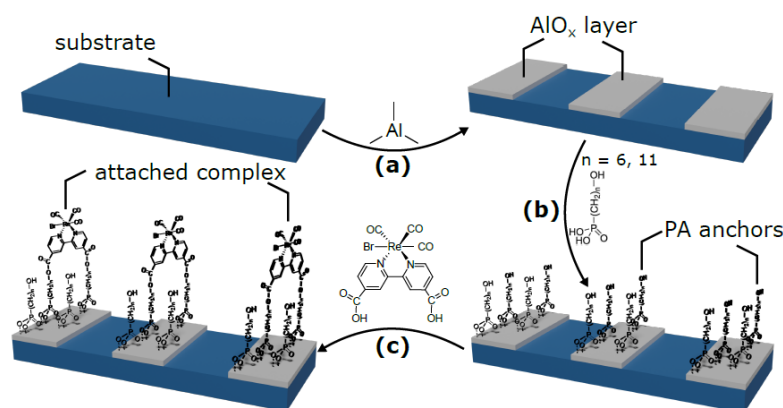
Figure 15: Schematic representation of the modular approach: a) The substrate (Si) is selectively coated with an aluminium oxide layer (grey) (approx. 0.3 to 3 nm) via ALD in strips with the aid of a polymer mask. b) The phosphonic acid linkers are applied by immersion and bind site-selectively to AlO_x on the structured surface. c) In the last step, the metal complex Re(2,2′-bipyridine-4,4′-dicarboxylic acid)(CO)$_3$Br is connected to the linker via a *Steglich*-esterification and thus fixed on the surface.[103c] Reprinted with permission from Ref. [103c]. Copyright 2021 American Chemical Society.

In summary, this approach combines the passivation of surface defects with targeted functionalisation. It can be applied to a large number of semiconductors in the future and enables the production of well-defined hybrid materials that can be used in a wide variety of fields. For CO_2 reduction, a hybrid of GaN and Re(I)-photocatalysts is promising due to the photon conductivity of GaN. It has already been shown that this approach also works for this semiconductor and achieves results comparable to silicon. Due to the flexibility of this modular hybrid synthesis, future application possibilities are broad. Photoelectrochemical applications, photovoltaics or even a wide variety of sensors can be realised with this approach, making it a new tool in the synthesis of hybrid systems.[85b, 106a, 112d, 132]

A second approach to increase the activity and thus the performance of Re(I)-based photocatalysts is based on the already mentioned studies by *Rieger et al.* regarding the availability of several active centres.[66a, 85a] In this work, it was shown that spatial proximity should be imposed via covalent bonds in such a way that several OERS can interact to enforce a more efficient bimetallic mechanism. These results in combination with the knowledge of the positive influence of Ru(II)-photosensitisers on the stability of multinuclear complexes, led to the idea of using polymer strands as macroligands. Subsequently, different ratios of Re(I)-photocatalysts and Ru(II)-photosensitisers were subjected to this bipyridine-based backbone, which was investigated in the photocatalytic reduction of CO_2.

In the first step, bipyridine-based monomers were synthesised, which in the later polymer offer the shortest, non-conjugated linkage between the metal centres in order to ensure electronic interaction in the excited state.[97b] This 4-vinyl-4′-methyl-2,2′-bipyridine was obtained in a highly pure form using sublimation and hence making it applicable for catalytic polymerisation

Summary and Outlook

for the first time. Different sterically hindered, frustrated *Lewis* pairs consisting of combinations of phosphines and aluminium compounds were screened as polymerisation catalysts. Al(i-Bu)$_3$ was used as the *Lewis* acid and PMe$_3$ as the *Lewis* base in a 2:1 ratio to achieve high conversion in monomodal polymers (Scheme 10). The system of choice allowed the monomer to be converted to a polymer with a narrow molecular weight distribution and high initiator efficiency ($Đ$ = 1.31-1.36, I.E. = 45-51%).
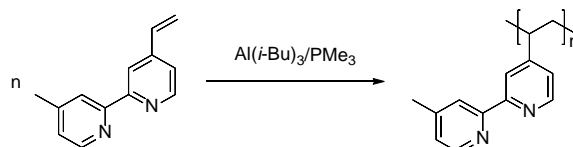
Scheme 10: Schematic representation of the catalytic polymerisation of 4-vinyl-4′-methyl-2,2′-bipyridine with an aluminium-based *Lewis* acid and a phosphorus-based *Lewis* base.

Using end-group analysis, two pathways of initiation could be identified, which start either by deprotonation or conjugated addition. However, these two pathways are controllable to produce the desired monomodal polymers with a narrow molecular mass distribution. The decomposition onset temperatures of the resulting polymer is 368 °C. Dynamic differential calorimetry was used to determine the glass transition temperature at 142 °C. It was also found that the polymer has no melting point, indicating an amorphous character. These catalytically polymerised bipyridine-based monomers thus provide defined polymers, which are to be loaded with photocatalytically active metal centres in the subsequent steps.

For this purpose, two successive synthesis protocols were developed with the precursor molecules Re(CO)$_5$Cl and Ru(dmb)$_2$Cl$_2$, by which the polymer is loaded, purified, and subsequently isolated. The loading quantity can be controlled qualitatively and easily via the added amount of the respective precursor (Scheme 11).
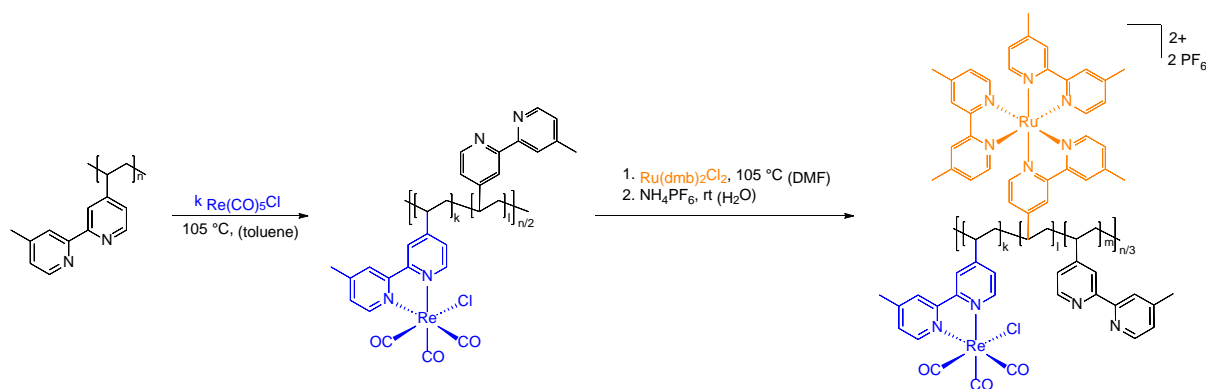
Scheme 11: Loading steps for the preparation of the photocatalytically active polymers PVBpy$^{Re/Ru}$. The first step is carried out by complexing the unloaded polymer with Re(CO)$_5$Cl. In the second step, the molecule Ru(dmb)$_2$Cl$_2$ is attached to some of the free bipyridines before the resulting polymer undergoes salt-induced precipitation with NH$_4$PF$_6$.[133] Reprinted with permission from Ref. [133]. Copyright 2022 American Chemical Society.

Summary and Outlook

Four different polymers with theoretical Re(I)/Ru(II)-ratios of 5/95, 10/90, 25/75 and 50/50 were produced using this two-step loading procedure (Figure 16). The qualitative loading with metals of these polymers could be determined by UV/Vis-, photoluminescence-, and infrared-spectroscopy. Additionally, the bound metal complexes were quantified by inductively coupled plasma mass spectrometry (ICP-MS). This revealed that the loading steps were not carried out quantitative and still a large proportion of the bipyridine units of the polymer chain remain unloaded. The reason for the incomplete loading was attributed to the sterically demanding metal complexes, which could cover more than one bipyridine structure. Additionally, secondary structures of the polymer may lead to lower loading as some bipyridine motifs are not freely accessible. In the future, the loading process should be optimised to further increase the photocatalytic performance of this system by reducing the number of free bipyridines. Improving the complexation degree of the bipyridines through longer loading durations could optimize the spatial proximity of the metal centers, which would increase the lifetime of the catalysts under light irradiation.

PVBpy$^{5/95}$ PVBpy$^{10/90}$ PVBpy$^{25/75}$ PVBpy$^{50/50}$
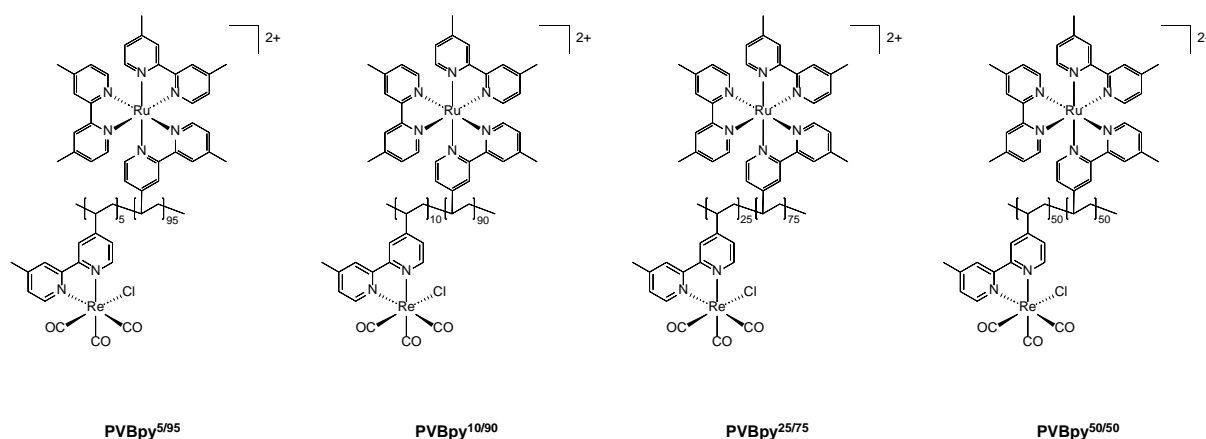
Figure 16: Illustration of the prepared poly(vinyl)bipyridine polymers (PVBpy) with different theoretical loading ratio of Re(I)-units to Ru(II)-units. The naming of the polymers follows the nomenclature PVBpy$^{Re/Ru}$.

Nevertheless, the trends of the loading density correspond to the desired ratios, which is why the resulting polymers PVBpy$^{5/95}$, PVBpy$^{10/90}$, PVBpy$^{25/75}$, and PVBpy$^{50/50}$ were subsequently investigated in the photocatalytic reduction of CO_2. Special attention was given to the influence of metal ratios on the stability and activity of the macromolecular photocatalysts under irradiation. Basically, the trend can be seen that polymers with low Re/Ru ratios achieve the highest turnover numbers. This could be attributed to two effects. On the one hand, this ratio has a high probability that catalyst molecules are fixed in the immediate vicinity of a photosensitiser and thus efficiently be supplied with electrons. As a further point, the high amount of photosensitisers can reduce the overexcitation of the Re(I)-centres by strong absorption, which additionally increases the stability of the macromolecule. The polymer PVBpy$^{5/95}$ thus achieved the highest activities and stabilities (TOF = 66 h^{-1}, TON = 5650) under

the irradiation conditions, which can compete with the best systems so far consisting of elaborately synthesised and strictly defined multinuclear photocatalysts.[85b] The turnover frequencies (TOFs) of the polymers at different concentrations give an insight into the role of intermolecular interactions between the polymer strands in the reduction of CO_2. For all tested Re concentrations (30-1.25 µM) the determined values range between 52-42 h^{-1}, from which it could be concluded that the necessary electron transfer takes place primarily along the chain and thus the desired intramolecular effect was achieved via covalent linkage.

In order to make these interactions even more efficient in the future, it would be an essential goal to precisely control the loading position on the polymer. This could be achieved by a random or even alternating copolymer with bipyridine and terpyridine units. Subsequently, a suitable precursor metal complex should be used to attach the Ru(II)-photosensitisers only to the terpyridine motif. In the last step, a maximum of the free bipyridine motifs needs to be occupied by the Re(I)-based photocatalyst-precursor to achieve a more even distribution. This should not only improve the light absorption properties of the macromolecule, but also ensure a short path for electron transfer to the neighbouring reduction centres.

Via copolymerisation, additional functional groups could be specifically linked to the bipyridines in a macroligand. Here, for example, isoquinoline[98a], terpyridines[134], porphyrins[135], tripodal ligands[136], quaterpyridines[98g] and phthalocyanines[137] could be introduced as ligands into the macromolecule. In addition to changing the electronic and steric properties of the polymer, this also makes it possible to bind not only rhenium and ruthenium, but also a variety of active metal centres that are more abundant on earth. These include manganese, iron, cobalt, nickel, or copper, which already play an important role in catalytic processes.[57d, 98d, 98g, 98i, 138] These could be straightforwardly attached to an appropriate ligand using our easily adaptable protocol. Furthermore, the extension of the described polymer via copolymerisation offers the possibility to control the solubility of the polymers in such a way that small mini-reactors form as micelles in the aqueous milieu.[127c] These could lead to more stable units, which selectively absorb CO_2, convert it, and release CO efficiently. It is also conceivable that the broad range of newly introduced functional structures could form fixations on semiconductors, thus further expanding the possible applications for photocatalytically-active macromolecular systems.

In this work, the monomer 4-vinyl-4′-methyl-2,2′-bipyridine was catalytically polymerised for the first time. A synthesis protocol was developed and optimised with which two different metal complexes in different ratios were quickly and simply fixed to this polymer. The loading was detected qualitatively via UV/Vis, PL, and IR, as well as quantitatively via ICP-MS. This allows the preparation of polymers that provide some of the best results for Re(I)/Ru(II)-based photocatalysts for CO_2 reduction. The developed methodology is not only extendable to many metal centres, but also facilitates the elucidation of the optimal interaction between PS and catalyst. With the simple procedure of loading, a wide range of loading densities and ratios

between the different metal centres can be obtained without much synthesis effort and can be investigated for beneficial interactions in irradiation experiments.

Similar to the photocatalytic polymer produced in the second project, a multinuclear system of Ru-photosensitisers and Re-catalysts was produced in the final part of this work. For this purpose, three Re(dmb)(CO)$_3$Cl building blocks (dmb = 4,4'-dimethyl-2,2'-bipyridines) were attached to a central [Ru(dmb)$_3$]$^{2+}$ unit via ethyl bridges. This new molecule RuRe3, was first investigated for its photophysical properties and compared with the literature-known photocatalysts RuRe and RuRe2.[85a, 96e, 126a] Both the FT-IR signals and the emission in photoluminescence spectroscopy were identical between the three catalysts tested. UV/Vis spectroscopy revealed an enhanced absorption at 360 nm (^{1}MLCT$_{Re}$) and, hence, confirmed the increased concentration of linked Re-centres. In the excitation experiment, it could be shown that the absorbed energy is most efficiently transported via the ethyl linkers in the case of RuRe3. In combination with the increased quantum yield of 12.2%, this tetramolecular system exhibits desirable electronic properties for light-induced catalysis that exceed those of RuRe and RuRe2.

Under irradiation, RuRe3 achieves a turnover number of 11800, the best performance reported for a Re/Ru-based photocatalyst. The molecule is superior to the individual components and the smaller reference molecules RuRe and RuRe2, especially at low concentrations (Scheme 12).
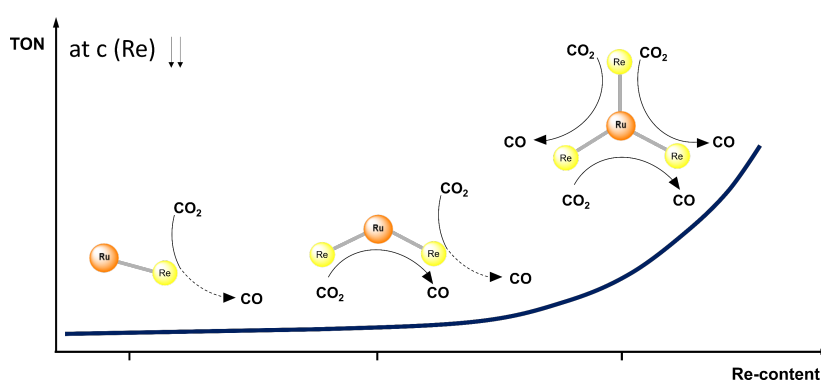
Scheme 12: Schematic representation of the turnover number (TON) vs the Re-content of RuRe, RuRe2 and RuRe3 at very low concentration of the catalyst unit (Re). Possible intramolecular Re-Re interactions in the two-electron reduction process of CO_2 are indicated by black arrows.[75a] Reprinted with permission from Ref. [75a]. Copyright 2022 John Wiley and Sons.

From this it was concluded that the second electron for the conversion of CO_2 to CO is more likely to be made available intramolecularly. The concentration-dependent impact processes thus limit the reduction process less often. This finding can be explained by the fact that the three Re-centres can cooperate in three different ways to transfer the two required electrons to CO_2 (Scheme 13).

Summary and Outlook
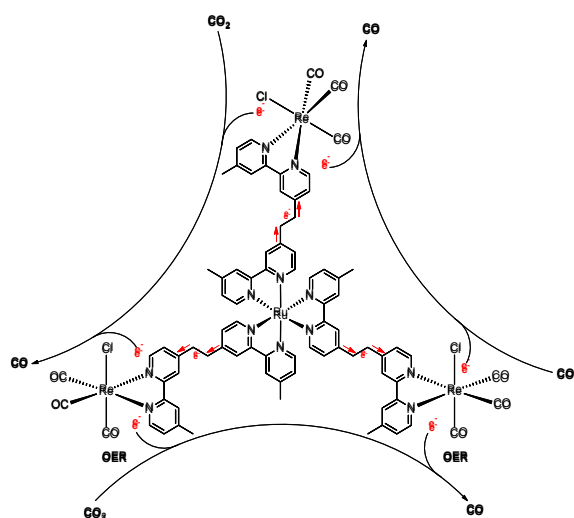
Scheme 13: Illustration of the multinuclear photocatalyst RuRe3 with schematic indication of the electron flow from the PS-unit to the catalysis centres. In addition, the possible intramolecular interactions between the Re(I)-catalysts are shown, which could take place for the two-electron transfer to CO_2.

It is important to note here that the turnover numbers are compared per molecule and not per catalysis centre. When comparing the performance of each individual Re-centre, the RuRe molecule appears to be the most efficient, but it should be noted that here the high Ru/Re ratio has stabilising effects, as discussed in the second project.

Another efficient way to provide the second electron is to combine RuRe (TON = 7582) with two mononuclear Re(I)-molecules. In this case, it is not the covalent bonds but the small and mobile Re molecules that provide and transfer the second electron efficiently. The RuRe + 2 Re system was able to achieve turnover figures (TON = 12100) in the same order of magnitude as RuRe3. This result, combined with the significantly poorer performance of systems such as RuRe + Re (TON = 6400) or RuRe + 3 Re (TON = 4100), led to the conclusion that a photosensitiser to catalysis centre ratio of three represents an optimum. The design of future supramolecular photocatalysts should be based on this metal-to-metal ratio. In the optimal design, the multinuclear complexes are enlarged in follow-up projects to increase the potential for intramolecular interactions. Here, similar to RuRe3, a dendrimeric structure would be advantageous, as it is strictly defined, but simultaneously remains scalable as desired. Via the covalent bonds, electron transfer from the PS to the catalysis centres can take place efficiently, whereafter they can then interact to carry out the reduction process. Separation of multiple photosensitisers in the centre of the molecule and the catalytic units radially arranged around it may favour this division of tasks. In addition, this design would make CO_2 diffusion to the catalysis centres on the outside as easy as possible.

This project represents the first step towards larger dendrimeric structures and shows their improved photocatalytic properties, which are expressed via the turnover number. The evaluation of the irradiation experiments carried out provided additional concrete information

on the origin of the second electron for the photocatalytic reduction of CO_2 and important approaches to optimise the electron transfers in the future.

8. Zusammenfassung und Ausblick

Ausgehend von den Arbeiten von *Gafney* und *Adamson* konnten *Lehn et al.* in den frühen 1980er-Jahren ein molekulares, photokatalytisches System auf Re(I)-Basis zur Reduktion von CO_2 aufbauen.[9, 64] Durch stetige Weiterentwicklung, insbesondere von der Gruppe um *Osamu Ishitani*, konnten die Katalysatoren stabiler, die Elektronendonatoren spezialisierter und der Reduktionsprozess effizienter gestaltet werden.[10a, 75b, 78, 84, 85b] Um mehr über den mechanistischen Hintergrund, den Elektronentransfer und die Deaktivierungsprozesse zu erfahren, untersuchten *Rieger et al.* die inter- und intramolekularen Wechselwirkungen der Metallzentren bei diesem Zwei-Elektronenprozess.[66a] Die dabei erhaltenen Erkenntnisse des binuklearen Mechanismus ermöglichten einen mehrkernigen Katalysator aus einem Ru(II)-Photosensibilisator verknüpft mit zwei Re(I)-Reduktionszentren, der die bis dato höchste Umsatzzahl erreichte.[85a] Zusätzlich wurde zwei unerwünschte Nebenreaktionen identifiziert, die zu Zersetzung des aktiven Katalysators führen.[10b] Beide dieser Deaktivierungswege starten nach der Anregung und dem ersten Elektronenübertrag auf den Re(I)-Katalysator von der Ein-Elektron-Reduzierten-Spezies (OERS). Erneute Anregung dieser radikalen Spezies kann zur Zersetzung und Deaktivierung des Katalysators führen. Da jedoch alle Prozesse nach der initialen Anregung im Dunklen ablaufen können, wurden diese Erkenntnisse genutzt und mit gepulster Strahlung, die das Metallzentrum einmalig am Anfang des Katalysezyklus anregt, die Stabilität des Systems erhöht.[82] Als zweiter Deaktivierungsmechanismus wurden Nebenreaktionen mit radikalischen Zwischenprodukten der Elektronendonatoren festgestellt.[10b] Aus diesem Grund ist es wichtig, die Konzentration dieser Radikale niedrig zu halten. Dies konnte realisiert werden, indem anstelle des Elektronendonators eine Hilfsbase zur Einstellung des pH-Wertes eingesetzt wurde.[80] Mit dieser transparenten und schwach nukleophilen Base kann die Konzentration des Elektronendonators, der zusätzlich als Base agiert, signifikant reduziert werden. Sowohl die Umsatzzahl als auch die Aktivität konnten durch diese Substitution erhöht werden.[80]

Trotz all dieser Verbesserungen erreichen Re(I)-Katalysatoren noch immer nur Umsatzzahlen im niedrigen zweistelligen Bereich und benötigen organische Elektronendonatoren, die verbraucht werden.[10a] Um auf diese Opferdonatoren zu verzichten und stabilere Re(I)-Katalysatoren zu erhalten, wurde in dieser Arbeit ein neues Prinzip für die Fixierung von (metall)organischen Molekülen auf Halbleiteroberflächen entwickelt, umgesetzt und untersucht.[103c] Der hier vorgestellte modulare Ansatz hat den Vorteil extrem flexibel zu sein, wodurch unterschiedlichste Trägermaterialien mit nahezu allen Katalysatoren verknüpft werden können. Die Oberfläche der Materialien wird dafür zunächst über Atomlagenabscheidung (ALD) mit Aluminiumoxid überzogen. Im Folgeschritt werden organischen Linker oder direkt die Zielmoleküle über Immersion mit der AlO_x-Schicht

verknüpft. An diese Anker kann jegliches katalytisch aktives Molekül mit einer Carbonsäureeinheit über einfache organische Synthese angeheftet werden. Die genannten Einzelschritte ermöglichen eine universelle Einsetzbarkeit dieser Methodik, wodurch diese auf alle Substrate übertragen werden kann, auf welchen Aluminiumoxidwachstum möglich ist. Dabei ist die Dicke der aufgebrachten Schicht präzise steuerbar und kann von 3 nm bis zu etwa 0.3 nm betragen, was die Möglichkeit eröffnet, die elektrische Leitfähigkeit zwischen Halbleiter und Katalysator zu regulieren. Die AlO$_x$-Ebene verändert aber nicht nur die physikalischen Eigenschaften, sondern dient auch zur Passivierung von Oberflächendefekten und kreiert einen geschlossenen und stabilen Überzug. Zusätzlich werden die chemischen Eigenschaften verändert, was eine einfache Phosphonsäure-Oberflächenchemie unter Standardbedingungen ermöglicht. Über Phosphonsäuregruppen können die (metall)organischen Moleküle oder Linker hochselektiv auf der Matrix fixiert werden. Die daraus resultierende Verknüpfung zwischen Halbleiter und Ankermolekülen eröffnet die Möglichkeit, über deren Kopplungsfunktionalitäten nahezu jedes Molekül kovalent an die Oberfläche mit sub-Nanometer-Präzision zu binden. Als Machbarkeitsstudie wurde in dieser Arbeit 1 cm × 1 cm zweidimensionale Silizium Halbleiter mit einer Aluminiumoxidschicht überzogen. Mit C$_6$- oder C$_{11}$-Phosphonsäurelinkern wurden anschließend zwei unterschiedlich lange, gesättigte Kohlenstoffketten aufgebracht und die Oberflächenschicht auf Rauigkeit mittels Rasterkraftmikroskopie (AFM) untersucht. Die C$_{11}$-Linker erreichen dabei eine ebenere Struktur, da sich die längeren Kohlenstoffketten sortierter nebeneinander positionieren und dadurch weniger Unordnungen entstehen. An denen am Kopfende befindlichen Hydroxygruppe können dann über die milde *Steglich*-Veresterung Re(I)-Komplexe kovalent gebunden werden, was über abgeschwächte Totalreflexion *Fourier*-Transform-Infrarotspektrometrie (ATR-FTIR) nachgewiesen wurde. Diese Verknüpfung des Hybriden mit dem Metallkomplex mildert die Rauheit der Oberfläche noch weiter. Das konnte mittels Röntgenreflektometrie (XRR) und Röntgen-Nahkanten-Absorptions-Spektroskopie (NEXAFS) auf die intermolekularen π-π-Wechselwirkungen der Bipyridine des Re(I)-Komplexes zurückgeführt werden konnte (Abbildung 17). Die aufgebrachten Photokatalysatoren zeigen starke intermolekulare Vibrationsinteraktion und elektronische Kopplung, wie durch Infrarot- (IR), Photolumineszenz- (PL) und Röntgenphotoelektronenspektroskopie (XPS) gezeigt werden konnte. Es konnten dabei große Unterschiede der intermolekularen Wechselwirkungen zwischen freien und den auf der Oberfläche fixierten Komplexen festgestellt werden. Gebunden an dem Halbleiter kommt es sogar zu einer Ladungsübertragung zwischen den Re(I)-Metallzentren, die durch XPS-Messungen identifiziert und durch ATR-FTIR-Spektren bestätigt werden konnte. Durch Änderung der Phosphonsäurelinker und der AlO$_x$-Schichtdicke konnten diese Wechselwirkungen nicht

beeinflusst werden, woraus sich schließen lässt, dass dieses Phänomen nur durch zwischenmolekulare Interaktion zustande kommt.
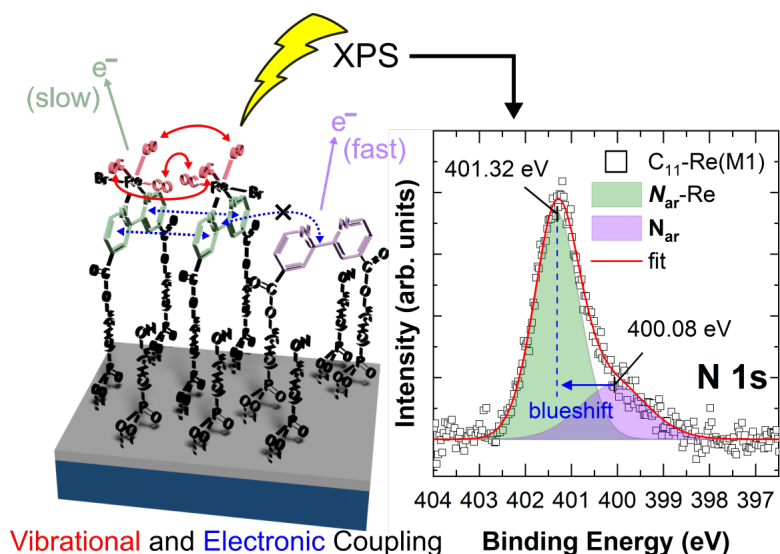
Abbildung 17: Graphische Zusammenfassung der Publikation mit dem Titel: "Modular Assembly of Vibrationally and Electronically Coupled Rhenium Bipyridine Carbonyl Complexes on Silicon". Diese wird in Kapitel 4 präsentiert. Dargestellt sind die fixierten Phosphonsäurelinker (schwarz) auf der mit AlOx (grau) beschichteten Si-Halbleiteroberfläche (blau). An einigen Linkern sind Bipyridinliganden (violett) oder Re(I)-Metallkomplexe (schwarz und rot) über eine Carbonsäureesterbrücke gebunden. Zusätzlich sind die Wechselwirkungen zwischen den Bipyridinen der Re(I)-Komplexen angedeutet, welche über XPS-Messungen identifiziert wurden.[103c] Abgedruckt mit Genehmigung von Quelle [103c]. Urheberrecht 2021 American Chemical Society.

Die Selektivität des vorgestellten, modularen Ansatzes wurde durch eine induzierte Oberflächenstruktur nachgewiesen (Abbildung 18). Dabei wurde der Silizium-Halbleiter mithilfe einer Polymermaske in Streifen mit AlO$_x$ überzogen und im Folgenden die Beladung nach oben beschriebenem Schema mit Linker und Metallkomplex durchgeführt. Im Anschluss wurde mit Raster-Photoelektronenmikroskopie (SPEM) die Oberfläche nach der Bindungsenergie von Re 4f abgesucht. Nur an den Stellen, an denen AlO$_x$ aufgebracht wurde, haben die Phosphonsäureanker gebunden, weshalb auch nur dort Re(I)-Komplexe gefunden wurden. Bei den Streifen, an denen Silizium nicht beschichtet wurde, konnte aufgrund der schlechten Reaktivität von Silizium und Phosphonsäuregruppen kein Linker binden und demnach kein Re-Katalysator aufgebracht werden. Dies kann in zukünftigen Ansätzen verwendet werden, um gezielt auf den unbeladenen Silizium andere Moleküle mit synergetischen Effekten ortsselektiv einzuführen. Möglich ist dies beispielsweise über Silanchemie oder die Aryldiazonium-Kation Reduktion.[131]

Zusammenfassung und Ausblick
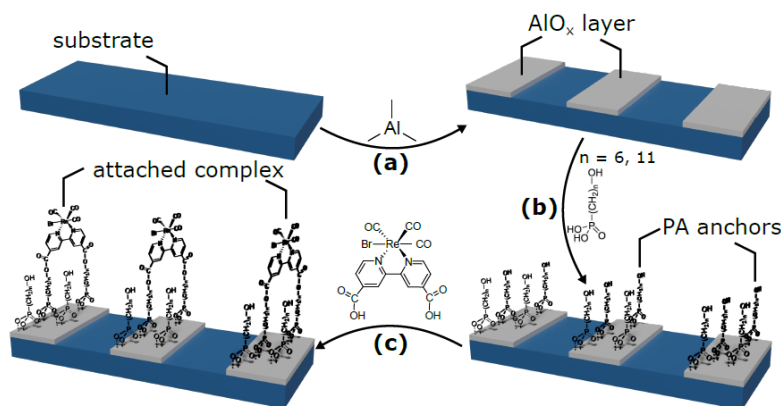
Abbildung 18: Schematische Darstellung des modularen Ansatzes: a) Das Substrat (Si) wird mithilfe einer Maske mit einer Aluminiumoxidschicht (grau) (ca. 0.3 bis 3 nm) durch ALD streifenweise überzogen. b) Phosphonsäurelinker werden mittels Immersion angebracht und binden ortsselektiv an die Stellen mit AlO_x auf der strukturierten Oberfläche. c) Im letzten Schritt wird der Metallkomplex Re(2,2′-bipyridin-4,4′-dicarbonsäure)(CO)$_3$Br über eine *Steglich*-Veresterung mit dem Linker verbunden und auf der Oberfläche fixiert.[103c] Abgedruckt mit Genehmigung von Quelle [103c]. Urheberrecht 2021 American Chemical Society.

Zusammenfassend kombiniert dieser Ansatz die Passivierung von Oberflächendefekten mit einer gezielten Funktionalisierung. Er lässt sich in Zukunft auf eine große Anzahl an Halbleitern anwenden und ermöglicht die Herstellung von gut definierten Hybridmaterialien, die in unterschiedlichsten Bereichen eingesetzt werden können. Für die CO_2-Reduktion ist ein Hybrid aus GaN und Re(I)-Photokatalysatoren aufgrund der Photonenleitfähigkeit von GaN vielversprechend. Hierfür wurde schon gezeigt, dass der beschriebene Ansatz für diesen Halbleiter auch funktioniert und vergleichbar gute Resultate zu Silizium erzielt. Durch die Flexibilität dieser modularen Hybridsynthese sind die zukünftigen Einsatzmöglichkeiten breit gestreut. Photoelektrochemische Anwendungen, Photovoltaik oder auch unterschiedlichste Sensoren sind mit diesem Ansatz realisierbar, wodurch er ein neues Werkzeug in der Synthese von Hybridsystemen bietet.[85b, 106a, 112d, 132]

Ein zweiter Ansatz, die Aktivität und damit die Leistungsfähigkeit von Re(I)-basierten Photokatalysatoren zu erhöhen, beruht auf den bereits erwähnten Arbeiten von *Rieger et al.*[66a, 85a] Darin konnte gezeigt werden, dass räumliche Nähe über kovalente Bindungen so erzwungen werden sollte, dass mehrere OERS interagieren können, wodurch ein effizienterer bimetallischer Mechanismus wahrscheinlicher wird. Diese Ergebnisse in Kombination mit der Kenntnis des positiven Einflusses von Ru(II)-Photosensibilisatoren auf die Stabilität von mehrkernigen Komplexe führte zu der Idee Polymerstränge als Makroliganden zu verwenden. An diese bipyridin-basierten Grundstruktur wurden anschließend unterschiedliche Verhältnisse an Re(I)-Photokatalsatoren und Ru(II)-Photosensibilisatoren angebracht werden, die in der photokatalytischen Reduktion von CO_2 untersucht wurden.

Im ersten Schritt wurden dafür Bipyridin-Einheiten synthetisiert, die im späteren Polymer eine möglichst kurzkettige und nicht-konjugierte Verknüpfung zwischen den Metallzentren anbieten, um die elektronische Interaktion im angeregten Zustand zu gewährleisten.[97b] Dieses 4-Vinyl-4′-methyl-2,2′-bipyridin konnte im Zuge dieser Arbeit das erste Mal katalytisch polymerisiert werden, da das Monomer durch vorherige Sublimation äußerst rein eingesetzt werden konnte. Mit unterschiedlichen sterisch gehinderten, frustrierten *Lewis*-Paaren bestehend aus einer Kombination von Phosphinen und Aluminiumverbindungen wurde die Polymerisation untersucht. Durch das Katalysesystem der Wahl konnte das Monomer zu einem Polymer mit einer engen Molmassenverteilung und hohen Initiatoreffektivität ($Đ$ = 1.31-1.36, I.E. = 45−51%) umgesetzt werden. Dabei wurde als *Lewis*-Säure Al(*i*-Bu)$_3$ und als *Lewis*-Base PMe$_3$ im Verhältnis 2:1 eingesetzt, um einen hohen Umsatz und gleichzeitig monomodal-verteilte Polymere zu erreichen (Schema 14).
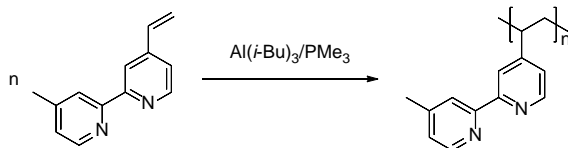
Schema 14: Schematische Darstellung der katalytischen Polymerisation von 4-Vinyl-4′-methyl-2,2′-bipyridin mit einer aluminiumbasierten *Lewis*-Säure und einer phosphorbasierten *Lewis*-Base.

Über Endgruppenanalyse konnten zwei Wege der Initiation identifiziert werden, welche entweder durch Deprotonierung oder konjugierte Addition starten. Diese beiden Pfade lassen sich jedoch so kontrollieren, dass die gewünschten monomodalen Polymere mit enger Molmassenverteilung entstehen. Die Zersetzungstemperatur des entstandenen Polymers liegt bei 368 °C. Mittels dynamischer Differenzkalorimetrie wurde die Glasübergangstemperatur bei 142 °C beobachtet. Zudem wurde dabei festgestellt, dass das Polymer keinen Schmelzpunkt aufweist, was auf einen amorphen Charakter hinweist. Diese katalytische polymerisierten bipyridin-basierten Monomere liefern demnach definierte Polymere, welche in den Folgeschritten mit photokatalytisch-aktiven Metallzentren beladen werden sollen.

Dazu wurden zwei aufeinanderfolgenden Syntheseprotokolle mit den Vorläufermolekülen Re(CO)$_5$Cl und Ru(dmb)$_2$Cl$_2$ entwickelt, mit denen das Polymer beladen und im Anschluss aufgereinigt und isoliert wird. Die Beladungsmenge kann dabei über die zugegebene Menge des jeweiligen Vorläufers einfach und qualitativ gesteuert werden (Schema 15).
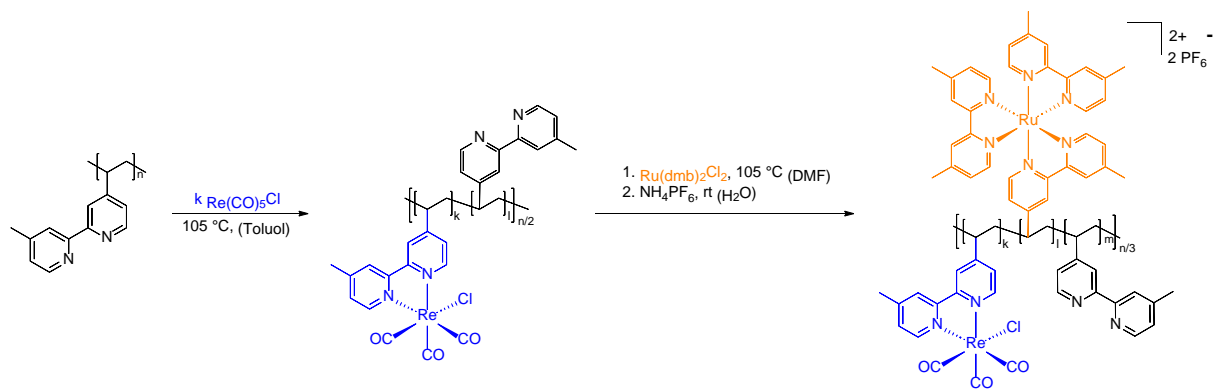
Schema 15: Beladungsschritte zur Herstellung der photokatalytisch aktiven Polymere PVBpy[Re/Ru]. Der erste Schritt erfolgt durch die Komplexierung des unbeladenen Polymers mit Re(CO)$_5$Cl. Im zweiten Schritt wird das Molekül Ru(dmb)$_2$Cl$_2$ an einige der freien Bipyridinen angebracht, bevor das resultierende Polymer mit NH$_4$PF$_6$ salzinduziert ausgefällt wird.[133] Abgedruckt mit Genehmigung von Quelle [133]. Urheberrecht 2022 American Chemical Society.

Mit diesen Beladungsschritten wurden vier unterschiedlich Polymere mit einem theoretischem Re(I)/Ru(II)-Verhältnis von 5/95, 10/90, 25/75 und 50/50 hergestellt (Abbildung 19). Die qualitative Beladung der Polymere mit Metallen konnte über UV/Vis-, Photolumineszenz- und Infratotspektroskopie bestimmt werden. Quantifiziert wurden die gebundenen Metallkomplexe zusätzlich über Massenspektrometrie mit induktiv gekoppeltem Plasma (ICP-MS). Damit konnte aufgedeckt werden, dass die Beladungsschritte nicht qualitativ erfolgen und noch ein großer Teil der Bipyridin-Einheiten an der Polymerkette unbeladen bleiben. Dies wurde den sterisch anspruchsvollen Metallkomplexen zugeschrieben, die mehr als eine Bipyridin-Struktur überdecken könnten. Zusätzlich können sekundäre Strukturen des Polymers zu niedrigerer Beladung führen, da manche Bipyridin-Motive nicht frei zugänglich sind. Zukünftig sollte versucht werden, die photokatalytische Performance dieses Systems noch weiter zu erhöhen, indem die Anzahl an unbeladenen Bipyridinen verringert wird. Durch zeitlich längere Beladungsschritte könnte die räumliche Nachbarschaft der Metallzentren optimiert werden, was die Lebenszeit der Katalysatoren unter der Lichtbestrahlung erhöhen würde.
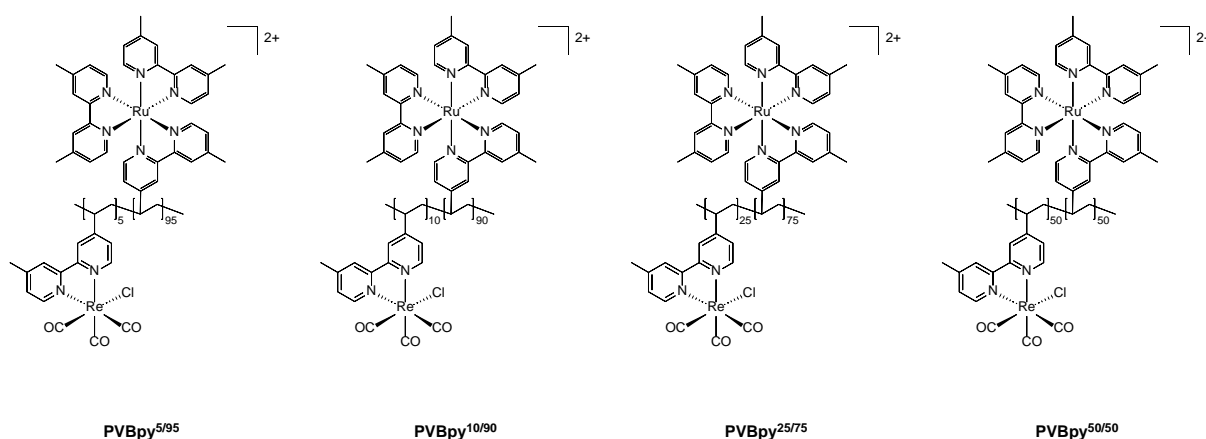
Abbildung 19: Darstellung der hergestellten Poly(vinyl)bipyridin-Polymere (PVBpy) mit unterschiedlichen theoretischem Beladungsverhältnis von Re(I)-Einheiten zu Ru(II)-Einheiten. Die Benennung der Polymere folgt der Nomenklatur PVBpy[Re/Ru].

Die Trends der Beladungsdichte entsprechen dennoch den erwünschten Verhältnissen, weshalb die entstandenen Polymere PVBpy[5/95], PVBpy[10/90], PVBpy[25/75] und PVBpy[50/50] im Anschluss in der photokatalytischen Reduktion von CO_2 untersucht wurden. Dabei wurde besonders auf den Einfluss der Metallverhältnisse auf die Stabilität und Aktivität der makromolekularen Photokatalysatoren unter Bestrahlung geachtet. Grundsätzlich lässt sich der Trend erkennen, dass Polymere mit niedrigem Re/Ru-Verhältnis die höchsten Umsatzzahlen erreichen. Dies konnte zwei Effekten zugeordnet werden. Einerseits hat dieses Verhältnis eine hohe Wahrscheinlichkeit, dass ein Katalysatormolekül in unmittelbarer Nähe zu einem Photosensibilisator fixiert ist und diese somit effizient mit Elektronen versorgt werden können. Als weiterer Punkt kann die hohe Anzahl an Photosensibilisatoren die Überanregung der Re(I)-Zentren durch starke Absorption reduzieren, wodurch zusätzlich die Stabilität des Makromoleküls erhöht wird. Das Polymer PVBpy[5/95] erreichte so die höchsten Aktivitäten und Stabilitäten (TOF = 66 h^{−1}, TON = 5650) unter den Bestrahlungsbedingungen, die mit den bisher besten Systemen, bestehend aus aufwendig synthetisierten und streng definierten mehrkernigen Photokatalysatoren, konkurrieren können.[85b] Die Wechselzahlen (TOFs) der Polymere bei unterschiedlichen Konzentrationen geben einen Einblick auf die Rolle von intermolekularen Wechselwirkungen zwischen den Polymersträngen bei der Reduktion von CO_2. Diese befinden sich bei allen getesteten Re-Konzentrationen (30-1.25 µM) bei ähnlichen Werten (52-42 h^{-1}), woraus geschlossen werden konnte, dass der notwendige Elektronentransfer primär entlang der Kette verläuft und somit der gewünschte intramolekulare Effekt über die kovalente Verknüpfung erreicht wurde.

Um diese Wechselwirkungen zukünftig noch effizienter zu gestalten, wäre es ein wichtiges Ziel, die Beladungsposition auf dem Polymer exakt zu steuern. Dies könnte durch ein statistisches oder sogar alternierendes Copolymer mit Bipyridin- und Terpyridineinheiten gelingen. Im Anschluss sollte durch einen geeigneten Vorläufer-Metallkomplex die Ru(II)-

Photosensibilisatoren nur an dem Terpyridin-Motiv angebracht werden und im letzten Schritt der Photokatalysator-Vorläufer auf Re(I)-Basis möglichst viele Bipyridine besetzen. Die damit erzielte gleichmäßigere Verteilung sollte nicht nur die Lichtabsorptionseigenschaften des Makromoleküls verbessern, sondern auch einen kurzen Weg für Elektronentransfer zu den benachbarten Reduktionszentren gewährleisten.

Über Copolymerisation könnten zusätzlich gezielt funktionelle Gruppen mit den Bipyridinen in einem Makroliganden verknüpft werden. Hier könnten beispielsweise Isochinolin[98a], Terpyridine[134], Porphyrine[135], tripodale Liganden[136], Quaterpyridine[98g] und Phthalocyanine[137] als Liganden in das Makromolekül eingeführt werden. Das ändert nicht nur die elektronischen und sterischen Eigenschaften des Polymers, sondern ermöglicht es neben Rhenium und Ruthenium auch eine Vielzahl an weiteren aktiven Metallzentren zu binden, die auf der Erde häufiger vorkommen. Dazu zählen Mangan, Eisen, Cobalt, Nickel oder Kupfer, die in katalytischen Vorgängen schon jetzt wichtige Rolle spielen.[57d, 98d, 98g, 98i, 138] Diese könnten mit dem leicht zu adaptierenden Protokoll unkompliziert an die passenden Liganden angebracht werden. Zusätzlich bietet die Erweiterung des beschriebenen Polymers über Copolymerisation die Möglichkeit, die Löslichkeit der Polymere so zu steuern, dass sich im wässrigen Milieu kleine Minireaktoren als Mizelle ausbilden.[127c] Diese könnten zu stabileren Einheiten führen, die gezielt CO_2 aufnehmen, umwandeln und CO effizient abgeben können. Auch wäre vorstellbar, dass die breite Möglichkeit an neu eingebrachten funktionellen Strukturen die Fixierung an Halbleitern bilden können, um so die Anwendungsmöglichkeiten für photokatalytisch-aktive, makromolekulare Systeme noch zu erweitern.

In dieser Arbeit wurde das Monomer 4-Vinyl-4′-methyl-2,2′-bipyridin das erste Mal katalytisch polymerisiert. Es wurde ein Syntheseprotokoll entwickelt und optimiert, mit welchem zwei verschiedene Metallkomplexe in unterschiedlichem Verhältnis schnell und einfach an diesem Polymer fixiert werden. Die Beladung kann sowohl qualitativ über UV/Vis, PL und IR, als auch quantitativ über ICP-MS nachgewiesen werden. Damit können Polymere hergestellt werden, die mit die besten Ergebnisse für Photokatalysatoren auf Re(I)/Ru(II)-Basis für die CO_2-Reduktion liefern. Die entwickelte Methodik ist nicht nur auf viele Metallzentren erweiterbar, sondern erleichtert die Aufklärung der optimalen Interaktion zwischen Photosensibilisator und Katalysator. Mit diesem einfachen Prozedere der Beladung kann ein großer Bereich an Beladungsdichten und Verhältnissen zwischen den unterschiedlichen Metallzentren ohne großen Syntheseaufwand abgedeckt und in Bestrahlungsexperimenten auf vorteilhafte Wechselwirkungen untersucht werden.

Ähnlich zu dem im zweiten Projekt hergestellten photokatalytischen Polymer wurde im finalen Teil dieser Arbeit ein mehrkerniges System aus Ru-Photosensibilisatoren und Re-Katalysatoren hergestellt. Dazu wurden drei Re(dmb)(CO)₃Cl-Bausteine (dmb = 4,4'-dimethyl-2,2'-bipyridine) über Ethylbrücken an eine zentrale [Ru(dmb)₃]²⁺-Einheit gebunden. Dieses

neue Molekül RuRe3 wurde zunächst auf seine photophysikalischen Eigenschaften untersucht und mit den literaturbekannten Photokatalysatoren RuRe und RuRe2 verglichen.[85a, 96e, 126a] Sowohl die FT-IR Signale, als auch die Emission in der Photolumineszenz-Spektroskopie waren identisch zwischen den drei getesteten Katalysatoren. In den UV/Vis-Spektren konnte die verstärkte Absorption bei 360 nm ($^1MLCT_{Re}$) nachgewiesen werden, was die erhöhte Konzentration von verbundenen Re-Zentren bestätigt. Im Anregungsversuch konnte gezeigt werden, dass die aufgenommene Energie bei RuRe3 am effizientesten über die Ethyllinker transportiert wird. In Kombination mit der erhöhten Quantenausbeute von 12.2% bietet dieses tetramolekulare System wünschenswerte elektronische Eigenschaften für die lichtinduzierte Katalyse, die denen von RuRe und RuRe2 übersteigen.

Unter Bestrahlung erreicht RuRe3 mit einer Umsatzzahl von 11800 die beste Leistung, die für ein Re/Ru-basieterten Photokatalysator berichtet ist. Dabei ist das Molekül gegenüber den Einzelkomponenten und den kleineren Vergleichsmolekülen RuRe und RuRe2 besonders in niedriger Konzentration überlegen (Schema 16).
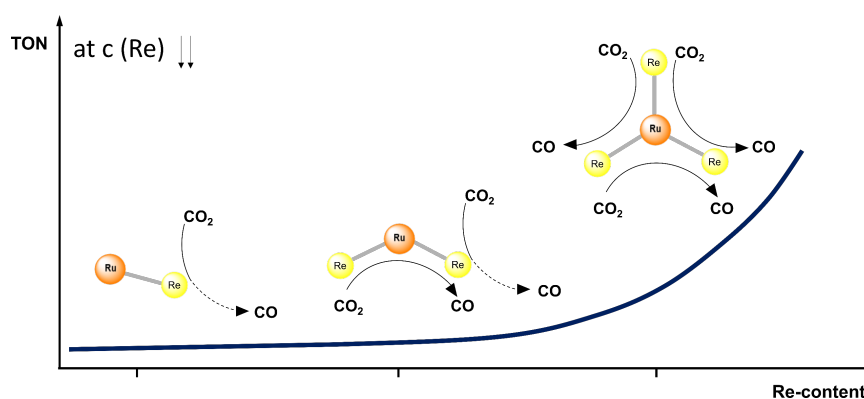
Schema 16: Schematische Darstellung der Umsatzzahl (TON) vs den Re-Gehalt (Re-content) von RuRe, RuRe2 und RuRe3 bei sehr niedriger Konzentration der Kataysatoreinheit (Re). Die möglichen intramolekularen Re-Re-Interaktionen in dem Zwei-Elektronen-Reduktionsprozess von CO_2 sind mit schwarzen Pfeilen angedeutet.[75a] Abgedruckt mit Genehmigung von Quelle [75a]. Urheberrecht 2022 John Wiley and Sons.

Daraus konnte geschlussfolgert werden, dass das zweite Elektron für die Umsetzung von CO_2 zu CO zu größerer Wahrscheinlichkeit intramolekular zur Verfügung gestellt wird und konzentrationsabhängige Stoßprozesse den Reduktionsvorgang weniger oft limitieren. Begründet werden kann diese Erkenntnis damit, dass die drei Re-Zentren auf drei verschiedene Wege kooperieren können, um die beiden benötigten Elektronen auf das CO_2 zu übertragen (Schema 17).

Zusammenfassung und Ausblick
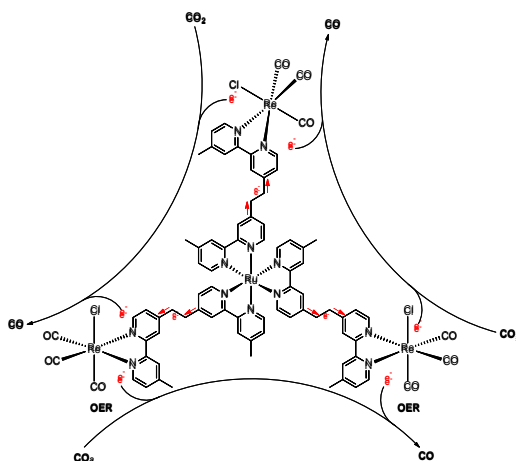
Schema 17: Darstellung des mehrkernigen Photokatalysators RuRe3 mit schematischer Andeutung des Elektronenflusses von der Photosensibilisator-Einheit zu den Katalysezentren. Zusätzlich sind die möglichen intramolekularen Kooperationen zwischen den Re(I)-Katalysatoren dargeboten, welche für den Zwei-Elektronentransfer zu CO_2 ablaufen könnten.

Wichtig ist es hier zu erwähnen, dass die Umsatzzahl pro Molekül verglichen wird und nicht pro Katalysezentrum. Bei einem Vergleich der Leistung jedes einzelnen Re-Zentrums scheint das Molekül RuRe (TON_{Re} = 7582) am effizientesten, aber es ist zu beachten, dass hier das hohe Ru/Re-Verhältnis stabilisierende Auswirkungen hat, wie im zweiten Projekt erörtert.

Ein weiterer effizienter Weg, das zweite Elektron zur Verfügung zu stellen, bietet die Kombination aus RuRe und zwei mononuklearen Re(I)-Molekülen. In diesem Fall sorgen nicht die kovalenten Bindungen, sondern die kleinen und mobilen Re-Moleküle für die effiziente Bereitstellung und Übertragung des zweiten Elektrons. Das System RuRe + 2 Re (TON = 12100) konnte Umsatzzahlen in derselben Größenordnung wie RuRe3 erreichen. Dieses Ergebnis in Kombination mit der deutlich schlechteren Performance von Systemen wie RuRe + Re (TON = 6400) oder RuRe + 3 Re (TON = 4100) ergab die Schlussfolgerung, dass ein Verhältnis von Photosensibilisator zu Katalysezentrum von drei einem Optimum entspricht. Das Design von zukünftigen supramolekularen Photokatalysatoren sollte nach diesem Metall-zu-Metall-Verhältnis ausgelegt werden. Im besten Fall werden die mehrkernigen Komplexe in Folgeprojekten vergrößert, um das Potential intramolekularer Wechselwirkungen zu erhöhen. Dabei wäre ähnlich zu RuRe3 eine dendrimere Struktur von Vorteil, da diese gleichzeitig streng definiert ist, aber nach Belieben skalierbar bleibt. Über die kovalenten Bindungen kann der Elektronentransfer von Photosensibilisator zu den Katalysezentren effizient erfolgen, wonach diese dann interagieren können, um den Reduktionsprozess zu vollziehen. Eine Trennung von mehreren Photosensibilisatoren im Zentrum des Moleküls und den Katalysatoreinheiten radial darum angeordnet kann diese Arbeitsteilung begünstigen. Zusätzlich wäre so die CO_2-Diffusion zu den außen liegenden Katalysezentren möglichst einfach gestaltet.

Zusammenfassung und Ausblick

Dieses Projekt stellt den ersten Schritt zu größeren Dendrimer-Strukturen dar und zeigt deren verbesserten photokatalytischen Eigenschaften, die sich über die Umsatzzahl ausdrücken. Die Evaluierung der durchgeführten Bestrahlungsexperimente gab zusätzlich konkrete Hinweise auf den Ursprung des zweiten Elektrons für die photokatalytischen Reduktion von CO_2 und wichtige Ansätze, die Elektronenübertragungen in der Zukunft zu optimieren.

9. Publications Beyond the Scope of this Thesis as Contributing Author

9.1 Entrapped Molecular Photocatalyst and Photosensitiser in Metal-Organic Framework Nanoreactors for Enhanced Solar CO_2 Reduction

Authors: Philip M. Stanley, <u>Christopher Thomas</u>, Erling Thyrhaug, Alexander Urstoeger, Michael Schuster, Jürgen Hauer, Bernhard Rieger, Julien Warnan*, and Roland A. Fischer*

Abstract

Herein, we report on a molecular catalyst embedding metal–organic framework (MOF) that enables enhanced photocatalytic CO_2 reduction activity. A benchmark photocatalyst *fac*-$ReBr(CO)_3$(4,4′-dcbpy) (dcbpy = dicarboxy-2,2′-bipyridine) and photosensitiser $Ru(bpy)_2$(5,5′-dcbpy)Cl_2 (bpy = 2,2′-bipyridine) were synergistically entrapped inside the cages of the nontoxic and inexpensive MIL-101-NH_2(Al) through noncovalent host–guest interactions. The heterogeneous material improved Re catalyst stabilisation under photocatalytic CO_2 reduction conditions as selective CO evolution was prolonged from 1.5 to 40 h compared to the MOF-free photosystem upon reactivation with additional photosensitiser. By varying ratios of immobilized catalyst to photosensitiser, we demonstrated and evaluated the effect of reaction environment modulation in defined MOF cages acting as a nanoreactor. This illustrated the optimal efficiency for two photosensitisers and one catalyst per cage and further led to the determination of ad hoc relationships between molecular complex size, MOF pore windows, and number of hostable molecules per cage. Differing from typical homogeneous systems, photosensitiser—and not catalyst—degradation was identified as a major

performance-limiting factor, providing a future route to higher TONs via a rational choice of parameters.

The abstract was reprinted with permission from Philip M. Stanley, <u>Christopher Thomas</u>, Erling Thyrhaug, Alexander Urstoeger, Michael Schuster, Jürgen Hauer, Bernhard Rieger, Julien Warnan*, and Roland A. Fischer*, *ACS Catal.* **2021**, *11*, 2, 871-882. Copyright 2021 American Chemical Society.

Reprint Permission Copyrighted Content

9.2 Host-Guest Interactions in a Metal-Organic Framework Isoreticular Series for Molecular Photocatalytic CO_2 Reduction

Authors: Philip M. Stanley, Johanna Haimerl, <u>Christopher Thomas</u>, Alexander Urstoeger, Prof. Dr. Michael Schuster, Prof. Dr. Natalia B. Shustova, Prof. Dr. Angela Casini, Prof. Dr. Bernhard Rieger, Dr. Julien Warnan*, Prof. Dr. Roland A. Fischer*

Abstract

A strategy to improve homogeneous molecular catalyst stability, efficiency, and selectivity is the immobilization on supporting surfaces or within host matrices. Herein, we examine the co-immobilization of a CO_2 reduction catalyst [ReBr(CO)$_3$(4,4′-dcbpy)] and a photosensitiser [Ru(bpy)$_2$(5,5′-dcbpy)]Cl$_2$ using the isoreticular series of metal–organic frameworks (MOFs) UiO-66, -67, and -68. Specific host pore size choice enables distinct catalyst and photosensitiser spatial location—either at the outer MOF particle surface or inside the MOF cavities—affecting catalyst stability, electronic communication between reaction center and photosensitiser, and consequently the apparent catalytic rates. These results allow for a rational understanding of an optimized supramolecular layout of catalyst, photosensitiser, and host matrix.

Publications Beyond the Scope of this Thesis as Contributing Author

Reprint Permission Copyrighted Content

10.　Appendix

10.1　Supporting Information of the Manuscript "Modular Assembly of Vibrationally and Electronically Coupled Rhenium Bipyridine Carbonyl Complexes on Silicon"

Supporting Information

Modular Assembly of Vibrationally and

Electronically Coupled Rhenium Bipyridine

Carbonyl Complexes on Silicon

Johannes D. Bartl [†,‡,||,*], Christopher Thomas [‡,||,*], Alex Henning [†], Martina F. Ober [%,¶], Gökcen

Savasci [§,+,€], Bahar Yazdanshenas [†,&], Peter S. Deimel [#], Elena Magnano [§,⌡], Federica Bondino [§],

Patrick Zeller [⌠,~], Luca Gregoratti [⌠], Matteo Amati [⌠], Claudia Paulus [†], Francesco Allegretti [#],

Anna Cattani-Scholz [†,¶], Johannes V. Barth [#], Christian Ochsenfeld [§,+,€], Bert Nickel [%,¶], Ian D.

Sharp [†], Martin Stutzmann [†], and Bernhard Rieger [‡]

[†] Walter Schottky Institute and Physics Department, Technische Universität München, Am

Coulombwall 4, 85748 Garching bei München, Germany

99

[‡] Department of Chemistry, WACKER-Chair for Macromolecular Chemistry, Technische Universität München, Lichtenbergstraße 4, 85747 Garching bei München, Germany

[℅] Faculty of Physics Ludwig-Maximilians-Universität München, Geschwister-Scholl-Platz 1, 80539 München, Germany

[¶] Center for Nanoscience (CeNS), Ludwig-Maximilians-Universität München, Geschwister-Scholl-Platz 1, 80539 München, Germany

[§] Max Planck Institute for Solid State Research, Heisenbergstr. 1, 70569 Stuttgart, Germany

[⁺] Department of Chemistry, University of Munich, LMU, Butenandtstr. 5-13, 81377 Munich, Germany

[€] Cluster of excellence e-conversion, Lichtenbergstr. 4a, 85748 Garching, Germany

[#] Physics Department E20, Technische Universität München, James-Franck-Str.1, 85748 Garching bei München, Germany

[§] IOM CNR, Laboratorio TASC S.S. 14 km 163.5, 34149 Basovizza, Trieste, Italy

2

Appendix

[/] Department of Physics, University of Johannesburg, PO Box 524, Auckland Park 2006, South

Africa

[/] Elettra-Sincrotrone Trieste SCpA, SS14-Km163.5 in Area Science Park, 34149, Trieste, Italy.

∥ contributed equally

Table of Contents

3

Appendix

4

Appendix

S0. Chemical structure and nomenclature of frequently used substances
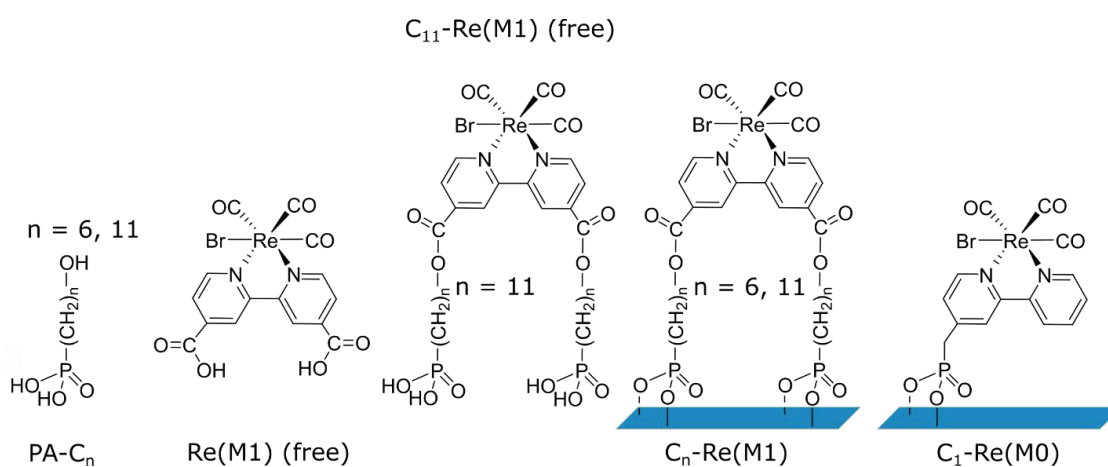
C_{11}-Re(M1) (free)

SI Scheme 1. Chemical structure of 6-hydroxyhexylphosphonic acid (referred to as **PA-C$_6$**), 11-hydroxyundecylphosphonic acid (**PA-C$_{11}$**), Re(2,2'-bipyridine-4,4'-dicarboxylic acid)(CO)$_3$Br (**Re(M1) (free)**), Re(((([2,2'-bipyridine]-4,4'-dicarbonyl)bis(oxy))bis(undecane-11,1-diyl))bis(phosphonic acid))(CO)$_3$Br (**C$_{11}$-Re(M1) (free)**), Re((6-((4'-(((6-phosphonohexyl)oxy)carbonyl)-[2,2'-bipyridine]-4-carbonyl)oxy)hexyl)phosphonic acid)(CO)$_3$Br (**C$_6$-Re(M1)**), Re((((([2,2'-bipyridine]-4,4'-dicarbonyl)bis(oxy))bis(undecane-11,1-diyl))bis(phosphonic acid))(CO)$_3$Br (**C$_{11}$-Re(M1)**), Re(([2,2'-bipyridin]-4-ylmethyl)phosphonic acid)(CO)$_3$Br (**C$_1$-Re(M0)**) (from left to right).

5

Appendix

S1. Atomic layer deposition (ALD) growth on Si(100) and hydroxyl (OH) surface termination

monitored by *in-situ* spectroscopic ellipsometry (SE)

3 nm and 1 nm thick AlO_x layers were grown in a hot-wall reactor (Fiji G2, manufactured by

Ultratech/Cambridge Nanotech, recently acquired by Veeco) in continuous flow mode at 200 ˚C

by sequential pulsing of trimethylaluminum (TMA; 99.999 %, STREM Chemicals Inc.) and

deionized water (dH$_2$O, LC-MS grade, VWR Chemicals BDH). TMA and dH$_2$O were supplied at

~0.14 and ~0.18 Torr, respectively, by an Argon (Ar, 99.9999 %, Linde) carrier gas through the

precursor manifold to the reactor chamber at a flow rate of 30 sccm. An additional Ar gas flow (80

sccm) was continuously provided through the plasma sapphire tube to direct the precursor onto the

substrate holder and inhibit precursor exposure of the remote plasma generation region. Prior to

aluminum oxide growth, an *in-situ* hydrogen plasma (HP) treatment (3 cycles, 3 sec, 100 W, 0.2

Torr) was performed to remove adsorbed contaminants (~ 1.6 Å in thickness) from the air-exposed

substrates. For thermal AlO_x growth (32 / 12 ALD cycles), each cycle followed the sequence: 0.08

s TMA dose, 8 s Ar purge, 0.08 s H_2O dose, and 10 s Ar purge. For purging, Ar was delivered at

110 sccm (base pressure of ~ 0.09 Torr). After AlO_x deposition, a remote oxygen plasma (OP) was

applied *in-situ* for 60 s to increase the OH surface density. Both the hydrogen and oxygen plasma

were generated in a sapphire tube with an inductively coupled plasma (ICP) source. AlO_x layers

with sub-monolayer (ML) coverage were grown by plasma enhanced-atomic layer deposition (PE-

ALD) (1), following a recently reported approach (2,3). For sub-ML AlO_x PE-ALD growth (3

ALD cycles, 200 ˚C), each cycle followed the sequence: 0.08 s TMA dose, 30 s Ar purge, 10 s H_2

purge, 2 s HP (100 W), 10 s Ar purge, 10 s H_2 purge, 2 s HP (100 W), and 10 s Ar purge. No

remote OP was applied. The treated wafer pieces were transferred to the ambient and immediately

used for PA surface grafting. A ~ 0.45 nm thick, AlO_x micropattern was grown on Si combining a

lithographic lift-off process with low-temperature PE-ALD. A resist double layer consisting of

7

poly-dimethylglutarimide (PMGI SF3, Microchem) and ma-P 1205 (micro resist technology) was

patterned with a maskless aligner (Heidelberg MLA100, PoliFAB) and developed in

tetramethylammonium hydroxide (TMAH, micro resist technology). For PE micropatterned AlO_x

growth (20 ALD cycles, 70 ˚C) (3), each cycle followed the sequence: 0.08 s TMA dose, 15 s Ar

purge, 10 s H_2 purge, 2 s HP (100 W), 15 s Ar purge. No remote OP was applied. Lift-off was

performed by ultrasonication (10 min, 40 ˚C) in *N*-methyl-2-pyrrolidone (NMP, micro resist

technology) and the treated wafer pieces were used for PA surface grafting. For both PE-ALD

TMA/HP processes, the native SiO_x serves as an oxygen source, causing a saturation of the growth

rate after roughly 10 cycles. AlO_x growth was monitored with an *in-situ* ellipsometer (M-2000, J.

A. Woollam, Inc. Lincoln, NE, USA). The light of a Xenon lamp (Hamamatsu, L2174-01) was

directed to a spot area of ca. 5×8 mm^2 onto the sample surface. The incoming and reflected light

passed through fused silica quartz windows (Lesker, VPZL-275DU) in a fixed angle (67˚)

geometry. The dwell (purge) times after each precursor, oxidant, and plasma step were

programmed to be at least three times the ellipsometer's integration time. The Si substrate was

modeled using the Woollam library Si JAW model for Si and the Ntve JAW3 model for the with

8

a native SiO$_x$ layer (Woollam database, CompleteEASE (ver. 6.53.)), whereas the AlO$_x$ was

modeled by a Cauchy layer (4).

SI Figure 1a shows a representative TMA/H$_2$O Al$_2$O$_3$ growth at 200 ˚C as a function of the

deposition time on a highly *p*-doped silicon Si(100) substrate determined by *in-situ* spectroscopic

ellipsometry (SE). The ALD growth can be divided into four distinct regions (**I-IV**). In a first step

(**I**) the substrate is pre-treated by three pulses of a remotely generated hydrogen plasma (HP) to

Appendix
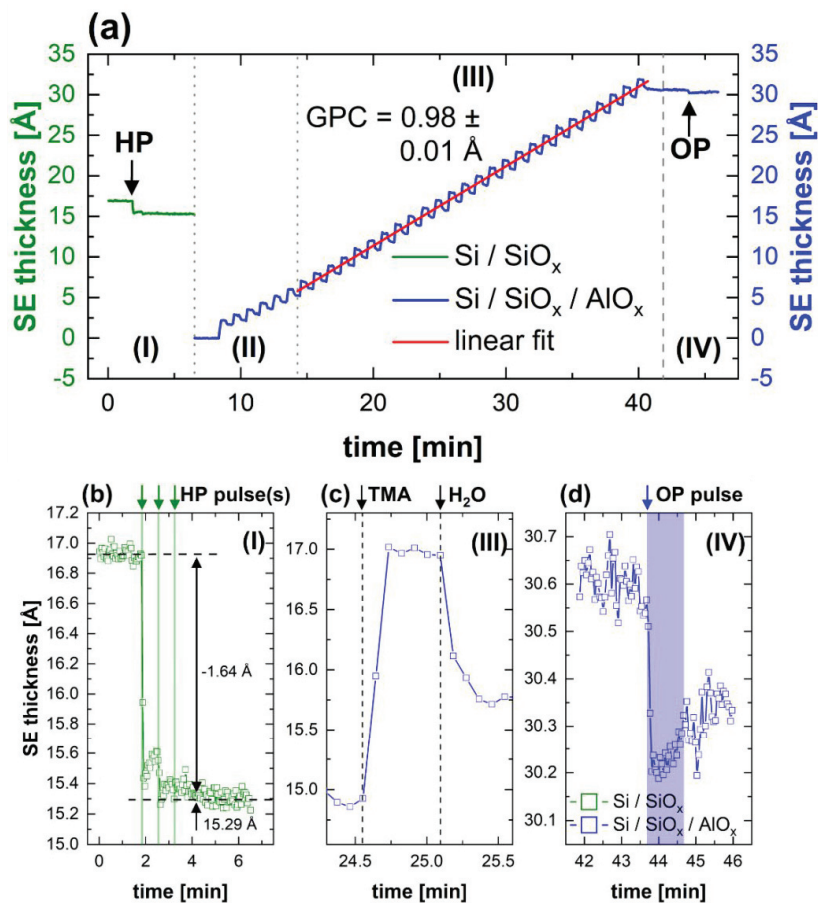
SI Figure 1. TMA/H$_2$O AlO$_x$ growth at 200 °C as a function of the deposition time on a highly p-doped Si(100)

substrate determined by *in-situ* spectroscopic ellipsometry (SE) (a). The ALD growth can be divided into four distinct

regions (I-IV). In a first step (I) the substrate is pre-treated by three pulses of a remotely generated hydrogen plasma

(HP) to remove adsorbed contamination from the air-exposed surface (~ 1.64 Å in thickness) allowing a carbon-free

interface between Si and AlO$_x$ (b). After the first 6 TMA injections (II) a linear growth regime with a growth per cycle

(GPC) of 0.98 ± 0.01 Å can be observed (III). A TMA and H$_2$O half cycle for the linear growth regime is shown in

(c). After ALD growth, the surface is exposed to a remotely generated oxygen plasma (OP) to increase the surface

hydroxyl (OH) density resulting in a slight decrease of the AlO$_x$ layer thickness (~ 0.5 Å in the first 10 s), followed

by a slight increase in thickness (d).

remove adsorbed contamination (~ 1.64 Å in thickness) from the air-exposed surface, allowing a

carbon-free interface between Si and AlO$_x$ (SI Figure 1b). Here, we note that for the applied

aluminum oxide model, the native silicon oxide thickness is kept constant after the HP step.

Considering X-ray reflectivity (XRR; SI Table 3) and XPS results (SI Figure 7) the thickness of

the silicon native oxide is, however, slightly increased during the ALD process. Modeling SE-

related changes in thickness of the native silicon oxide independent of the aluminum oxide

thickness is, however, challenging and led to unreasonable changes of the SiO$_x$ thickness.

However, the mean squared error (MSE) for the applied model was always ≤ 3.46 indicating a

good fit to the experimental data. After the first 6 TMA injections (**II**) a linear growth regime with a growth per cycle (GPC) of 0.98 ± 0.01 Å can be observed (**III**). We attribute the delayed initial growth regime to the HP pre-treatment. A TMA and H_2O half cycle for the linear growth regime is shown in **SI Figure 1c**. After the ALD growth, the surface is exposed to a remotely generated oxygen plasma (OP) to increase the surface OH density resulting in a slight decrease of the AlO_x layer thickness (~ 0.5 Å in the first 10 s). After the initial exposure, the thickness increased again, which we explain by a slight variation of the AlO_x layer's optical properties, since an increase in surface roughness can be neglected (**SI Figure 3**). We note that the AlO_x-coated surface is already sufficiently hydrophilic after the last dH_2O pulse (**SI Table 1**). However, the additional OP treatment ensures an increased homogeneity of the OH termination with slightly higher phosphonic acid (PA) loadings.

SI Figure 2 depicts a representative TMA/HP AlO_x growth at 200 ˚C as a function of the deposition time on a *p*-doped Si substrate determined by *in-situ* SE. The black and green arrows indicate TMA injection and HP pulses, respectively. The 3 cycle growth results in an AlO_x thickness of 2.5 ± 0.1 Å, which is slightly thinner compared to a fully formed monolayer AlO_x grown on gallium nitride

11

(GaN) (2). Considering the AlO$_x$ layer thickness and the steric hindrance of the TMA precursor, a

sub-monolayer AlO$_x$ film is formed. Exposure to air generates Al-OH
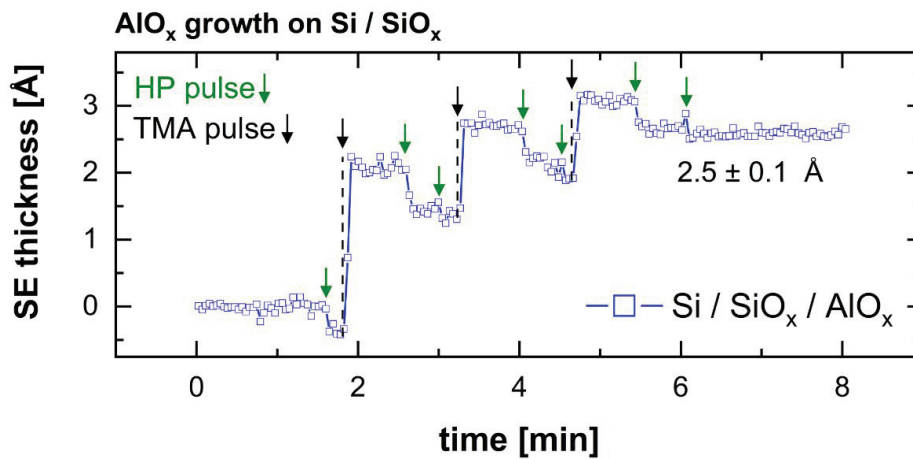
SI Figure 2. TMA/HP AlO$_x$ growth at 200 °C as a function of the deposition time on a highly *p*-doped Si substrate

determined by *in-situ* SE. The black and green arrows indicate TMA injection and HP pluses, respectively. The 3

cycle growth results in an AlO$_x$ thickness of ~ 2.5 ± 0.1 Å.

binding sites necessary for phosphonate surface chemistry. Due to the ultra-thin nature of the PE-

ALD grown AlO$_x$ layer, no remote OP plasma prior to surface functionalization was applied.

12

S2. Water static contact angle (SCA) measurements

Static contact angle (SCA) measurements were performed on the contact angle system OCA 15Pro

(DataPhysics Instruments GmbH, Baden-Wuerttemberg, Germany) under ambient conditions at

room temperature (27.3 ˚C, 32.7 % relative humidity). Data acquisition and evaluation was

performed with the basic module SCA 20 - contact angle (DataPhysics Instruments GmbH, Baden-

Wuerttemberg, Germany, ver. 2.0). To estimate an average Young-LaPlace's contact angle (θ),

1 µL of DI H_2O was dispensed with a rate of 1 µL·s^{-1} from a high-precision syringe (Hamilton, DS

500/GT, gas-tight, 500µl) onto the sample surface and after ~3 s (reaching equilibrium) the side

13

profile of the droplet was taken for further processing. The procedure was repeated at least five times on different spots, except for highly hydrophilic samples, on which only 3 droplets could be placed, and the standard deviation (error) was calculated.

In SI Table 1 an overview of water static contact angles (SCA) for different fabrication stages of the MSA approach is presented. After 3 nm AlO_x growth the surface is rather hydrophilic (10 ± 1°), indicating a high density of OH surface groups. The additional *in-situ* OP activation step further increases the OH density (5.8 ± 0.3°). Interestingly, the small variations suggest a rather homogeneous OH distribution. The OH density is less important for the PA surface chemistry (5), however, a crucial parameter, *e.g.*, for silanization reactions (6). After introduction of the PA anchor layers the water SCA increases slightly compared to an activated surface, which was stored in parallel in vacuum for three days. Notably, the SCA of a PA-C_6 functionalized substrate is roughly 10° larger than of a PA-C_{11} functionalized sample, suggesting a higher disorder in the SAMPs, *i.e.*, the fraction of the surface-exposed alkyl-backbones is higher. Surprisingly, the SCA is increased after probe attachment for both PA types, suggesting that mainly hydrophobic moieties of the molecular complexes are exposed to the surface. The water SCAs of C_6-Re(M1) (69 ± 1°)

14

Appendix

SI Table 1. Water static contact angle (SCA) for different stages of the MSA approach.

System Si / AlO$_X$ (3nm)	Water SCA [°]	Representative image
w/o *in-situ* OP activation	10 ± 1	
in-situ OP activation	5.8 ± 0.3	
in-situ OP activation after 3 d storage in vacuum	47 ± 1	
PA-C$_6$	62 ± 1	
PA-C$_{11}$	52 ± 1	
C$_6$-Re(M1)	69 ± 1	
C$_{11}$- Re(M1)	70 ± 1	
C$_1$-Re(M0)	74 ± 1	

and C$_{11}$-Re(M1 (70 ± 1°) are identical within the experimental error, which might be explained

considering the induced change of the surface morphology upon Re(M1) attachment (**Figure 1**).

15

Here we note that SCA measurements related to the investigation of the surface activation were performed immediately after opening the ALD chamber. However, a slight measurement delay of ~ 5 min could not be avoided.

S3. Atomic force microscopy (AFM) topography and AFM "scratching" of organic overlayers

Standard TM surface imaging (MultiMode 8) was performed with NSG30 cantilevers (single crystal Si, *n*-type (Sb-doped), 0.025-0.01 Ω·cm; TipsNano, Tallinn, Estonia) with a typical nominal tip radius of 8 nm, resonance frequency of ~ 320 kHz and force constant of ~ 40 N·m^{-1}. In TM the integral gain (IG) and the proportional gain (PG) was set to 2 V and 4 V, respectively. TM micrographs were taken with a scan rate of 0.8 Hz and 512 samples/line over an area of 5 × 5 µm^2 and 1 × 1 µm^2. On every sample at least three different areas distributed over the sample surface were measured and the RMS was averaged over all recorded micrographs. We note that contamination, *i.e.*, white agglomerates visible in the inset of **Figure 1d**, are not considered in the surface roughness, as they are not representative of the actual surface morphology. For TM surface imaging and operation in CM (Nanoscope V Controller, Dimension V Controller) Tap190DLC cantilevers (diamond-like-carbon (DLC) tip coating; Budget Sensor, Innovative Solutions

16

Bulgaria Ltd., Sofia, Bulgaria) with a typical nominal tip radius of 15 nm, resonance frequency of

160 kHz and force constant of ~ 60 N·m^{-1} were used. In TM the integral gain (IG) and the

proportional gain (PG) was set to 0.6 V and 3.0 V, respectively. In CM IG was set to 7 V, PG to

16 V, and the deflection setpoint was kept at a constant value of 1 V. Images were taken with a

scan rate of 0.5 Hz and 256 samples/line over an area of 1×1 μm^2 (CM) and 0.8 Hz and 512

samples/line over an area of 3×3 μm^2 (TM). Following an approach described in (2), a tip-sample

force of ~ 0.65 μN was determined. Data processing was performed with Gwyddion (7). The

surface roughness was evaluated as arithmetic mean of root mean square (RMS) value of the height

irregularities.

Appendix
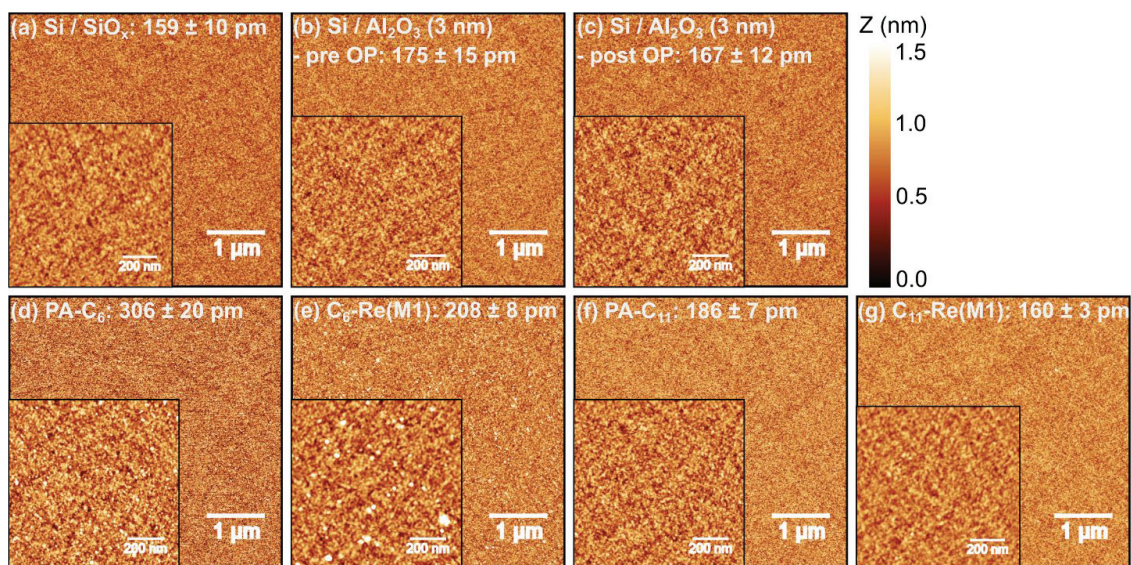
SI Figure 3. Tapping mode atomic force microscopy (AFM) micrographs (5 × 5 μm² and 1 × 1 μm² inset) of a series

of Si substrates after solvent cleaning: before ALD growth (a), after deposition of 3 nm AlO$_x$ (b), and after deposition

of 3 nm AlO$_x$ and *in-situ* OP activation (c), after surface functionalization with the PA-C$_6$ (d) and PA-C$_{11}$ (f) anchors

layers, and after attachment of the molecular complex, C$_6$-Re(M1) (e) and the C$_{11}$- Re(M1) anchors (g). The integrated

in-situ OP activation step does not increase the surface roughness appreciably.

The thickness of the different organic layers was determined from the step heights after removal

of the organic layer in contact mode AFM, which is illustrated for a C$_6$-Re(M1) (SI Figure 4a).

The extracted height profiles, generated by a B-Spline interpolation over 64 pixels (indicated by

the black, dotted arrow in SI Figure 4a), of three different regions disturbed over the same substrate

are shown in SI Figure 4b. Diamond-like carbon (DLC) tips in contact mode are known to be able

to abrade ALD grown aluminum oxide layers (2). Therefore, the applied force regime was chosen

carefully to selectively remove the organic overlayer (SI Figure 4b, black). The comparability of

the three profiles illustrates the homogeneity of the MSA. To increase the
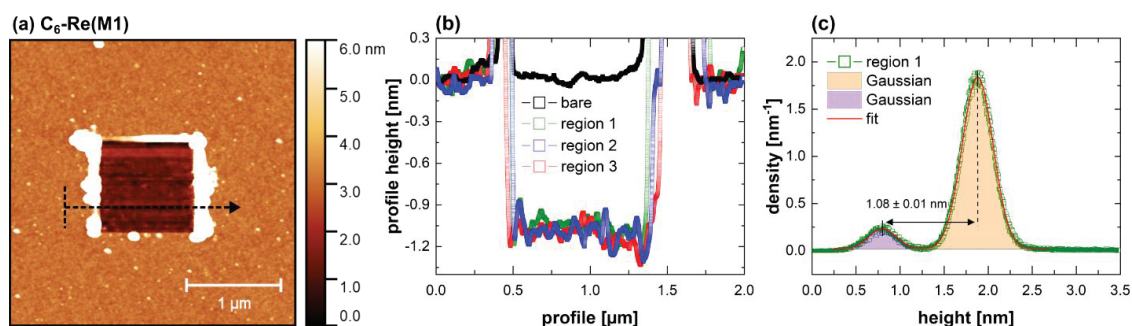
SI Figure 4. Tapping mode AFM micrograph of C_6-Re(M1) on a 3 nm AlO_x-coated Si substrate after removal of ~ 1

× 1 µm^2 of the organic overlayer in contact AFM mode **(a)**. Extracted height profiles of three different regions disturbed

over the same sample indicate the homogeneity of the MSA **(b)**. The applied force regime is sufficient to remove the

organic layers, but not the inorganic substate (black). The height distribution of region 1 shows two distinct Gaussian

shaped peaks, from which an accurate profile step height can be determined **(c)**. Thickness determination from AFM

"scratching" experiments are summarized in **Table 1**.

statistical relevance of the extracted layer thickness, the height distribution over the whole TM

micrograph (**SI Figure 4c**) is determined and fitted to a Gaussian line profile. This approach is

particularly suited for rough surfaces, for which the selection of an accurate baseline can be

difficult, but less appropriate for surfaces with small height variations. The AFM-derived

molecular tilt angle, θ, with respect to the surface normal can be calculated considering **eq. S1**:

$$\theta = arccos\left(\frac{d_{layer}}{l}\right) \text{ (S1)},$$

where d_{layer} is the experimentally determined organic layer thickness and l the length a freely

elongated (interaction-free) organic layer building block (**SI Table 2**). The AFM-derived thickness

and molecular tilt angle of the different organic layer of the MSA are summarized in **Table 1**. The

PA-C_{11} tilt angle (56.4 ± 0.3˚) is in good agreement with a previous result of 54˚ obtained on a

SiO_2-termiated silicon surface (8). Interestingly, the molecular tilt of both PA anchors is rather

19

similar ($\Delta\theta = 1.0 \pm 0.4°$). Considering that the attachment of the molecular complexes does not induce a significant structural change in the underlying PA anchor layers, which will be investigated by X-ray reflectivity in more detail, a complex layer thickness of 0.53 ± 0.17 nm (C_6-Re(M1)) and 0.59 ± 0.16 nm (C_{11}- Re(M1)) can be determined, which corresponds to a molecular tilt angle of $54.9 \pm 0.2°$ and $50.2 \pm 0.2°$, respectively.

20

S4. Quantum-Chemical Calculations (QCC): Optimized structure, coverage, and physical

density of PA anchor molecules and molecular complexes
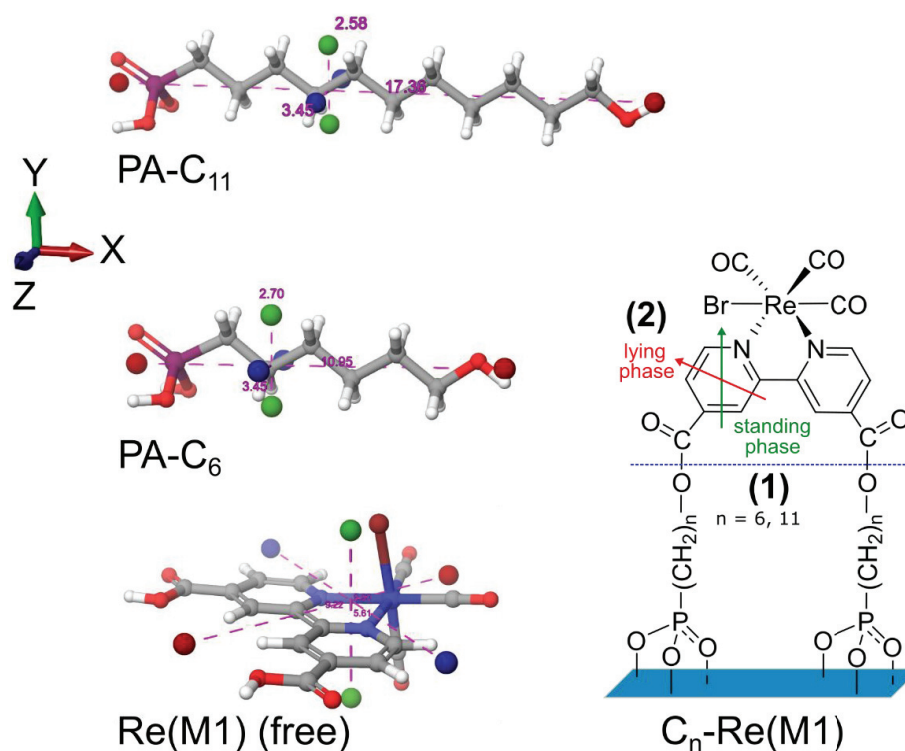
SI Figure 5. Chemical structure of 6-hydroxyhexylphosphonic acid (PA-C$_6$), 11-hydroxyundecylphosphonic acid (PA-C$_{11}$), and Re(2,2'-bipyridine-4,4'-dicarboxylic acid)(CO)$_3$Br (Re(M1) (free)) optimized on PBE0-D3/def2-TZVP level of theory (left-hand part of **SI Figure 5**). Optimized molecular geometries (presented in **SI Table 2**) are used to determine a theoretical monolayer (ML) coverage and physical ML density.

In **SI Figure 5** the structure of the two unbound PA anchor molecules and the unbound molecular complex (Re(M1)) is presented. Structures were optimized on PBE0-D3/def2-TZVP (9-12) level of theory using the TURBOMOLE (13,14) program package version V7.3, assuming an

22

interaction-free unit. The obtained structural parameters for the individual units are presented in

SI Table 2.

SI Table 2. Overview of the molecular geometries and theoretical monolayer (ML) coverage and physical ML density calculated on PBE0-D3/def2-TZVP level of theory compared to experimentally determined values. The molecular tilt angles (in brackets) are used to calculate the theoretical, angle-dependent coverage.

System	X [Å]	Y [Å]	Z [Å]	$N_{\theta=0°}$ [nm^{-2}] (standing)	$N_{\theta=90°}$ [nm^{-2}] (lying)	$N_{\theta/\alpha=X°}$ [nm^{-2}] (<u>AFM</u>/NEXAFS)	$\rho_{PA/Re(ML)}$ [g·cm^{-3}]
PA-C$_6$	10.95	2.70	3.45	10.74	2.65	5.57 ± 0.01 (at 57.40 ± 0.1˚)	2.97
PA-C$_{11}$	17.36	2.58	3.45	11.24	1.67	5.26 ± 0.03 (at 56.43 ± 0.3˚)	2.71
C$_6$-Re(M1)	9.22	9.90	5.61	1.90	1.10	<u>1.43 ± 0.01</u>/1.58 ± 0.29 (at <u>54.91 ± 0.2˚</u>/34 ± 7˚)	1.84
C$_{11}$-Re(M1)	9.22	9.90	5.61	1.90	1.10	<u>1.43 ± 0.01</u>/1.62 ± 0.33 (at <u>50.22 ± 0.2˚</u>/38 ± 7˚)	1.84

Under the assumption that all molecular unit cells can be approximated by a cuboid and are densely

packed, *i.e.*, no overlap and no spacing between individual unit cells, the monolayer (ML) physical

23

density, $\rho_{PA/Re(ML)}$, which describes the physical density of a single PA or molecular complex

layer, respectively, can be calculated using **eq. S2**:

$$\rho_{PA/Re(ML)} = \frac{N_\theta \cdot M_{PA/Re(ML)}}{N_A \cdot V_{PA/Re(ML)}} \text{ (S2)},$$

where N_θ is the tilt angle-dependent, ML surface coverage defined by the projection of the

respective unit cell on a two-dimensional surface, $M_{PA/Re(ML)}$ the ML molar mass of the PA anchor

and the molecular complex, respectively, if the oxygen atoms of ester bonds are attributed to the

PA anchor layer (blue, dotted line in **SI Figure 5**), N_A the Avogadro constant, and $V_{PA/Re(ML)}$ the

respective ML unit cell volume. Two boundary conditions can be identified: the molecules are

oriented in a standing phase **(1)**, *i.e.*, the PA backbone and the bipyridine moiety of the molecular

complexes are parallel to the surface normal ($\theta = 0°$) or in a lying phase **(2)**, *i.e.*, the PA backbone

and bipyridine moiety of the molecular complexes are perpendicular to the surface normal ($\theta =$

90°). The respective values for these upper and lower limits are shown in **SI Table 2** and compared

to AFM results. We note that the physical ML density of the PA anchor and the Re complex layer

will change upon surface grafting. However, the presented methodology is plausible, since the

calculated ML coverages are in good agreement with other experimentally derived values (*e.g.*, by

24

XPS) and, therefore, serve as a good approximation to set physical meaningful boundary

conditions.

25

Appendix

S5. X-ray reflectivity (XRR) experimental procedure and data processing methodology for organic layer thickness determination

The intensity of measured reflectivity curves was normalized to 1 and the scattering angle, 2θ, converted to the scattering vector, q, via $q = \frac{4\pi}{\lambda}\sin\left(\frac{2\theta}{2}\right)$. The range of q extended up to $q_{max} \approx 0.7$ Å^{-1}, implying that the scattering length density (SLD) distribution normal to the surface can be decomposed in layers with a resolution of approximately 4 Å (15). The SLD profiles were modelled by the refnx software package, which converts the SLD profile to a theoretical reflectivity curve using Abeles' formalism. A differential evolution algorithm was used for fitting. To estimate the uncertainties of individual fitting parameters, the last fitting step was performed by a Bayesian Markov-chain Monte Carlo sampling, which yielded approximations of the standard deviation for all parameters (16). We used a four-layer slab model to describe the SLD profile on the Si/SiO$_x$ substrate. After the backing, $i.e.$, the bulk silicon, we simulated a silicon dioxide (SiO$_2$) layer, which is the predominant stoichiometry of the native silicon oxide (**SI Figure 7**), followed by an AlO$_x$ layer and two surface layers. All parameters are summarized in **SI Table 3**.

A clear discrimination of the signal originating from an ultrathin organic layer (PA-C$_6$ thickness ~ 0.6 nm (AFM, **Table 1**)) is challenging due to the apparent layer resolution of 0.4 nm and the AlO$_x$

26

surface roughness of 3.5 ± 0.2. Contrarily, the molecular complexes with the heavy (Z = 75) Re

metal centers possess an excellent scattering contrast. Therefore, we composed the "surface layers"

so that the mean value of their SLDs add up to the theoretical C_n-Re(M1) SLD value obtained from

their respective molecular structure (determined by QCC (**S4**) and verified by XPS measurement

(**SI Table 4** and **5**) to reduce the fitting parameters' degree of freedom. Furthermore, surface layer

1 is created with a low SLD, necessary to create a sufficient scattering contrast to simulate a sharp,

delta peak-like slab for the Re metal center. The parameters for the SiO_2 layer were obtained from

the mean values of five different reference systems (Si/AlO$_x$ (3 nm) and Si/AlO$_x$ (3 nm) / PA-C_n)

(not shown).

To determine the distance from the metal centers of the molecular complexes to the AlO$_x$-coated

substrate surface, obtained SLD profiles were modeled by a Gaussian peak representing the Re

complex and an error function (erf) representing the Si/AlO$_x$ substrate. The distance to the surface

was calculated *via* the spacing from Gaussian peak center to the inflection point of the error

function. Individual XRR measurements can take several hours, in which the samples are exposed

to the ambient. We note that no detectable variations of the measurement signal were observed,

indicating the high stability of the assembled layers.

27

SI Table 3. Overview of thickness, SLD, and roughness determined by X-ray reflectivity (XRR) measurements (**Figure 2**) of C_6-Re(M1) and C_{11}- Re(M1) on 3 nm AlO_x-covered Si substrates, by fitting the XRR data to a four-layer SLD model. Values marked in blue were kept constant during the fitting process and errors correspond to the standard

28

deviation. The SiO_2 parameters were obtained from the mean values of five different reference systems (Si/AlO$_x$ (3

nm) and Si/AlO$_x$ (3 nm) / PA-C$_n$).

Si/AlO$_x$ (3nm)		C$_6$-Re(M1)	C$_{11}$-Re(M1)
Surface layer 2	thickness (Å)	4.1 ± 2.3	6.3 ± 1.8
	SLD (10^{-6} Å^{-2})	21.4	21.4
	roughness	6.8 ± 1.1	7.3 ± 1.9
Surface layer 1	thickness (Å)	13.7 ± 3.4	13.1 ± 1.0
	SLD (10^{-6} Å^{-2})	7.4	7.4
	roughness	9.3 ± 2.4	3.0 ± 0.4
AlO$_x$	thickness (Å)	26.4 ± 1.2	29.2 ± 2.4
	SLD (10^{-6} Å^{-2})	25.7 ± 1.3	25.8 ± 1.7
	roughness	3.6 ± 0.3	4.3 ± 0.8
SiO$_2$	thickness (Å)	22.7	22.7
	SLD (10^{-6} Å^{-2})	21.4	21.4
	roughness	5.0	5.0
Si	SLD (10^{-6} Å^{-2})	19.8	19.8
	roughness	0	0
χ^2		3.6	2.9

29

S6. Near edge X-ray absorption fine structure (NEXAFS) determination of the molecular orientation for different Re complex surface layers

For NEXAFS data acquisition, the N K-edge spectrum was divided into three different regions with varying photon energy step size to reduce the overall scan duration and allow higher resolution in the main region of interest. Spectra were recorded at an angle of incidence, θ, of 90, 60, and 30° (with respect to the surface plane), by rotating the sample holder with an estimated accuracy of ± <1°. All N K-edge spectra were normalized to the current, I_0, which was measured by total-electron-yield (TEY) from a freshly coated gold (Au) grid with a typical transmittance of 25 %, placed in the optical X-ray beam path to the sample. Technical details of the BACH end station can be found in (17). The photon energy was calibrated by applying a linear interpolation of the Au $4f_{7/2}$ core level binding energy obtained from an Au-coated part of the manipulator before

30

and after each NEXAFS experiment (start and end photon energy of the N K-edge scan range).

Following a standard analysis procedure (18), all spectra were divided by the respective clean

background spectrum, and the pre-edge and post-edge signals were set to 0 and 1, respectively.

In **SI Figure 6**, the N K-edge spectra of C_6-Re(M1) (blue) and C_{11}-Re(M1) (cyan) **(a)** as well as of

a C_1-Re(M0) (grey) **(b)** on 3 nm AlO_x-covered Si substrates are shown for $\theta = 90°$, 60°, and 30°

along with the difference spectrum (linear dichroism) between the 30° and 90° spectra (denoted as

30°-90°). A strong and relatively sharp $1\pi^*$ resonance present in all N K-edge spectra was

attributed to the N 1s $\rightarrow \pi^*$ resonant transition of the aromatic nitrogen in the bipyridyl moiety

(19) and used to evaluate the molecular orientation of the molecular complex. With ~ 399.3 eV,

the resonance is found at higher photon energies compared to a single bipyridine molecule (397.7

eV) (19), which is, however, in good agreement with surface-confined heterometallic molecular

31
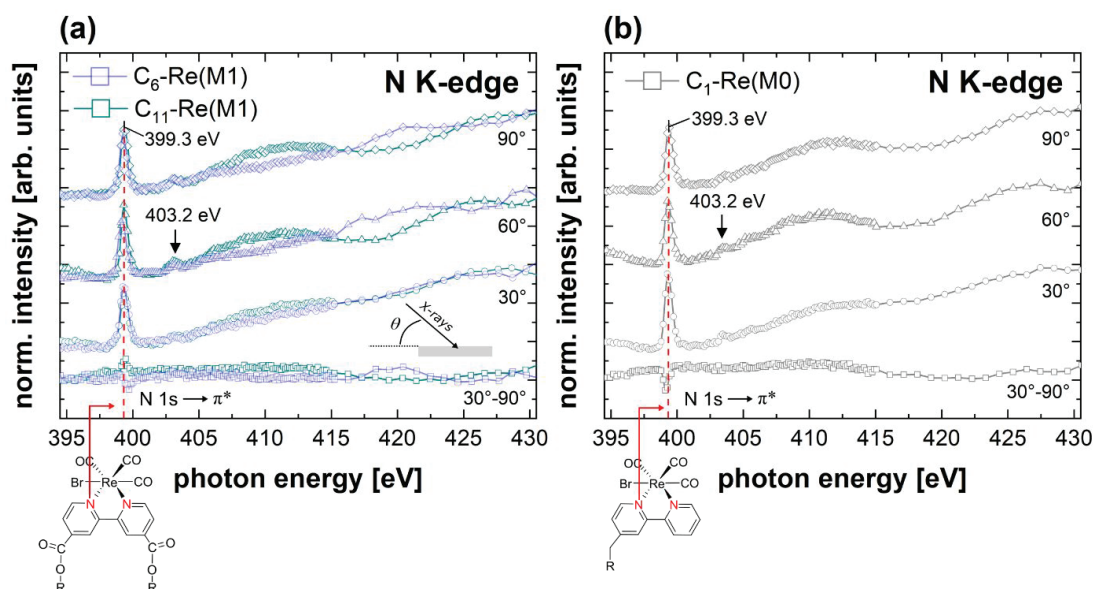
SI Figure 6. N K-edge NEXAFS spectra of C_6-Re(M1) (blue) and C_{11}-Re(M1) (cyan) **(a)** as well as a C_1-Re(M0) (grey) **(b)** on 3 nm AlO$_x$-covered Si substrates for photon incident angles, θ, of 90˚, 60˚, and 30˚ (with respect to the surface plane) along with the difference spectrum between the 30˚ and 90˚ spectra (denoted as 30˚-90˚). The spectra are vertically stacked for clarity. The strong 1π* resonance at ~399.3 eV, arising from a N 1s → π* transition of the aromatic nitrogen in the bipyridyl moiety, was used to evaluate the molecular orientation. Both MSA systems and the directly attached molecular complex exhibit a small, but measurable dichroism, which may be indicative of a preferential surface orientation.

dyads comprised of terpyridyl-based Ru complexes (399.6 eV) (20). A weaker resonance feature is found at ~ 403.2 eV, which we attribute to a transition into a higher energy, unoccupied, $π^*$, molecular orbital (21). Both the modular assembled and the directly attached molecular complex

32

exhibit a small, but notable dichroism, which may indicate a preferential orientation of the molecules. Considering a threefold or higher substrate symmetry and an X-ray polarization factor, P, of 1, the NEXAFS-derived molecular tilt angle with respect to the surface plane, α_S, can be determined using **eq. S3** (18):

$$I_v \approx \left[1 + \tfrac{1}{2}\left(3\cos^2(\theta_p) - 1\right)\left(3\cos^2(\alpha_S) - 1\right)\right] \text{ (S3)},$$

where I_v is the resonance intensity and θ_p the photon angle of incidence with respect to the surface plane. The fitting analysis yields molecular tilt angles of 56°, 52°, and 58°, also, for the C_6-Re(M1), the C_{11}-Re(M1), and C_1-Re(M0), respectively. Generally, a large inaccuracy is related to the normalization of the NEXAFS data (18). We empirically estimate the error of the molecular tilt angles by repeating the data analysis with other procedures reported in the literature (22) and find that the results can be reproduced within a variation of ≤ 7°. Thus, the molecular tilt angle with respect to the surface normal, α_N, is 34 ± 7°, 38 ± 7°, and 32 ± 7° for C_6-Re(M1), the C_{11}-Re(M1), and C_1-Re(M0), respectively. We note that NEXAFS is a spatial averaging technique and that the derived tilt angles, α_S, are close to the magic angle of 54.7° (*vide supra*), which can be related to either a random orientation or to a mean orientation averaged over several distinct surface orientations. The occurrence of π-π stacking between individual bipyridyl moieties is documented

33

(23), suggesting that the formation of ordered domains within the Re(M1) terminal layer with tilt angles close to the magic angle is possible. We note, however, that the accuracy of a NEXAFS-derived molecular tilt angles increases significantly, if an angular distribution far from the magic angle, *i.e.*, either flat or upright, is adopted.

S7. X-ray photoelectron spectroscopy (XPS)-based oxide thickness and molecular coverage determination

All recorded spectra were processed with CasaXPS (Casa Software Ltd, ver. 2.3.19) by subtracting a Shirley background, followed by fitting the photoemission lines to synthetic components modelled by pseudo-Voigt (Gaussian-Lorentzian product) functions. The photoelectron intensity

34

was corrected by taking the transmission function of the analyzer and the respective relative

sensitivity factor (RSF; CasaXPS KratosAxis-F1s and Scofield cross sections-based (24) CasaXPS

C1s library, respectively) of the element and the corresponding orbital transition into account. The

intensity was further normalized over the total number of counts, integrated over all the relevant

element peaks. A detailed description of the XPS data processing can be found elsewhere (25).

The processed XPS data was further used to determine the coverage of the PA anchors and the

molecular complex (*vide infra*).

SI Figure 7 shows X-ray photoelectron spectroscopy (XPS) high resolution spectra of the Si 2p

region for a Si / SiO$_x$ before **(a)** and after deposition of a 3 nm AlO$_x$ overlayer **(b)** together with

the respective fit solution. To illustrate changes in the SiO$_x$ composition the two Si 2p spectra are

overlayed in **SI Figure 7c**. The SiO$_x$ layer thickness, d_{ox}, was calculated using **eq. S4** by following

a method described by Strohmeier (26) and Carlson (27):

$$d_{ox} = \lambda_{ox}\sin\theta\ln\left(\frac{N_s\,\lambda_s\,A_{ox}}{N_{ox}\lambda_{ox}\,A_s} + 1\right) \text{(S4)},$$

where λ_{ox} is the inelastic mean free path (IMFP) of Si 2p photoelectrons with a kinetic energy of

1383 eV in SiO$_2$ (3.77 nm) and in Al$_2$O$_3$ (3.77 nm), respectively, θ is the photoelectron take-off

angle between the sample surface and the electron analyzer (90˚), N_s (4.997·10^{22} cm^{-3}) and N_{ox}

35

($2.201 \cdot 10^{22}$ cm^{-3}) are the volume densities of atoms in bulk silicon and the native silicon oxide, and A_s and A_{ox} are the transmission-corrected, integrated intensities of the substrate (s) and oxide layer components (ox) of the Si 2p core level, respectively. Considering a predominant SiO$_2$ stoichiometry of the native silicon oxide (**SI Figure 7a**), the volume density, $N = \rho \cdot M$, was calculated using the physical density, ρ, determined from the SLD values presented in **SI Table 3** and the molar mass, M. A molar mass of 28.09 g·mol^{-1} and 60.08 g·mol^{-1} and a density of 2.330 g·cm^{-3} and 2.196 g·cm^{-3} were used to calculate the volume densities of Si and SiO$_2$, respectively.

The IMFPs were calculated based on the work of Werner (28), using the TPP-2M (Tanuma-Powell-Penn) method (29) in the NIST database (30) by assuming an AlO$_{1.5}$ stoichiometry (**SI Figure 7d** and **e**). The determined SiO$_x$ thickness on bare (solvent cleaned) Si of 1.46 ± 0.02 nm is in excellent agreement with the thickness obtained by *in-situ* SE measurements after the initial HP pre-treatment (**S1**). During ALD growth the SiO$_x$ thickness is increased appreciably by 0.46 ± 0.04 nm, attributed to the formation of a mixed SiO$_x$ / AlO$_x$, interlayer mainly consisting of Si^{3+}-species (**SI Figure 7b** and **c**) and is, thus, slightly lower compared to the thickness obtained from XRR measurement (2.27 nm). In addition, the SiO$_2$ component (light cyan) is slightly decreased, suggesting that the mixed interlayer protrudes into the native oxide layer of the underlying Si

substrate. We note that surface contaminants, such as adventitious carbon or the presence of an

aluminum oxide and the modular assembled organic overlayers should not significantly impact the

SiO_x thickness determination, since the kinetic energy range of the emitted photoelectrons is only

3.41 eV and, therefore, the corresponding signal attenuation is comparable.

Following a procedure introduced by Kim *et al.* (31) and recently refined in (2), the number of

phosphorus (P) and rhenium (Re) atoms and, therefore, the PA anchor molecules and molecular

complexes per unit area N_p and N_{Re} can be determined using **eq. S5**:

$$N_{P,Re} = \frac{A_{P2p/Re4f}}{A_{Si2p}} \cdot \frac{RSF_{Si2p}}{RSF_{P2p/Re4f}} \cdot \rho_{Si} \cdot \lambda_{Si2p,Si} \cdot sin(\theta) \cdot \frac{e^{\frac{d_{OL}}{\lambda_{P2p/Re4f,organic} \cdot sin\theta}}}{e^{\frac{d_{OL}}{\lambda_{Si2p,organic} \cdot sin\theta}}} \text{ (S5),}$$

where $A_{P2p/Re4f}$ and A_{Si2p} are the integrated, transmission-corrected P 2p/Re 4f and Si 2p XPS

intensities, $RSF_{P2p/Re4f}$ and RSF_{Si2p} (0.486/3.96 and 0.328; 1.192/11.08 and 0.817) the

corresponding relative sensitivity factors (RSF) taken from the CasaXPS KratosAxis-F1s and

Scofield cross sections-based (24) CasaXPS C1s library, respectively, ρ_{Si} the number of Si atoms

per unit volume, $\lambda_{Si2p,Si}$ (3.16 nm) the IMFP of Si 2p photoelectrons in Si (28-30), d_{OL} the thickness

of the organic overlayer, $\lambda_{P2p/Re4f,organic}$ and $\lambda_{Si2p,organic}$ the IMFPs of the P 2p/Re 4f and Si 2p

photoelectrons in the organic overlayer, respectively. θ is the take-off angle of photoelectrons with

respect to the sample plane (θ = 90˚). We note that the KratosAxis-F1s RSF account for element-

37

specific photoionization cross sections and, amongst other parameters, for the device-specific

transmissions function, whereas the Scofield cross sections-based RSF account only for the

photoionization cross sections. In addition, the RSF presented above can be applied only for a

source-to-detector geometry of 54.7˚.

Using an empirical approximation for the IMFP in self-assembled overlayer from a previous study

(32), $\lambda_{X,organic}$ [nm] = 0.9 + 0.0022 · E_{kin} [eV], where X is the photoelectron transition of interest

and E_{kin} [eV] the corresponding kinetic energy in electron volts, we find that $\lambda_{P2s,organic}$ = 3.75 nm

≈ $\lambda_{P2p,organic}$ = 3.88 nm ≈ $\lambda_{Re4f,organic}$ = 4.07 nm ≈ $\lambda_{Si2p,organic}$ = 3.95 nm and neglecting surface

roughness (33), the exponential term in **eq. S5** can be approximated by $\dfrac{e^{\frac{d_{OL}}{\lambda_{P2p/Re4f,\,organic} \cdot \sin\theta}}}{e^{\frac{d_{OL}}{\lambda_{Si2p,\,organic} \cdot \sin\theta}}} \approx 1$, with

less than an error of 5 % for d_{OL} < 4 nm (31). To account for the attenuation of the Si 2p signal

(Si^0, E_{kin} = 1383 eV) due to the native silicon oxide and aluminum oxide overlayers **eq. S6** (34)

was used:

$$A_{Si2p} = A_{Si2p}^{\infty} \cdot e^{\frac{-d_{SiOx/AlOx}}{\lambda_{Si2p,SiOx/AlOx} \cdot \sin\theta}} \text{ (S6)},$$

where A_{Si2p}^{∞} is Si 2p peak area of an oxide free substrate, $d_{SiOx/AlOx}$ the thickness of the SiO$_x$ and

AlO$_x$ overlayer, respectively, and $\lambda_{SiOx/AlOx}$ the IMFP of Si 2p photoelectrons in SiO$_x$ (3.767 nm)

38

and AlO_x (3.768 nm for Al_2O_3), respectively. Since the stoichiometry and density of AlO_x layer <

3 nm are unknown, we compared the Si 2p signal intensity of freshly HF-etched Si, Si with an

SiO_x layer to the Si 2p signal of a series of Si substrates covered by AlO_x films of different

thickness. Using **eq. S6** the apparent IMFP of the different AlO_x layers were calculated: 0.90 nm

(~ 0.25 nm AlO_x), 1.05 nm (~0.45 nm AlO_x), 2.13 nm (1 nm Al_2O_3), and 2.83 nm (3 nm AlO_x).

The apparent IMFP obtained for a 3 nm AlO_x layer is close to the calculated IMFP of 2.65 nm

(deviation of 6.4 %) for bulk Al_2O_3 using the NIST database (28-30), indicating the validity of our

approach.

39
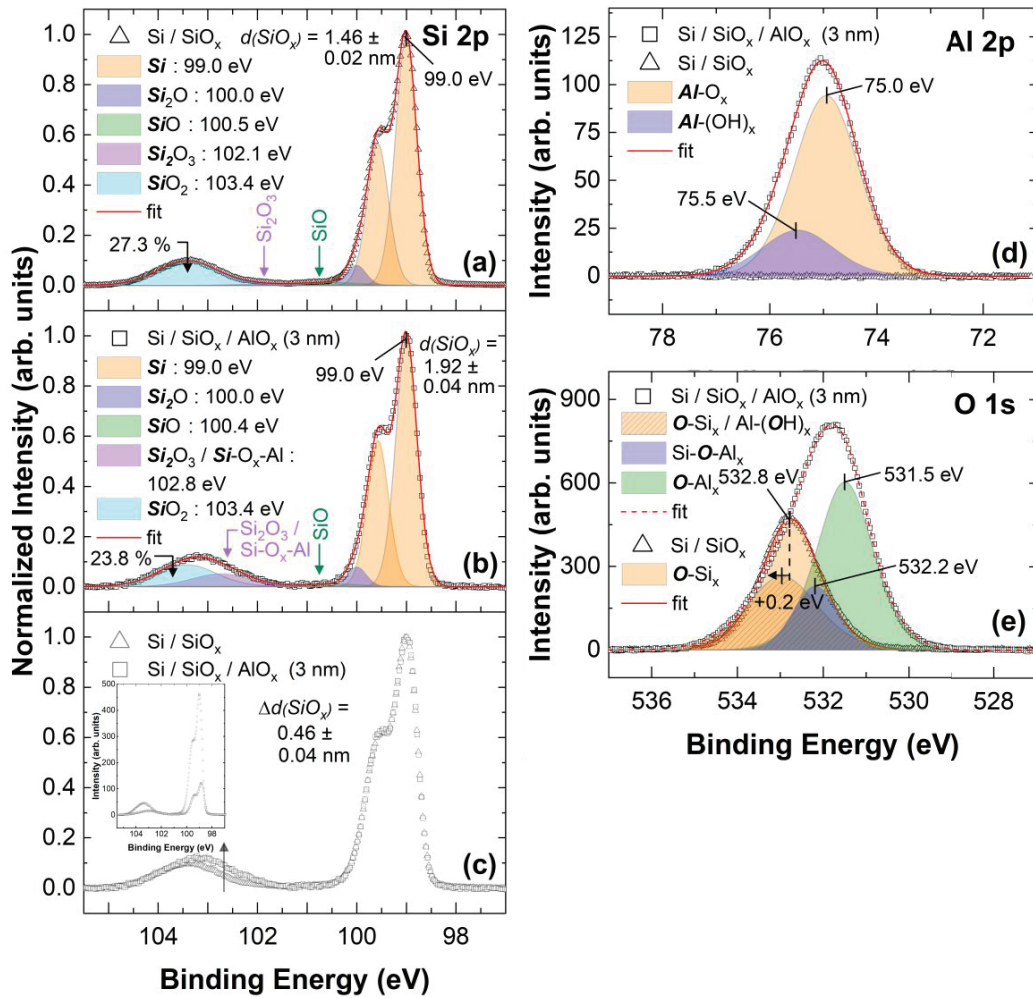
SI Figure 7. High resolution X-ray photoelectron spectroscopy (XPS) spectra of the Si 2p region for a Si substrate covered by a thin native oxide layer (Si / SiO_x) before **(a)** and after deposition of a 3 nm AlO_x overlayer **(b)** together with the best fit solution (red). The Si 2p spectra are overlaid to illustrate changes in the SiO_x composition **(c)**. To increase visibility XPS intensities are normalized to one, whereas the inset in **(c)** shows the relative intensity. After ALD growth the SiO_x thickness is increased by 0.46 ± 0.04 nm, which is attributed to the formation of a mixed SiO_x / AlO_x interlayer, mainly consisting of Si^{3+}-species **(b)**. Corresponding high resolution spectra of the Al 2p **(d)** and O 1s region **(e)**, together with the respective best fit solutions (red).

40

Appendix
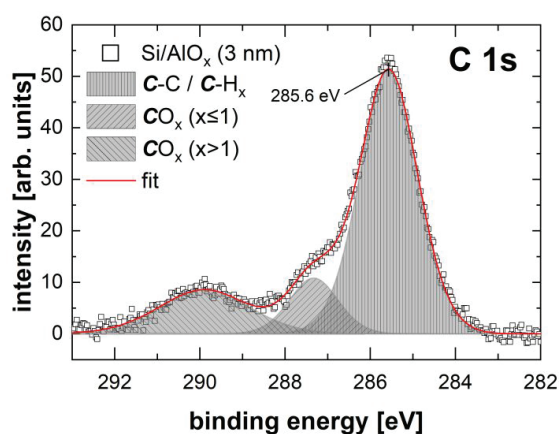
SI Figure 8. High resolution XPS spectra of the C 1s region, together with the best fitting solution for an unfunctionalized Si substrate covered by a 3 nm AlO_x overlayer. The identified components are used to refine the fit of the PA-C_6 C 1s spectrum presented in **Figure 4a**.
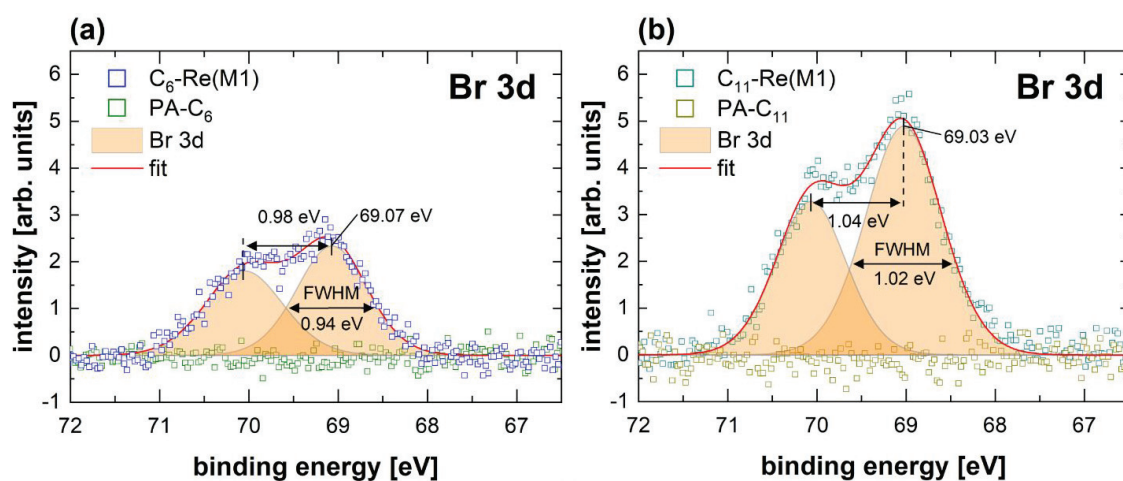
SI Figure 9. Representative high resolution XPS spectra of the Br 3d region, together with the best fitting solution for

PA-C$_6$ and C$_6$-Re(M1) (a) as well as PA-C$_{11}$ and a C$_{11}$-Re(M1) (b) on Si substrates covered by a 3 nm AlO$_x$ layer.

After the attachment of the molecular complexes, the presence of bromine (Br) in one distinct chemical environment

can be confirmed.

SI Table 4. Overview of the phosphonic acid (PA) and molecular complex surface coverage obtained from XPS

measurements for a series of differently functionalized, AlO$_x$-coated Si substrates. Apart from C$_1$-Re(M0), the PA

coverage is obtained from uncoupled PA anchors layer (no attached molecular complexes). The AlO$_x$ coverage on the

micropatterned Si is ~ 47 %, as determined from AFM measurements. For comparison, the obtained PA loading is

scaled to a 100 % AlO$_x$ coverage.

AlO$_x$ thickness	surface functionalization	PA coverage [nm^2]	Re coverage [nm^2]	PA/Re ratio
3 nm	C$_1$-Re(M0)	1.79	1.87	0.96
	C$_6$-Re(M1)	5.89	0.61	9.66
	C$_{11}$- Re(M1)	6.19	1.24	4.99
1 nm	C$_{11}$- Re(M1)	5.86	1.30	4.51
0.45 nm (patterned)	C$_{11}$- Re(M1)	4.22	1.06	3.98

0.25 nm (sub-ML)	C$_{11}$- Re(M1)	2.28	0.55	4.15

SI Table 5. Theoretical (in brackets) and experimental carbon ratios, obtained from the molecular structure and from

XPS measurements presented in **Figure 4**, respectively. Components A and B are related to the carbon moieties of the

PA backbone and end group, respectively, whereas components C, D, and E are attributed to the molecular complex

(Re(M1)): bipyridine moieties, neighbors to the ester group and carbonyl ligands, and the ester group, respectively

(compare insets in **Figure 4c** and **d**). Errors correspond to the standard deviation considering three different samples

of each PA type.

43

Components Surface functionalization	A	B (set to 1)	C/P		
PA-C$_6$	5.01 ± 0.05 (5)	1 ± 0.01 (1)	6.78 ± 0.12 (6)		
PA-C$_{11}$	10.77 ± 0.04 (10)	1 ± 0.14 (1)	11.27 ± 0.71 (11)		
	A	C	D	E (set to 2)	N/Re
C$_6$-Re(M1)	13.18 ± 0.31 (10)	8.01 ± 0.31 (8)	7.55 ± 0.31 (7)	2 ± 0.31 (2)	3.47 ± 0.13 (2)
C$_{11}$-Re(M1)	21.02 ± 0.39 (20)	9.04 ± 0.30 (8)	7.68 ± 0.20 (7)	2 ± 0.07 (2)	2.99 ± 0.07 (2)

Theoretical (in brackets) and experimental carbon ratios are in good agreement with the chemical structure of the PA anchors and slightly overestimated for the molecular complexes. We explain this overestimation with the BE difference between carbon moieties of metallized and metal-free (demetallized) bipyridine, by considering the observed N 1s redshift of the pyridinic nitrogen by ~ 1.2-1.4 eV after removal of the Re metal center (**Figure 4 e** and **f**). For C$_{11}$-Re(M1), for example, the amount of pyridinic nitrogen (free pyridine) is 25.9 ± 1.6 %. Component D possesses four carbon moieties, assuming 3 CO ligands are lost upon demetallization. If we consider that 26 %

44

143

of the complexes a metal free and a BE redshift occurs, an additional 1.04 carbon moieties should

be observed in component C, which agrees well with the determined overestimation of 1.04 ± 0.3.

45

SI Table 6. Overview of the relative binding energy (BE) shift vs. the BE of a Re(M1) (free) powder sample drop-casted on a platinum (Pt) surface. Values marked in blue were obtained by non-monochromatic X-ray source (**see Exp. Section**). If present, errors correspond to the standard deviation considering at least three different measurements. [#]The signal-to-noise ratio was insufficient for a reliable fitting solution of the Br 3d doublet. [%]A Cr/Au (15/150 nm) layer was grown on top of a Si substrate by physical vapor deposition and a thin layer of uncoupled PA-modified bipyridine ligands (PA-C_1-Bpy; **SI Scheme 1**) was deposited on the Au-covered surface *via* drop-casting (physisorption).

AlO_x thickness	surface functionalization	Re $4f_{7/2}$ [eV]	N 1s [eV]	Br $3d_{5/2}$ [eV]	C 1s (CO_2X) [eV]	N 1s - Re $4f_{7/2}$ [eV]
3 nm	C_1-Re(M0)	0.87	0.74	0.79	N/A	358.65
3nm	C_6-Re(M1)	1.12 ± 0.01	1.18 ± 0.02	1.14 ± 0.07	1.00 ± 0.01	358.93 ± 0.02
	C_6-Re(M1)	1.22	1.04	0.90	0.97	358.69
	C_{11}-Re(M1)	1.14 ± 0.05	1.13 ± 0.05	1.02 ± 0.01	1.00 ± 0.04	358.86 ± 0.07

46

	C$_{11}$-Re(M1)	1.18	1.02	0.92	0.90	358.72
1 nm	C$_{11}$-Re(M1)	1.06	0.99	0.86	1.00	358.79
0.45 nm (patterned)	C$_{11}$-Re(M1)	1.29	0.90	0.88	0.79	358.49
0.25 nm (sub-ML)	C$_{11}$-Re(M1)	1.07	0.55	1.06	#	358.86
Pt	*Re(M1) (free)*	*41.45 ± 0.14*	*400.24 ± 0.03*	*68.17 ± 0.01*	*289.17 ± 0.11*	*358.79 ± 0.14*
Au$^{%}$	*PA-C$_I$-Bpy*	*N/A*	*399.85 ± 0.07*	*N/A*	*N/A*	*N/A*

S8. Attenuated total reflectance Fourier-transform infrared (ATR-FTIR) spectroscopy of differently modified molecular complexes

47
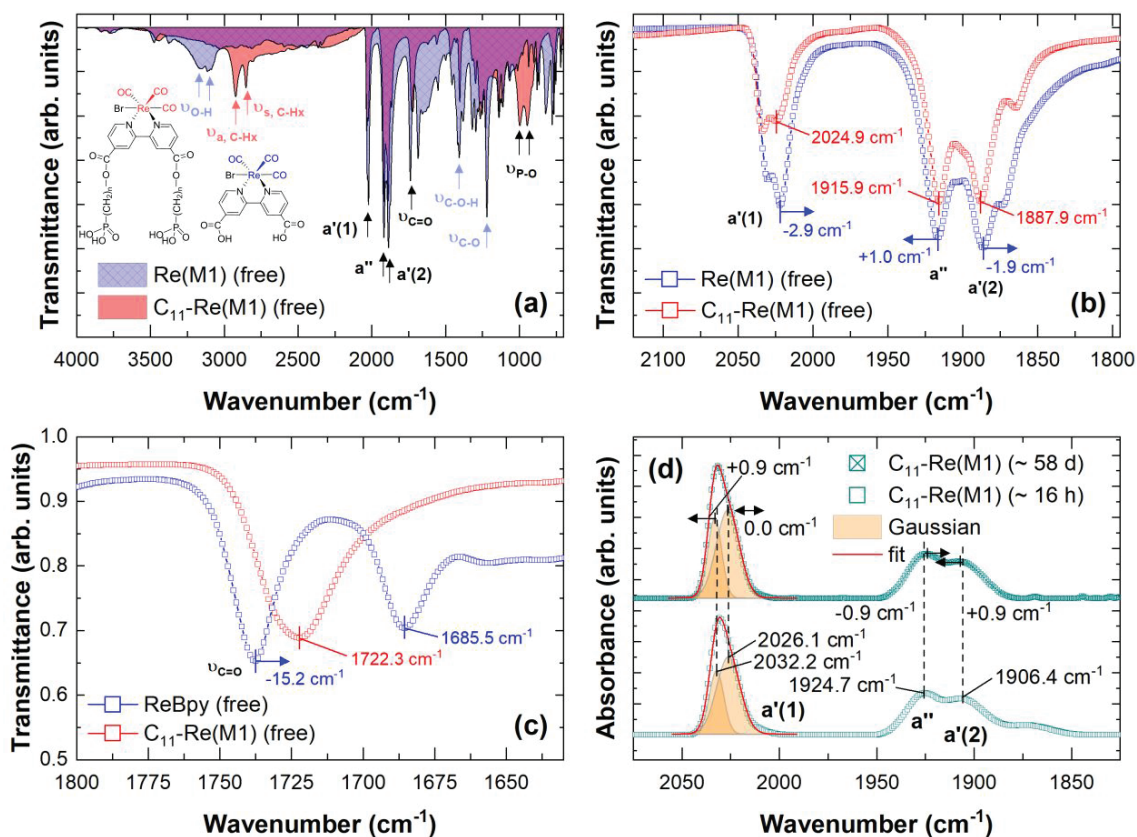
SI Figure 10. Attenuated total reflectance-Fourier transform infrared (ATR-FTIR) powder spectra of an unbound and uncoupled molecular complex (Re(M1) (free); blue) and an unbound molecular complex coupled to PA-C_{11} anchor molecules (C_{11}-Re(M1) (free); red) **(a)**. Corresponding ATR-FTIR spectra of the three Re-carbonyl (C=O) stretching modes: in-phase symmetric a′(1), antisymmetric a″, and out of-phase symmetric a′(2) stretch **(b)** and the C=O stretching mode of the carboxylic acid and ester functionality, respectively **(c)**. The inset in **(a)** shows a sketch of the two molecular complexes. ATR-FTIR spectra of the Re-C=O stretching modes for C_{11}-Re(M1) on a 3 nm AlO_x-covered Si substrate after ~ 16 h (cyan, open squares) and after ~ 58 d (cyan, crossed squares) post-fabrication.

SI Figure 10 shows representative ATR-FTIR powder spectra of an unbound and uncoupled

molecular complex (Re(M1) (free); blue) and an unbound molecular complex coupled to PA-C_{11}

anchor molecules (C_{11}-Re(M1) (free); red). A sketch of the two molecular complexes is provided

in the bottom left corner of **SI Figure 10**. The most relevant vibrational modes are labeled in **SI**

Figure 10a. In particular, the loss of the υ_{O-H} and the appearance of υ_{C-H} and υ_{P-O} is indicative of a

complete coupling between the Re(M1) (free) and the PA anchor. **SI Figure 10b** depicts a

magnification of the spectral region attributed to the Re-carbonyl (C=O) stretching modes with

three distinct features: in-phase symmetric a′(1), antisymmetric a″, and out of-phase symmetric

a′(2) stretch (35). The attachment of Re(M1) to the PA anchor has little effect on the Re-CO

vibrational modes' maxima and relative intensities, although a slight relative decrease of the a′(1)

stretching mode and an intensity inversion of the a′(1) doublet can be observed. By a relative

decrease, we refer to an intensity decrease of the specific vibrational mode relative to the other

modes and compared to the uncoupled molecular complex. In the unbound state, the orientation of

the PA anchor groups relative to the molecular complex is on average completely random and

changes of the Re-CO spectral modes cannot unambiguously be related to a structural change. We

note, however, that the small and uncorrelated shifts of the vibrational energies might be related

49

to the electron withdrawing effect of the attached PA anchor molecules (ester group). In **SI Figure**

10c the C=O stretching mode of the carboxylic acid (blue) and ester functionality (red) are shown.

$\upsilon_{C=O}$ of the uncoupled (1737.5 cm^{-1}) complex is relatively high compared to the coupled variant

(1722.3 cm^{-1}) suggesting the presence of intermolecular hydrogen (H)-bonding (36). The

vibrational energies of the C=O stretching mode relative to the ester group of C_{11}-Re(M1) (free),

both identical for the surface-bound molecular complexes (1728.9 cm^{-1}), confirms that both

carboxylic acids modifications of the bipyridyl moiety are involved in the covalent attachment of

the molecular complexes. We explain the slight blueshift by the reduced degree of freedom of the

ester group embedded in the SAM layer. Therefore, the degrees of freedom of the anchored

molecular complexes are severely limited, which is in good agreement with the obtained thickness

estimation (AFM, XRR) as well as surface orientation of the molecular complexes (NEXAFS).

51

S9. Photoluminescence (PL) spectroscopy of free and surface-bound C$_{11}$-Re(M1)

Photoluminescence (PL) measurements were performed on an in-house built setup equipped with a 403 nm, continuous wave laser (iBeam Smart high-performance single mode diode) operated at 105 mW, a (asymmetric) Czerny-Turner monochromator (iHR550, HORIBA Scientific) mounted with three gratings (300, 1200, and 2400 gr/mm) with a focal length of 0.55 m, and a HORIBA Symphony II Cryogenic CCD detector with a 1024 × 256 array and pixel size of 26 μm × 26 μm. The detector was operated at -133 ˚C (liquid nitrogen) to increase sensitivity and minimize the dark counts. Signal read-out was achieved *via* LabVIEW Virtual Instrument.
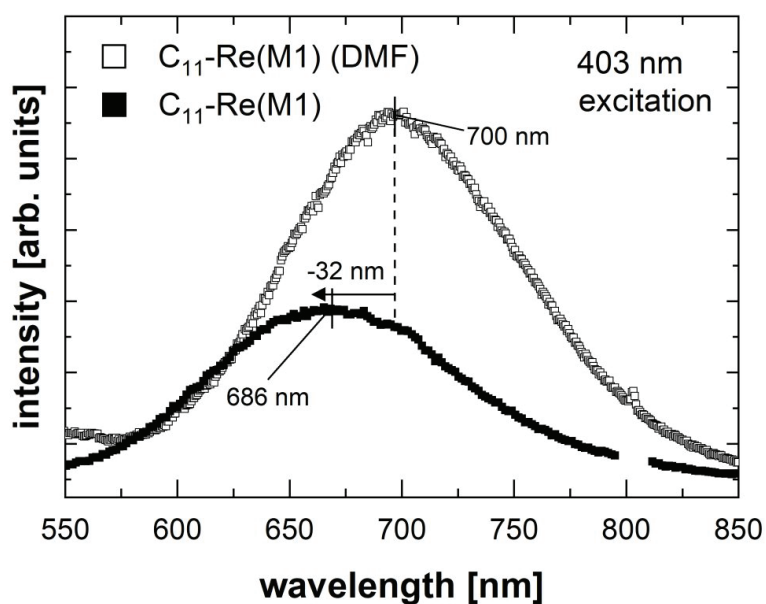
SI Figure 11. Photoluminescence (PL) spectra of C_{11}-Re(M1) (free) dissolved in DMF (open squares) and a C_{11}-Re(M1) MSA on 3 nm AlO_x-covered Si substrate (solid squares). The PL spectra were collected under the ambient at an excitation energy of 403 nm.

52

S10. AFM measurements of AlO$_x$-patterned n-type Si
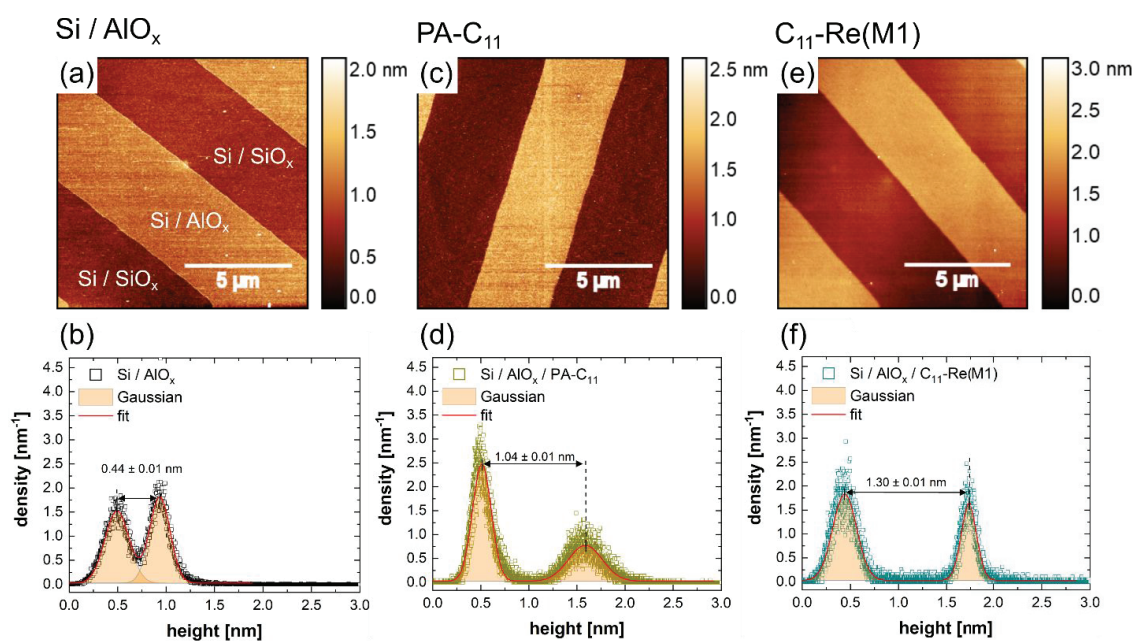
SI Figure 12. AFM micrographs of the topography **(a)**, **(c)**, **(e)** and corresponding height distribution **(b)**, **(d)**, **(f)** of a bare, a PA-C$_{11}$-, and a C$_{11}$-Re(M1)-terminated AlO$_x$-patterned, n-type Si substrate, respectively. The step height was determined by following the method described in **S3**.

SI Figure 12 shows AFM micrographs of the topography (**a, c, e**) and the corresponding height distribution (**b, d, f**) of a bare, a PA-C$_{11}$-, and C$_{11}$-Re(M1)-terminated on AlO$_x$-patterned n-type Si

53

substrate, respectively. The height steps introduced by the selective PE-ALD AlO$_x$ growth are clearly visible on all three samples. An accurate step height was determined by the height distribution following the method described in **S3**. The PE-ALD-grown AlO$_x$ layer thickness is 0.44 ± 0.01 nm, confirming the *in-situ* SE results. The PA anchor layer thickness is 0.6 ± 0.02 nm and, thus, appreciably smaller compared to the thickness on a 3 nm AlO$_x$ (0.96 ± 0.09 nm). However, this finding is in excellent agreement with the PA-C$_{11}$ layer thickness of 0.58 ± 0.04 nm, grafted on a monolayer AlO$_x$ (~ 0.3 nm) grown on gallium nitride (GaN) (2). Since the two AlO$_x$ layers provide comparable accessibility to the PA molecules (PA coverage: 3.98 nm^{-2} on Si (**SI Table 4**) vs. 4.5 ± 0.3 nm^{-2} on GaN (2)), we attribute the decrease of the PA thickness exclusively to the unique properties of the AlO$_x$ layer close to the monolayer limit. After probe attachment a small thickness increase of 0.26 ± 0.02 nm can be observed.

Appendix

S11. XPS measurements obtained by an in-house built setup
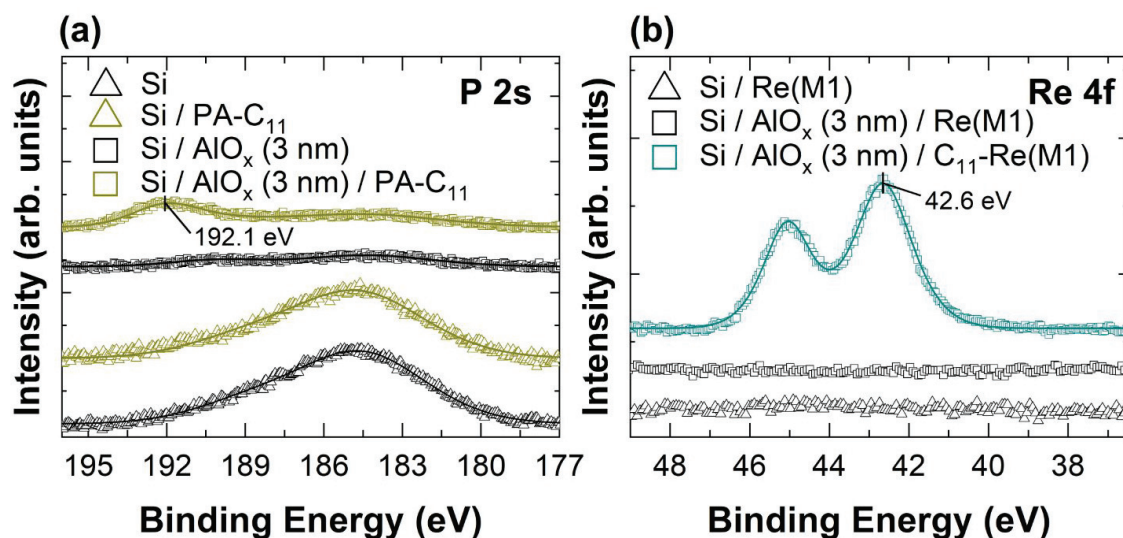
SI Figure 13. XPS spectra obtained by an in-house built setup of the P 2s region of a bare (solvent cleaned) Si substrate before (black, triangles) and after surface functionalization with PA-C_{11} (yellow, triangles) and a Si substrate covered by a 3 nm AlO_x layer before (black, squares) and after surface functionalization with PA-C_{11} (yellow, squares) **(a)**. A P 2s signal (~ 192.1 eV) related to the phosphorus of the PA molecules can only be observed on the AlO_x-coated substrate. The broad feature at ~ 185 eV is a Si 2s plasmon loss feature, which is nearly fully suppressed by the AlO_x layer. Corresponding XPS spectra of the Re 4f region of a bare (solvent cleaned) Si substrate (black, triangles), a Si substrate covered by a 3 nm AlO_x layer (black, squares), and a 3 nm AlO_x-covered Si substrate functionalized by a PA-C_{11} layer (cyan) after coupling reaction of the molecular complex (Re(M1)) **(b)**. A Re signal (~ 42.6 eV) related to molecular complex can be found exclusively on a PA-C_{11}-terminated surface. We note that a series of Si and Si / AlO_x (3 nm) substrates treated by an *ex-situ* oxygen plasma (OP) at 200 W for 300 s exhibited the exact same behavior (data not shown).

Additional XPS measurements were performed with an in-house built XPS system (system components from SPECS Surface Nano Analysis GmbH, Berlin Germany; base pressure ≤7×10^{-9} mbar) equipped with a twin (Al and Mg) non-monochromatic X-ray tube anode, a PHOIBOS 100 concentric hemispherical analyzer, and a MCD-5 detector. The Al X-ray source (Al K_α = 1486.6 eV) was operated at an emission current of 20 mA with a voltage of 12.5 kV. XPS spectra were recorded with a pass energy of 25 eV in normal emission (90° $\pm$ 2° relative to the surface) in medium area mode (circular electron collection area of 2 mm diameter). Entrance and exit slit were set to 5:7×20 and 2:open, respectively. Measurement parameters are transmission optimized, resulting in an acceptance angle up to $\pm$ 7°. With these settings an instrumental resolution of 1.2 eV was determined by measuring the full width at half maximum (FWHM) of a gold (Au) 4f$_{7/2}$ XPS spectrum taken from a 100 nm Au layer evaporated on a Si (100) wafer piece. XPS spectra were recorded with SpecsLab (SPECS Surface Nano Analysis GmbH, ver. 2.85). Corresponding XPS measurements are highlighted (marked in blue throughout the manuscript). The applied method to determine the surface coverage (**S7**) relies only on integrated peak areas, which can be reliably determined for Si, independent of the instrumental resolution.

57

S12. Synthesis and characterization of rhenium(I) tricarbonyl molecular complexes

FTIR. Fourier transform infrared spectra were measured on a Bruker Vertex-70 FTIR spectrometer

with a platinum attenuated total reflectance (ATR) averaging 16 scans from 4000 cm^{-1} to 700 cm^{-1}

at ambient conditions.

58

EA. Elemental analyses were measured on a Vario EL (Elementar) at the Laboratory for Microanalysis at the Institute of Inorganic Chemistry at the Technical University of Munich

ESI-MS. ESI-MS spectra were measured on a Varian 500-MS spectrometer in acetonitrile or methanol (LC-MS grade).

NMR. NMR spectra were recorded on a Bruker AVIII-300 or Bruker Ascend 400 MHz spectrometer. ^{1}H-, ^{13}C-, and ^{31}P-NMR spectroscopic chemical shifts, δ, are reported in parts per million (ppm). $\delta(^1$H) is calibrated to the residual proton signal, $\delta(^{13}$C) to the carbon signal of the solvent. Coupling constants (J) are averaged values in Hertz (Hz) and refer to couplings between two protons. Deuterated solvents were obtained from Sigma-Aldrich and dried over 3 Å molecular sieves.

UV/Vis. UV/Vis-spectra were measured on a Varian Cary 50 Scan UV/Vis-spectrophotometer in a quartz cuvette (40 mm x 10 mm x 2 mm) at a range from 200 nm to 800 nm.

Synthesis.

2-((6-bromohexyl)oxy)tetrahydro-2*H*-pyran (**Br-C6-Py**)
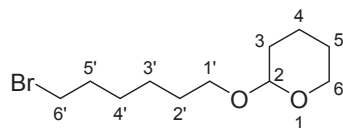
The product was prepared by following a modified method from Besse *et al.* (37).

6-Bromohexan-1-ol (361 μL, 500 mg, 2.76 mmol, 1.0 equiv.) and pyridinium *p*-toluenesulfonate (6.94 mg, 27.6 μmol, 0.001 equiv.) were dissolved in anhydrous dichloromethane (8 mL). After the addition of 3,4-dihydro-2*H*-pyran (252 μL, 232 mg, 2.76 mmol, 1.0 equiv.) the solution was stirred at room temperature for three hours. The crude product was washed with distilled water (10 mL). The organic phase was dried over $MgSO_4$, filtered, and evaporated under reduced pressure to receive the product as colorless oil in quantitative yield.

^{1}H-NMR (400 MHz, $CDCl_3$): δ (ppm) = 4.57 (dd, J = 4.6, 2.7 Hz, 1H, O-CH-O), 3.86 (ddd, ^3J = 11.1 Hz, ^3J = 7.3 Hz, ^4J = 3.4 Hz, 1H, C-6), 3.73 (dt, ^3J = 9.7 Hz, ^4J = 6.7 Hz, 1H, C-1'-H), 3.54-3.46 (m, 1H, C-6-H), 3.44-3.35 (m, 3H, C-1'-H, C-6'-H_2), 1.92-1.34 (m, 14H).

The signals in the ^{1}H-NMR-spectrum are in accordance with the literature (37).

Diethyl (6-((tetrahydro-2H-pyran-2-yl)oxy)hexyl)phosphonate (**PE-C6-Py**)
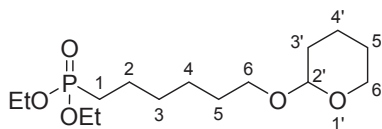
The product was prepared by following a modified method from Besse *et al.* (37). To **Br-C6-Py**

(2.76 mmol, 1.0 equiv.) triethylphosphite (9.49 g, 57.1 mmol, 20.7 equiv.) was added and the

mixture was heated to 150 ˚C for 16 h. Excess triethylphosphite was removed by heating under

reduced pressure (p = 0.03 mbar, T = 110 ˚C) affording a colorless liquid that was used in the next

step without further purification.

¹H-NMR (400 MHz, CDCl$_3$): δ (ppm) = 4.56 (dd, J = 4.6, 2.7 Hz, 1H, O-CH-O), 4.14-4.03 (m,

4H, 2 × OC*H$_2$*CH$_3$), 3.86 (ddd, ^3J = 11.1 Hz, ^3J = 7.3 Hz, ^4J = 3.4 Hz, 1H, C-6'-H), 3.72 (dt,

^3J = 9.6 Hz, ^4J = 6.7 Hz, 1H, C-6-H), 3.52-3.46 (m, 1H, C-6'-H), 3.37 (dt, ^3J = 9.6 Hz, ^4J = 6.7 Hz,

1H, C-6-H), 1.88-1.67 (m, 4H), 1.64-1.49 (m, 8H), 1.43-1.23 (m, 10H, 2 × OCH$_2$C*H$_3$*);

³¹P-NMR (162 MHz, CDCl$_3$): δ (ppm) = 32.5 (PO(OEt)$_2$).

The signals in the ¹H- and ³¹P-NMR-spectrum are in accordance with the literature (37).

Diethyl (6-hydroxyhexyl)phosphonate (**PE-C6-OH**)
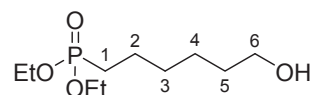
The product was prepared by following a modified method from Besse *et al.* (37). Amberlyst H15

(60 mg) was added to **PE-C6-Py** in MeOH (10 mL). The reaction was heated to 60 ˚C under reflux

61

for 22 h. After filtration and concentration under reduced pressure, the product (658 mg, 2.76 mmol, 100%) was obtained with a quantitative yield as colorless oil.

^{1}H-NMR (400 MHz, CDCl$_3$): δ (ppm) = 4.13-4.01 (m, 4H, 2 × OCH_2CH$_3$), 3.63 (t, ^{3}J = 6.5 Hz, 2H, C-6-H$_2$), 2.02 (br s, 1H, C-6-OH), 1.78-1.51 (m, 6H), 1.44-1.26 (m, 10H, 2 × OCH$_2$CH_3);

^{13}C-NMR (101 MHz, CDCl$_3$): δ (ppm) = 62.9 (C-6), 61.6 (d, ^{2}J = 6.6 Hz, 2 × OCH$_2$CH$_3$), 32.6 (C-5), 30.3 (d, ^{3}J = 16.5 Hz, C-3), 25.7 (d, ^{1}J = 140.6 Hz, C-1), 25.3 (C-4), 22.5 (d, ^{2}J = 5.2 Hz, C-2), 16.6 (d, ^{3}J = 6.1 Hz, 2 × OCH$_2$$CH_3$);

^{31}P-NMR (162 MHz, CDCl$_3$): δ (ppm) = 32.4 (PO(OH)$_2$).

The signals in the ^{1}H-, ^{13}C-, and ^{31}P-NMR-spectrum are in accordance with the literature (37).

(6-Hydroxyhexyl)phosphonic acid (**PA-C$_6$**)

The product was prepared by following a modified method from Chougrani *et al.* (38). **PE-C6-OH** (658 mg, 2.76 mmol, 1.0 equiv.) was dissolved in anhydrous dichloromethane (10 mL) before trimethylsilyl bromide (18.2 mL, 21.1 g, 138 mmol, 50.0 equiv.) was added dropwise. The reaction was stirred for 15 h at room temperature. The excess TMSBr and the solvent was removed under

62

reduced pressure before water/MeOH (1:20, 15 mL) was added and the mixture was stirred for

two hours. The solvent was removed again under reduced pressure resulting in a brown product

(450 mg, 2.48 mmol, 90%).

¹H-NMR (400 MHz, MeOD-d_4): δ (ppm) = 3.55 (t, ^3J = 6.6 Hz, 2H, C-6-H$_2$), 1.78 – 1.34

(m, 10H);

¹³C-NMR (101 MHz, MeOD-d_4): δ (ppm) = 62.9 (C-6), 33.4 (C-5), 31.5 (d, ^3J = 16.7 Hz,

C-3), 27.8 (d, 1J = 137.7 Hz, C-1), 26.5 (C-4), 23.8 (d, 2J = 4.8 Hz, C-2);

³¹P-NMR (162 MHz, MeOD-d_4): δ (ppm) = 31.1 (PO(OH)$_2$);

ESI-MS (MeOH) *m/z*: 181.2 [M-H]$^-$, 183.4 [M+H]$^+$;

IR (ATR): $\bar{\nu}$ = 2933 cm^{-1} (C-H$_x$), 2858 cm^{-1} (C-H$_x$), 2330 cm^{-1} (O-H), 1462 cm^{-1} (C-H$_x$),

1127 cm^{-1} (P=O), 1046 cm^{-1} (P-O), 985 cm^{-1} (P-O), 938 cm^{-1} (P-O), 770 cm^{-1} (C-H$_x$),

714 cm^{-1} (C-H$_x$).

The signals in the IR-spectrum are in accordance with the literature (39).

2-((11-bromoundecyl)oxy)tetrahydro-2*H*-pyran (**Br-C11-Py**)

The product was prepared by following a modified method from Reetz *et al.* (40).

11-Bromo-1-undecanol (1.00 g, 3.98 mmol, 1.0 equiv.) and pyridinium *p*-toluenesulfonate

(11.0 mg, 43.8 µmol, 0.01 equiv.) were dissolved in anhydrous dichloromethane (5 mL). After the

addition of 3,4-dihydro-2*H*-pyran (363 µL, 335 mg, 3.98 mmol, 1.0 equiv.) the solution was stirred

at room temperature for three hours. The crude product was washed with distilled water (10 mL).

The organic phase was dried over $MgSO_4$, filtered, and evaporated under reduced pressure to

receive the product (946 mg, 2.82 mmol, 71%) as colorless oil.

^{1}H-NMR (400 MHz, $CDCl_3$): δ (ppm) = 4.57 (dd, J = 4.5, 2.7 Hz, 1H, O-CH-O), 3.87 (ddd,

^3J = 11.1 Hz, ^3J = 7.3 Hz, ^4J = 3.4 Hz, 1H, C-6-H), 3.73 (dt, ^3J = 9.6 Hz, ^4J = 6.9 Hz, 1H,

C-1'-H), 3.53-3.45 (m, 1H, C-6-H), 3.44-3.36 (m, 3H, C-1'-H, C-11'-H2), 1.90-1.24 (m,

24H).

The signals in the ^{1}H-NMR-spectrum are in accordance with the literature (40,41).

Diethyl (11-(((tetrahydro-2H-pyran-2-yl)oxy)undecyl)phosphonate (**PE-C11-Py**)

64

The product was prepared by following a modified method from Besse *et al.* (37). To **Br-C11-Py**

(946 mg, 2.82 mmol, 1.0 equiv.) triethylphosphite (9.69 g, 58.3 mmol, 20.7 equiv.) was added and

the mixture was heated to 150 ˚C for 16 h. Excess triethylphosphite was removed by heating under

reduced pressure (p = 0.03 mbar, T = 110 ˚C) affording a colorless liquid that was used in the next

step without further purification.

^{1}H-NMR (400 MHz, CDCl$_3$): δ (ppm) = 4.57 (dd, J = 4.4, 2.7 Hz, 1H, O-CH-O), 4.14-4.02 (m,

4H, 2 × OCH_2CH$_3$), 3.87 (ddd, ^{3}J = 11.1 Hz, ^{3}J = 7.3 Hz, ^{4}J = 3.5 Hz, 1H, C-6'-H), 3.72 (dt,

^{3}J = 9.6 Hz, ^{4}J = 6.8 Hz, 1H, C-11-H), 3.53-3.45 (m, 1H, C-6'-H), 3.38 (dt, ^{3}J = 9.6 Hz,

^{4}J = 6.8 Hz, 1H, C-11-H), 1.91-1.45 (m, 12H), 1.41-1.21 (m, 20H, 2 × OCH$_2$CH_3);

^{13}C-NMR (101 MHz, CDCl$_3$): δ (ppm) = 99.0 (O-CH-O), 67.8 (C-11), 62.5 (C-6'), 61.5 (d,

^{2}J = 6.4 Hz, 2 × OCH$_2$CH$_3$), 31.0, 30.8 (d, ^{3}J = 17.0 Hz, C-3), 29.9, 29.7, 29.7, 29.6, 29.5, 29.2 (d,

^{4}J = 1.2 Hz, C-4), 26.4, 25.9 (d, ^{1}J = 140.2 Hz, C-1), 25.7, 22.6 (d, ^{2}J = 5.2 Hz, C-2), 19.9, 16.6 (d,

^{3}J = 6.1 Hz, 2 × OCH$_2$$CH_3$);
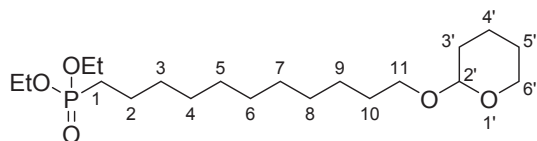
^{31}P-NMR (162 MHz, CDCl$_3$): δ (ppm) = 32.7 (PO(OEt)$_2$).

65

The signals in the ^{1}H- and ^{13}C-spectrum are in accordance with the literature (40,41).

Diethyl (11-hydroxyundecyl)phosphonate (**PE-C11-OH**)
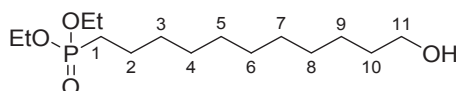
The product was prepared by following a modified method from Besse *et al.* (37). Amberlyst H15

(60 mg) was added to **PE-C11-Py** in MeOH (10 mL). The reaction was heated to 45 ˚C under

reflux for 17 h. After filtration and concentration under reduced pressure, the product (860 mg,

2.79 mmol, 99%) was obtained as colorless oil.

^{1}H-NMR (400 MHz, CDCl$_3$): δ (ppm) = 4.15-4.02 (m, 4H, 2 × OC*H$_2$*CH$_3$), 3.68-3.58 (m, 2H,

C-11-H$_2$), 1.77-1.49 (m, 7H, C-10-H$_2$, C-9-H$_2$, C-1-H$_2$, C-11-OH), 1.41-1.21 (m, 20H,

2 × OCH$_2$C*H$_3$*);

The signals in the ^{1}H-NMR-spectrum are in accordance with the literature (41).

^{13}C-NMR (101 MHz, CDCl$_3$): δ (ppm) = 63.2 (C-11), 61.5 (d, ^2J = 6.5 Hz, 2 × O*C*H$_2$CH$_3$), 32.9

(C-10), 30.7 (d, ^3J = 16.8 Hz, C-3), 29.7, 29.6, 29.5, 29.4, 29.2, 25.9 (C-9), 25.8 (d, ^1J = 139.9 Hz,

C-1), 22.5 (d, ^2J = 5.2 Hz, C-2), 16.6 (d, ^3J = 5.9 Hz, 2 × OCH$_2$*C*H$_3$);

^{31}P-NMR (162 MHz, CDCl$_3$): δ (ppm) = 32.7 (PO(OEt)$_2$);

66

The signals in the ^{13}C-, ^{31}P-NMR-spectrum are in accordance with the literature (40).

ESI-MS (MeCN) *m/z*: 309.6 [M+H]$^+$, 331.5 [M+Na]$^+$.

(6-Hydroxyundecyl)phosphonic acid (**PA-C$_{11}$**)
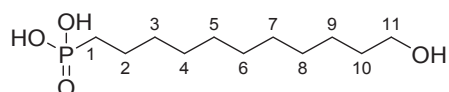
The product was prepared by following a modified method from Chougrani *et al.* (38). **PE-C11-OH** (200 mg, 649 μmol, 1.0 equiv.) was dissolved in anhydrous dichloromethane (2.7 mL) before trimethylsilyl bromide (4.28 mL, 4.96 g, 32.4 mmol, 50.0 equiv.) was added dropwise. The reaction was stirred for 24 h at room temperature. The excess TMSBr and the solvent was removed under reduced pressure before water/MeOH (1:20, 10 mL) was added and the mixture was stirred for two hours. The solvent was removed again under reduced pressure resulting in a grey product (131 mg, 519 μmol, 80%).

^{1}H-NMR (400 MHz, MeOD-d_4): δ (ppm) = 3.54 (t, ^3J = 6.6 Hz, 2H, C-11-H$_2$), 1.73-1.56 (m, 4H, C-1-H$_2$, C-10-H$_2$), 1.56-1.48 (m, 2H, C-9-H$_2$), 1.45-1.28 (m, 14H);

The signals in the ^{1}H-NMR-spectrum are in accordance with the literature (41).

67

¹³C-NMR (101 MHz, MeOD-d_4): δ (ppm) = 63.0 (C-11), 33.7 (C-9), 31.8 (d, ^3J = 16.9 Hz, C-3),

30.7, 30.7, 30.6, 30.5, 30.3, 28.1 (d, ^1J = 138.3 Hz, C-1), 27.0 (C-10), 23.9 (d, ^2J = 4.9 Hz, C-2);

³¹P-NMR (162 MHz, MeOD-d_4): δ (ppm) = 30.43 (PO(OH)$_2$);

ESI-MS (MeOH) m/z: 251.3 [M-H]$^-$, 253.3 [M+H]$^+$, 275.4 [M+Na]$^+$;

IR (ATR): $\bar{\nu}$ = 3173 cm^{-1} (br s, O-H), 2913 cm^{-1} (C-H$_x$), 2846 cm^{-1} (C-H$_x$), 2346 cm^{-1} (O-H),

1463 cm^{-1} (C-H$_x$), 1138 cm^{-1} (P=O), 1074 cm^{-1} (O-H), 1020 cm^{-1} (P-O), 998 cm^{-1} (P-O), 931 cm^{-1}

(P-O), 777 cm^{-1} (C-H$_x$), 719 cm^{-1} (C-H$_x$).

The signals in the IR-spectrum are in accordance with the literature (39).

Re(2,2′-bipyridine-4,4′-dicarboxylic acid)(CO)$_3$Br (**Re(M1) (free)**):
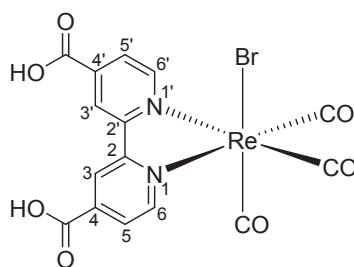
The product was prepared by following a modified method from Pfennig *et al.* (42). 2,2′-

Bipyridine-4,4′-dicarboxylic acid (180 mg, 737 µmol, 1.0 equiv.) was added to

bromopentacarbonylrhenium (299 mg, 737 µmol, 1.0 equiv.) in ethylene glycoldimethyl ester

68

(DME) (20 mL) and heated to 90 ˚C under reflux and light exclusion for four hours. The solvent was removed under reduced pressure and the crude product was solved in *N,N*-Dimethylformamide and filtered *via* syringe filter (0.45 μm) to remove the rhenium precursor. The orange product was solved in DME again, hexane (100 mL) was added and the mixture was cooled to 0 ˚C. The resulting precipitate was received by centrifugation followed by decantation and drying as an orange powder (385 mg, 648 μmol, 88%).

¹H-NMR (400 Hz, DMSO-d_6): δ (ppm) = 8.11 (dd, $3J$ = 5.7 Hz, $4J$ = 1.7 Hz, 2 H, C6*H*, C6'*H*), 9.13 (s, 2 H, C3*H*, C3'*H*), 9.21 (d, $3J$ = 5.7 Hz, 2 H, C5*H*, C5'*H*);

The signals in the ¹H-NMR-spectrum are in accordance with the literature (37,43).

Elemental analysis: calcd (%): C 30.31, H 1.36, N 4.71;

found (%): C 30.23, H 1.78, N 4.44;

IR (ATR): $\bar{\nu}$ = 2022 cm⁻¹ (M-CO), 1917 cm⁻¹ (M-CO), 1886 cm⁻¹ (M-CO);

The signals in the IR-spectrum are in accordance with the literature (42).

UV/Vis (DMF): λ_{max} = 311.4 nm, 408.5 nm.

Bis(11-(diethoxyphosphoryl)undecyl) [2,2'-bipyridine]-4,4'-dicarboxylate (**PE-C11-OH / Bpy**)

69
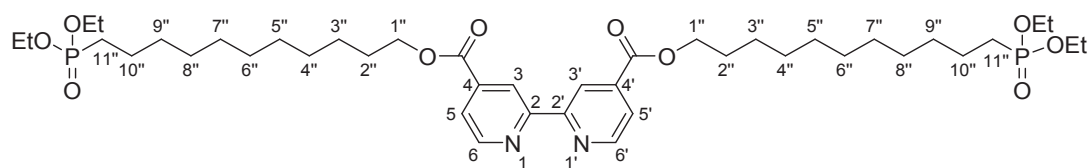
The product was prepared by following a modified method from Cabrera *et al.* (44). 2,2′-Bipyridine-4,4′-dicarboxylic acid (186 mg, 761 μmol, 1.0 equiv.) was suspended in dry dichloromethane (6 mL) before triethylamine (636 μL, 462 mg, 4.57 mmol, 6.00 equiv.) and *N,N*-Dimethylformamide (9.43 μL, 8.90 mg, 122 μmol, 0.16 equiv.) were added subsequently. After the dropwise addition of oxalyl chloride (196 μL, 290 mg, 2.28 mmol, 3.00 equiv.) the reaction mixture was stirred for six hours at room temperature. After the addition of **PE-C11-OH** (704 mg, 2.28 mmol, 3.00 equiv.) the solution was heated to reflux for 18 h. The solvent was removed under reduced pressure and the crude product was purified *via* column chromatography (aluminum oxide, Brockmann I, ethyl acetate/triethylamine (33:1)). The product (301 mg, 365 μmol, 48%) was obtained as orange crystals.

TLC: R_f = 0.10 (ethyl acetate/triethylamine (33:1)) [UV, KMnO$_4$];

^{1}H-NMR (400 MHz, CDCl$_3$): δ (ppm) = 8.94 (s, 2H, C-3-H, C-3'-H), 8.86 (d, ^3J = 4.9 Hz, 2H, C-6-H, C-6'-H), 7.90 (dd, ^3J = 4.9 Hz, ^4J = 1.2 Hz, 2H, C-5-H, C-5'-H), 4.39 (t, ^3J = 6.8 Hz, 4H,

70

168

$2 \times$ C-1''-H_2), 4.07 (t, $^3J = 7.0$ Hz, 8H, $4 \times$ OCH_2CH$_3$), 1.86-1.51 (m, 24H), 1.48-1.22 (m, 28H,

$4 \times$ OCH$_2$CH_3);

^{13}C-NMR (101 MHz, CDCl$_3$): δ (ppm) = 150.2, 123.4, 120.7, 66.2, 61.5 (d, $^2J = 6.5$ Hz,

$2 \times$ OCH$_2$CH$_3$), 30.8 (d, $^3J = 16.9$ Hz, C-9''), 29.6, 29.5, 29.4, 29.2, 28.8, 26.1, 25.8 (d,

$^1J = 140.1$ Hz, C-11''), 22.6 (d, $^2J = 5.3$ Hz, C-10''), 16.6 (d, $^3J = 6.0$ Hz, $2 \times$ OCH$_2$$CH_3$);

The signals in the ^{1}H-NMR and ^{13}C-NMR-spectrum are in accordance with the literature (44).

^{31}P-NMR (162 MHz, CDCl$_3$): δ (ppm) = 32.64 (PO(OEt)$_2$);

ESI-MS (MeCN) *m/z*: 826.3 [M+H]$^+$, 848.3 [M+Na]$^+$.

Re(bis(11-(diethoxyphosphoryl)undecyl) [2,2'-bipyridine]-4,4'-dicarboxylate)(CO)$_3$Br (**PE-C11-**

OH / ReBpy)
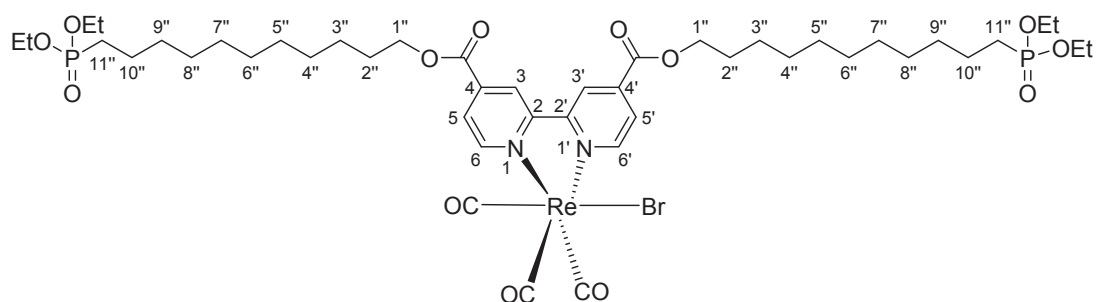
PE-C11-OH/Bpy (162 mg, 196 μmol, 1.0 equiv.) was added to bromopentacarbonylrhenium (79.8 mg, 196 μmol, 1.0 equiv.) in anhydrous toluene (4 mL) and heated to 105 ˚C under reflux and light exclusion for 18 hours. The solvent was removed under reduced pressure and the crude product was purified *via* column chromatography (silica gel, dichloromethane/methanol/triethylamine (96:3:1 → 95:4:1)). The product (178 mg, 151 μmol, 77%) was obtained as red-orange powder.

¹H-NMR (400 MHz, CDCl₃): δ (ppm) = 9.22 (d, ^3J = 5.6 Hz, 2H, C-6-H, C-6'-H), 8.83 (s, 2H, C-3-H, C-3'-H), 8.06 (dd, ^3J = 5.6 Hz, ^4J = 1.6 Hz, 2H, C-5-H, C-5'-H), 4.47 (t, ^3J = 6.8 Hz, 4H, 2 × C-1''-H₂), 4.17-3.97 (m, 8H, 4 × OC*H₂*CH₃), 1.90-1.50 (m, 22H), 1.49-1.14 (m, 30H, 4 × OCH₂C*H₃*);

¹³C-NMR (101 MHz, CDCl₃): δ (ppm) = 163.0 (C=O), 156.3 (C-2, C-2'), 154.2 (C-6, C-6'), 140.6 (C-4, C-4'), 126.7 (C-5, C-5'), 123.2 (C-3, C-3'), 67.4 (C-1''), 61.6 (d, ^2J = 5.2 Hz, 2 × OCH₂CH₃), 30.7 (d, ^3J = 16.5 Hz, C-9''), 29.6, 29.5, 29.3, 29.2, 28.7, 26.0, 25.8 (d, ^1J = 140.1 Hz, C-11''), 22.5 (d, ^2J = 5.8 Hz, C-10''), 16.6 (d, ^3J = 6.0 Hz, 2 × OCH₂*C*H₃);

³¹P-NMR (162 MHz, CDCl₃): δ (ppm) = 32.7 (2 × PO(OEt)₂);

ESI-MS (Lösungsmittel: MeCN) *m/z*: 1198.2 ([M+Na]⁺).

72

Re(bis(11-(diethoxyphosphoryl)undecyl)   [2,2'-bipyridine]-4,4'-dicarboxylate)(CO)$_3$Br   (**C$_{11}$-**

Re(M1))
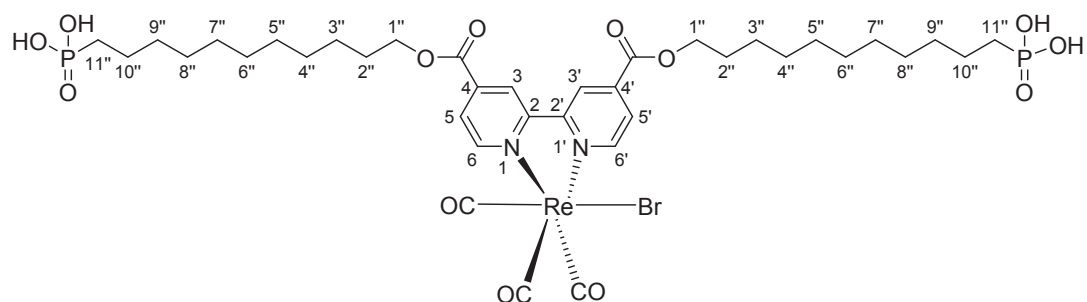
The product was prepared by following a modified method from Chougrani *et al.* (38). **PE-C11-**

OH / ReBpy (85 mg, 72.4 µmol, 1.0 equiv.) was dissolved in anhydrous dichloromethane (5 mL)

before trimethylsilyl bromide (0.48 mL, 554 mg, 3.62 mmol, 50.0 equiv.) was added dropwise.

The reaction was stirred at room temperature for 24 h. The excess TMSBr and the solvent was

removed under reduced pressure before water/MeOH (1:20, 15 mL) was added and the mixture

was stirred for two hours. The solvent was removed again under reduced pressure and the solid

was solved in MeOH. After the addition of toluene (10 mL) and the removal of MeOH the

precipitated product was dried and obtained as orange powder (47 mg, 44.2 µmol, 61%).

¹H-NMR (400 MHz, MeOD-d_4): δ (ppm) = 9.26 (d, ^3J = 5.7 Hz, 2H, C-6-H, C-6-H'), 9.06 (s, 2H,

C-3-H, C-3-H'), 8.18 (d, ^3J = 5.7 Hz, 2H, C-5-H, C-5-H'), 4.49 (t, ^3J = 6.6 Hz, 4H, 2 × C-1''-H$_2$),

1.87 (q, ^3J = 7.0 Hz, 4H, 2 × C-2''-H$_2$), 1.73-1.26 (m, 36H);

³¹P-NMR (162 MHz, MeOD-d_4): δ (ppm) = 30.3 (2 × PO(OH)$_2$);

ESI-MS (MeOH) *m/z*: 982.1 [M-Br-2H]⁻, 984.2 [M-Br]⁺, 1062.2 [M-H]⁻;

Elemental analysis: calcd (%): C 41.81, H 5.12, N 2.64;

found (%): C 41.38, H 5.18, N 2.78;

IR (ATR): $\bar{v}$ = 2920 cm⁻¹ (C-H$_x$), 2851 cm⁻¹ (C-H$_x$), 2033 cm⁻¹ (M-CO), 1916 cm⁻¹ (M-CO),

1888 cm⁻¹ (M-CO), 1865 cm⁻¹ (M-CO), 1722 cm⁻¹ (C=O), 1403 cm⁻¹ (C=C$_{ar}$), 1264 cm⁻¹ (C-O),

1228 cm⁻¹ (C-O), 1137 cm⁻¹ (P=O), 995 cm⁻¹ (P-O), 945 cm⁻¹ (P-O), 766 cm⁻¹ (C-H$_x$), 718 cm⁻¹

(C-H$_x$).

The signals in the IR-spectrum are in accordance with the literature (39).

UV/Vis (DMF): λ_{max} = 313.4 nm, 416.5 nm.

4-Methyl-2,2'-bipyridine (**C1-Bpy**)

74
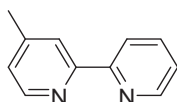
4-Methyl-2,2'-bipyridine is prepared *via* a two-step synthesis according to literature procedure and

stored over 3 Å molecular sieves (45).

4-((Trimethylsilyl)methyl)-2,2'-bipyridine (**TMS-C1-Bpy**)
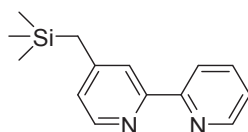
The product was prepared by following a modified method from Jurss *et al.* (46).

Diisopropylamine (1.52 mL, 11.5 mmol, 1.3 equiv.) in anhydrous THF (40 mL) was cooled to 0

˚C before a *n*-butyllithium solution (2.5 M, 4.24 mL, 10.6 mmol, 1.2 equiv.) was added and the

reaction was stirred at 0 ˚C for two hours. A solution of **C1-Bpy** (1.5 g, 8.82 mmol, 1.0 equiv.) in

anhydrous THF (20 mL) was added and the reaction mixture was stirred at 0 ˚C for one more hour.

Followed by the dropwise addition of trimethylsilyl chloride (1.46 mL, 11.5 mmol, 1.3 equiv.) the

reaction was stirred at room temperature for 10 minutes before ethanol (5 mL) was added. To the

yellow solution saturated $NaHCO_3$-solution (200 mL) and ethyl acetate (100 mL) was added after

five minutes. The mixture was extracted with ethyl acetate (1 × 100 mL) and the combined organic

phases were washed with saturated NaCl-solution (1 × 100 mL), dried over Na_2SO_4, filtered and

the solvent was removed under reduced pressure. After purification *via* column chromatography

75

(silica gel, cyclohexane/ethyl acetate/triethylamine (6:3:1)) the product (803 mg, 3.32 mmol, 38%) was obtained as colorless oil.

TLC: R_f = 0.69 (cyclohexane/ethyl acetate/triethylamine (6:3:1));

¹H-NMR (300 MHz, CDCl$_3$, 296 K) δ (ppm) = 8.67 (ddd, J = 4.8, 1.8, 0.9 Hz, 1H, CH), 8.47 (d, J = 5.0 Hz, 1H, CH), 8.38 (dt, J = 8.0, 1.1 Hz, 1H, CH), 8.05 (d, J = 1.1 Hz, 1H, CH), 7.80 (ddd, J = 8.1, 7.5, 1.8 Hz, 1H, CH), 7.34 – 7.27 (m, 1H, CH), 6.95 (dd, J = 5.1, 1.8 Hz, 1H, CH), 2.21 (s, 2H, CH$_2$), 0.04 (s, 9H, CH$_3$).

The signals in the ¹H-NMR-spectrum are in accordance with the literature (44).

4-(Chloromethyl)-2,2'-bipyridine (**Cl-C1-Bpy**)
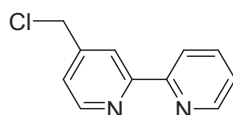
The product was prepared by following a modified method from Jurss *et al.* (46). **TMS-C1-Bpy** (803 mg, 3.32 mmol, 1.0 equiv.) was suspended in anhydrous acetonitrile (30 mL) before caesium fluoride (0.98 mg, 6.50 mmol, 1.95 equiv.) and hexachloroethane (1.73 g, 7.30 mmol, 2.2 equiv.) was added and the suspension was stirred at 60 ˚C for four hours. After the addition of distilled

76

water (60 mL) the product was extracted with EtOAc (4 × 60 mL) and the combined organic layer

was washed with brine (1 × 60 mL), dried over Na_2SO_4, filtered and the solvent was removed

under reduced pressure. The crude product was purified *via* column chromatography (silica gel,

cyclohexane/triethylamine (9:1)) to result the product (393 mg, 1.93 mmol, 58%) as colorless oil.

TLC: R_f = 0.20 (cyclohexane/triethylamine (9:1));

¹H-NMR (300 MHz, CDCl₃, 298 K) δ (ppm) = 8.68 (d, *J* = 5.0 Hz, 2H, CH), 8.41 (d, *J* = 8.0 Hz,

2H, CH), 7.83 (td, *J* = 7.8, 1.8 Hz, 1H, CH), 7.39 – 7.30 (m, 2H, CH), 4.63 (s, 2H, CH₂).

The signals in the ¹H-NMR-spectrum are in accordance with the literature (45).

Diethyl ([2,2'-bipyridin]-4-ylmethyl)phosphonate (**PE-C1-Bpy**)
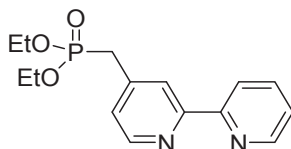
The product was prepared by following a modified method from Jurss *et al.* (46). To **Cl-C1-Bpy**

(393 mg, 1.93 mmol, 1.0 equiv.) triethylphosphite (6.41 g, 38.6 mmol, 20.0 equiv.) was added and

the mixture was heated to 180 ˚C for 24 h. Excess triethylphosphite was removed by heating under

reduced pressure (p = 0.1 mbar, T = 110 ˚C) and the crude product was purified *via* column

77

chromatography (cyclohexane/ethyl acetate/triethylamine (5:3:2)) affording a yellow oil (474 mg, 1.55 mmol, 80%).

TLC: $R_f = 0.23$ (ethyl acetate/triethylamine (5:3:2));

¹H-NMR (300 MHz, CDCl$_3$, 298 K) δ (ppm) = 8.67 (ddd, J = 4.8, 1.7, 0.9 Hz, 1H, CH), 8.61 (d, J = 5.0 Hz, 1H, CH), 8.39 (t, 1H, CH), 8.33 (t, 1H, CH), 7.81 (td, J = 7.8, 1.8 Hz, 1H, CH), 7.35 – 7.27 (m, 2H, CH), 4.13 – 3.99 (m, 4H, CH$_3$CH_2), 3.23 (d, J = 22.2 Hz, 2H, CCH$_2$), 1.26 (t, J = 7.1 Hz, 6H, CH$_3$);

³¹P-NMR (121 MHz, CDCl$_3$, 298 K) δ (ppm) = 24.38.

Re(diethyl ([2,2'-bipyridin]-4-ylmethyl)phosphonate)(CO)$_3$Br (**PE-C1-ReBpy**)
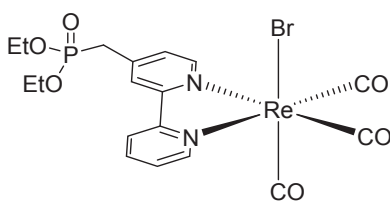
The product was prepared by following a modified method from *Pschenitza et al.* (47). **PE-C1-Bpy** (100 mg, 330 µmol, 1.0 equiv.) was added to bromopentacarbonylrhenium (132 mg, 330 µmol, 1.0 equiv.) in anhydrous toluene (10 mL) and heated to 105 ˚C under reflux and light exclusion for three hours. After cooling to room temperature, the yellow precipitate was filtered

78

off, washed with toluene (10 mL) and diethyl ether (2 × 10 mL) and dried under vacuum to result

a yellow powder (125 mg, 190 µmol, 58%).

¹H-NMR (300 MHz, MeOD, 298 K) δ (ppm) = 9.11 – 9.05 (m, 1H, CH), 8.98 (d, J = 5.7 Hz, 1H,

CH), 8.60 (d, J = 8.2 Hz, 1H, CH), 8.55 (t, 1H, CH), 8.26 (td, J = 8.0, 1.5 Hz, 1H, CH), 7.75 – 7.61

(m, 2H, CH), 4.22 – 4.09 (m, 4H, CH$_3$CH_2), 3.63 (s, 1H, CCH$_2$), 3.56 (s, 1H, CCH$_2$), 1.31 (t, J =

7.0 Hz, 6H, CH$_3$);

³¹P-NMR (121 MHz, MeOD, 299 K) δ (ppm) = 24.04;

UV/Vis (DMF): λ_{max} = 294.0 nm, 476.5 nm.

Re((([2,2'-bipyridin]-4-ylmethyl)phosphonic acid)(CO)$_3$Br (**C1-Re(M0)**)
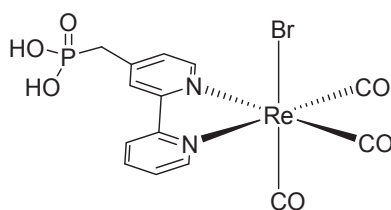
The product was prepared by following a modified method from Chougrani *et al.* (38). **PE-C1-**

ReBpy (56 mg, 85 µmol, 1.0 equiv.) was dissolved in anhydrous dichloromethane (17 mL) before

79

trimethylsilyl bromide (0.23 mL, 1.74 mmol, 20.0 equiv.) was added dropwise and the reaction

was stirred at room temperature for 24 h. The excess TMSBr and the solvent was removed under

reduced pressure before water/MeOH (1:20, 5 mL) was added and the mixture was stirred for two

hours. The solvent was removed again under reduced pressure resulting in a yellow product

(41 mg, 69 μmol, 81%)

¹H-NMR (300 MHz, MeOD, 298 K) δ (ppm) = 9.05 (d, J = 5.3 Hz, 1H, CH), 8.94 (d, J = 5.6 Hz,

1H, CH), 8.59 (d, J = 8.2 Hz, 1H, CH), 8.53 (s, 1H, CH), 8.23 (t, J = 7.9 Hz, 1H, CH), 7.74 – 7.58

(m, 2H, CH), 3.47 (s, 1H, CH$_2$), 3.39 (s, 1H, CH$_2$);

³¹P-NMR (121 MHz, MeOD, 298 K) δ (ppm) = 19.98;

ESI-MS (MeCN) m/z: 518.9 [M-Br-2H]⁻;

Elemental analysis: calcd (%): C 28.01, H 1.85, N 4.67;

found (%): C 28.26, H 2.09, N 4.48;

UV/Vis (DMF): λ_{max} = 293.0 nm, 374.0 nm.

Appendix

REFERENCES

(1) Carter, A. D.; Mitchell, W. J.; Thibeault, B. J.; Law, J. J. M.; Rodwell, M. J. W. Al_2O_3 Growth on (100) In0.53Ga0.47As Initiated by Cyclic Trimethylaluminum and Hydrogen Plasma Exposures. *Appl. Phys. Express* **2011**, *4*, 091102.

(2) Henning, A.; Bartl, J. D.; Zeidler, A.; Qian, S.; Bienek, O.; Jiang, C.-M.; Paulus, C.; Rieger, B.; Stutzmann, M., Sharp, I. D. Aluminum Oxide at the Monolayer Limit via Oxidant-Free Plasma-Assisted Atomic Layer Deposition on GaN. *Adv. Funct. Mater.* **2021**, *31*, 2101441.

(3) Henning, A.; Bartl, J. D.; Wolz, L.; Christis, M.; Zeidler, A.; Bissolo, M.; Grünleitner, T.; Eichhorn, J.; Zeller, P.; Amati, M.; Gregoratti, L.; Finley, J. J.; Rieger, B.; Stutzmann, M.; Sharp, I. D. Sub-nanometer thin Conformal Aluminum Oxide Coating Created by Interconversion of SiO_2 *via* Hydrogen Plasma-assisted Atomic Layer Deposition. 2021, 2111.00054 [cond-mat.mtrl-sci]. arXiv. https://arxiv.org/abs/2111.00054 (accessed 11 02, 2021).

(4) Fujiwara, H.; Collins, R. W.; Spectroscopic Ellipsometry for Photovoltaics, vol. 212. Cham: Springer International Publishing, 2018.

81

(5) Heijink, A.; Schwartz, J.; Zobitz, M. E.; Nicole Crowder, K.; Lutz, G. E.; Sibonga, J. D. Self-assembled monolayer films of phosphonates for bonding RGD to titanium. *Clin. Orthop. Relat. Res.* **2008**, *466(4)*, 977–984.

(6) Cattani-Scholz, A. Functional Organophosphonate Interfaces for Nanotechnology: A Review. *ACS Appl. Mater. Interfaces* **2017**, *9*, 25643-25655.

(7) Nečas, D.; Klapetek, P. Gwyddion: an open-source software for SPM data analysis. *Centr. Eur. J. Phys.* **2012**, *10*, 181-188.

(8) Cattani-Scholz, A.; Pedone, D.; Dubey, M.; Neppl, S.; Nickel, B.; Feulner, P.; Schwartz, J.; Abstreiter, G.; Tornow, M. Organophosphonate-Based PNA-Functionalization of Silicon Nanowires for Label-Free DNA Detection. *ACS Nano* **2008**, *2*, 1653-1660.

(9) Ernzerhof, M.; Scuseria, G. E. Assessment of the Perdew-Burke-Ernzerhof exchange-correlation functional. *J. Chem. Phys.* **1999***, 110*, 5029-5036.

(10) Adamo, C.; Barone, V. Toward reliable density functional methods without adjustable parameters: The PBE0 model. *J. Chem. Phys.* **1999***, 110*, 6158-6170.

82

(11) Grimme, S.; Antony, J.; Ehrlich, S.; Krieg, H. A consistent and accurate ab initio parametrization of density functional dispersion correction (DFT-D) for the 94 elements H-Pu. *J. Chem. Phys.* **2010**, *132*, 154104.

(12) Schäfer, A.; Huber, C.; Ahlrichs, R. Fully optimized contracted Gaussian basis sets of triple zeta valence quality for atoms Li to Kr. *J. Chem. Phys.* **1994**, *100*, 5829-5835.

(13) TURBOMOLE V7.3 2018, a development of University of Karlsruhe and Forschungszentrum Karlsruhe GmbH, 1989–2007, TURBOMOLE GmbH, since 2007; available from http://www.turbomole.com (accessed: 26.08.2021).

(14) Ahlrichs, R.; Bär, M.; Häser, M.; Horn, H.; Kölmel, C. Electronic structure calculations on workstation computers: The program system turbomole. *Chem. Phys. Lett.* **1989**, *162*, 165-169.

(15) Pershan, P. S. X-ray or neutron reflectivity: Limitations in the determination of interfacial profiles. *Phys. Rev. E: Stat. Phys., Plasmas, Fluids, Relat. Interdiscip. Top.* **1994**. *50(3)*, 2369-2372.

(16) Nelson, A. R. J.; Prescott, S. W. refnx: neutron and X-ray reflectometry analysis in Python. *J. Appl. Crystallogr.* **2019**, *52*, 193-200.

83

(17) Zangrando, M.; Finazzi, M.; Paolucci, G.; Comelli, G.; Diviacco, B.; Walker, R. P.; Cocco, D.; Parmigiani, F. BACH, the beamline for advanced dichroic and scattering experiments at ELETTRA. *Rev. Sci. Instrum.* **2001**, *72*, 1313-1319.

(18) Stöhr, J.; Outka, D. A. Determination of molecular orientations on surfaces from the angular dependence of near-edge x-ray-absorption fine-structure spectra. *Phys. Rev. B* **1987**, *36*, 7891.

(19) Stevens, J. S.; Newton, L. K.; Jaye, C.; Muryn, C. A.; Fischer, D. A.; Schroeder, S. L. M. Proton Transfer, Hydrogen Bonding, and Disorder: Nitrogen Near-Edge X-ray Absorption Fine Structure and X-ray Photoelectron Spectroscopy of Bipyridine-Acid Salts and Co-crystals. *Cryst. Growth Des.* **2015**, *15,* 1776-1783.

(20) Gupta, T.; Mondal, P. C.; Kumar, A.; Jeyachandran, Y. L.; Zharnikov, M. Surface-Confined Heterometallic Molecular Dyads: Merging the Optical and Electronic Properties of Fe, Ru, and Os Terpyridyl Complexes. *Adv. Funct. Mater.* **2013**, *23*, 4227-4235.

(21) Kolczewski, C.; Püttner, R.; Plashkevych, O.; Ågren, H.; Staemmler, V.; Martins, M.; Snell, G.; Schlachter, A. S.; Sant'Anna, M.; Kaindl, G.; Pettersson, L. G. M. Detailed study of pyridine

84

at the C 1s and N 1s ionization thresholds: The influence of the vibrational fine structure. *J. Chem. Phys.* **2001**, *115*, 6426-6437.

(22) Stöhr, J. NEXAFS Spectroscopy, vol. 25. Berlin, Heidelberg: Springer Berlin, Heidelberg, 1992.

(23) Benson, E. E.; Kubiak, C. P. Structural investigations into the deactivation pathway of the CO_2 reduction electrocatalyst Re(bpy)(CO)$_3$Cl. *Chem. Commun.* **2012**, *48*, 7374-7376.

(24) Scofield, J. Hartree-Slater subshell photoionization cross-sections at 1254 and 1487 eV. *J. Electron Spectrosc. Relat. Phenom.* **1976**, *8*, 129-137.

(25) Bartl, J. D.; Scarbolo, P.; Brandalise, D.; Stutzmann, M.; Tornow, M.; Selmi, L.; Cattani-Scholz, A. Role of Different Receptor-Surface Binding Modes in the Morphological and Electrochemical Properties of Peptide-Nucleic-Acid-Based Sensing Platforms. *Langmuir* **2019**, *35*, 3272-3283.

(26) Strohmeier, B. R. An ESCA method for determining the oxide thickness on aluminum alloys. *Surf. Interface Anal.* **1990**, *15*, 51-56.

85

(27) Carlson, T.A.; McGuire, G.E. Study of the X-ray photoelectron spectrum of tungsten-tungsten oxide as a function of thickness of the surface oxide layer. *J. Electron Spectrosc. Relat. Phenom.* **1972**, *1(2)*, 161-168.

(28) Werner, W. S. M. Towards a universal curve for electron attenuation: Elastic scattering data for 45 elements. *Surf. Interface Anal.* **1992**, *18*, 217-228.

(29) Tanuma, S.; Powell, C. J.; Penn, D. R. Calculation of electron inelastic mean free paths (IMFPs) VII. Reliability of the TPP-2M IMFP predictive equation. *Surf. Interface Anal.* **2003**, *35*, 268-275.

(30) Powell, C. NIST Electron Inelastic-Mean-Free-Path Database. NIST Standard Reference Database 71.

(31) Kim, H.; Colavita, P. E.; Paoprasert, P.; Gopalan, P.; Kuech, T.; Hamers, R. J. Grafting of molecular layers to oxidized gallium nitride surfaces via phosphonic acid linkages. *Surf. Sci.* **2008**, *602*, 2382-2388.

(32) Laibinis, P. E.; Bain, C. D.; Whitesides, G. M. Attenuation of photoelectrons in monolayers of n-alkanethiols adsorbed on copper, silver, and gold. *J. Phys. Chem.* **1991**, *95*, 7017-7021.

86

(33) Franking, R. A.; Landis, E. C.; Hamers, R. J. Highly Stable Molecular Layers on Nanocrystalline Anatase TiO_2 through Photochemical Grafting. *Langmuir* **2009**, *25*, 10676-10684.

(34) Vitchev, R.; Pireaux, J.; Conard, T.; Bender, H.; Wolstenholme, J.; Defranoux, C. X-ray photoelectron spectroscopy characterisation of high-k dielectric Al_2O_3 and HfO_2 layers deposited on SiO_2/Si surface. *Appl. Surf. Sci.* **2004**, *235*, 21-25.

(35) Hawecker, J.; Lehn, J.-M.; Ziessel, R. Photochemical and Electrochemical Reduction of Carbon Dioxide to Carbon Monoxide Mediated by (2,2′-Bipyridine)tricarbonylchlororhenium(I) and Related Complexes as Homogeneous Catalysts. *Helv. Chim. Acta* **1986**, *69*, 1990-2012.

(36) Smith, B. C. The C=O Bond, Part III: Carboxylic Acid. *Spectroscopy* **2018**, *33(1)*, 14-20.

(37) Besse, V.; Le Pluart, L.; Cook, W. D.; Pham, T.-N.; Madec, P.-J. Synthesis and polymerization kinetics of acrylamide phosphonic acids and esters as new dentine adhesives. *J. Polym. Sci., Part A: Polym. Chem.* **2013**, *51*, 149-157.

(38) Chougrani, K.; Niel, G.; Boutevin, B.; David, G. Regioselective ester cleavage during the preparation of bisphosphonate methacrylate monomers. *Beilstein J. Org. Chem.* **2011**, *7*, 364–368.

(39) Andrews, B.; Almahdali, S.; James, K.; Ly, S.; Crowder, K. N. Copper oxide surfaces modified by alkylphosphonic acids with terminal pyridyl-based ligands as a platform for supported catalysis. *Polyhedron* **2016**, *114*, 360-369.

(40) Reetz, M. T.; Rüggeberg, C. J.; Dröge, M. J.; Quax, W. J. Immobilization of chiral enzyme inhibitors on solid supports by amide-forming coupling and olefin metathesis. *Tetrahedron* **2002**, *58*, 8465-8473.

(41) Pulsipher, A.; Westcott, N. P.; Luo, W.; Yousaf, M. N. Rapid in Situ Generation of Two Patterned Chemoselective Surface Chemistries from a Single Hydroxy-Terminated Surface Using Controlled Microfluidic Oxidation. *J. Am. Chem. Soc.* **2009**, *131*, 7626-7632.

(42) Pfennig, B. W.; Chen, P.; Meyer, T. J. Photophysics and Photochemistry of Chromophore−Quencher Assemblies on Glass and Powdered Silica. *Inorg. Chem.* **1996**, *35*, 2898-2901.

(43) Komreddy, V.; Ensz, K.; Nguyen, H.; Paul Rillema, D. Synthesis and characterization of rhenium(I) 4,4′-dicarboxy-2,2′-bipyridine tricarbonyl complexes for solar energy conversion. *Inorg. Chim. Acta* **2020**, *511*, 119815.

88

(44) Cabrera, P. J.; Yang, X.; Suttil, J. A.; Brooner, R. E. M.; Thompson, L. T.; Sanford, M. S. Evaluation of Tris-Bipyridine Chromium Complexes for Flow Battery Applications: Impact of Bipyridine Ligand Structure on Solubility and Electrochemistry. *Inorg. Chem.* **2015**, *54*, 10214-10223.

(45) Savage, S. A.; Smith, A. P.; Fraser C. L. Efficient Synthesis of 4-, 5-, and 6-Methyl-2,2'-bipyridine by a Negishi Cross-Coupling Strategy Followed by High-Yield Conversion to Bromo- and Chloromethyl-2,2'-bipyridines. *J. Org. Chem.* **1998**, *63(26)*, 10048–10051.

(46) Jurss, J. W.; Concepcion, J. C.; Norris, M. R.; Templeton, J. L.; Meyer, T. J. Surface Catalysis of Water Oxidation by the Blue Ruthenium Dimer. *Inorg. Chem.* **2010**, *49*, 3980-3982.

(47) Pschenitza, M.; Meister, S.; von Weber, A.; Kartouzian, A.; Heiz, U.; Rieger, B. Suppression of Deactivation Processes in Photocatalytic Reduction of CO_2 Using Pulsed Light. *ChemCatChem* **2016**, *8*, 2688-2695.

89

10.2 Supporting Information of the Manuscript "Macromolecular Rhenium–Ruthenium Complexes for Photocatalytic CO₂ Conversion: From Catalytic Lewis Pair Polymerization to Well-Defined Poly(vinyl bipyridine)-Metal Complexes"

Macromolecular rhenium-ruthenium complexes for photocatalytic CO$_2$ conversion – from catalytic Lewis pair polymerization to well-defined poly(vinyl bipyridine)-metal complexes

Anton S. Maier[‡], Christopher Thomas[‡], Moritz Kränzlein[‡], Thomas M. Pehl and Bernhard Rieger[*]

WACKER-Chair of Macromolecular Chemistry, Department of Chemistry, Technical University of Munich, Lichtenbergstr. 4, 85748 Garching (Germany)

[‡] These authors contributed equally.

Corresponding Authors

* rieger@tum.de

TABLE OF CONTENTS

1. GENERAL EXPERIMENTAL

All air and moisture sensitive compounds were prepared using standard *Schlenk* techniques with argon (99.996 vol.-%) from *Westfalen* as inert gas.

Unless otherwise stated, all chemicals were purchased from *Sigma-Aldrich*, *ABCR GmbH* or *TCI Chemicals* and used without further purification.

The monomers for the polymerization were purified and dried by column chromatography followed by twofold sublimation and subsequently stored under argon atmosphere. Dry solvents were obtained from an *MBraun* MB-SPS-800 solvent purification system or by drying over activated alumina and stored over activated 3 Å molecular sieve. Solvents for polymerizations and for the Lewis acid and base stock solutions were degassed by three consecutive freeze-pump-thaw cycles. Deuterated solvents were purchased from *Sigma-Aldrich* and dried over activated 3 Å molecular sieve.

As stationary phase in column chromatography, Silica 60 (*Acros Organics*, 0.060-0.200 mm) and aluminum oxide (*Sigma-Aldrich*, activated, neutral, *Brockmann* activity I), respectively, were used. Thin layer chromatography (TLC) was done on silica coated polyester plates (Macherey-Nagel, Silica 60) or aluminum oxide coated polyester plates (Macherey-Nagel, ALOX N/UV$_{254}$) with subsequent detection in UV light ($\lambda = 254$ nm).

Elemental analysis (EA). All elemental analysis were performed by the Laboratory for Microanalysis at the Institute of Inorganic Chemistry at the Technical University of Munich. **Electrospray ionization mass spectrometry (ESI-MS).** ESI-MS spectra were recorded on a *Varian* ESI-MS 500 spectrometer in positive ionization mode (70 eV). The samples were

3

dissolved in acetonitrile or methanol and filtered prior to the measurements. The recorded spectra were analyzed using the *MS Data Review* software. **Differential scanning calorimetry (DSC).** DSC measurements were recorded on a DSC Q2000 from *TA Instruments* in *exo down* mode. The temperature program consisted of three consecutive heating and cooling cycles with a continuous heating ramp of 10 K/min between 0 °C and 200 °C and a sample mass of roughly 8 mg. The measurement data were analyzed using the *TA Universal Analysis* software. **Thermogravimetric analysis (TGA).** Thermogravimetric analysis was recorded on a Q5000 SA from *TA Instruments*. Roughly 1 mg of the polymer sample was applied in a tared platinum crucible and heated to 1000 °C under inert gas with a continuous heating ramp of 10 K/min. The measurement data were analyzed using the *TA Universal Analysis* software. **Micro gas chromatography (Micro-GC).** The gas phase composition in the reaction flask headspace during the photocatalytic reactions was analyzed with a *Varian* Micro 490-GC, equipped with a CO_x 1m heated column at 80 °C column temperature, 140 kPa column pressure, auto detector sensitivity, 5 s sampling time and 300 s run time using helium (99.999 vol.-%) as a carrier gas. The parameters were chosen to ensure a complete and quantitative separation of potential hydrogen, nitrogen/air, CO, methane, and CO_2 in the sample. **Refractive index increment determination (dn/dc).** For dn/dc determination, a *WGE Dr. Bures* dn/dc-2010 from PSS equipped with a 620 nm light source was used. Calibration is done using different potassium chloride in water; dn/dc measurements were performed in DMF with 25 mmol/L LiBr at 30 °C with 9 different polymer concentrations. For calculation details, see Figure S2. **Infrared spectroscopy (FT-IR).** The IR-spectra were recorded on a Vertex-70 FT-IR spectrometer from *Bruker* at room temperature. **Size-exclusion chromatography (SEC).** Average absolute molecular weights and polydispersities of the polymers were determined *via* size-exclusion chromatography (SEC) with sample concentrations in the range of 2-5 mg mL^{-1}.

4

The measurements of PVBpy were performed on an *Agilent* PL-GPC 50 (Santa Clara, CA, USA) with an integrated RI unit, two light scattering detectors (15° and 90°) and a differential pressure viscosimeter with two *Agilent* PolarGel M columns at 30 °C. As the eluent, *N,N*-dimethylformamide + 25 mmol/L LiBr was used. Absolute molecular weights and polydispersities of PVBpy were determined using the experimentally determined value for dn/dc of 0.190 mL g^{-1}. **Nuclear magnetic resonance spectroscopy (NMR).** ^{1}H-NMR- and ^{13}C-NMR spectra, as well as 2D-NMR-experiments of small molecules, polymers and metal complexes were recorded on a *Bruker Ascend* 400 MHz NMR-spectrometer at 400 MHz (^{1}H) and 101 MHz (^{13}C), respectively. All chemical shifts are given in parts per million (ppm) and referenced to the residual proton signal of the respective solvent (CDCl$_3$: δ = 7.26 ppm, DMSO-d$_6$: δ = 2.50 ppm). The NMR spectra were analyzed using the *MestReNova* software. Signal multiplicities are abbreviated as following: s - singlet, d - dublet, dd – dublet of dublets, m – multiplet, q - quartet, t – triplet. **Lyophilization.** The polymer samples subject to freeze-drying were dissolved in benzene and frozen under constant rotation in liquid nitrogen. For lyophilization, a VaCo 5-II-D from *Zirbus technology GmbH* was applied and the pressure adjusted to 2 mbar with a condenser temperature of -90 °C. **Microwave reactions.** The microwave reactions were conducted in a reactor from CEM with a focused microwave beam. The syntheses were conducted at 50 W, a temperature of 125 °C and dynamic power supply. **Photoluminescence spectroscopy (PL).** Emission spectra were recorded on an *Edinburgh Instruments* FS5 spectrofluorometer with a 150 W CW ozone-free xenon arc lamp, Czerny-Turner design monochromators and a R928P photomultiplier emission detector. Spectra were measured from 400 nm to 900 nm with 5 nm scan slit width, and a resolution of 1 nm at 25 °C. The samples were dissolved in *N,N*-dimethylformamide and analyzed in a QS 10×10 mm quartz glass cuvette from *Hellma GmbH & Co. KG*. **UV/Vis spectroscopy (UV/Vis).**

5

UV/Vis spectra were recorded on a *PerkinElmer, Inc.* Lambda 365 UV/Vis spectrophotometer in an UV quartz cuvette (40 mm x 10 mm x 2 mm). Spectra were measured from 250 nm to 950 nm with a spectral bandwidth (SBW) of 1 nm and a scan rate of 300 nm/min at 25 °C. The samples were dissolved in *N,N*-dimethylformamide and analyzed in a QS 10×10 mm quartz glass cuvette from *Hellma GmbH & Co. KG*. A base line correction with the pure solvent was performed prior to sample measurements. **Inductively coupled plasma mass spectrometry (ICP-MS).** To accurately quantify the Re and Ru amount loaded onto the polymers, ICP-MS for rhenium and ruthenium, respectively was conducted on a *Perkin Elmer* Nexlon 350D ICP-MS instrument. The respective samples were immersed in concentrated 7.5 mL nitric acid and 2.5 mL H_2O_2 30% (v/v) and treated in the microwave at 150 °C for 5 min. Subsequently, the microwave-digested samples were diluted 1/200 with Millipore Milli-Q® water. The extra pure solvents were checked for possible analyte contaminations before measurement. ^{104}Ru and ^{187}Re were used as target masses for the analytes and ^{103}Rh as an internal standard. Analyte quantification was carried out in standard mode with correction equation to avoid polyatomic interferences. Detection limit for Ru was 0.13 µg L^{-1} and 0.05 µg L^{-1} for Re. External calibration was performed in the range of 0 µg L^{-1} to 100 µg L^{-1}. Each sample was measured with five measurement replicates, a dwell time per 50 ms and an integration time of 750 ms. The Ru and Re concentrations were blank corrected *via* measurement of blank samples. **Gas-Phase infrared spectroscopy (IR)** has been measured on a *Thermo Fisher Scientific Nicolet 380 FT-IR* in transmittance mode with a resolution of 0.5 (0.241 cm^{-1}) in the range of 4000-400 cm^{-1} and 128 scans.

6

2. SYNTHESIS PROCEDURES

4-Hydroxyethyl-4-methyl-2,2'-bipyridine

C$_{12}$H$_{12}$N$_2$
M = 184.24 g/mol

C$_{13}$H$_{14}$N$_2$O
M = 214.27 g/mol
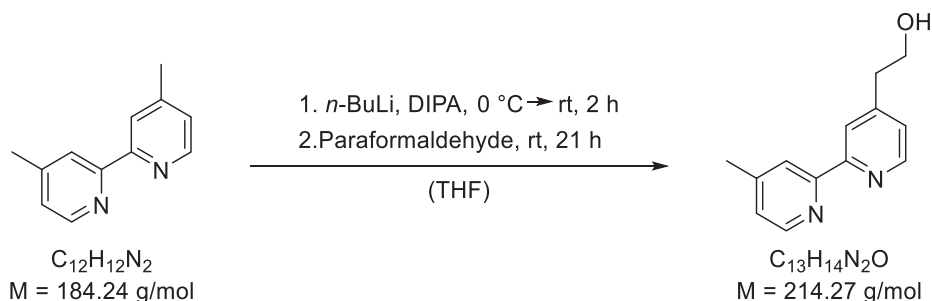
The synthesis of 4-hydroxyethyl-4'-methyl-2,2'-bipyridine was adapted from a literature-known procedure.[1] In an oven-dried Schlenk flask, 8.58 mL di-*iso*-propylamine (6.15 g, 60.8 mmol, 1.60 eq.) was dissolved in 50 mL of dry THF and cooled to 0 °C. To the resulting solution, 24.3 mL *n*-butyl lithium (2.5 M in hexanes, 60.8 mmol, 1.60 eq.) were added slowly and the reaction mixture was stirred at room temperature for one hour. To the previous solution, a solution of 7.00 g 4,4'-dimethyl-2,2'-bipyridil (38.0 mmol, 1.00 eq.) in 200 mL dry THF was transferred using a canula. The reaction mixture was stirred for two hours at room temperature and 4.56 g paraformaldehyde (152 mmol, 4.00 eq.) were added before stirring another 21 hours at room temperature. The reaction was quenched upon addition of 50 mL cold water and the mixture was extracted with diethyl ether (5 × 100 mL). The combined organic phases were dried over anhydrous Na$_2$SO$_4$, and the solvent was removed under reduced pressure to yield a brownish oil. The crude product was purified *via* column chromatography (Al$_2$O$_3$; CH$_2$Cl$_2$/MeOH = 50/1) to yield 4.57 g 4-hydroxyethyl-4'-methyl-2,2'-bipyridine (21.3 mmol, 56%) as a yellow oil.

7
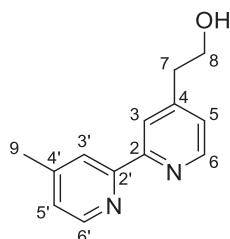
¹H-NMR (400 MHz, CDCl₃): δ (ppm) = 8.58 (d, ^3J = 5.0 Hz, 1 H, C-6-H), 8.52 (d, ^3J = 4.9 Hz, 1 H, C-6'-H), 8.27 (s, 1 H, C-3-H), 8.22 (s, 1 H, C-3'-H), 7.19 (dd, ^3J = 5.0 Hz, $^4J_{H,H}$ = 1.7 Hz, 1 H, C-5-H), 7.15 - 7.08 (m, 1 H, C-5'-H), 3.96 (q, ^3J = 6.2 Hz, 2 H, C-8-H), 2.95 (t, ^3J = 6.5 Hz, 2 H, C-7-H), 2.44 (s, 3 H, C-9-H).

TLC: R_f = 0.22 (CH₂Cl₂/MeOH = 50/1) [UV]

ESI-MS (solvent: MeCN) m/z: 214.9 ([M+H]⁺).

8

4-Vinyl-4'-methyl-2,2'-bipyridine (VBpy)

C$_{13}$H$_{14}$N$_2$O
M = 214.27 g/mol

C$_{13}$H$_{12}$N$_2$
M = 196.25 g/mol
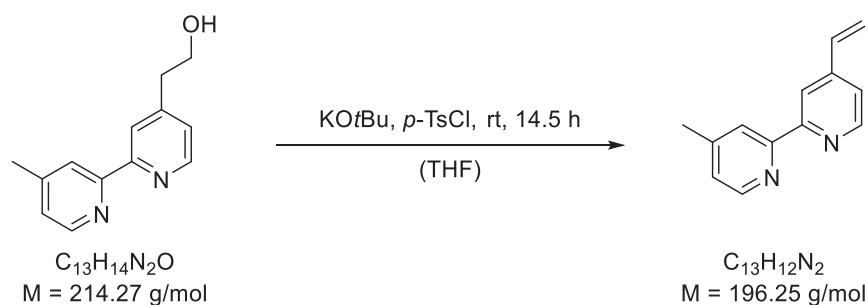
The synthesis of 4-vinyl-4'-methyl-2,2'-bipyridine was adapted from a literature-known procedure.[2] To a solution of 2.00 g 4-hydroxyethyl-4'-methyl-2,2'-bipyridine (9.33 mmol, 1.00 eq.) in 40 mL dry THF, 2.62 g potassium *tert*-butoxide (23.3 mmol, 2.50 eq.) were added at -10 °C. Subsequently, a solution of 2.67 g *p*-toluene sulfonyl chloride (14.0 mmol, 1.50 eq.) in 40 mL dry THF was added to the reaction mixture dropwise at -10 °C. The reaction mixture was stirred at -10 °C for another hour and at room temperature for additional 16 hours. The reaction was quenched by addition of 25 mL of a half saturated NaHCO$_3$ solution and the mixture extracted with diethyl ether (5 × 100 mL). The combined organic phases were dried over anhydrous Na$_2$SO$_4$, and the solvent was removed under reduced pressure to yield a yellowish solid. The crude product was purified *via* column chromatography (SiO$_2$; P/Et$_2$O/NEt$_3$ = 6/4/0.4) followed by twofold sublimation (80 °C, 2·10^{-2} mbar) to yield 1.34 g 4-vinyl-4'-methyl-2,2'-bipyridine (6.81 mmol, 73%) as a white, crystalline solid.

9
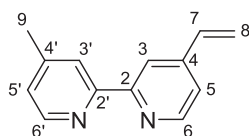
¹H-NMR (400 MHz, CDCl₃): δ (ppm) = 8.63 (d, ³*J* = 5.1 Hz, 1 H, C-6-H), 8.56 (d, ³*J* = 5.1 Hz, 1 H, C-6'-H), 8.44 (s, 1 H, C-3-H), 8.27 (s, 1 H, C-3'-H), 7.31 (dd, ³*J* = 5.1 Hz, ⁴*J* = 1.7 Hz, 1 H, C-5-H), 7.17 (dd, ³*J* = 5.1 Hz, ⁴*J* = 1.6 Hz, 1 H, C-5'-H), 6.77 (dd, ³*J* = 17.6 Hz, ³*J* = 10.9 Hz, 1 H, C-7-H), 6.11 (d, ³*J* = 17.6 Hz, 1 H, C-8-H), 5.54 (d, ³*J* = 10.9 Hz, 1 H, C-8-H), 2.46 (s, 3 H, C-9-H).

¹³C-NMR (101 MHz, CDCl₃): δ 156.67 (C-2), 155.83 (C-2'), 149.53 (C-6), 148.98 (C-6'), 148.48 (C-4'), 146.03 (C-4), 135.08 (C-7), 124.96 (C-5'), 122.22 (C-3'), 120.79 (C-5), 119.05 (C-8), 118.67 (C-3), 21.35 (C-9).

TLC: R_f = 0.35 (P/Et₂O/NEt₃ = 6/4/0.4) [UV]

ESI-MS (solvent: MeCN) m/z: 196.6 ([M+H]⁺).

Elemental analysis of C₁₃H₁₂N₂ (196.1): Calculated (%): **C** 79.56, **H** 6.16, **N** 14.27.

Found (%):   **C** 79.44, **H** 6.16, **N** 14.27.
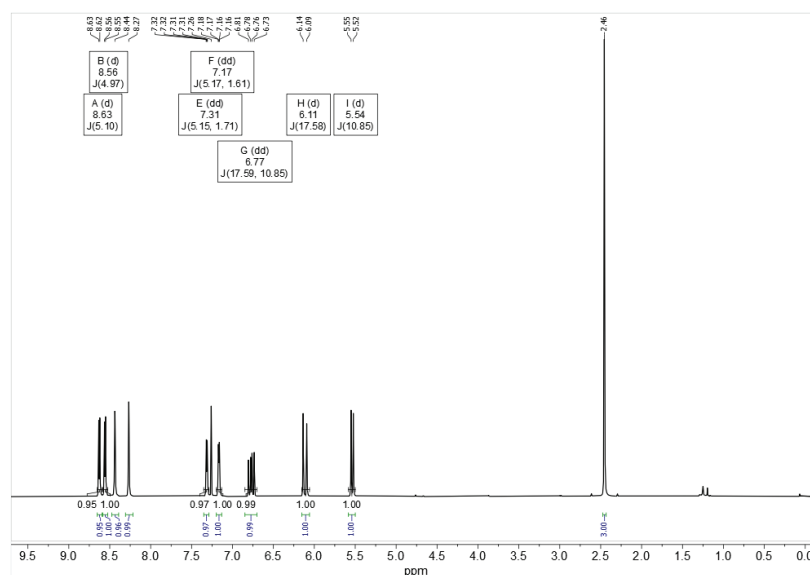
Figure S1: ¹H-NMR (400 MHz, CDCl₃, 300K) of the monomer 4-vinyl-4'-methyl-2,2'-bipyridine.

10

Synthesis of ruthenium precursor complex Ru(dmb)₂Cl₂

C₈H₁₂Cl₂Ru
M = 280.16 g/mol

C₂₄H₂₄Cl₂N₄Ru
M = 540.45 g/mol
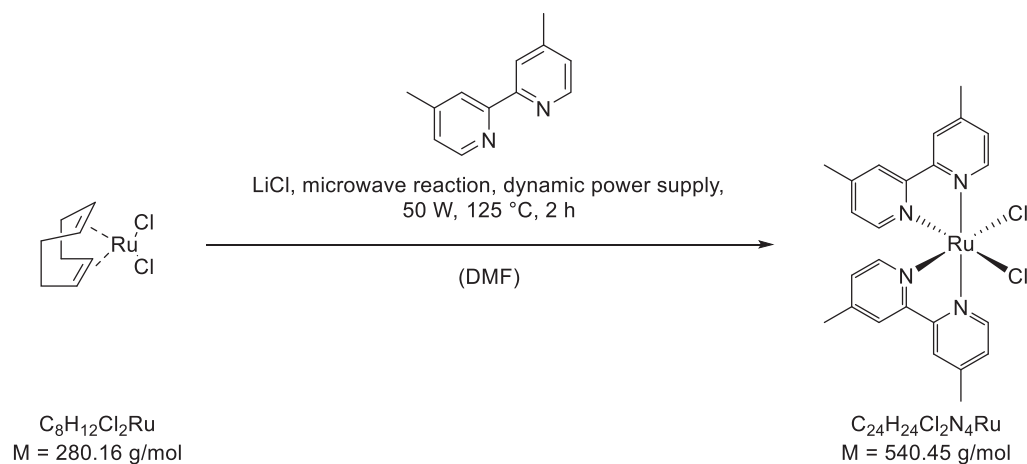
The synthesis of Ru(dmb)₂Cl₂ was adapted from a literature-known procedure.[3] Under inert gas atmosphere, 76.1 mg Ru(cod)Cl₂ (27.2 µmol, 1.00 eq.) and 98.9 mg lithium chloride (2.33 mmol, 8.59 eq.) are weighed into an oven-dried microwave vessel. Further, 100 mg 4,4-dimethyl-2,2'-bipyridine (54.3 µmol, 2.00 eq.) were added, the reactants suspended in 20 mL of dry *N,N*-dimethylformamide and heated in a closed vessel setup in a microwave reactor (125 °C, 50 W, dynamic mode) for two hours. After cooling to room temperature, the reaction mixture was filtered through a syringe filter and the solvent removed under reduced pressure. The residue was suspended in water, filtered over a fine frit (Por. 4) and washed with 100 mL of a 9/1 solution of water and acetonitrile. The crude product was eluted from the frit with chloroform and the solvent removed under reduced pressure. Recrystallisation of the crude product in acetonitrile (15 mL) yielded 60.5 mg Ru(dmb)₂Cl₂ (11.2 µmol, 41%) as a black powder.

ESI-MS (Solvent: MeCN) m/z: 541.5 ([M+H]⁺). The ESI-MS spectrum exhibited the expected isotope distribution.

UV/Vis (DMF): λ_{max} (nm) = 567, 384.

11

Synthesis of the electron donor 1,3-dimethyl-2-phenyl-2,3-dihydro-1*H*-benzo[*d*]imidazole (BIH)
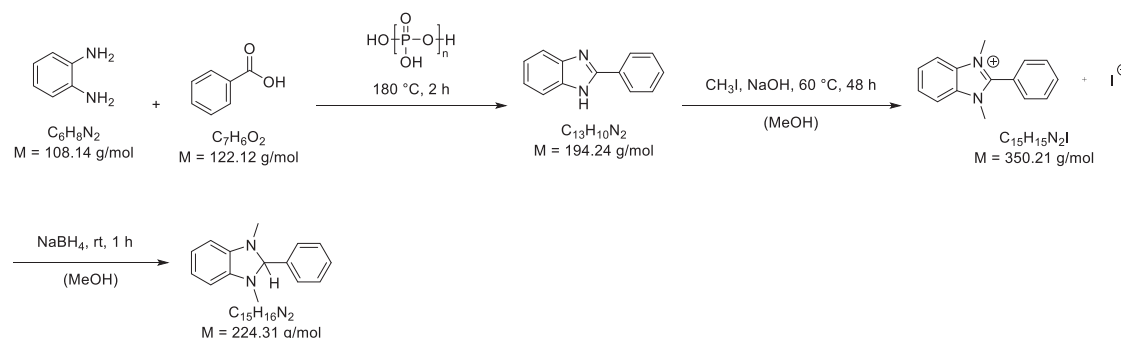
The synthesis of 2-phenyl-1*H*-benzo[*d*]imidazole was adapted from a literature-known procedure.[4] In a round bottom flask 6.14 g of benzoic acid (50.3 mmol, 1.00 eq.), 5.44 g *o*-phenylenediamine (50.3 mmol, 1.00 eq.) and 21.0 g polyphosphoric acid were heated to 180 °C for two hours. After slowly cooling to room temperature, the acid was neutralized by addition of 100 mL of ammonia solution (6wt% in water) and the crude product filtered off using a frit. The crude product was washed with ammonia solution (6wt% in water) until the blue colour disappeared and then dried in vacuo, yielding 9.77 g 2-phenyl-1*H*-benzo[*d*]imidazole (50.3 mmol, quant.) as a pink solid.

^{1}H-NMR (400 MHz, CDCl$_3$): δ (ppm) = 8.11 - 8.03 (m, 2 H, C-H$_{Ar}$), 7.70 - 7.62 (m, 2 H, C-H$_{Ar}$), 7.52 - 7.46 (m, 3 H, C-H$_{Ar}$), 7.31 - 7.26 (m, 2 H, C-H$_{Ar}$).

The synthesis of 1,3-dimethyl-2-phenyl-1*H*-benzo[*d*]imidazole-3-ium iodide was adapted from a literature-known procedure.[5] In a round bottom flask, 9.77 g 2-phenyl-1*H*-benzo[*d*]imidazole (50.3 mmol, 1.00 eq.) and 2.01 g sodium hydroxide (50.3 mmol, 1.00 eq.) were dissolved in 50 mL of dry methanol. Under vigorous stirring, 11.4 mL methyl iodide (26.0 g, 183 mmol, 3.60 eq.) were added dropwise and the solution heated to 60 °C for 48 hours. After cooling to room

temperature, the solvent was removed under reduced pressure and the residue dissolved in 320 mL of a hot ethanol/water mixture ($EtOH/H_2O = 5/1$). Subsequently, three spatula tips of activated charcoal were suspended in this solution and after 30 minutes removed via filtration over Celite®. Finally the solvent was removed under reduced pressure and the crude product recrystallized from ethanol (250 mL). Drying of the product in vacuo yielded 8.19 g 1,3-dimethyl-2-phenyl-1*H*-benzo[*d*]imidazole-3-ium iodide (23.4 mmol, 46%) as a yellow solid.

¹H-NMR (400 MHz, DMSO-d$_6$): δ (ppm) = 8.18 - 8.09 (m, 2 H, C-H$_{Ar}$), 7.96 - 7.88 (m, 2 H, C-H$_{Ar}$), 7.87 - 7.74 (m, 5 H, C-H$_{Ar}$), 3.90 (s, 6 H, N-CH$_3$).

The synthesis of 1,3-dimethyl-2-phenyl-2,3-dihydro-1*H*-benzo[*d*]imidazole was adapted from a literature-known procedure.[5] Under inert gas atmosphere, 8.19 g 1,3-dimethyl-2-phenyl-1*H*-benzo[*d*]imidazole-3-ium iodide (23.4 mmol, 1.00 eq.) were dissolved in 300 mL of dry methanol and 4.00 g sodium borohydride (106 mmol, 4.50 eq.) slowly added. The reaction mixture was stirred for one hour at room temperature and the solvent then removed under reduced pressure. The crude product was purified via twofold recrystallization from an ethanol/water mixture ($EtOH/H_2O = 2/1$, 200 mL). The product was dried in vacuo to yield 5.24 g of 1,3-dimethyl-2-phenyl-2,3-dihydro-1*H*-benzo[*d*]imidazole (23.4 mmol, quant.) as yellow, crystalline needles.

¹H-NMR (400 MHz, DMSO-d$_6$): δ (ppm) = 7.58 – 7.40 (m, 5 H, C-2-*Ph*), 6.62 (m, 2 H, C-H$_{Ar}$), 6.45 (m, 2 H, C-H$_{Ar}$), 4.87 (s, 1 H, C-2-H), 2.48 (s, 6 H, N-CH$_3$).

13

3. POLYMERIZATION RESULTS

3.1 POLYMERIZATION PROCEDURE

The calculated amount of Lewis acid was dissolved in 0.5 mL dry toluene. Subsequently, a solution of 1.02 mmol of the monomer in 1.5 mL dry toluene was added to the mixture. The polymerization was started by addition of the Lewis base and the conversion of the monomer was monitored via ^{1}H-NMR by periodically removing aliquots (0.1 mL of the reaction mixture + 0.4 mL of undried CDCl$_3$). When no further conversion could be detected in the NMR, the reaction was quenched by addition of 0.5 mL undried CDCl$_3$ and the polymer was precipitated in pentane. After decanting of the supernatant, the residual polymer was dissolved in benzene and freeze-dried to yield the pure polymer as a white solid.

3.2 POLYMER SYNTHESIS RESULTS FOR METAL LOADING

Table S1: Characterization of PVBpy1-3 prepared with the Lewis pair Al(i-Bu)$_3$/PMe$_3$.

Polymer	[VBpy]/[LA]/[LB][a] [eq.]/[eq.]/[eq.]	t_R [b] [h]	X_{VBpy} [c] [%]	$M_{n,theo}$ [d] [kg/mol]	$M_{n,abs}$ [e] [kg/mol]	Đ [e] [-]	I.E. [f] [%]
PVBpy 1	100/2/1	17	85	16.7	33.8	1.36	50
PVBpy 2	100/2/1	17	80	15.7	23.3	1.48	68
PVBpy 3	100/2/1	17	92	18.0	36.7	1.66	49

[a] Desired reactant ratio; [b] 1.02 mmol monomer in 2 mL toluene, room temperature, Lewis-acid and monomer were pre-mixed and the polymerization was started by addition of Lewis-base; [c] determination of conversion via aliquot-^{1}H-NMR; [d] theoretical molecular weight determined via $M_{n,theo} = X_{VBpy} \times M_{VBpy} \times$ [VBpy]/[LA]/[LB] assuming full initiator efficiency; [e] absolute molecular weight and polydispersity determined using SEC with triple detection in DMF with added LiBr (25 mmol/L) at 30 °C using the experimentally determined dn/dc = 0.190 mL g^{-1}; [f] initiator efficiency I.E. = $M_{n,theo}/M_{n,abs} \times$ 100%.

14
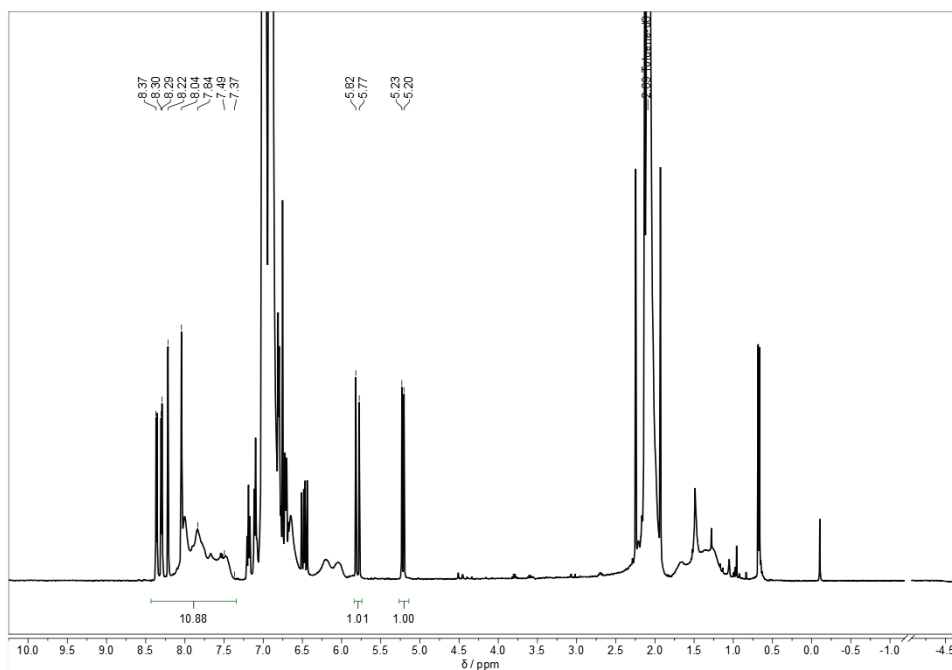
Figure S2: Aliquot-^{1}H-NMR (400 MHz, CDCl$_3$, 300K) for polymerization determination via integration of the signals between 7.37-8.37 ppm I$_{Pol}$ versus vinyl signals from 5.20-5.23 I$_V$ set to one with conversion X = (I$_{Pol}$ - 4)/I$_{Pol}$ x 100%.
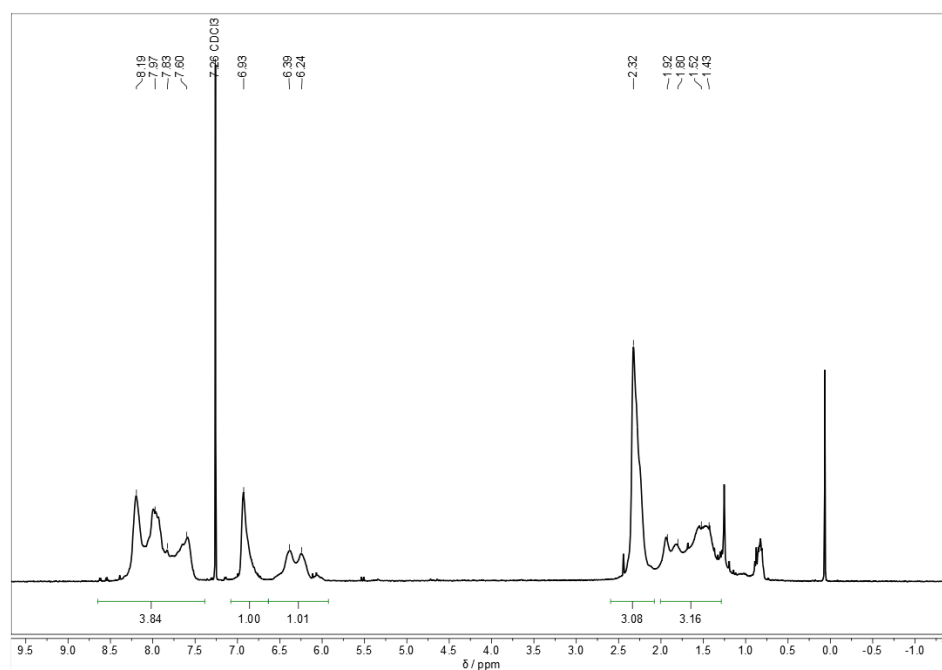
Figure S3: ^{1}H-NMR (400 MHz, CDCl$_3$, 300 K) of PVBpy (Table 1, entry 2).

15
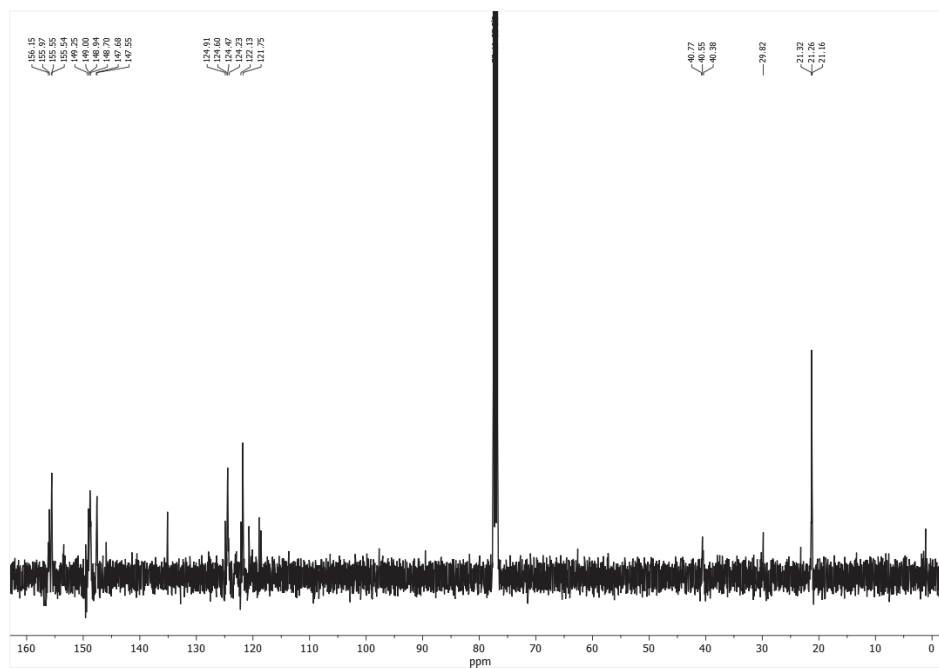
Figure S4: ^{13}C-NMR (101 MHz, CDCl$_3$, 300 K) of PVBpy (Table 1, entry 8).

3.3 SIZE-EXCLUSION CHROMATOGRAPHY DATA
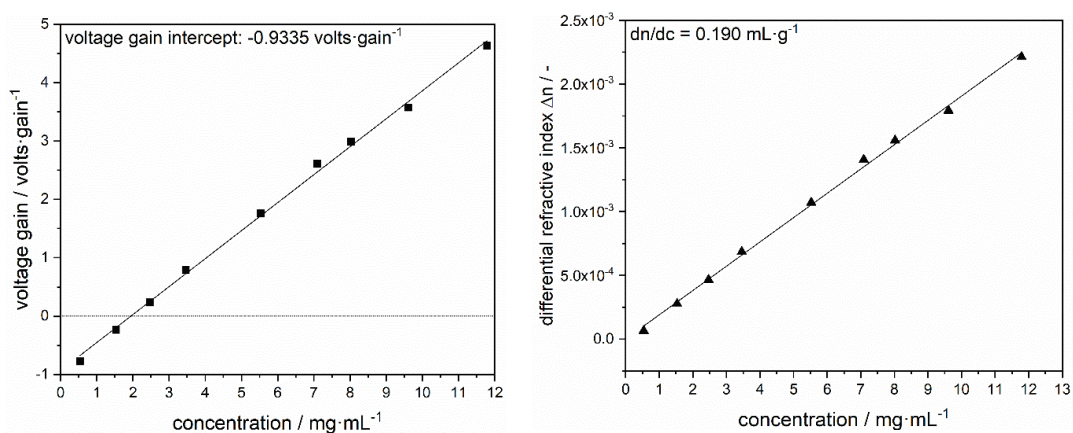
Figure S5: Voltage gain-concentration plot (left) and calculated differential refractive index-concentration plot (right) for the dn/dc determination using 9 different concentrations in the range of 0.5 to 12 mg/mL of the same PVBpy sample. The differential refractive index is calculated by the difference between each voltage gain at a certain concentration and the extrapolated voltage gain intercept at zero concentration multiplied by the detector constant from calibration. The dn/dc is the slope of the linear fit in the differential refractive index-concentration plot.
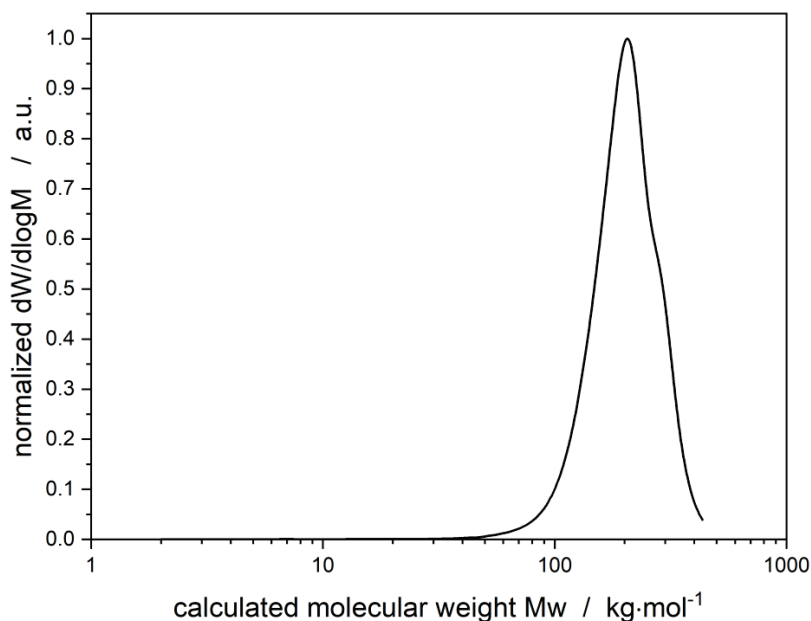
Figure S6: Molecular weight distribution of PVBpy (Table 1, entry 1) determined via SEC (DMF + 25 mmol/L LiBr, 30 °C, triple detection).

17
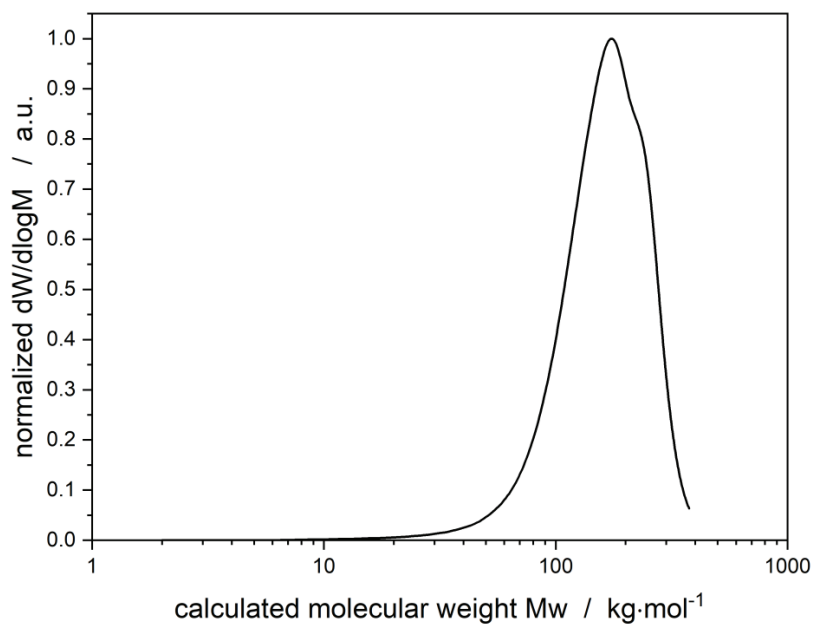
Figure S7: Molecular weight distribution of PVBpy (Table 1, entry 2) determined via SEC (DMF + 25 mmol/L LiBr, 30 °C, triple detection).
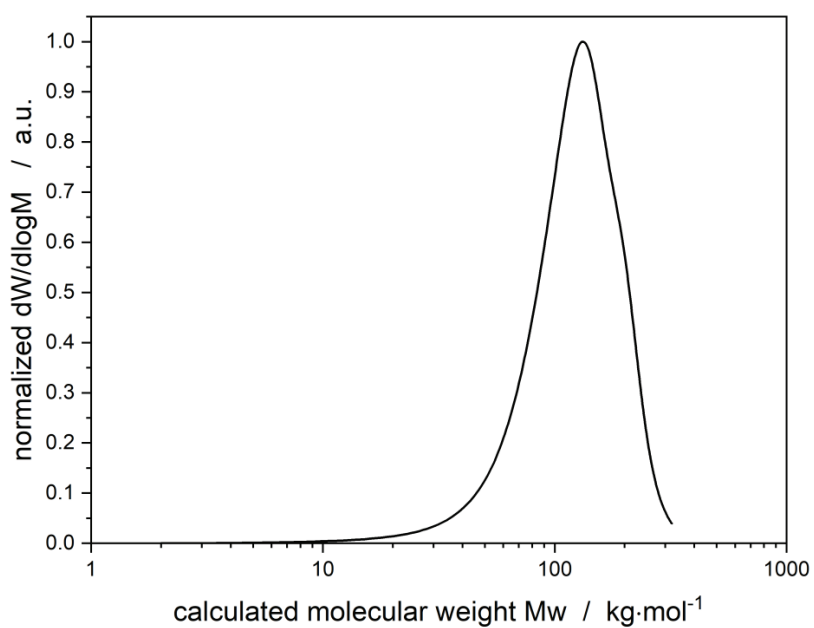
Figure S8: Molecular weight distribution of PVBpy (Table 1, entry 3) determined via SEC (DMF + 25 mmol/L LiBr, 30 °C, triple detection).

18
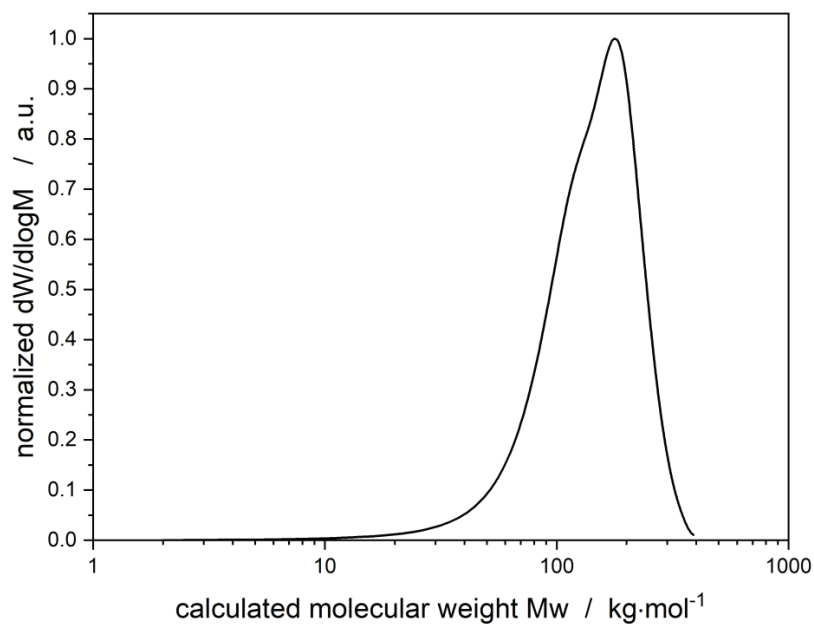
Figure S9: Molecular weight distribution of PVBpy (Table 1, entry 4) determined via SEC (DMF + 25 mmol/L LiBr, 30 °C, triple detection).
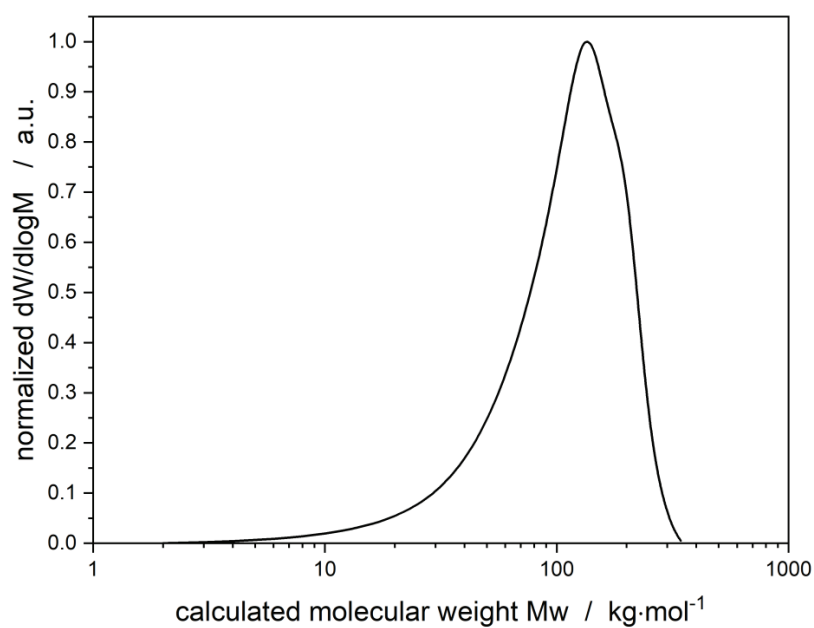
Figure S10: Molecular weight distribution of PVBpy (Table 1, entry 5) determined via SEC (DMF + 25 mmol/L LiBr, 30 °C, triple detection).

19
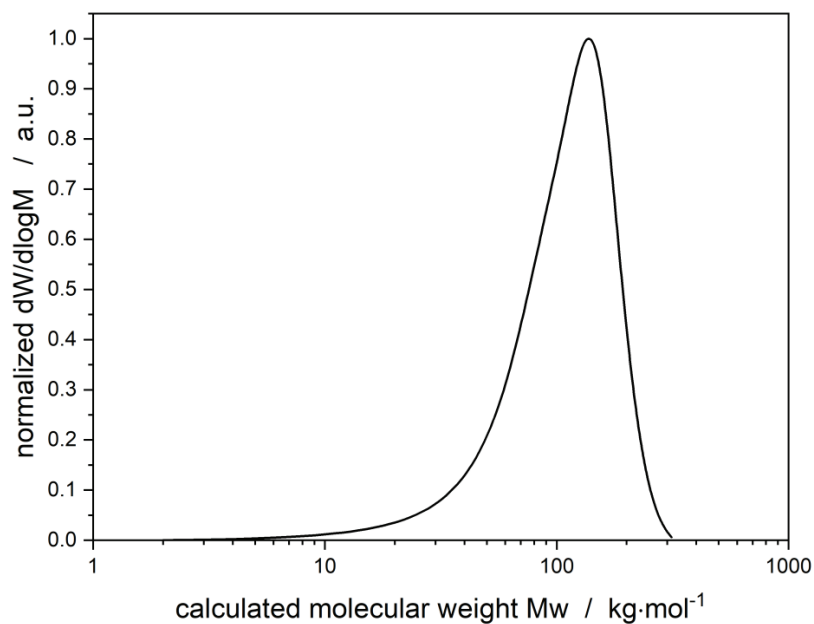
Figure S11: Molecular weight distribution of PVBpy (Table 1, entry 6) determined via SEC (DMF + 25 mmol/L LiBr, 30 °C, triple detection).
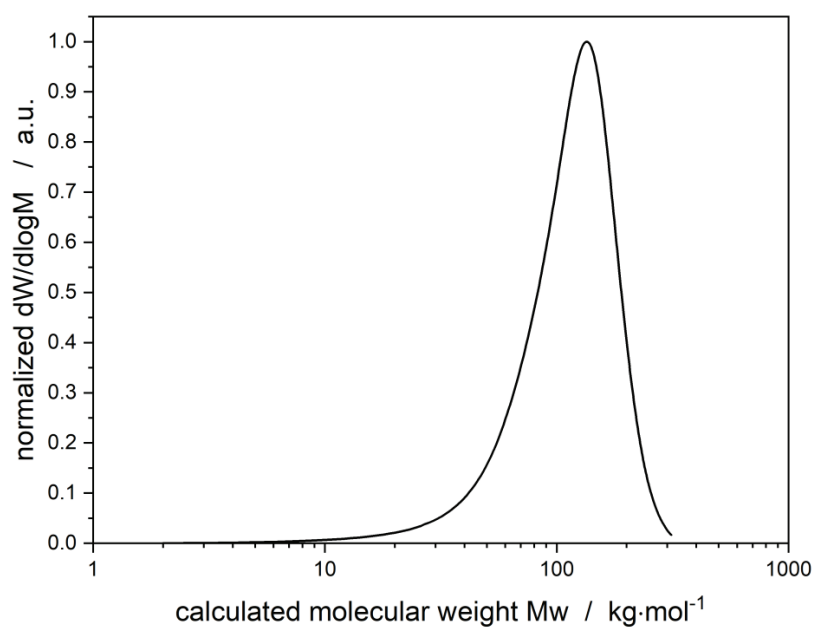
Figure S12: Molecular weight distribution of PVBpy (Table 1, entry 7) determined via SEC (DMF + 25 mmol/L LiBr, 30 °C, triple detection).

20
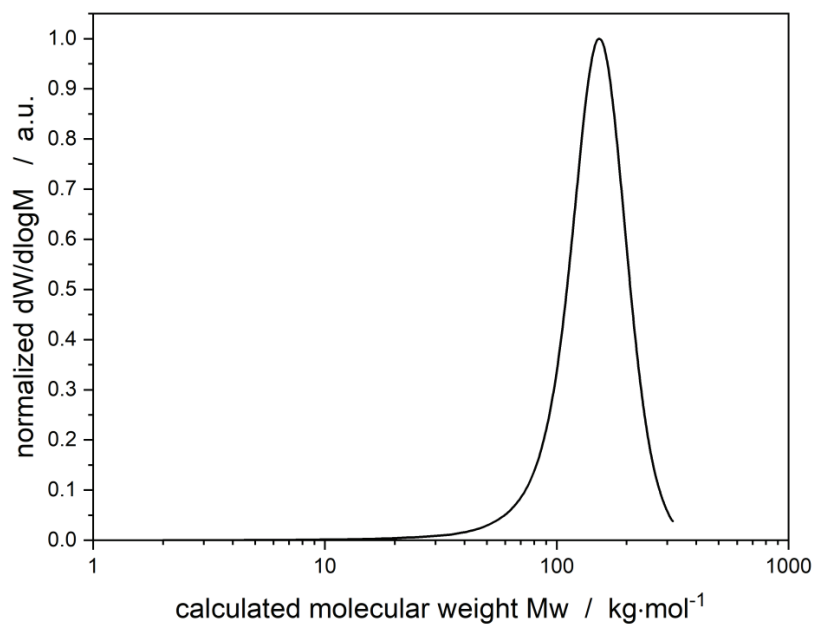
Figure S13: Molecular weight distribution of PVBpy (Table 1, entry 8) determined via SEC (DMF + 25 mmol/L LiBr, 30 °C, triple detection).
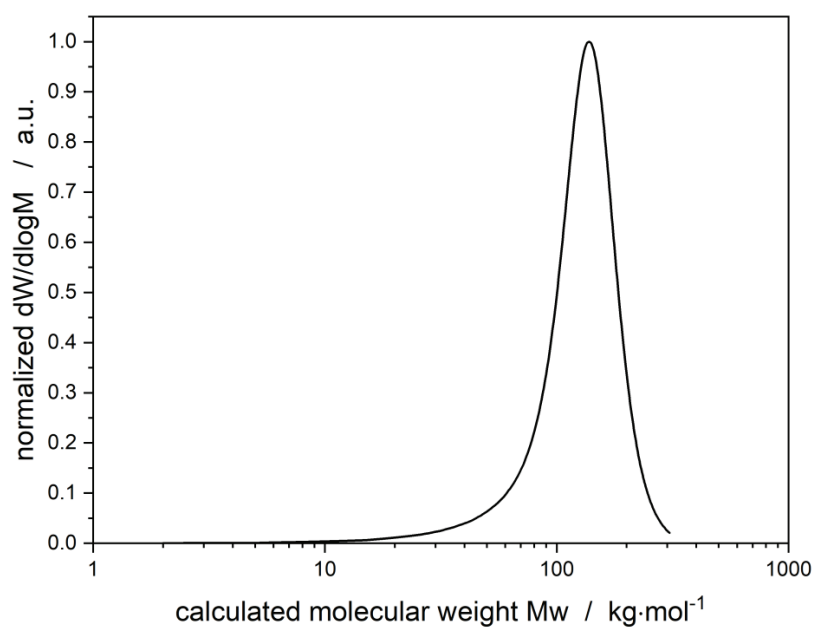
Figure S14: Molecular weight distribution of PVBpy (Table 1, entry 9) determined via SEC (DMF + 25 mmol/L LiBr, 30 °C, triple detection).
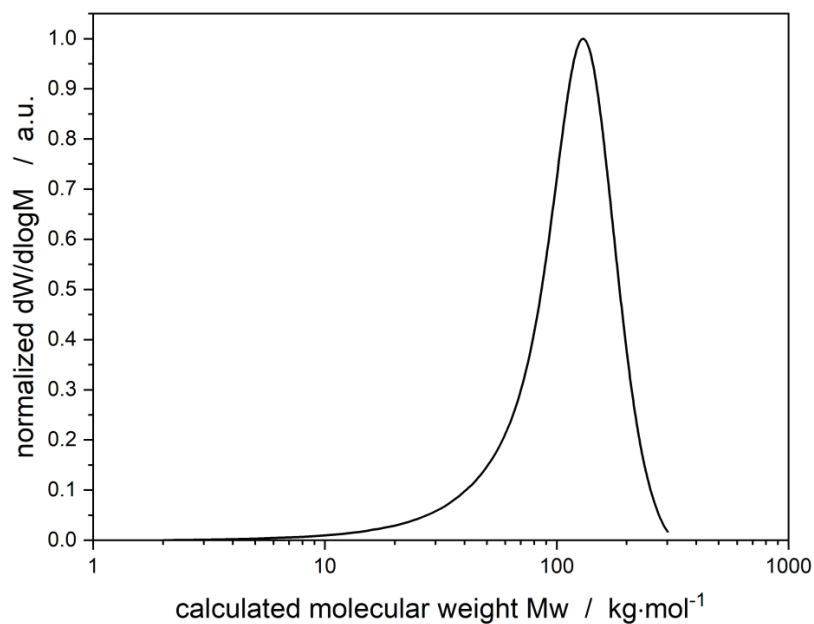
Figure S15: Molecular weight distribution of PVBpy (Table 1, entry 10) determined via SEC (DMF + 25 mmol/L LiBr, 30 °C, triple detection).
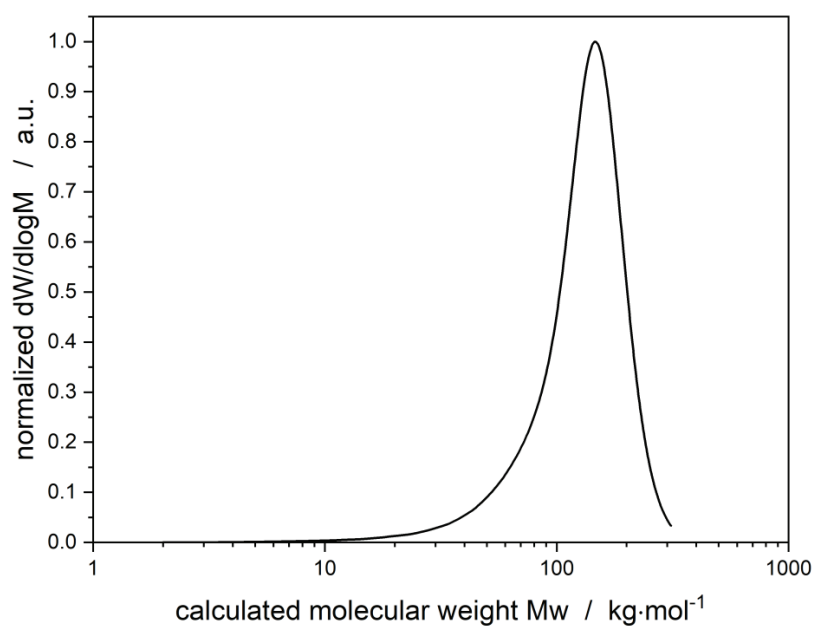
Figure S16: Molecular weight distribution of PVBpy (Table 1, entry 11) determined via SEC (DMF + 25 mmol/L LiBr, 30 °C, triple detection).

22
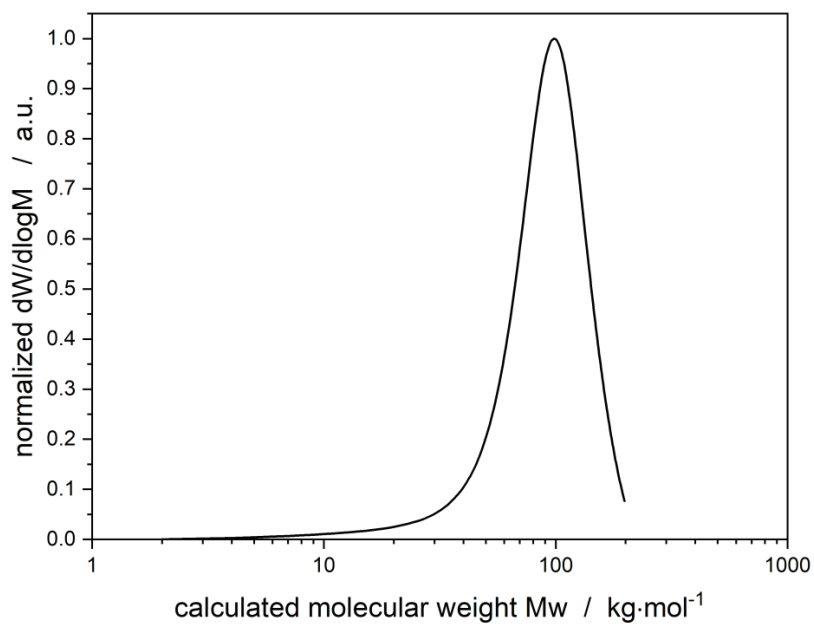
Figure S17: Molecular weight distribution of PVBpy1 (Table S1, entry 1) determined via SEC (DMF + 25 mmol/L LiBr, 30 °C, triple detection).
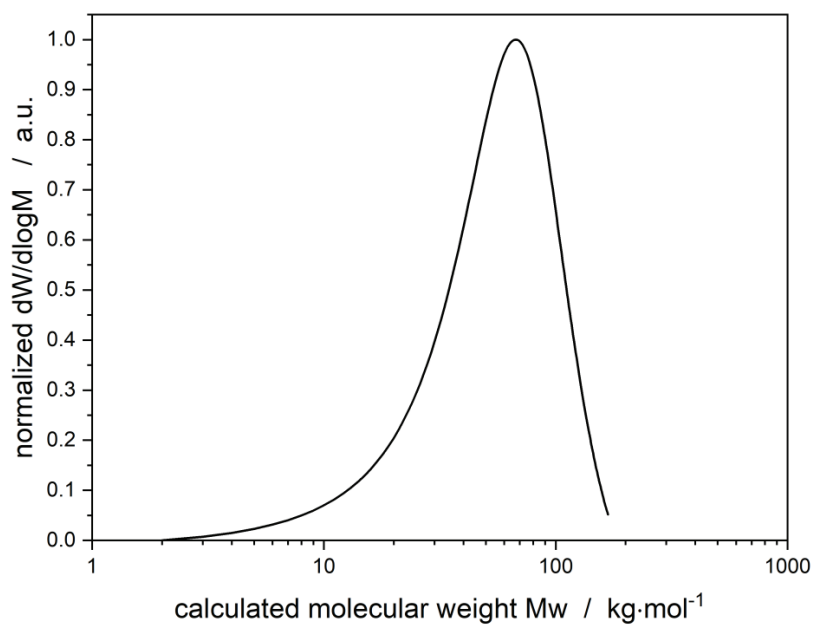
Figure S18: Molecular weight distribution of PVBpy2 (Table S1, entry 2) determined via SEC (DMF + 25 mmol/L LiBr, 30 °C, triple detection).

23
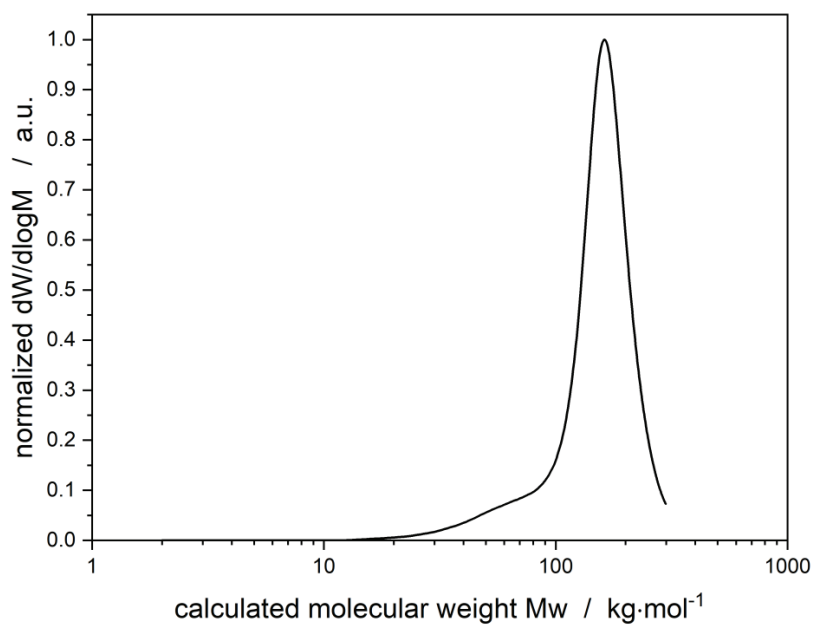
Figure S19: Molecular weight distribution of PVBpy3 (Table S1, entry 3) determined via SEC (DMF + 25 mmol/L LiBr, 30 °C, triple detection).

24

3.4 ADDITIONAL POLYMER ANALYTICS

conjugate addition:
◇: [n x M_{VBpy} + M_{PMe3} + Na]$^+$; n = 1-4
deprotonation:
∇: [n x M_{VBpy} + H]$^+$; n = 1-6
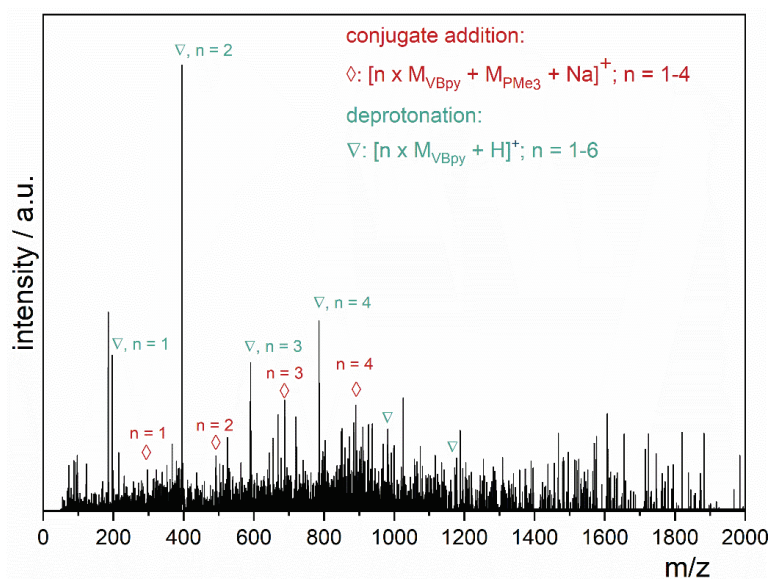
Figure S20: ESI-MS of PVBpy oligomers prepared with the Lewis pair Al(*i*-Bu)$_3$/PMe$_3$ in acetonitrile, positive ionization; assignments of series to phosphine-terminated oligomers (red) from conjugate addition initiation and olefin-terminated oligomers (green) from deprotonation initiation.
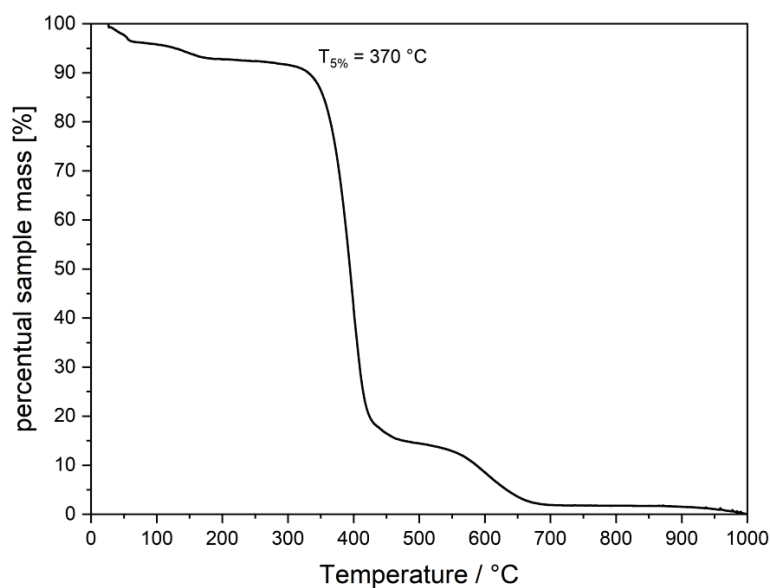
Figure S21: TGA measurement of PVBpy (Table 1, entry 7) from 23 to 1000 °C under argon atmosphere.

25
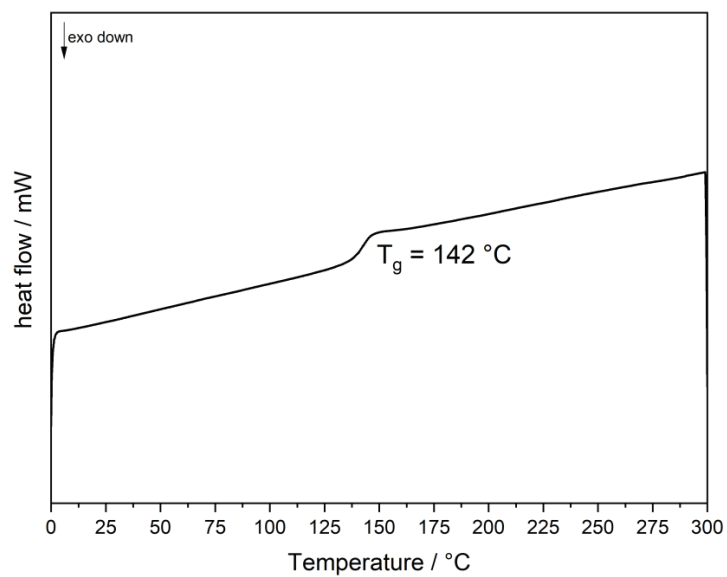
Figure S22: DSC measurement of PVBpy (Table 1, entry 9) in the range of 0 to 300 °C measured in exo down mode.

4. PHOTOCATALYSIS

4.1 METAL LOADING OF POLYMERS

Rhenium loading
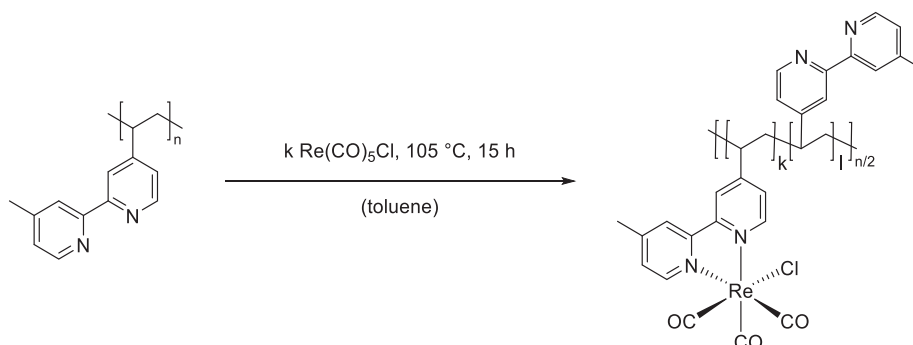
The synthesis of Re loaded PVBpy was adapted from the literature-known procedure for the synthesis of mononuclear Re complexes with bipyridine ligands.[6] The polymer was dissolved in dry toluene in an oven-dried pressure Schlenk flask and the Re precursor $Re(CO)_5Cl$ added. Subsequently, the Schlenk flask was sealed, and the reaction mixture heated to 105 °C overnight. After cooling to room temperature, the solvent was removed under reduced pressure and the polymer dried in vacuo.

IR: v (cm^{-1}) = 2014 (v (C=O), s), 1872 (v (C=O), s), 1608 (v (C=C/C=N), m), 1487 (v (C=C/C=N), m), 1423 (v (C=C/C=N), m), 1029 (v (CH$_x$), m), 907 (v (CH$_x$), m), 830 (v (CH$_x$), m).

PL (DMF): λ_{max} (nm) = 614.

UV/Vis (DMF): λ_{max} (nm) = 372, 290.

27

Ru loading of Re loaded polymers
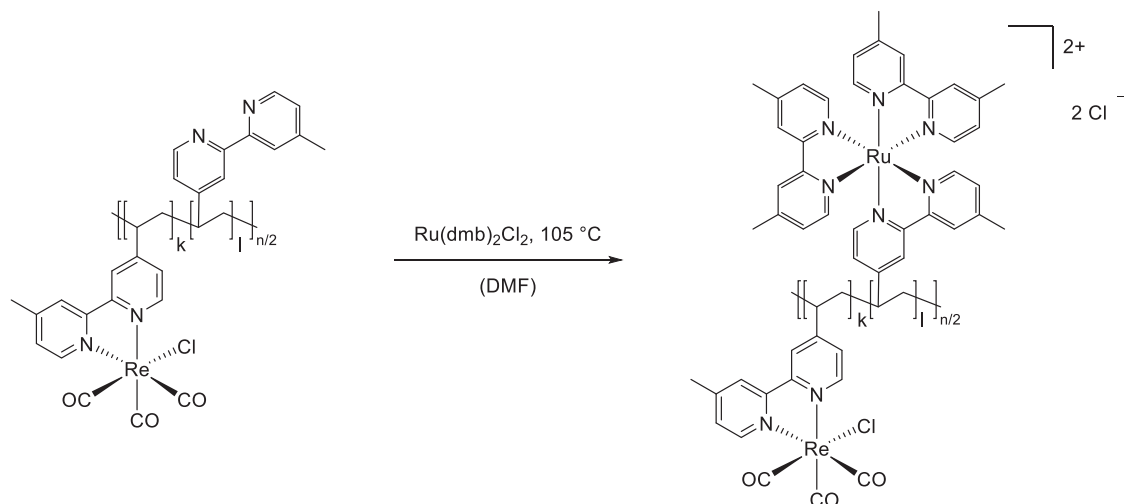
In a pressure Schlenk flask, the Re loaded polymer was dissolved in 5 mL of dry *N,N*-dimethylformamide and a solution of the respective amount of Ru(dmb)$_2$Cl$_2$ (1.10 eq. with regard to free bipyridine coordination sites) in 15 mL *N,N*-dimethylformamide added. The Schlenk flask was sealed, and the reaction mixture heated to 105 °C overnight. After cooling to room temperature, the solvent was removed under reduced pressure, the residue dissolved in methanol and precipitated from an aqueous NH$_4$PF$_6$ solution. For purification, the precipitates were washed with methanol and dried in vacuo. For the UV/Vis investigation PVBpy^{Ru} was prepared according to the same procedure with unloaded polymer instead of a rhenium-loaded polymer.

PL (DMF): λ_{max} = 640 nm.

UV/Vis (DMF): λ_{max} (nm) = 464, 371, 290.

4.2 CHARACTERIZATION OF PHOTOCATALYSTS
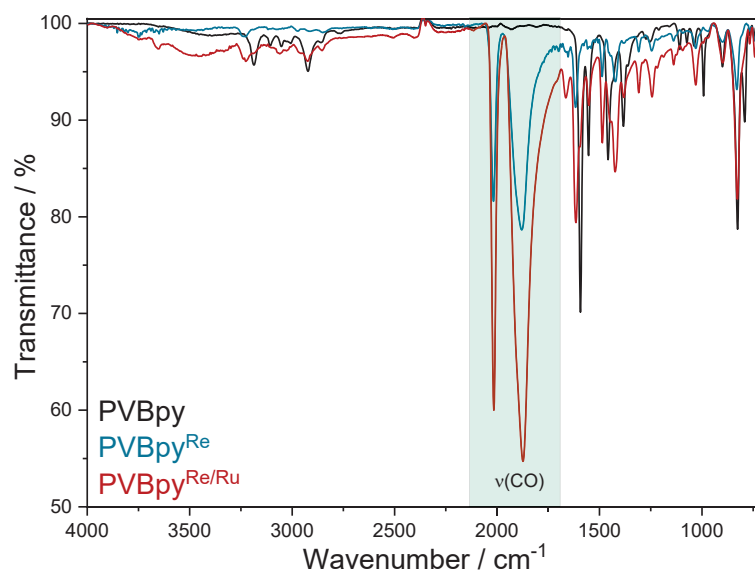
Figure S23: FT-IR spectra of unloaded PVBpy (black), PVBpy after loading with $Re(CO)_5Cl$ precursor (blue) and PVBpy after loading with $Re(CO)_5Cl$ precursor and $Ru(dmb)_2Cl_2$ precursor (red). The characteristic Re-CO signals, inphase a`(1) (v = 2015 cm^{-1}), antisymmetric a`` (v = 1908 cm^{-1}), and out of-phase symmetric a`(2) (v = 1873 cm^{-1}) of PVBpy^{Re} and PVBpy$^{Re/Ru}$ are marked. The IR band at 1616 cm^{-1} can be assigned to the stretching of the bipyridine ligands.[7]
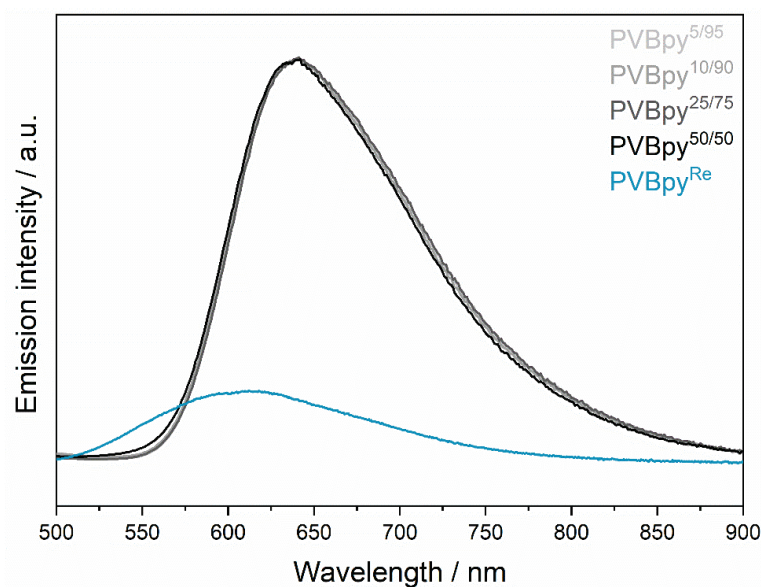
Figure S24: Photoluminescence spectra of **PVBpy$^{5/95}$**, **PVBpy$^{10/90}$**, **PVBpy$^{25/75}$**, **PVBpy$^{50/50}$** and **PVBpy^{Re}** upon irradiation at λ = 365 nm.

29

Table S2: ICP-MS measurement values for Re and Ru in various polymer samples, the resulting catalyst/photosensitizer ratios immobilized ($R_{Re/Ru}$) and the calculated catalyst (Re) loading on the respective polymer.

Sample	Re mass (m) [µg]	Ru mass (m) [µg]	Sample mass (m) [mg]	Re [µmol/mg$_{polymer}$]	Ru [µmol/mg$_{polymer}$]	$R_{Re/Ru,calc}$	Catalyst loading [nmol$_{Re}$/mg$_{polymer}$]
PVBpy$^{5/95}$	26.9	66.0	1.70	0.094	0.384	0.25	478
PVBpy$^{10/90}$	66.0	44.6	1.50	0.236	0.294	0.80	530
PVBpy$^{25/75}$	164	52.1	1.53	0.575	0.336	1.70	912
PVBpy$^{50/50}$	234	27.0	1.31	0.959	0.204	4.70	1163

$$n(Re_{per\,mg\,polymer}) = \frac{m_{Re}}{M_{Re}} \cdot \frac{1}{m_{sample}} = \frac{26.9\,\mu g}{186.207\,\frac{g}{mol}} \cdot \frac{1}{1.70\,mg_{polymer}} = 0.094\,\frac{\mu mol}{mg_{polymer}} \quad (1)$$

$$n(Ru_{per\,mg\,polymer}) = \frac{m_{Ru}}{M_{Ru}} \cdot \frac{1}{m_{sample}} = \frac{66.0\,\mu g}{101.070\,\frac{g}{mol}} \cdot \frac{1}{1.70\,mg_{polymer}} = 0.384\,\frac{\mu mol}{mg_{polymer}} \quad (2)$$

$$R_{P(VBpy),calc} = \frac{n(Re_{per\,mg\,polymer})}{n(Ru_{per\,mg\,polymer})} = \frac{0.094\,\frac{\mu mol}{mg_{polymer}}}{0.384\,\frac{\mu mol}{mg_{polymer}}} = 0.25 \quad (3)$$

The percentage ratio of Re loaded, Ru loaded and unloaded vinyl bipyridines in the polymer chain was calculated using the following formulas. The amounts of metal centers required for this calculation were determined by ICP-MS (see above) and corrected to one milligram of polymer each. For this reason, all masses and amounts of substances given here are based on one milligram of polymer. The abbreviations Re and Ru stand for the corresponding units Re(VBpy)(CO)$_3$Cl and

30

$Ru(dmb)_2(VBpy)(PF_6)_2$, respectively. With equation 11, the percentage ratio of Re loaded und Ru loaded vinyl bipyridines can be calculated in analogy. An exemplary calculation is provided below for PVBpy$^{5/95}$ with full measurement data.

$$m_{Re}[\mu g]= n_{Re}[\mu mol]\cdot M_{Re}\left[\frac{\mu g}{\mu mol}\right] \tag{4}$$

$$m_{Re(PVBpy^{5/95})}[\mu g]= 94.33\cdot10^{-3}\ \mu mol\cdot502.01\frac{\mu g}{\mu mol} = 47.36\ \mu g \tag{5}$$

$$m_{Ru}[\mu g]= n_{Ru}[\mu mol]\cdot M_{Ru}\left[\frac{\mu g}{\mu mol}\right] \tag{6}$$

$$m_{Ru(PVBpy^{5/95})}[\mu g]= 384.01\cdot10^{-3}\ \mu mol\cdot956.13\frac{\mu g}{\mu mol} = 367.16\ \mu g \tag{7}$$

$$m_{VBpy(PVBpy^{5/95})}[\mu g]=m_{PVBpy^{5/95}}\ [\mu g]-m_{Re}\ [\mu g]-m_{Re}\ [\mu g] \tag{8}$$

$$m_{VBpy(PVBpy^{5/95})}[\mu g]=1000\ \mu g-47.36\ \mu g-367.16\ \mu g=585.48\ \mu g \tag{9}$$

$$n_{VBpy}[\mu mol]=\frac{m_{VBpy}[\mu g]}{M_{VBpy}\left[\frac{\mu g}{\mu mol}\right]}= \frac{585.48\ \mu g}{196.10\ \frac{\mu g}{\mu mol}}=2.99\ \mu mol \tag{10}$$

$$X_{unoccupied\ VBpy}\ [\%]=$$
$$\frac{n_{VBpy}[nmol]}{n_{VBpy}[nmol]+n_{Re}[nmol]+n_{Ru}[nmol]} =\frac{2990\ nmol}{2990\ nmol+94.33\ nmol+384.01\ nmol}=86.2\% \tag{11}$$

31

4.3 PHOTOCATALYTIC RESULTS

To avoid any light-induced deactivation processes, all photocatalytic experiments were conducted in a darkened room and respective reaction flasks were protected from visible light irradiation by wrapping them in aluminum foil outside of the irradiation times. The photocatalytic experiments were performed in Schlenk tubes with known total volume, with a constant volume of catalyst solution of 11 mL. Prior to the photocatalysis, the calculated amount of respective catalyst is weighed-in, dissolved in *N,N*-dimethylformamide and transferred to the Schlenk tube. Subsequently, the electron donor 1,3-dimethyl-2-phenyl-2,3-dihydro-1*H*-benzo[*d*]imidazole (BIH), as well as the base triethanolamine (TEOA) are added. The reaction mixture is then saturated with CO_2 (4.5) for ten minutes by bubbling the gas into the stirred solution under exclusion of visible light irradiation. Finally, the reaction flask is pressurized with CO_2 to an overpressure of 1.45 bar and sealed with a septum. For the photocatalytic experiments, the prepared samples are placed in front of a green LED ($\lambda = 520 \pm 30$ nm) and the gas phase composition in the reaction flask headspace is analyzed via Micro-GC in regular time intervals.

Photocatalysis turnover number (TON) calculations. The turnover numbers for the photocatalytic CO_2 reduction experiments were calculated from the exact molar catalyst amounts in each experiment. The catalyst amount was obtained through multiplying the $\mu mol/mg_{polymer}$ values from ICP-MS analysis (Table S2) with the weigh-in. The Micro-GC measurements yielded area% results for each of the gasses present in the headspace of the reaction flasks. For carbon monoxide, those values were converted to vol%, volume, and moles utilizing the total gas phase volume of the reaction vessel. An exemplary TON calculation for PVBpy$^{5/95}$ with full measurement data is provided below. The TOF was derived from the slope between the first two GC measurements.

32

Note: The headspace volume $V_{headspace}$ is obtained by subtracting the solvent volume (11 mL in this case) from the total volume of the reaction flask, which was predetermined by filling the vessel with water. The pressure p includes the applied CO_2 overpressure for a total pressure of 1.45 bar and solvated CO in DMF is neglected in this calculation.

$$n_{Re}[\mu mol]= n_{Re}\left[\frac{\mu mol}{mg_{polymer}}\right]\cdot m_{sample}[mg]=0.094\ \frac{\mu mol}{mg_{polymer}}\cdot 2.33\ mg=0.22\ \mu mol \tag{12}$$

$$Vol\%_{CO}=Area\%_{CO}\cdot 1.195=12.64\%\cdot 1.195=15.10\% \tag{13}$$

$$V_{CO,gas}[mL]=\frac{Vol\%_{CO}}{100}\cdot V_{headspace}[mL]=\frac{15.10\%}{100}\cdot 149.1\ mL=22.51\ mL \tag{14}$$

$$n_{CO,gas}[mmol]=\frac{p\cdot V_{CO}}{R\cdot T}=\frac{1.45\cdot 10^5\ Pa\cdot 22.51\ mL}{8.314\frac{J}{mol\cdot K}\cdot 293.15\ K}=1.34\ mmol \tag{15}$$

$$TON_{CO}=\frac{n_{CO,total}[mmol]}{n_{Re}[\mu mol]}=\frac{1.34\ mmol}{0.22\ \mu mol}=6088 \tag{16}$$

$$TOF_{CO,\ t(1)}=\frac{n_{CO,t(1)}[mmol]}{n_{Re}[\mu mol]*time\ intervall\ (1)\ [h]}=\frac{0.27\ mmol}{0.22\ \mu mol * 18.5\ h}=66\ h^{-1} \tag{17}$$

33

Table S3: TOFs and TONs of the Re/Ru loaded polymers in CO_2-saturated (15 min) DMF solution with BIH ([BIH]/[Re] = 10000) and TEOA (1.7 M). Irradiation was performed at λ = 520 nm. The calculation of the TON was performed according to the equations 12-16. The TOF was derived from the slope between the first two GC measurements. In-depth analysis of the gas phase composition after irradiation with an RGD (reduction gas detector) revealed traces of hydrogen evolution.

Catalyst	Rhenium concentration [μM]	Irradiation time [h]	TOF [h^{-1}]	TON [-]
PVBpy$^{10/90}$	20.0	280	38	898
PVBpy$^{25/75}$	20.0	260	6.9	724
PVBpy$^{50/50}$	20.0	335	4.2	927
PVBpy$^{5/95}$	20.0	713	66	5650
PVBpy$^{5/95}$	1.25	160	42	677
PVBpy$^{5/95}$	2.50	91	51	1176
PVBpy$^{5/95}$	5.00	91	42	990
PVBpy$^{5/95}$	10.0	234	46	1704
PVBpy$^{5/95}$	30.0	503	52	5493

34
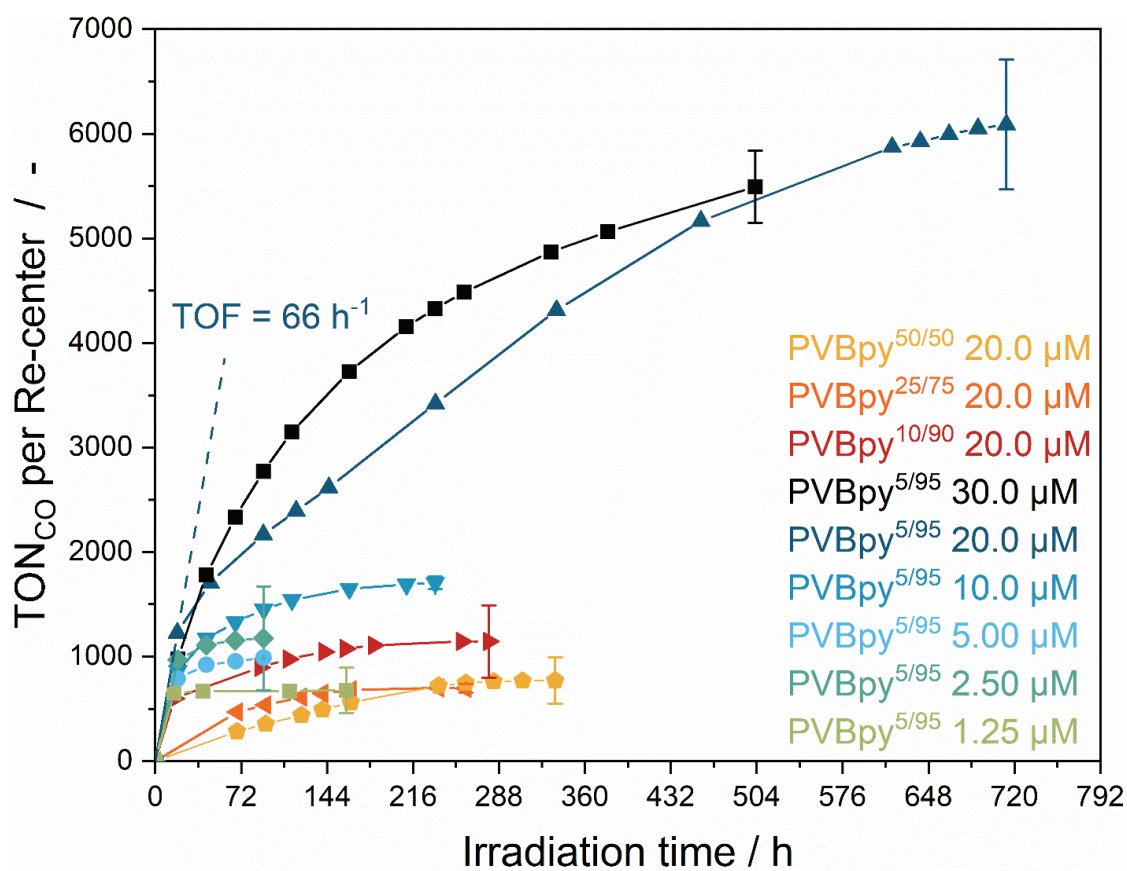
Figure S25: Turnover numbers of different macromolecular photocatalysts with varying rhenium concentrations in the photocatalytic reduction of CO_2. The catalyst-containing, CO_2-saturated (15 min) DMF solution with BIH ([BIH]/[Re] = 10000) and TEOA (1.72 M) was irradiated at $\lambda = 520$ nm.

Table S4: TOFs and TONs of the control experiments for the Re/Ru loaded polymers and suiting combinations in CO_2-saturated (15 min) DMF solution with BIH ([BIH]/[Re] = 10000) and TEOA (1.7 M). Irradiation was performed at λ = 520 nm. The calculation of the TON was performed according to the equations 12-16. The TOF was derived from the slope between the first two GC measurements. Deviations from the standard experiment are denoted under condition variation.

Catalyst / Combination	Rhenium concentration [μM]	Condition variation	Irradiation time [h]	TOF [h^{-1}]	TON [-]
PVBpy^{Ru}	-	no rhenium	74	0.3 [a]	21 [a]
PVBpy^{Re}	20.0 [b]	no ruthenium	74	0.4	30
PVBpy^{Ru} + PVBpy^{Re}	20.0 [b]	mixed catalysts	188	7.3	1365
PVBpy$^{25/75}$	20.0	no light	2	0	0
PVBpy$^{50/50}$	20.0	no BIH	3	-	-
-	-	no catalyst	3	0	0
PVBpy$^{50/50}$	20.0	no CO_2 overpressure	16	-	traces of CO (via FID)
PVBpy$^{5/95}$	10.0	$^{13}CO_2$ for IR-experiment	150	n. d. [c]	n. d. [c]

[a] related to ruthenium concentration assuming quantitative loading; [b] assuming quantitative rhenium loading; [c] not determined.

36
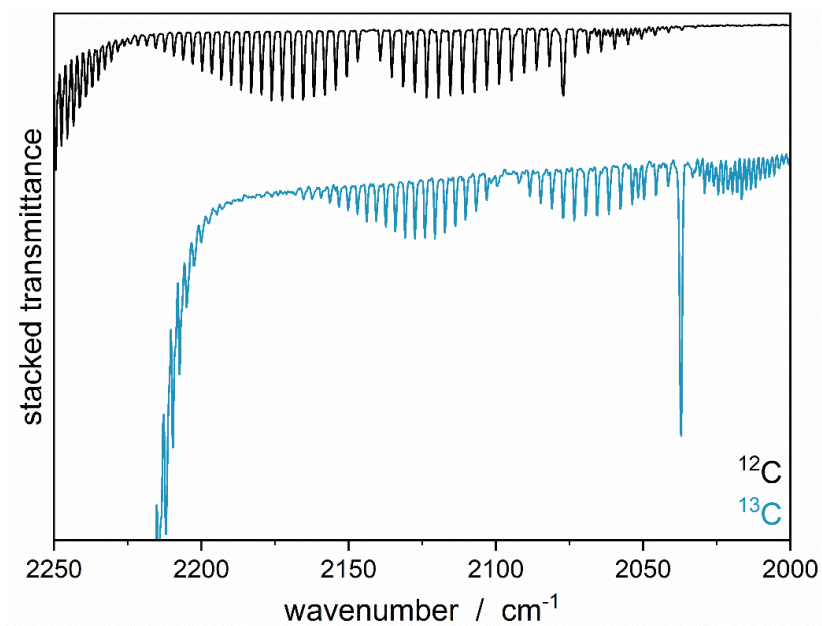
Figure S26: Gas-phase IR of the headspace taken after 150 h of irradiation time from $^{12}C/^{13}C$ CO_2 reduction isotope labelling control experiment with PVBpy5/95 under standard conditions.

37

REFERENCES

(1) Lu, Z.; Ladrak, T.; Roubeau, O.; van der Toorn, J.; Teat, S. J.; Massera, C.; Gamez, P.; Reedijk, J. Selective, catalytic aerobic oxidation of alcohols using CuBr^2 and bifunctional triazine-based ligands containing both a bipyridine and a TEMPO group. *Dalton Trans.* **2009** (18), 3559–3570. DOI: 10.1039/b820554j.

(2) Abruna, H. D.; Breikss, A. I.; Collum, D. B. Improved synthesis of 4-vinyl-4'-methyl-2,2'-bipyridine. *Inorg. Chem.* **1985**, *24* (7), 987–988. DOI: 10.1021/ic00201a003.

(3) Meister, S.; Reithmeier, R. O.; Ogrodnik, A.; Rieger, B. Bridging Efficiency within Multinuclear Homogeneous Catalysts in the Photocatalytic Reduction of Carbon Dioxide. *ChemCatChem* **2015**, *7* (21), 3562–3569. DOI: 10.1002/cctc.201500674.

(4) Jiang, S.; Tian, X.-J.; Feng, S.-Y.; Li, J.-S.; Li, Z.-W.; Lu, C.-H.; Li, C.-J.; Liu, W.-D. Visible-Light Photoredox Catalyzed Double C-H Functionalization: Radical Cascade Cyclization of Ethers with Benzimidazole-Based Cyanamides. *Org. Let.* **2021**, *23* (3), 692–696. DOI: 10.1021/acs.orglett.0c03853.

(5) Lee, I.-S. H.; Jeoung, E. H.; Kreevoy, M. M. Marcus Theory of a Parallel Effect on α for Hydride Transfer Reaction between NAD + Analogues. *J. Am. Chem. Soc.* **1997**, *119* (11), 2722–2728. DOI: 10.1021/ja963768l.

(6) Smieja, J. M.; Kubiak, C. P. Re(bipy-tBu)(CO)$_3$Cl-improved catalytic activity for reduction of carbon dioxide: IR-spectroelectrochemical and mechanistic studies. *Inorg. Chem.* **2010**, *49* (20), 9283–9289. DOI: 10.1021/ic1008363.

(7) Bian, Z.-Y.; Wang, H.; Fu, W.-F.; Li, L.; Ding, A.-Z. Two bifunctional RuII/ReI photocatalysts for CO$_2$ reduction: A spectroscopic, photocatalytic, and computational study. *Polyhedron* **2012**, *32* (1), 78–85. DOI: 10.1016/j.poly.2011.08.037.

10.3 Supporting Information of the Manuscript "The Puzzling Question about the Origin of the Second Electron in the Molecular Photocatalytic Reduction of CO_2"

ChemCatChem

Supporting Information

The Puzzling Question about the Origin of the Second Electron in the Molecular Photocatalytic Reduction of CO_2

Christopher Thomas[+], Marina Wittig[+], and Bernhard Rieger*

Appendix

TABLE OF CONTENTS

1

227

Appendix

1. NMR- AND ESI-MS SPECTRA OF RuRe3
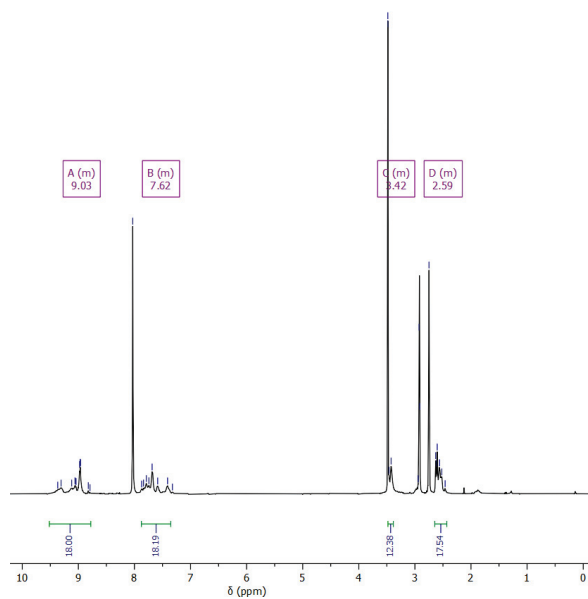
Figure S1. ^{1}H-NMR spectrum of **RuRe3** with residual solvent (δ(MeOH) = 3.48 ppm), recorded at 400 MHz in DMF-d$_7$.
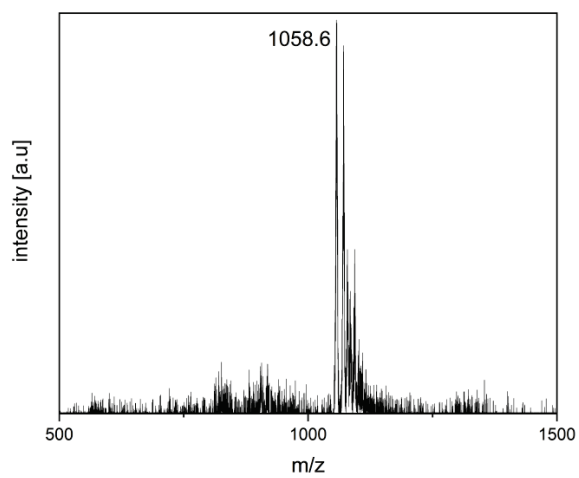
Figure S2. ESI-MS spectrum of **RuRe3** with the corresponding m/z (1058.6 ([M–2Cl]$^{2+}$)) and the expected isotope distribution, recorded in MeOH.

2. PHOTOPHYSICAL PROPERTIES
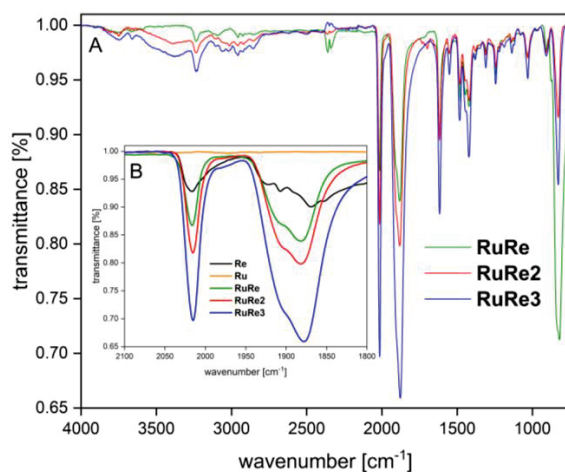
Figure S3. Attenuated total reflectance-Fourier transform infrared (ATR-FTIR) powder spectra of (**A**) the multinuclear complexes **RuRe** (green), **RuRe2** (red), and **RuRe3** (blue) and (**B**) additionally the corresponding monometallic building blocks **Re** (black) and **Ru** (orange) displaying the Re-CO modes.

Table S1. Infrared data of the carbonyl groups in the complexes.

complex	a`(1)[a]	a``[a]	a`(2)[a]
RuRe	2014	1901	1879
RuRe2	2015	1901	1881
RuRe3	2015	1901	1877

[a]unit: cm^{-1}.

Table S2. Spectroscopic and photophysical properties for the three multinuclear model systems and their single components in Ar-saturated DMF solution at room temperature. [a] Maximum of the MLCT bands. [b] Molar extinction coefficients at λ_{abs}. [c] Emission maxima at an irradiation of λ_{ex} = 460 nm, unless otherwise stated. [d] Irradiation at 365 nm. [e] Quantum yields at λ_{ex} = 460 nm, unless otherwise stated. [f] Quantum yields at λ_{ex} = 365 nm. [g] Excitation with a short laser pulse (λ_{ex} = 373 nm) to determine the lifetimes of the excited systems by using decay functions.

complex	$\lambda_{abs}{}^a$ [nm]	ε^b [×10^3 M^{-1} cm^{-1}]	$\lambda_{em}{}^c$ [nm]	$\Phi_{em}{}^e$	$\tau_1{}^g$ [ns]
Re	365	2.6	618^d	0.016^f	33
Ru	460	6.3	640	0.080	703
RuRe	462	9.7	642	0.075	823
Ru + Re	462	9.5	642	0.062	692
RuRe2	460	7.2	641	0.083	727
Ru + 2 Re	461	9.4	640	0.070	647
RuRe + Re	461	8.4	641	0.092	722
RuRe3	461	8.4	640	0.122	730
Ru + 3 Re	460	9.0	641	0.071	688
RuRe + 2 Re	461	9.1	641	0.086	699

3

RuRe2 + Re	461	9.5	642	0.073	731
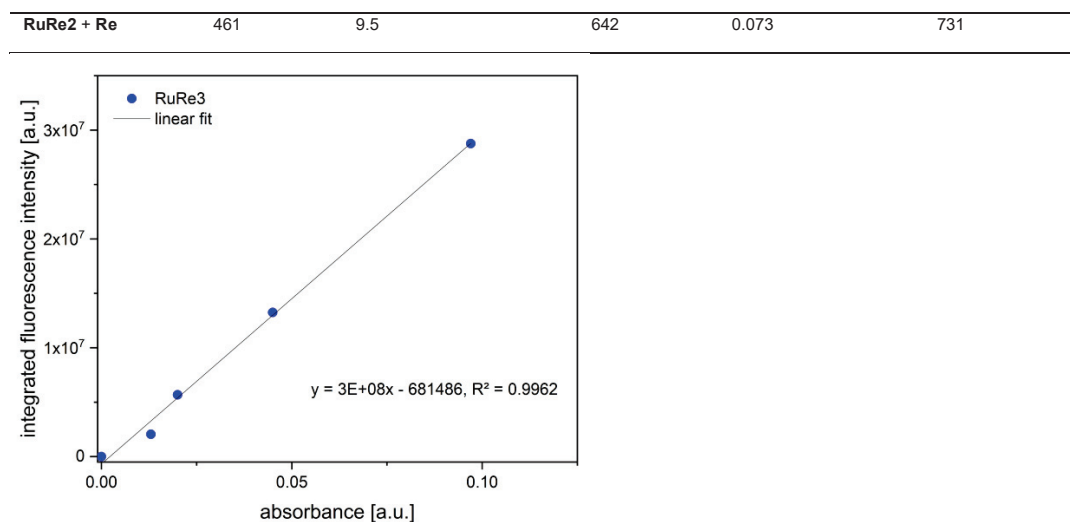
Figure S4. Linear fit of the integrated fluorescence intensity vs. the absorbance of **RuRe3** in degassed DMF in different concentrations. The gradients obtained are proportional to the corresponding quantum yield. Absolute values are calculated using Ru(dmb)$_3^{2+}$ which has a fixed and known fluorescence quantum yield value, according to the following equation:

$$\Phi_x = \Phi_{st}\left(\frac{Grad_x}{Grad_{st}}\right)\left(\frac{\eta_x^{2}}{\eta_{st}^{2}}\right)$$

where the subscripts st and x denote standard and test respectively, Φ is the fluorescence quantum yield, Grad the gradient from the plot of integrated fluorescence intensity vs. absorbance, and η the refractive index of the solvent.
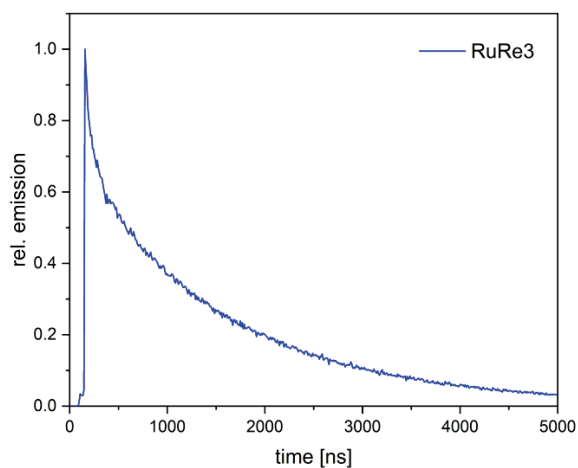
Figure S5. Time-resolved measurement of **RuRe3** in degassed DMF with a 373 nm laser diode. A pulse length of 65 ps and an instrument response of 70-80 ps were used. Each decay was measured over 5 µs. Decay functions were used to determine the lifetimes of the excited molecule.

4
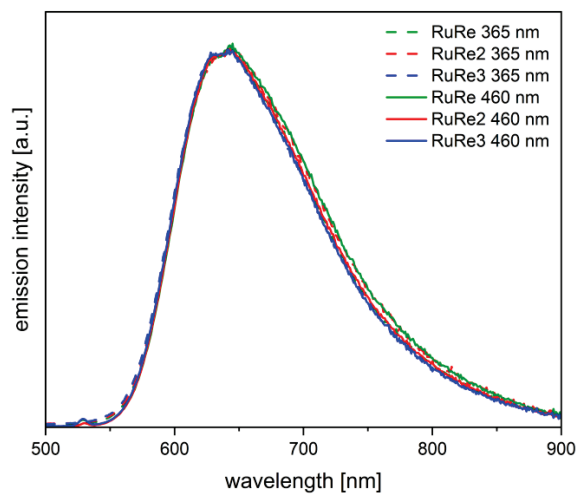
Figure S6. Normalized photoluminescence emission spectra of the multinuclear catalysts **RuRe**, **RuRe2**, and **RuRe3** after excitation with light of λ = 365 nm (dashed lines) and 460 nm (solid lines), respectively.
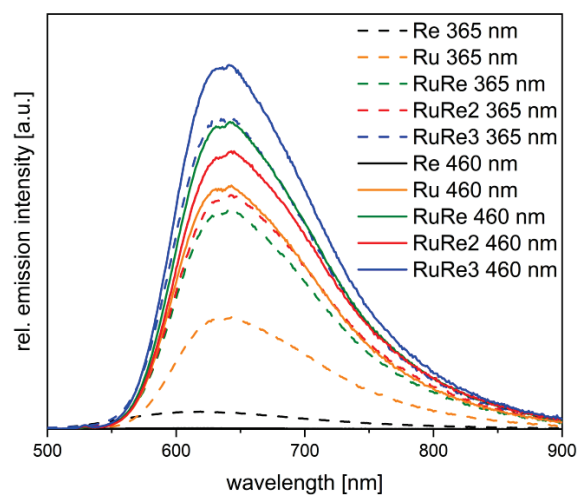
Figure S7. Normalized photoluminescence emission spectra of the multinuclear catalysts **RuRe**, **RuRe2**, and **RuRe3** after excitation with light of λ = 365 nm (dashed lines) and 460 nm (solid lines), respectively.

5
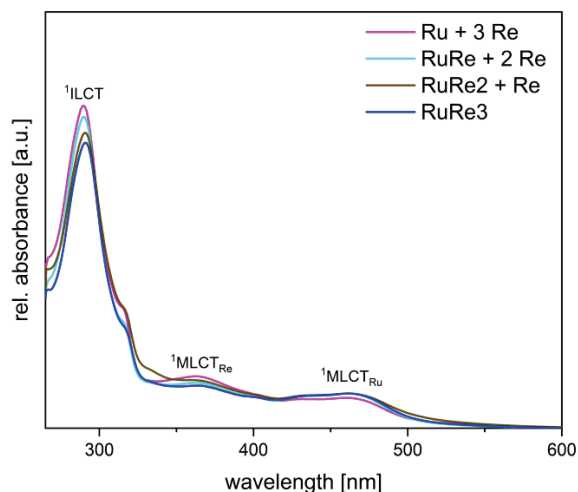
Figure S8. Absorbance spectra of **Ru** + 3 **Re** (magenta), **RuRe** + 2 **Re** (cyan), **RuRe2** + **Re** (brown), **RuRe3** (blue) in DMF (c(Ru-center) = 16.0 µM, 25 °C).

3. PHOTOCATALYSIS

Turnover number (TON) calculations

The TONs for the photocatalytic CO_2 reduction experiments were calculated from the exact molar catalyst amount from each experiment. The GC measurements yielded area% results for each gas present in the headspace of the reaction flasks. For carbon monoxide, these were converted to vol%, volume, and moles utilizing the total gas phase volume of the reaction vessel. The TOF was derived from the slope between the first two GC measurement points. The following equations state an example for the TONs and TOF calculation based on the photocatalytic CO_2 reduction using **RuRe3**.

$$\text{Vol\%}_{CO} = \text{Area\%}_{CO} \cdot 1.195 = 5.22\% \cdot 1.195 = 6.23\% \tag{1}$$

$$V_{CO,gas}[mL] = \frac{\text{Vol\%}_{CO}}{100} \cdot V_{headspace}[mL] = \frac{6.23\%}{100} \cdot 149 \text{ mL} = 9.29 \text{ mL} \tag{2}$$

$$n_{CO,gas}[mmol] = \frac{p \cdot V_{CO}}{R \cdot T} = \frac{1.45 \cdot 10^5 \text{ Pa} \cdot 9.29 \text{ mL}}{8.314 \frac{J}{mol \cdot K} \cdot 293.15 \text{ K}} = 0.55 \text{ mmol} \tag{3}$$

$$TON = \frac{n_{CO,total}[mmol]}{n_{RuRe3}[\mu mol]} = \frac{0.55 \text{ mmol}}{0.055 \text{ } \mu mol} = 10000 \tag{4}$$

$$TON_{Re} = \frac{n_{CO,total}[mmol]}{n_{Re(RuRe3)}[\mu mol]} = \frac{0.55 \text{ mmol}}{0.165 \text{ } \mu mol} = 3349 \tag{5}$$

$$TOF_{t(1)} = \frac{n_{CO,t(1)}[\mu mol]}{n_{RuRe3}[\mu mol] \cdot \text{time interval (1) [h]}} = \frac{58 \text{ } \mu mol}{0.055 \text{ } \mu moll \cdot 18.5 \text{ h}} = 57.3 \text{ h}^{-1} \tag{6}$$

$$TOF_{Re,\, t(1)} = \frac{n_{CO,t(1)}[\mu mol]}{n_{Re(RuRe3)}[\mu mol] \cdot \text{time interval (1) [h]}} = \frac{58 \text{ } \mu mol}{0.165 \text{ } \mu mol \cdot 18.5 \text{ h}}$$
$$= 19.1 \text{ h}^{-1} \tag{7}$$

6

Appendix

Results of the irradiation experiments
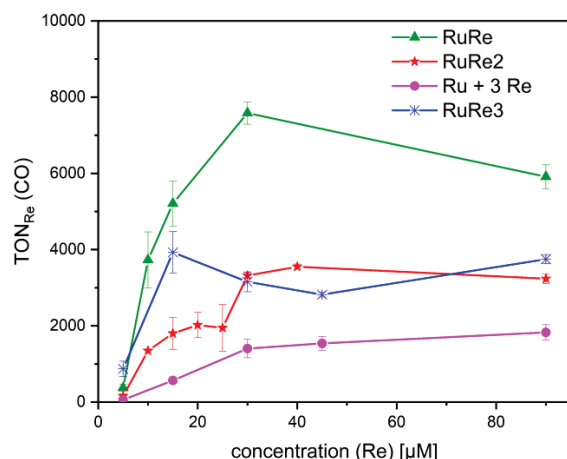
Figure S9. TON$_{Re}$ (CO) of the multinuclear catalysts **RuRe** (green), **RuRe2** (red), **RuRe3** (blue), and the model system **Ru** + 3 **Re** (magenta) at different concentrations of the Re-units. Turnovers were calculated based on the number of Re-centers. BIH and catalyst containing CO_2-saturated DMF/TEOA (3.4/1) solutions were irradiated at 520 nm.

Table S3. CO_2-saturated DMF-TEOA (8.5 mL/2.5 mL) solution containing the catalyst and the sacrificial electron donor in excess was irradiated at λ = 520 nm if not stated otherwise until no more CO_2-conversion was detectable. The calculation of the TON and the TON$_{Re}$ was performed according to the equations (1)-(5). The calculation of the TOF was performed according to the equations (6) and (7). The time interval for TOF calculation was approximately 20 h of irradiation. In-depth analysis of the gas phase composition after irradiation with an RGD (reduction gas detector) revealed traces of hydrogen evolution). The catalyst concentration is given as the concentration of Ru(II)-centers to ensure comparability.

Catalyst concentration [µM]	BIH concen-tration [mM]	Irradiation time [h]	TON$_{Re}$ [-]	TON [-]	TOF [h^{-1}]
RuRe3 (1.67 µM)	BIH (22 mM)	261	1100	3299	53
RuRe3 (1.67 µM)	BIH (10 mM)	183	769	2308	49
RuRe3 (1.67 µM)	BIH (10 mM)	183	746	2237	46
RuRe3 (5.0 M)	BIH (100 mM)	75	3739	11217	71
RuRe3 (5.0 µM)	BIH (100 mM)	89	4562	13685	121
RuRe3 (5.0 µM)	BIH (100 mM)	330	3489	10468	58
RuRe3 (10.0 µM)	BIH (150 mM)	75	3079	9238	70
RuRe3 (10.0 µM)	BIH (150 mM)	96	2938	8813	84
RuRe3 (10.0 µM)	BIH (150 mM)	86	3444	10333	99
RuRe3 (15.0 µM)	BIH (200 mM)	331	2854	8562	73
RuRe3 (15.0 µM)	BIH (200 mM)	426	2853	8560	31
RuRe3 (15.0 µM)	BIH (200 mM)	426	2747	8241	35
RuRe3 (30.0 µM)	BIH (375 mM)	331	3829	11488	85
RuRe3 (30.0 µM)	BIH (375 mM)	426	3777	11330	61
RuRe3 (30.0 µM)	BIH (375 mM)	426	3605	10815	25
RuRe2 (2.5 µM)	BIH (13 mM)	45	195	390	14
RuRe2 (2.5 µM)	BIH (13 mM)	116	125	249	12
RuRe2 (2.5 µM)	BIH (13 mM)	72	160	319	21
RuRe2 (5.0 µM)	BIH (37 mM)	259	1347	2693	79
RuRe2 (7.5 µM)	BIH (75 mM)	96	1453	2906	54
RuRe2 (7.5 µM)	BIH (75 mM)	213	2267	4533	71
RuRe2 (7.5 µM)	BIH (75 mM)	260	1691	3381	52
RuRe2 (10.0 µM)	BIH (75 mM)	91	1649	3298	70
RuRe2 (10.0 µM)	BIH (75 mM)	139	2298	4595	56
RuRe2 (10.0 µM)	BIH (75 mM)	284	2114	4228	54
RuRe2 (12.5 µM)	BIH (100 mM)	310	2381	4761	47
RuRe2 (12.5 µM)	BIH (100 mM)	234	1515	3030	26
RuRe2 (15.0 µM)	BIH (125 mM)	94	3377	6753	147
RuRe2 (15.0 µM)	BIH (125 mM)	261	3348	6696	52

7

RuRe2 (15.0 µM)	BIH (125 mM)	256	3232	6463	106
RuRe2 (20.0 µM)	BIH (200 mM)	408	3501	7002	62
RuRe2 (20.0 µM)	BIH (200 mM)	371	3604	7208	54
RuRe2 (45.0 µM)	BIH (450 mM)	241	3145	6290	20
RuRe2 (45.0 µM)	BIH (450 mM)	241	3328	6655	43
RuRe (5.0 µM)	BIH (100 mM)	17	453	453	26
RuRe (5.0 µM)	BIH (30 mM)	94	386	386	37
RuRe (5.0 µM)	BIH (100 mM)	93	280	280	11
RuRe (10.0 µM)	BIH (100 mM)	65	2900	2900	125
RuRe (10.0 µM)	BIH (30 mM)	20	3988	3988	199
RuRe (10.0 µM)	BIH (100 mM)	59	4300	4300	161
RuRe (15.0 µM)	BIH (100 mM)	89	5636	5636	132
RuRe (15.0 µM)	BIH (100 mM)	94	5456	5456	160
RuRe (15.0 µM)	BIH (150 mM)	89	4539	4539	182
RuRe (30.0 µM)	BIH (300 mM)	188	7375	7375	67
RuRe (30.0 µM)	BIH (300 mM)	408	7790	7790	45
RuRe (90.0 µM)	BIH (675 mM)	208	5690	5690	61
RuRe (90.0 µM)	BIH (675 mM)	178	6130	6130	77
Ru + 3 Re (1.67 µM)	BIH (20 mM)	91	64	193	10
Ru + 3 Re (1.67 µM)	BIH (20 mM)	42	55	165	13
Ru + 3 Re (5.0 µM)	BIH (70 mM)	280	507	1520	56
Ru + 3 Re (5.0 µM)	BIH (70 mM)	190	564	1694	28
Ru + 3 Re (10.0 µM)	BIH (120 mM)	306	1573	4718	37
Ru + 3 Re (10.0 µM)	BIH (120 mM)	275	1270	3809	29
Ru + 3 Re (15.0 µM)	BIH (180 mM)	306	1410	4230	30
Ru + 3 Re (15.0 µM)	BIH (180 mM)	306	1670	5009	27
Ru + 3 Re (30.0 µM)	BIH (300 mM)	478	1683	5050	21
Ru + 3 Re (30.0 µM)	BIH (300 mM)	478	1971	5913	27
RuRe + Re (5.0 µM)	BIH (100 mM)	137	3214	6427	186
RuRe + Re (5.0 µM)	BIH (100 mM)	254	1320	5281	153
RuRe + 2 Re (5.0 µM)	BIH (100 mM)	137	4031	12094	245
RuRe + 2 Re (5.0 µM)	BIH (100 mM)	254	3508	10524	170
RuRe + 3 Re (5.0 µM)	BIH (100 mM)	113	1031	4125	98
RuRe + 3 Re (5.0 µM)	BIH (100 mM)	94	966	3862	94
RuRe2 + Re (5.0 µM)	BIH (50 mM)	292	1338	4014	31
RuRe2 + Re (5.0 µM)	BIH (100 mM)	112	1167	3500	52
RuRe2 + Re (5.0 µM)	BIH (100 mM)	93	1809	5427	56
RuRe3 + Re (5.0 µM)	BIH (100 mM)	141	1794	7176	86
RuRe3 + 2 Re (5.0 µM)	BIH (100 mM)	153	1427	7135	170
RuRe3 (5 µM)	BIH (100 mM)	21 (450 nm)	782	2346	111
RuRe3 (5 µM)	BIH (100 mM)	94 (450 nm)	523	1569	127
RuRe3 (5 µM)	BIH (100 mM)	14 (360 nm)	244	731	96
RuRe3 (5 µM)	BIH (100 mM)	22 (360 nm)	173	521	76
RuRe2 (15 µM)	BIH (125 mM)	47 (450 nm)	805	1609	72
RuRe2 (15 µM)	BIH (125 mM)	88 (450 nm)	1036	2072	88
RuRe2 (15 µM)	BIH (125 mM)	63 (360 nm)	254	508	45
RuRe2 (15 µM)	BIH (125 mM)	41 (360 nm)	297	593	27
RuRe (30 µM)	BIH (300 mM)	45 (450 nm)	1686	1686	51
RuRe (30 µM)	BIH (300 mM)	55 (450 nm)	1550	1550	72
RuRe (30 µM)	BIH (300 mM)	38 (360 nm)	387	387	71
RuRe (30 µM)	BIH (300 mM)	24 (360 nm)	297	297	56

8

Appendix

Control experiments

Table S4. TONs of the control experiments for **RuRe3** in CO_2-saturated (15 min) DMF solution with BIH ([BIH]/[Re] = 10000) and TEOA (1.7 M). Irradiation was performed at λ = 520 nm. The calculation of the TON was performed according to the equations (1) – (5). Deviations from the standard experiment are denoted under condition variation.

Catalyst concen-tration [µM]	Condition variation	Irradiation time [h]	TON [-]
RuRe3 (5 µM)	no light	20 (dark)	0
-	no catalyst	20	0
RuRe3 (5 µM)	no CO_2 overpressure	20	traces of CO (via FID)
RuRe3 (5 µM)	$^{13}CO_2$ for IR-experiment	140	n. d. [a]

[a] not determined, but CO presence confirmed via gas phase IR (Figure S10).
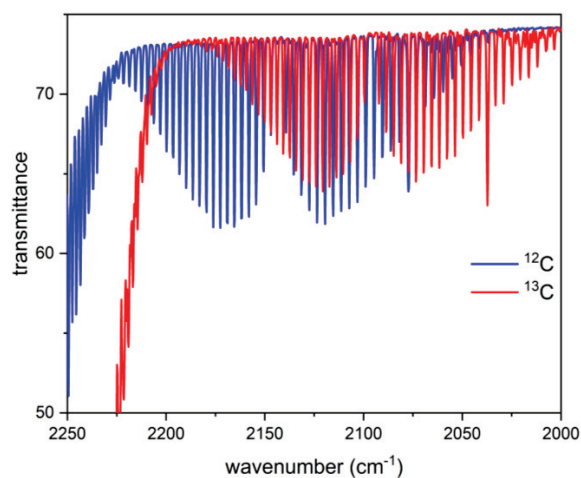
Figure S10. Isotope labelling control experiment. Gas phase IR spectra of the reaction headspace taken after 140 h irradiation under a $^{12}CO_2$ and $^{13}CO_2$ environment, respectively. The IR-vibrations of the resulting ^{13}CO (red) are shifted compared to the ^{12}CO (blue) and no ^{12}CO-vibrations can be detected in the $^{13}CO_2$-labelling experiment. As catalyst RuRe3 (5 µM) was used in standard reactions conditions (DMF/TEOA (3.4:1), 75 mM BIH, 520 nm).

11.   Copyright Licenses

WILEY

Thank you for your order!

Dear Christopher Thomas,

Thank you for placing your order through Copyright Clearance Center's RightsLink® service.

Order Summary
Licensee: Technical University of Munich
Order Date: Jan 22, 2023
Order Number: 5474160198003
Publication: Wiley Books
Title: Characteristics of Fluorescence Emission
Type of Use: Dissertation/Thesis
Order Total: 0.00 USD

View or print complete details of your order and the publisher's terms and conditions.

Sincerely,

Copyright Clearance Center

Tel: +1-855-239-3415 / +1-978-646-2777
customercare@copyright.com
https://myaccount.copyright.com

CCC   RightsLink

CCC | RightsLink   Home   Help ˅   Live Chat   Christopher Thomas ˅

ACS Publications
Most Trusted. Most Cited. Most Read.

Ultrafast Excited-State Dynamics of Rhenium(I) Photosensitizers [Re(Cl)(CO)3(N,N)] and [Re(imidazole)(CO)3(N,N)] : Diimine Effects

Author: Amal El Nahhas, Cristina Consani, Ana María Blanco-Rodríguez, et al
Publication: Inorganic Chemistry
Publisher: American Chemical Society
Date: Apr 1, 2011

Copyright © 2011, American Chemical Society

**PERMISSION/LICENSE IS GRANTED FOR YOUR ORDER AT NO CHARGE**

This type of permission/license, instead of the standard Terms and Conditions, is sent to you because no fee is being charged for your order. Please note the following:
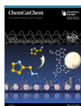
- Permission is granted for your request in both print and electronic formats, and translations.
- If figures and/or tables were requested, they may be adapted or used in part.
- Please print this page for your records and send a copy of it to your publisher/graduate school.
- Appropriate credit for the requested material should be given as follows: "Reprinted (adapted) with permission from {COMPLETE REFERENCE CITATION}. Copyright {YEAR} American Chemical Society." Insert appropriate information in place of the capitalized words.
- One-time permission is granted only for the use specified in your RightsLink request. No additional uses are granted (such as derivative works or other editions). For any uses, please submit a new request.

If credit is given to another source for the material you requested from RightsLink, permission must be obtained from that source.

BACK   CLOSE WINDOW

Order Details

1. Energy & environmental science
Article: Exciton diffusion in organic semiconductors

Billing Status:
Open

Print License

Order License ID	1314356-1	**Type of use**	Republish in a thesis/dissert…
Order detail status	Completed	**Publisher**	RSC Publishing
ISSN	1754-5706	**Portion**	Chart/graph/table/figure

0.00 USD
Republication Permission

⊡ View Details

Copyright Licenses

Thank you for your order!

Dear Christopher Thomas,

Thank you for placing your order through Copyright Clearance Center's RightsLink® service.

Order Summary

|	
Licensee:	Technical University of Munich
Order Date:	Jan 22, 2023
Order Number:	5474320382861
Publication:	Angewandte Chemie International Edition
Title:	Visible-Light-Induced Selective CO2 Reduction Utilizing a Ruthenium Complex Electrocatalyst Linked to a p-Type Nitrogen-Doped Ta2O5 Semiconductor
Type of Use:	Dissertation/Thesis
Order Total:	0.00 USD

View or print complete details of your order and the publisher's terms and conditions.

Sincerely,

Copyright Clearance Center

CCC | RightsLink

Home | Help ∨ | Live Chat | Christopher Thomas ∨

Photocatalysis of a Dinuclear Ru(II)–Re(I) Complex for CO2 Reduction on a Solid Surface

ACS Publications
Most Trusted. Most Cited. Most Read.

Author: Daiki Saito, Yasuomi Yamazaki, Yusuke Tamaki, et al
Publication: Journal of the American Chemical Society
Publisher: American Chemical Society
Date: Nov 1, 2020

Copyright © 2020, American Chemical Society

PERMISSION/LICENSE IS GRANTED FOR YOUR ORDER AT NO CHARGE

This type of permission/license, instead of the standard Terms and Conditions, is sent to you because no fee is being charged for your order. Please note the following:

- Permission is granted for your request in both print and electronic formats, and translations.
- If figures and/or tables were requested, they may be adapted or used in part.
- Please print this page for your records and send a copy of it to your publisher/graduate school.
- Appropriate credit for the requested material should be given as follows: "Reprinted (adapted) with permission from {COMPLETE REFERENCE CITATION}. Copyright {YEAR} American Chemical Society." Insert appropriate information in place of the capitalized words.
- One-time permission is granted only for the use specified in your RightsLink request. No additional uses are granted (such as derivative works or other editions). For any uses, please submit a new request.

If credit is given to another source for the material you requested from RightsLink, permission must be obtained from that source.

BACK

CLOSE WINDOW

Copyright Licenses

Copyright Licenses

Copyright Licenses

12. References

[1]   a) C. Wolfram, O. Shelef, P. Gertler, *Journal of Economic Perspectives* **2012**, *26*, 119-138; b) N. S. Lewis, D. G. Nocera, *Proceedings of the National Academy of Sciences* **2006**, *103*, 15729-15735; c) U. S. E. I. Administration, **2016**.

[2]   bp Energy Outlook: 2022 edition, https://www.bp.com/content/dam/bp/business-sites/en/global/corporate/pdfs/energy-economics/energy-outlook/bp-energy-outlook-2022.pdf, (accessed October 4th, 2022), **2022**.

[3]   R. Lindsey, https://www.climate.gov/news-features/understanding-climate/climate-change-atmospheric-carbon-dioxide, (accessed October 4th, 2022), **2022**.

[4]   a) T. S. Ledley, E. T. Sundquist, S. E. Schwartz, D. K. Hall, J. D. Fellows, T. L. Killeen, *Eos, Transactions American Geophysical Union* **1999**, *80*, 453-458; b) J. E. Szulejko, P. Kumar, A. Deep, K.-H. Kim, *Atmospheric Pollution Research* **2017**, *8*, 136-140.

[5]   E. Alper, O. Yuksel Orhan, *Petroleum* **2017**, *3*, 109-126.

[6]   A. Y. Khodakov, W. Chu, P. Fongarland, *Chemical Reviews* **2007**, *107*, 1692-1744.

[7]   S. C. Roy, O. K. Varghese, M. Paulose, C. A. Grimes, *ACS Nano* **2010**, *4*, 1259-1278.

[8]   Y. Kuramochi, O. Ishitani, H. Ishida, *Coordination Chemistry Reviews* **2018**, *373*, 333-356.

[9]   J. Hawecker, J.-M. Lehn, R. Ziessel, *J. Chem. Soc., Chem.* **1983**, 536-538.

[10]   a) Y. Yamazaki, H. Takeda, O. Ishitani, *J. Photochem. Photobiol. C* **2015**, *25*, 106-137; b) S. Meister, R. O. Reithmeier, M. Tschurl, U. Heiz, B. Rieger, *ChemCatChem* **2015**, *7*, 690-697.

[11]   V. Ramanathan, *Science* **1988**, *240*, 293-299.

[12]   a) M. Aresta, *Carbon dioxide as chemical feedstock*, John Wiley & Sons, **2010**; b) C. L. Sabine, R. A. Feely, N. Gruber, R. M. Key, K. Lee, J. L. Bullister, R. Wanninkhof, C. S. Wong, D. W. Wallace, B. Tilbrook, F. J. Millero, T. H. Peng, A. Kozyr, T. Ono, A. F. Rios, *Science* **2004**, *305*, 367-371; c) W. Roedel, *Physik unserer Umwelt: Die Atmosphäre*, Springer-Verlag, **2013**; d) J. Blunden, T. Boyer, *Bulletin of the American Meteorological Society* **2021**, *102*.

[13]   C. D. Keeling, S. C. Piper, R. B. Bacastow, M. Wahlen, T. P. Whorf, M. Heimann, H. A. Meijer, **2001**.

[14]   D. Reay, *Greenhouse gas sinks*, Cabi, **2007**.

[15]   P. Agreement, in *Report of the Conference of the Parties to the United Nations Framework Convention on Climate Change (21st Session, 2015: Paris). Retrived December, Vol. 4*, HeinOnline, **2015**, p. 2017.

[16]   a) G. A. Olah, G. K. S. Prakash, A. Goeppert, *Journal of the American Chemical Society* **2011**, *133*, 12881-12898; b) M. Aresta, A. Dibenedetto, A. Angelini, *Chemical Reviews* **2014**, *114*, 1709-1742.

[17]   N. L. Panwar, S. C. Kaushik, S. Kothari, *Renewable and Sustainable Energy Reviews* **2011**, *15*, 1513-1524.

[18]   B. Matek, K. Gawell, *The Electricity Journal* **2015**, *28*, 101-112.

[19]   C. R. Matos, J. F. Carneiro, P. P. Silva, *Journal of Energy Storage* **2019**, *21*, 241-258.

[20]   a) L. Drude, L. C. Pereira Junior, R. Rüther, *Renewable Energy* **2014**, *68*, 443-451; b) G. Crabtree, *Nature* **2015**, *526*, S92-S92.

[21]   a) W. Shen, L. Cao, Q. Li, W. Zhang, G. Wang, C. Li, *Renewable and Sustainable Energy Reviews* **2015**, *50*, 1004-1012; b) R. Latawiec, P. Woyciechowski, K. J. Kowalski, *Environments* **2018**, *5*, 27.

[22]   R. Steeneveldt, B. Berger, T. A. Torp, *Chemical Engineering Research and Design* **2006**, *84*, 739-763.

[23]   a) C. Song, in *CO2 Conversion and Utilization, Vol. 809*, American Chemical Society, **2002**, pp. 2-30; b) H. Arakawa, M. Aresta, J. N. Armor, M. A. Barteau, E. J. Beckman, A. T. Bell, J. E. Bercaw, C. Creutz, E. Dinjus, D. A. Dixon, K. Domen, D. L. DuBois, J. Eckert, E. Fujita, D. H. Gibson, W. A. Goddard, D. W. Goodman, J. Keller, G. J. Kubas, H. H. Kung, J. E. Lyons, L. E. Manzer, T. J. Marks, K. Morokuma, K. M. Nicholas, R. Periana, L. Que, J. Rostrup-Nielson, W. M. H. Sachtler, L. D. Schmidt, A. Sen, G. A.

References

Somorjai, P. C. Stair, B. R. Stults, W. Tumas, *Chemical Reviews* **2001**, *101*, 953-996; c) W. B. Tolman, *Activation of small molecules: organometallic and bioinorganic perspectives*, John Wiley & Sons, **2006**; d) C. Song, *Catalysis Today* **2006**, *115*, 2-32.

[24] a) M. Aresta, A. Dibenedetto, *Dalton Transactions* **2007**, 2975-2992; b) E. E. Benson, C. P. Kubiak, A. J. Sathrum, J. M. Smieja, *Chemical Society Reviews* **2009**, *38*, 89-99.

[25] T. Oliver, P. Sánchez-Baracaldo, A. W. Larkum, A. W. Rutherford, T. Cardona, *Biochimica et Biophysica Acta (BBA) - Bioenergetics* **2021**, *1862*, 148400.

[26] M. W. T. D. Wöhrle, W.-D. Stohrer *Photochemie: Konzepte, Methoden, Eperimente*, Wiley-VCH, Weinheim, **1998**.

[27] a) H. M. D. Bandara, S. C. Burdette, *Chemical Society Reviews* **2012**, *41*, 1809-1825; b) M. A. Ischay, M. E. Anzovino, J. Du, T. P. Yoon, *Journal of the American Chemical Society* **2008**, *130*, 12886-12887; c) S. Sato, Y. Matubara, K. Koike, M. Falkenström, T. Katayama, Y. Ishibashi, H. Miyasaka, S. Taniguchi, H. Chosrowjan, N. Mataga, N. Fukazawa, S. Koshihara, K. Onda, O. Ishitani, *Chemistry – A European Journal* **2012**, *18*, 15722-15734.

[28] P. Atkins, *Physical Chemistry*, W. H. Freeman and Company, New York, **2010**.

[29] E. U. Condon, *Physical Review* **1928**, *32*, 858-872.

[30] C. S. Czeslik, H.; Winter, R. , *Basiswissen Physikalische Chemie*, Vieweg+Teubner, Wiesbaden, **2010**.

[31] B. Valeur, in *Molecular Fluorescence*, **2001**, pp. 34-71.

[32] H. G. O. Becker, *Einführung in die Photochemie*, Thieme, Stuttgart, **1983**.

[33] J. R. Lakowicz, *Principles of Fluorescence Spectroscopy*, Springer, New York, **2007**.

[34] B. König, *Chemical Photocatalysis*, De Gruyter, Berlin/Boston, **2013**.

[35] a) M. A. El-Sayed, *The Journal of Chemical Physics* **1963**, *38*, 2834-2838; b) P. Klán, J. Wirz, *Photochemistry of organic compounds: from concepts to practice*, John Wiley & Sons, **2009**.

[36] J. C. Koziar, D. O. Cowan, *Accounts of Chemical Research* **1978**, *11*, 334-341.

[37] S. E. Braslavsky, *Pure and Applied Chemistry* **2007**, *79*, 293-465.

[38] a) K. Kalyanasundaram, *Journal of the Chemical Society, Faraday Transactions 2: Molecular and Chemical Physics* **1986**, *82*, 2401-2415; b) C. Kutal, M. A. Weber, G. Ferraudi, D. Geiger, *Organometallics* **1985**, *4*, 2161-2166; c) A. C. Bhasikuttan, M. Suzuki, S. Nakashima, T. Okada, *Journal of the American Chemical Society* **2002**, *124*, 8398-8405.

[39] A. Juris, V. Balzani, F. Barigelletti, S. Campagna, P. Belser, A. von Zelewsky, *Coordination Chemistry Reviews* **1988**, *84*, 85-277.

[40] D. J. Liard, M. Busby, P. Matousek, M. Towrie, A. Vlček, *J. Phys. Chem. A* **2004**, *108*, 2363-2369.

[41] A. El Nahhas, C. Consani, A. M. Blanco-Rodríguez, K. M. Lancaster, O. Braem, A. Cannizzo, M. Towrie, I. P. Clark, S. Záliš, M. Chergui, A. Vlček, *Inorg. Chem.* **2011**, *50*, 2932-2943.

[42] D. L. Dexter, *The Journal of Chemical Physics* **1953**, *21*, 836-850.

[43] T. Förster, *Annalen der Physik* **1948**, *437*, 55-75.

[44] G. A. Jones, D. S. Bradshaw, *Frontiers in Physics* **2019**, *7*.

[45] T. Főrster, *Discussions of the Faraday Society* **1959**, *27*, 7-17.

[46] O. V. Mikhnenko, P. W. M. Blom, T.-Q. Nguyen, *Energy & Environmental Science* **2015**, *8*, 1867-1888.

[47] C. B. Murphy, Y. Zhang, T. Troxler, V. Ferry, J. J. Martin, W. E. Jones, *The Journal of Physical Chemistry B* **2004**, *108*, 1537-1543.

[48] X. Zhao, Y. Hou, L. Liu, J. Zhao, *Energy & Fuels* **2021**, *35*, 18942-18956.

[49] C. M. Marian, *Wiley Interdiscip. Rev. Comput. Mol. Sci.* **2012**, *2*, 187-203.

[50] M. Mońka, I. E. Serdiuk, K. Kozakiewicz, E. Hoffman, J. Szumilas, A. Kubicki, S. Y. Park, P. Bojarski, *Journal of Materials Chemistry C* **2022**, *10*, 7925-7934.

[51] G. J. Kavarnos, N. J. Turro, *Chemical Reviews* **1986**, *86*, 401-449.

[52] R. Reithmeier, C. Bruckmeier, B. Rieger, *Catalysts* **2012**, *2*, 544.

References

[53] K. Kalyanasundaram, M. Grätzel, *Photosensitization and photocatalysis using inorganic and organometallic compounds, Vol. 14*, Springer Science & Business Media, **1993**.

[54] A. M. Appel, J. E. Bercaw, A. B. Bocarsly, H. Dobbek, D. L. DuBois, M. Dupuis, J. G. Ferry, E. Fujita, R. Hille, P. J. Kenis, C. A. Kerfeld, R. H. Morris, C. H. Peden, A. R. Portis, S. W. Ragsdale, T. B. Rauchfuss, J. N. Reek, L. C. Seefeldt, R. K. Thauer, G. L. Waldrop, *Chem Rev* **2013**, *113*, 6621-6658.

[55] ESRI Global Monitoring Laboratory - Global Greenhouse Gas Reference Network, https://gml.noaa.gov/ccgg/trends/global.html, (accessed October 20th, 2022), **2022**.

[56] A. T. Bell, B. C. Gates, D. Ray, M. R. Thompson, Pacific Northwest National Lab.(PNNL), Richland, WA (United States), **2008**.

[57] a) J. L. White, M. F. Baruch, J. E. Pander Iii, Y. Hu, I. C. Fortmeyer, J. E. Park, T. Zhang, K. Liao, J. Gu, Y. Yan, T. W. Shaw, E. Abelev, A. B. Bocarsly, *Chem Rev* **2015**, *115*, 12888-12935; b) J. Fu, K. Jiang, X. Qiu, J. Yu, M. Liu, *Materials Today* **2020**, *32*, 222-243; c) P. M. Stanley, J. Haimerl, C. Thomas, A. Urstoeger, M. Schuster, N. B. Shustova, A. Casini, B. Rieger, J. Warnan, R. A. Fischer, *Angewandte Chemie International Edition* **2021**, *60*; d) M. Khalil, J. Gunlazuardi, T. A. Ivandini, A. Umar, *Renewable and Sustainable Energy Reviews* **2019**, *113*, 109246; e) Y. Zhao, Z. Liu, *Chinese Journal of Chemistry* **2018**, *36*, 455-460; f) G. Sahara, R. Abe, M. Higashi, T. Morikawa, K. Maeda, Y. Ueda, O. Ishitani, *Chemical Communications* **2015**, *51*, 10722-10725; g) B. Kumar, M. Llorente, J. Froehlich, T. Dang, A. Sathrum, C. P. Kubiak, *Annual Review of Physical Chemistry* **2012**, *63*, 541-569; h) B. M. Pirzada, A. H. Dar, M. N. Shaikh, A. Qurashi, *ACS Omega* **2021**, *6*, 29291-29324; i) Y. Tamaki, O. Ishitani, *ACS Catalysis* **2017**, *7*, 3394-3409.

[58] a) M. Cokoja, C. Bruckmeier, B. Rieger, W. A. Herrmann, F. E. Kühn, *Angewandte Chemie International Edition* **2011**, *50*, 8510-8537; b) Q.-W. Song, Z.-H. Zhou, L.-N. He, *Green Chemistry* **2017**, *19*, 3707-3728; c) A. Denk, S. Kernbichl, A. Schaffer, M. Kränzlein, T. Pehl, B. Rieger, *ACS Macro Letters* **2020**, *9*, 571-575; d) S. Kernbichl, M. Reiter, F. Adams, S. Vagin, B. Rieger, *Journal of the American Chemical Society* **2017**, *139*, 6787-6790; e) H. Seo, M. H. Katcher, T. F. Jamison, *Nature Chemistry* **2017**, *9*, 453-456.

[59] T. Sakakura, J.-C. Choi, H. Yasuda, *Chemical Reviews* **2007**, *107*, 2365-2387.

[60] P. Kedzierzawski, J. Augustynski, *Journal of The Electrochemical Society* **1994**, *141*, L58.

[61] a) J. Hawecker, J.-M. Lehn, R. Ziessel, *Helvetica Chimica Acta* **1986**, *69*, 1990-2012; b) Y. Wang, D. He, H. Chen, D. Wang, *Journal of Photochemistry and Photobiology C: Photochemistry Reviews* **2019**, *40*, 117-149.

[62] a) L. Alibabaei, H. Luo, R. L. House, P. G. Hoertz, R. Lopez, T. J. Meyer, *Journal of Materials Chemistry A* **2013**, *1*, 4133-4145; b) Y. S. Chaudhary, T. W. Woolerton, C. S. Allen, J. H. Warner, E. Pierce, S. W. Ragsdale, F. A. Armstrong, *Chemical Communications* **2012**, *48*, 58-60; c) K. Maeda, *Advanced Materials* **2019**, *31*, 1808205.

[63] J. Qiao, Y. Liu, F. Hong, J. Zhang, *Chemical Society Reviews* **2014**, *43*, 631-675.

[64] a) J. M. Lehn, R. Ziessel, *Proc Natl Acad Sci U S A* **1982**, *79*, 701-704; b) H. D. Gafney, A. W. Adamson, *Journal of the American Chemical Society* **1972**, *94*, 8238-8239.

[65] J. L. Grant, K. Goswami, L. O. Spreer, J. W. Otvos, M. Calvin, *Journal of the Chemical Society, Dalton Transactions* **1987**, 2105-2109.

[66] a) C. Bruckmeier, M. W. Lehenmeier, R. Reithmeier, B. Rieger, J. Herranz, C. Kavakli, *Dalton Transactions* **2012**, *41*, 5026-5037; b) C. Kutal, A. J. Corbin, G. Ferraudi, *Organometallics* **1987**, *6*, 553-557; c) H. Takeda, K. Koike, H. Inoue, O. Ishitani, *J. Am. Chem. Soc.* **2008**, *130*, 2023-2031; d) P. Lang, R. Giereth, S. Tschierlei, M. Schwalbe, *Chemical Communications* **2019**, *55*, 600-603.

[67] P. Kurz, B. Probst, B. Spingler, R. Alberto, *European Journal of Inorganic Chemistry* **2006**, *2006*, 2966-2974.

References

[68]   a) J. K. Hino, L. Della Ciana, W. J. Dressick, B. P. Sullivan, *Inorganic Chemistry* **1992**, *31*, 1072-1080; b) H. Hori, J. Ishihara, K. Koike, K. Takeuchi, T. Ibusuki, O. Ishitani, *Journal of Photochemistry and Photobiology A: Chemistry* **1999**, *120*, 119-124.

[69]   a) O. Ishitani, M. W. George, T. Ibusuki, F. P. Johnson, K. Koike, K. Nozaki, C. Pac, J. J. Turner, J. R. Westwell, *Inorganic Chemistry* **1994**, *33*, 4712-4717; b) H. Hori, F. P. A. Johnson, K. Koike, K. Takeuchi, T. Ibusuki, O. Ishitani, *Journal of the Chemical Society, Dalton Transactions* **1997**, 1019-1024; c) H. Hori, F. P. A. Johnson, K. Koike, O. Ishitani, T. Ibusuki, *Journal of Photochemistry and Photobiology A: Chemistry* **1996**, *96*, 171-174.

[70]   a) C.-O. Ng, S.-M. Yiu, C.-C. Ko, *Inorganic Chemistry* **2014**, *53*, 3022-3031; b) S. Meister, Technische Universität München **2015**.

[71]   E. E. Benson, K. A. Grice, J. M. Smieja, C. P. Kubiak, *Polyhedron* **2013**, *58*, 229-234.

[72]   a) Y. Kou, Y. Nabetani, D. Masui, T. Shimada, S. Takagi, H. Tachibana, H. Inoue, *Journal of the American Chemical Society* **2014**, *136*, 6021-6030; b) T. W. Schneider, M. Z. Ertem, J. T. Muckerman, A. M. Angeles-Boza, *ACS Catalysis* **2016**, *6*, 5473-5481.

[73]   a) B. P. Sullivan, C. M. Bolinger, D. Conrad, W. J. Vining, T. J. Meyer, *Journal of the Chemical Society, Chemical Communications* **1985**, 1414-1416; b) H. Takeda, K. Koike, T. Morimoto, H. Inumaru, O. Ishitani, in *Advances in Inorganic Chemistry, Vol. 63* (Eds.: R. v. Eldik, G. Stochel), Academic Press, **2011**, pp. 137-186.

[74]   a) A. J. Morris, G. J. Meyer, E. Fujita, *Accounts of Chemical Research* **2009**, *42*, 1983-1994; b) Y. Hayashi, S. Kita, B. S. Brunschwig, E. Fujita, *Journal of the American Chemical Society* **2003**, *125*, 11976-11987.

[75]   a) C. Thomas, M. Wittig, B. Rieger, *ChemCatChem* **2022**, *14*, e202200841; b) B. Gholamkhass, H. Mametsuka, K. Koike, T. Tanabe, M. Furue, O. Ishitani, *Inorg. Chem.* **2005**, *44*, 2326-2336; c) R. Giereth, P. Lang, E. McQueen, X. Meißner, B. Braun-Cula, C. Marchfelder, M. Obermeier, M. Schwalbe, S. Tschierlei, *ACS Catalysis* **2021**, *11*, 390-403.

[76]   a) M. Hammouche, D. Lexa, J. M. Savéant, M. Momenteau, *Journal of Electroanalytical Chemistry and Interfacial Electrochemistry* **1988**, *249*, 347-351; b) K. A. Grice, N. X. Gu, M. D. Sampson, C. P. Kubiak, *Dalton Transactions* **2013**, *42*, 8498-8503; c) T. Morimoto, T. Nakajima, S. Sawa, R. Nakanishi, D. Imori, O. Ishitani, *Journal of the American Chemical Society* **2013**, *135*, 16825-16828.

[77]   a) C. Riplinger, M. D. Sampson, A. M. Ritzmann, C. P. Kubiak, E. A. Carter, *Journal of the American Chemical Society* **2014**, *136*, 16285-16298; b) E. E. Benson, C. P. Kubiak, *Chemical Communications* **2012**, *48*, 7374-7376; c) C. W. Machan, S. A. Chabolla, J. Yin, M. K. Gilson, F. A. Tezcan, C. P. Kubiak, *Journal of the American Chemical Society* **2014**, *136*, 14598-14607.

[78]   Y. Tamaki, K. Koike, T. Morimoto, O. Ishitani, *J. Catal.* **2013**, *304*, 22-28.

[79]   K. Kalyanasundaram, *Photochemistry of polypyridine and porphyrin complexes*, Academic Press, **1991**.

[80]   M. Pschenitza, S. Meister, B. Rieger, *Chemical Communications* **2018**, *54*, 3323-3326.

[81]   a) B. Probst, A. Rodenberg, M. Guttentag, P. Hamm, R. Alberto, *Inorganic Chemistry* **2010**, *49*, 6453-6460; b) Y. Pellegrin, F. Odobel, *Comptes Rendus Chimie* **2017**, *20*, 283-295.

[82]   M. Pschenitza, S. Meister, A. von Weber, A. Kartouzian, U. Heiz, B. Rieger, *ChemCatChem* **2016**, *8*, 2688-2695.

[83]   a) H. Tsubaki, A. Sekine, Y. Ohashi, K. Koike, H. Takeda, O. Ishitani, *Journal of the American Chemical Society* **2005**, *127*, 15544-15555; b) M. P. Thekaekara, *Solar Energy* **1976**, *18*, 309-325.

[84]   H. Takeda, O. Ishitani, *Coordination Chemistry Reviews* **2010**, *254*, 346-354.

[85]   a) S. Meister, R. O. Reithmeier, A. Ogrodnik, B. Rieger, *ChemCatChem* **2015**, *7*, 3562-3569; b) A. M. Cancelliere, F. Puntoriero, S. Serroni, S. Campagna, Y. Tamaki, D. Saito, O. Ishitani, *Chemical Science* **2020**, *11*, 1556-1563; c) G. Li, D. Zhu, X. Wang, Z. Su, M. R. Bryce, *Chemical Society Reviews* **2020**, *49*, 765-838.

[86]   D. J. Stufkens, A. Vlček, *Coordination Chemistry Reviews* **1998**, *177*, 127-179.

References

[87]   S. Rau, B. Schäfer, D. Gleich, E. Anders, M. Rudolph, M. Friedrich, H. Görls, W. Henry, J. G. Vos, *Angewandte Chemie International Edition* **2006**, *45*, 6215-6218.
[88]   H. Ishida, T. Terada, K. Tanaka, T. Tanaka, *Inorganic chemistry* **1990**, *29*, 905-911.
[89]   S. Fukuzumi, S. Koumitsu, K. Hironaka, T. Tanaka, *Journal of the American Chemical Society* **1987**, *109*, 305-316.
[90]   a) Y. Tamaki, T. Morimoto, K. Koike, O. Ishitani, *Proceedings of the National Academy of Sciences* **2012**, *109*, 15673-15678; b) Y. Tamaki, K. Watanabe, K. Koike, H. Inoue, T. Morimoto, O. Ishitani, *Faraday Discussions* **2012**, *155*, 115-127.
[91]   Y. Tamaki, K. Koike, O. Ishitani, *Chemical Science* **2015**, *6*, 7213-7221.
[92]   P. Matthias, K. Yoshihiro, S. Tomoyoshi, F. Shunichi, *Chemistry Letters* **1997**, *26*, 567-568.
[93]   X.-Q. Zhu, M.-T. Zhang, A. Yu, C.-H. Wang, J.-P. Cheng, *Journal of the American Chemical Society* **2008**, *130*, 2501-2516.
[94]   E. Hasegawa, S. Takizawa, T. Seida, A. Yamaguchi, N. Yamaguchi, N. Chiba, T. Takahashi, H. Ikeda, K. Akiyama, *Tetrahedron* **2006**, *62*, 6581-6588.
[95]   H. Hukkanen, T. T. Pakkanen, *Inorganica Chimica Acta* **1986**, *114*, L43-L45.
[96]   a) Z.-Y. Bian, K. Sumi, M. Furue, S. Sato, K. Koike, O. Ishitani, *Inorganic Chemistry* **2008**, *47*, 10801-10803; b) Z.-Y. Bian, K. Sumi, M. Furue, S. Sato, K. Koike, O. Ishitani, *Dalton Transactions* **2009**, 983-993; c) K. Koike, S. Naito, S. Sato, Y. Tamaki, O. Ishitani, *Journal of Photochemistry and Photobiology A: Chemistry* **2009**, *207*, 109-114; d) S. Sato, K. Koike, H. Inoue, O. Ishitani, *Photochemical & Photobiological Sciences* **2007**, *6*, 454-461; e) A. Umemoto, Y. Yamazaki, D. Saito, Y. Tamaki, O. Ishitani, *Bulletin of the Chemical Society of Japan* **2020**, *93*, 127-137.
[97]   a) Z.-Y. Bian, S.-M. Chi, L. Li, W. Fu, *Dalton Transactions* **2010**, *39*, 7884-7887; b) Z.-Y. Bian, H. Wang, W.-F. Fu, L. Li, A.-Z. Ding, *Polyhedron* **2012**, *32*, 78-85.
[98]   a) V. S. Thoi, N. Kornienko, C. G. Margarit, P. Yang, C. J. Chang, *Journal of the American Chemical Society* **2013**, *135*, 14413-14424; b) H. Takeda, C. Cometto, O. Ishitani, M. Robert, *ACS Catalysis* **2017**, *7*, 70-88; c) F. Wang, *ChemSusChem* **2017**, *10*, 4393-4402; d) Z. Guo, F. Yu, Y. Yang, C.-F. Leung, S.-M. Ng, C.-C. Ko, C. Cometto, T.-C. Lau, M. Robert, *ChemSusChem* **2017**, *10*, 4009-4013; e) H. Takeda, K. Ohashi, A. Sekine, O. Ishitani, *Journal of the American Chemical Society* **2016**, *138*, 4354-4357; f) A. Rosas-Hernández, C. Steinlechner, H. Junge, M. Beller, *Green Chemistry* **2017**, *19*, 2356-2360; g) Z. Guo, S. Cheng, C. Cometto, E. Anxolabéhère-Mallart, S.-M. Ng, C.-C. Ko, G. Liu, L. Chen, M. Robert, T.-C. Lau, *Journal of the American Chemical Society* **2016**, *138*, 9413-9416; h) T. Ouyang, H.-H. Huang, J.-W. Wang, D.-C. Zhong, T.-B. Lu, *Angewandte Chemie International Edition* **2017**, *56*, 738-743; i) H. Takeda, H. Koizumi, K. Okamoto, O. Ishitani, *Chemical Communications* **2014**, *50*, 1491-1493.
[99]   a) W.-M. Liao, J.-H. Zhang, Y.-J. Hou, H.-P. Wang, M. Pan, *Inorganic Chemistry Communications* **2016**, *73*, 80-89; b) Y. Tamaki, K. Koike, T. Morimoto, Y. Yamazaki, O. Ishitani, *Inorganic Chemistry* **2013**, *52*, 11902-11909; c) R. O. Reithmeier, S. Meister, A. Siebel, B. Rieger, *Dalton Transactions* **2015**, *44*, 6466-6472; d) C. D. Windle, E. Pastor, A. Reynal, A. C. Whitwood, Y. Vaynzof, J. R. Durrant, R. N. Perutz, E. Reisner, *Chemistry – A European Journal* **2015**, *21*, 3746-3754; e) Y. Yamazaki, O. Ishitani, *Chemical Science* **2018**, *9*, 1031-1041.
[100]   T. Inoue, A. Fujishima, S. Konishi, K. Honda, *Nature* **1979**, *277*, 637.
[101]   a) T. Yui, A. Kan, C. Saitoh, K. Koike, T. Ibusuki, O. Ishitani, *ACS Applied Materials & Interfaces* **2011**, *3*, 2594-2600; b) K. Iizuka, T. Wato, Y. Miseki, K. Saito, A. Kudo, *Journal of the American Chemical Society* **2011**, *133*, 20863-20868.
[102]   a) M. Ogawa, K. Kuroda, *Chemical Reviews* **1995**, *95*, 399-438; b) T. Shichi, K. Takagi, *Journal of Photochemistry and Photobiology C: Photochemistry Reviews* **2000**, *1*, 113-130; c) T. Takashi, Y. Tatsuto, F. Mamoru, T. Katsuhiko, M. Tetsuro, *Chemistry Letters* **2005**, *34*, 1522-1523; d) T. Yui, H. Takeda, Y. Ueda, K. Sekizawa, K. Koike, S. Inagaki, O. Ishitani, *ACS Appl. Mater. Interfaces.* **2014**, *6*, 1992-1998; e) S. Zhong, Y. Xi, S. Wu, Q. Liu, L. Zhao, S. Bai, *Journal of Materials Chemistry A* **2020**, *8*, 14863-14894.

References

[103]   a) C. Costentin, S. Drouet, M. Robert, J.-M. Savéant, *Science* **2012**, *338*, 90-94; b) N. Miyamoto, Y. Yamada, S. Koizumi, T. Nakato, *Angew. Chem.* **2007**, *119*, 4201-4205; c) J. D. Bartl, C. Thomas, A. Henning, M. F. Ober, G. Savasci, B. Yazdanshenas, P. S. Deimel, E. Magnano, F. Bondino, P. Zeller, L. Gregoratti, M. Amati, C. Paulus, F. Allegretti, A. Cattani-Scholz, J. V. Barth, C. Ochsenfeld, B. Nickel, I. D. Sharp, M. Stutzmann, B. Rieger, *Journal of the American Chemical Society* **2021**, *143*, 19505-19516; d) S. Oh, J. R. Gallagher, J. T. Miller, Y. Surendranath, *Journal of the American Chemical Society* **2016**, *138*, 1820-1823; e) P. D. Tran, L. H. Wong, J. Barber, J. S. C. Loo, *Energy & Environmental Science* **2012**, *5*, 5902-5918.

[104]   a) T. Yui, Y. Kobayashi, Y. Yamada, K. Yano, Y. Fukushima, T. Torimoto, K. Takagi, *ACS Appl. Mater. Interfaces.* **2011**, *3*, 931-935; b) M. Schreier, J. Luo, P. Gao, T. Moehl, M. T. Mayer, M. Grätzel, *Journal of the American Chemical Society* **2016**, *138*, 1938-1946; c) A. Ge, B. Rudshteyn, P. E. Videla, C. J. Miller, C. P. Kubiak, V. S. Batista, T. Lian, *Acc. Chem. Res.* **2019**, *52*, 1289-1300.

[105]   a) K. Maeda, K. Sekizawa, O. Ishitani, *Chem. Commun.* **2013**, *49*, 10127-10129; b) K. V. Rao, K. K. R. Datta, M. Eswaramoorthy, S. J. George, *Chemistry – A European Journal* **2012**, *18*, 2184-2194; c) Y. Ishida, T. Shimada, D. Masui, H. Tachibana, H. Inoue, S. Takagi, *Journal of the American Chemical Society* **2011**, *133*, 14280-14286; d) D. Saito, Y. Yamazaki, Y. Tamaki, O. Ishitani, *Journal of the American Chemical Society* **2020**, *142*, 19249-19258.

[106]   a) P. M. Stanley, C. Thomas, E. Thyrhaug, A. Urstoeger, M. Schuster, J. Hauer, B. Rieger, J. Warnan, R. A. Fischer, *ACS Catalysis* **2021**, *11*, 871-882; b) S. Sato, T. Morikawa, S. Saeki, T. Kajino, T. Motohiro, *Angewandte Chemie International Edition* **2010**, *49*, 5101-5105; c) H. Takeda, M. Ohashi, T. Tani, O. Ishitani, S. Inagaki, *Inorganic chemistry* **2010**, *49*, 4554-4559; d) Y. Ueda, H. Takeda, T. Yui, K. Koike, Y. Goto, S. Inagaki, O. Ishitani, *ChemSusChem* **2015**, *8*, 439-442; e) Y. Kou, S. Nakatani, G. Sunagawa, Y. Tachikawa, D. Masui, T. Shimada, S. Takagi, D. A. Tryk, Y. Nabetani, H. Tachibana, *Journal of catalysis* **2014**, *310*, 57-66; f) F. Yoshitomi, K. Sekizawa, K. Maeda, O. Ishitani, *ACS applied materials & interfaces* **2015**, *7*, 13092-13097; g) C. S. Diercks, Y. Liu, K. E. Cordova, O. M. Yaghi, *Nature materials* **2018**, *17*, 301-307.

[107]   C. Ci, J. J. Carbó, R. Neumann, C. d. Graaf, J. M. Poblet, *ACS Catalysis* **2016**, *6*, 6422-6428.

[108]   a) A. Nakada, T. Nakashima, K. Sekizawa, K. Maeda, O. Ishitani, *Chemical Science* **2016**, *7*, 4364-4371; b) G. Sahara, H. Kumagai, K. Maeda, N. Kaeffer, V. Artero, M. Higashi, R. Abe, O. Ishitani, *Journal of the American Chemical Society* **2016**, *138*, 14152-14158; c) H. Kumagai, G. Sahara, K. Maeda, M. Higashi, R. Abe, O. Ishitani, *Chemical Science* **2017**, *8*, 4242-4249.

[109]   a) T. Arai, S. Sato, T. Kajino, T. Morikawa, *Energy & Environmental Science* **2013**, *6*, 1274-1282; b) T. M. Suzuki, S. Yoshino, T. Takayama, A. Iwase, A. Kudo, T. Morikawa, *Chemical Communications* **2018**, *54*, 10199-10202.

[110]   a) L. Veronese, E. Q. Procopio, F. De Rossi, T. M. Brown, P. Mercandelli, P. Mussini, G. D'Alfonso, M. Panigati, *New Journal of Chemistry* **2016**, *40*, 2910-2919; b) E.-G. Ha, J.-A. Chang, S.-M. Byun, C. Pac, D.-M. Jang, J. Park, S. O. Kang, *Chemical Communications* **2014**, *50*, 4462-4464.

[111]   Y. Izumi, *Coordination Chemistry Reviews* **2013**, *257*, 171-186.

[112]   a) E. Torralba-Peñalver, Y. Luo, J.-D. Compain, S. Chardon-Noblat, B. Fabre, *ACS Catalysis* **2015**, *5*, 6138-6147; b) Y. M. A. Yamada, Y. Yuyama, T. Sato, S. Fujikawa, Y. Uozumi, *Angewandte Chemie International Edition* **2014**, *53*, 127-131; c) L. B. Hoch, P. G. O'Brien, A. Jelle, A. Sandhel, D. D. Perovic, C. A. Mims, G. A. Ozin, *ACS Nano* **2016**, *10*, 9017-9025; d) S. Ahoulou, E. Perret, J.-M. Nedelec, *Nanomaterials* **2021**, *11*, 999; e) D. Voiry, H. S. Shin, K. P. Loh, M. Chhowalla, *Nature Reviews Chemistry* **2018**, *2*, 0105.

[113]   N. Lu, I. Ferguson, *Semiconductor Science and Technology* **2013**, *28*, 074023.

[114]   a) I. Vurgaftman, J. R. Meyer, *Journal of Applied Physics* **2003**, *94*, 3675-3696; b) H. S. Jung, Y. J. Hong, Y. Li, J. Cho, Y. J. Kim, G. C. Yi, *ACS Nano* **2008**, *2*, 637-642; c) B. J. Baliga, *Semiconductor Science and Technology* **2013**, *28*, 074011.

References

[115] H. Jeong, R. Salas-Montiel, G. Lerondel, M. S. Jeong, *Scientific Reports* **2017**, *7*, 45726.
[116] M. Stutzmann, J. A. Garrido, M. Eickhoff, M. S. Brandt, *physica status solidi (a)* **2006**, *203*, 3424-3437.
[117] a) D. Wang, A. Pierre, M. G. Kibria, K. Cui, X. Han, K. H. Bevan, H. Guo, S. Paradis, A.-R. Hakima, Z. Mi, *Nano Letters* **2011**, *11*, 2353-2357; b) B. AlOtaibi, S. Fan, D. Wang, J. Ye, Z. Mi, *ACS Catalysis* **2015**, *5*, 5342-5348.
[118] G. Sahara, O. Ishitani, *Inorganic Chemistry* **2015**, *54*, 5096-5104.
[119] a) J. Winnerl, R. Hudeczek, M. Stutzmann, *Journal of Applied Physics* **2018**, *123*, 203104; b) M. Hetzl, F. Schuster, A. Winnerl, S. Weiszer, M. Stutzmann, *Materials Science in Semiconductor Processing* **2016**, *48*, 65-78.
[120] a) B. AlOtaibi, M. Harati, S. Fan, S. Zhao, H. P. T. Nguyen, M. G. Kibria, Z. Mi, *Nanotechnology* **2013**, *24*, 175401; b) J. B. Park, N.-J. Kim, Y.-J. Kim, S.-H. Lee, G.-C. Yi, *Current Applied Physics* **2014**, *14*, 1437-1442; c) F. Schuster, M. Hetzl, S. Weiszer, J. A. Garrido, M. de la Mata, C. Magen, J. Arbiol, M. Stutzmann, *Nano Letters* **2015**, *15*, 1773-1779; d) J. Zhang, Y. Wang, J. Jin, J. Zhang, Z. Lin, F. Huang, J. Yu, *ACS Applied Materials & Interfaces* **2013**, *5*, 10317-10324; e) M. Hetzl, F. Schuster, A. Winnerl, S. Weiszer, M. Stutzmann, *Materials Science in Semiconductor Processing* **2016**, *55*, 32-45.
[121] H. Kim, P. E. Colavita, P. Paoprasert, P. Gopalan, T. F. Kuech, R. J. Hamers, *Surface Science* **2008**, *602*, 2382-2388.
[122] B. Neises, W. Steglich, *Angewandte Chemie International Edition in English* **1978**, *17*, 522-524.
[123] J. D. Bartl, Technische Universität München **2022**.
[124] a) R. Zhao, P. Rupper, S. Gaan, *Coatings* **2017**, *7*, 133; b) A. Ringk, X. Li, F. Gholamrezaie, E. C. P. Smits, A. Neuhold, A. Moser, C. Van der Marel, G. H. Gelinck, R. Resel, D. M. de Leeuw, P. Strohriegl, *Advanced Functional Materials* **2013**, *23*, 2016-2023.
[125] C. Pac, Y. Miyauchi, O. Ishitani, M. Ihama, M. Yasuda, H. Sakurai, *The Journal of Organic Chemistry* **1984**, *49*, 26-34.
[126] a) K. Kamogawa, Y. Shimoda, K. Miyata, K. Onda, Y. Yamazaki, Y. Tamaki, O. Ishitani, *Chemical Science* **2021**, *12*, 9682-9693; b) Y. Yamazaki, K. Ohkubo, D. Saito, T. Yatsu, Y. Tamaki, S. i. Tanaka, K. Koike, K. Onda, O. Ishitani, *Inorganic Chemistry* **2019**, *58*, 11480-11492; c) K. Koike, D. C. Grills, Y. Tamaki, E. Fujita, K. Okubo, Y. Yamazaki, M. Saigo, T. Mukuta, K. Onda, O. Ishitani, *Chemical Science* **2018**, *9*, 2961-2974.
[127] a) R. Kamata, H. Kumagai, Y. Yamazaki, G. Sahara, O. Ishitani, *ACS Applied Materials & Interfaces* **2019**, *11*, 5632-5641; b) U. S. Schubert, C. Eschbaumer, *Angewandte Chemie International Edition* **2002**, *41*, 2892-2926; c) F. Adams, M. Pschenitza, B. Rieger, *ChemCatChem* **2018**, *10*, 4309-4316.
[128] a) M. G. M. Knaus, M. M. Giuman, A. Pöthig, B. Rieger, *Journal of the American Chemical Society* **2016**, *138*, 7776-7781; b) M. Weger, M. M. Giuman, M. G. Knaus, M. Ackermann, M. Drees, J. Hornung, P. J. Altmann, R. A. Fischer, B. Rieger, *Chemistry – A European Journal* **2018**, *24*, 14950-14957.
[129] K. Ohkubo, Y. Yamazaki, T. Nakashima, Y. Tamaki, K. Koike, O. Ishitani, *Journal of Catalysis* **2016**, *343*, 278-289.
[130] M. Furue, M. Naiki, Y. Kanematsu, T. Kushida, M. Kamachi, *Coordination Chemistry Reviews* **1991**, *111*, 221-226.
[131] a) N. Herzer, S. Hoeppener, U. S. Schubert, *Chemical Communications* **2010**, *46*, 5634-5652; b) L. Wang, U. S. Schubert, S. Hoeppener, *Chemical Society Reviews* **2021**, *50*, 6507-6540; c) T. Cottineau, M. Morin, D. Bélanger, *RSC Advances* **2013**, *3*, 23649-23657.
[132] M. A. H. Khan, M. V. Rao, *Sensors* **2020**, *20*, 3889.
[133] A. S. Maier, C. Thomas, M. Kränzlein, T. M. Pehl, B. Rieger, *Macromolecules* **2022**, *55*, 7039-7048.
[134] R. O. Reithmeier, S. Meister, B. Rieger, A. Siebel, M. Tschurl, U. Heiz, E. Herdtweck, *Dalton Transactions* **2014**, *43*, 13259-13269.

References

[135] M. Hammouche, D. Lexa, M. Momenteau, J. M. Saveant, *Journal of the American Chemical Society* **1991**, *113*, 8455-8466.
[136] D.-C. Liu, H.-H. Huang, J.-W. Wang, L. Jiang, D.-C. Zhong, T.-B. Lu, *ChemCatChem* **2018**, *10*, 3435-3440.
[137] S. Kapusta, N. Hackerman, *Journal of The Electrochemical Society* **1984**, *131*, 1511.
[138] a) D. Hong, Y. Tsukakoshi, H. Kotani, T. Ishizuka, T. Kojima, *Journal of the American Chemical Society* **2017**, *139*, 6538-6541; b) L. Chen, Z. Guo, X.-G. Wei, C. Gallenkamp, J. Bonin, E. Anxolabéhère-Mallart, K.-C. Lau, T.-C. Lau, M. Robert, *Journal of the American Chemical Society* **2015**, *137*, 10918-10921.